Anisotropic Diffusion Approximations for Time-dependent Particle Transport

by

Seth R. Johnson

A dissertation submitted in partial fulfillment
of the requirements for the degree of
Doctor of Philosophy
(Nuclear Engineering and Radiological Sciences)
in The University of Michigan
2012

Doctoral Committee:

Professor Edward W. Larsen, Chair
Professor Thomas J. Downar
Professor James P. Holloway
Professor William R. Martin
Professor Katsuyo S. Thornton

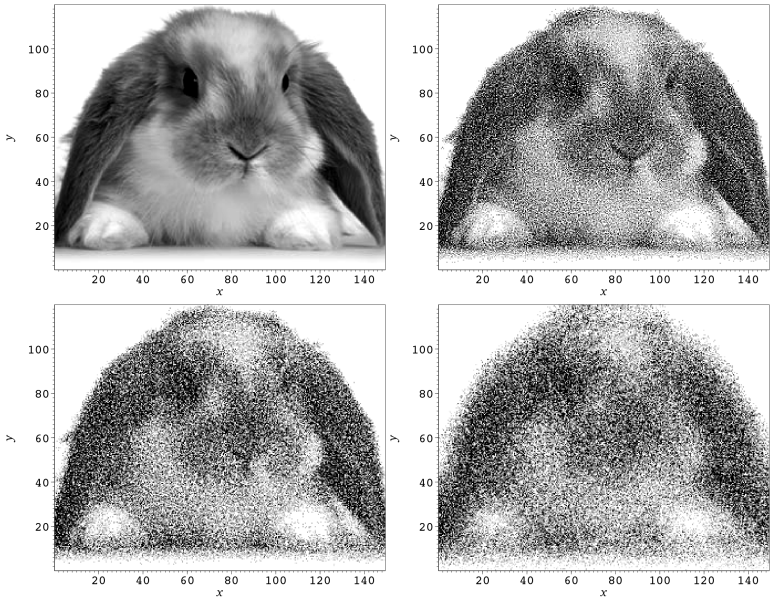
y
x
20
40
60
80
100
120
140

© Seth R. Johnson

All Rights Reserved

2012

To my parents, Doug and Carol.

Acknowledgments

This dissertation would not have been possible without a lifetime of edification by others. The foremost of these mentors are my parents, who helped my interest in science to blossom at an early age [1]. Other strong influences over the years include Kristen Jones, whose leadership in high school Science Bowl stands out particularly; Bruce Freeman, who gave invaluable opinions, advice, and support during my undergraduate internships; Kevin Clarno, an integral force in shaping my interest in reactor analysis and transport methods; and the inimitable Todd Urbatsch, whose work and mentoring at LANL gave me a solid foundation for my TRT research projects and codes.

My most recent mentor, Dr. Ed Larsen, has my greatest appreciation and thanks. His methodical derivations—as well as his practically limitless patience for an upstart like myself—were essential in my graduate education and research experiences. The members of my committee also have my grateful appreciation for their help in this work.

In addition to these more formal mentors are my friends over the years who have taken something of a mentoring role. Greg Davidson, Jesse Cheatham, and Troy Becker transitioned me into graduate school and have remained fast friends since. The particular friendship of Shaun and Adrianne Clarke have helped me to grow during these years in Michigan. My brother Aaron and sister Naomi have remained a source of motivation and endurance. Among the many other friends and family members who have encouraged me in my endeavors are Y. Trump, M. Graham, S. Joshi, K. Wichman, and D. Jabaay; but space does not permit me to enumerate all whom I value and appreciate.

I also thank the National Science Foundation for its financial support via the Graduate Research Fellowship Program, the Department of Energy for its Nuclear Energy University Programs fellowship, and the NERS department for its support and its management of the day-to-day necessities.

Finally, I offer all glory and praise to Jesus Christ, the Creator and my Redeemer. Apart from Him, nothing could be possible—especially not this dissertation.

Table of Contents

List of Tables

Table

List of Figures

Figure

Abstract

In this thesis, we develop and numerically test new approximations to time-dependent radiation transport with the goal of obtaining more accurate solutions than the diffusion approximation can generate, yet requiring less computational effort than full transport. The first method is the nascent anisotropic diffusion (AD) approximation, which we extend to time-dependent problems in finite domains; the second is a novel anisotropic P_1-like (AP_1) approximation. These methods are "anisotropic" in that, rather than operating under the assumption of linearly anisotropic radiation, they incorporate an arbitrary amount of anisotropy via a transport-calculated diffusion coefficient. This anisotropic diffusion tensor is the second angular moment of a simple, purely absorbing transport problem.

In this thesis, much of the computational testing of the new methods is performed in "flatland" geometry, a fictional two-dimensional universe that provides a realistic but computationally inexpensive testbed. As work ancillary to anisotropic diffusion and the numerical experiments, a complete description of flatland diffusion, including boundary conditions, is developed. Also, implementation details for both Monte Carlo and S_N transport in flatland are provided.

The two new anisotropic methods, along with a "flux limited" modification to anisotropic diffusion, are tested in a variety of problems. Some aspects of the theory, including the newly formulated boundary conditions, are tested first with diffusive, steady-state problems. The new methods are compared against existing ones in linear, time-dependent radiation transport problems. Finally, the efficacy and performance of the anisotropic methods are investigated in several thermal radiative transfer (TRT) computational experiments.

Our results demonstrate that for many multi-dimensional problems, the new anisotropic methods perform much better than their conventional counterparts. In every time-dependent test, the flux-limited anisotropic diffusion approach produced the most accurate solutions of the new methods. Based on our numerical testing, we believe this method to be a strong contender for accurate, inexpensive simulations of time-dependent transport and thermal radiative transfer problems.

Chapter 1
Introduction

Nuclear engineering consists primarily of the development of tools to harness the power of the atomic nucleus and of high-energy radiation. This field encompasses such disparate areas as plasma physics, radiation detection, nuclear reactor design, and atomic particle transport. The last area is the study of how statistically large numbers of fundamental particles interact with (and are *transported* through) matter: it accounts for the behavior of neutrons in a nuclear reactor, gamma rays in shielding applications, electrons in cancer therapy, and photons in radiative transfer problems. This thesis is concerned with a particular regime of radiative transfer known as *thermal radiative transfer* (TRT).

The difficulty, expense, and impracticality of performing physical experiments in many fields has produced a tremendous drive to *simulate* physical experiments using powerful computers. The exponentially increasing power and decreasing cost of transistor-based technology have led to the rise of computational methods development: researching and implementing accurate, practical approximations to the physical equations that describe reality. Our work is in the field of computational particle transport, and our goal is to develop a new, accurate, inexpensive approximation to the equations of thermal radiative transfer.

A recent advance in computational methods development is the anisotropic diffusion (AD) approximation, recently used to model steady-state neutron transport for nuclear reactor analysis, viz. a very high temperature reactor (VHTR) mock-up [2, 3], for which AD showed promising results. A similar tensor diffusion method was also independently formulated for steady-state photon transport [4], but it has not been numerically tested. Both derivations assumed an infinite medium operating at steady state. Those two assumptions rarely hold for TRT problems, which typically change rapidly as a function of time and necessarily operate in a finite volume. In the new work presented here, we derive a complete theory describing the anisotropic diffusion approximation for time-dependent transport problems in finite media. A similar derivation leads to a new "anisotropic P_1" (AP_1) method.

Although we develop the theory for a general three-dimensional (3-D) space, true 3-D

simulations are expensive because of the expansive problem phase space: the monoenergetic time-dependent transport equations operate in three spatial coordinates (x, y, z), two angular coordinates (μ, ω), and time t. Even two-dimensional (2-D) problems, which model a system invariant in the z direction, operate in a five-dimensional phase space (x, y, μ, ω, t). A "toy" geometry called *flatland* [5], recently used in particle transport methods development [6, 2], reduces the phase space to (x, y, ω, t) by constraining particles to a two-dimensional plane. Flatland retains the complexity of multi-dimensional space while decreasing the computational burden. A notable part of this thesis is the investigation of flatland and its application to transport methods development.

To verify the accuracy of the newly developed anisotropic approximations, it is necessary to compare their performance and accuracy against that of existing, proven methods. Therefore, we compare the AD and AP_1 methods against their competitors in several numerical experiments, most of them using flatland geometry. Due to the complexity of the thermal radiative transfer process, we first test individual aspects of the theory. In particular, we verify the predicted boundary conditions in several steady-state flatland problems [7], and we test the time-dependent behavior in "linear" radiation transport problems, which omit the nonlinear material–radiation coupling of TRT.

Finally, we apply the new anisotropic approximations to thermal radiative transfer problems. We begin with a simple one-dimensional problem used to test various nonlinear schemes [8] that demonstrates behaviors characteristic of the methods. A second TRT test problem is a flatland simulation [9] inspired by a particular TRT experiment—the behavior of a laser-driven shock wave in a small tube filled with xenon gas—in the Center for Radiative Shock Hydrodynamics (CRASH) program [10]. We assess the efficacy of the AD methods in more strongly multi-dimensional geometry: an optically thin tube with two bends in it. To test its behavior in problems that lack thin channels, we compare other difficult two-dimensional benchmark problems seen in the literature [11]. This range of test problems provides a wide and fair assessment of the AD methods, demonstrating both their limitations and their strengths.

1.1 Thermal radiative transfer

As stated earlier, thermal radiative transfer models the behavior of photons in hot materials as they move energy about the system. Radiation is the primary means of heat transfer in many physical problems, such as stellar astrophysics and fusion experiments [12, 13]. These systems operate at the extreme temperatures necessary to apply the TRT model used in this thesis.

Engineering students know from their heat transfer classes that conduction and convection transfer energy proportionally to the material temperature T, but radiative energy transfer via black-body emission is proportional to T^4. Thus, when T is very large, conduction and convection can be neglected, but emission cannot. Other reasonable assumptions reduce the phenomena of TRT to the coupling of two dependent variables: the space- and time-dependent material temperature T, and the radiation intensity I.

The intensity I, analogous to the "angular flux" in the reactor physics world, describes the state and distribution of photons in space $\boldsymbol{x}$, angle $\boldsymbol{\Omega}$, and time t. (In this discussion, we ignore the frequency-dependent nature of radiation.) The spatial and temporal variables are self-explanatory; the angular variable essentially determines a photon's velocity = $c\boldsymbol{\Omega}$, using the speed of light c.[1] More photons traveling in a certain direction at a certain point in space-time give rise to a larger value in the intensity—an example (outside of TRT) could be an "intense" flashlight being shone in one's eyes. The time-dependent behavior of the intensity is described by the Boltzmann transport equation [14], sometimes referred to in the astrophysics literature as the transfer equation [13]. The transport equation will be discussed in further detail later.

The second quantity, the material temperature $T(\boldsymbol{x}, t)$, is a measure of the amount of energy stored in the atoms and electrons in the problem at point $\boldsymbol{x}$ at time t. When an electron absorbs a photon, the material energy increases by exactly the amount that the radiation intensity lost by the absorption event. When the material emits a photon via the black body process, the lost material energy is transferred to the radiation field.

The absorption of photons by the material, the black body emission process, and the straight-line travel of "streaming" photons constitute the thermal radiative transfer process. The rate of absorption of photons is proportional to the opacity σ, analogous to the neutron cross section in reactor physics. Unlike the neutron cross section, the value of σ is a strong function of the material temperature, usually proportional to T^{-3}, and therefore colder regions of a given material are more opaque (optically thick).

Because of the inverse cubic proportionality of the opacity and the quartic proportionality of radiative emission, most TRT problems share a qualitative behavior. The evolution of a system through time tends to show the problem equilibrating by the progressive deposition of energy within a few mean free paths of a hot region. In other words, a layer of cold material will absorb a great quantity of radiation, heating up and beginning to emit radiation into the adjacent cold material. This time-dependent evolution is often

[1] "Photons" as used in radiation transport actually represent statistically large numbers of particles. Quantum uncertainty is not applicable to the particle transport with which we are concerned: we can know both the position and velocity of a "particle" exactly.

called a radiation shock or Marshak wave [15].

In summary, the thermal radiative transfer equations describe a physically complex phenomenon. The transport equation alone is difficult to model, but the strong nonlinearity in σ and in T^4 black body emission make the TRT equations particularly formidable. Analytically solving the TRT equations even in the simplest realistic problem is essentially impossible, hence the need for numerical solutions. The anisotropic diffusion approximation provides a new method for numerically solving the radiation transport aspect of the TRT equations.

1.2 Overview of TRT solution methods

The TRT equations have a large solution phase space and are strongly nonlinear; thus, they are difficult to solve accurately and quickly. Since the first simulations of radiative transfer at the dawn of the computer age [16, 17], numerous computational solution methods have been formulated. The more useful of these have been reviewed extensively in previous works [16, 17, 18, 19, 20, 21]; to give a proper context for the new AD method, we give a brief overview of them here.

1.2.1 Monte Carlo methods

The Monte Carlo (MC) method models a random physical process by simulating the random "history" of a statistically large number of particles [22]. Each stochastic aspect of particle transport—birth, collision, scattering, etc.—is described by a set of probability distribution functions. Between events, the simulated particle travels along its stored direction $\boldsymbol{\Omega}$ from its stored position $\boldsymbol{x}$. The average behavior of large numbers of particles (and how large is "large" depends on the complexity of the problem) gives the solution. Each particle history can be expensive, and the accuracy of the solution is roughly inversely proportional to the square root of the number of simulated particles: the Monte Carlo process gives accurate answers, but it is computationally expensive.

For linear source-driven transport, which is used e.g. in reactor analysis, the solution methodology is largely intuitive, because each particle is completely independent from every other. However, the nonlinear nature of the TRT equations—specifically that the behavior of the photons influence the state of the material, which in turn influences the behavior of other photons—makes a Monte Carlo interpretation of TRT far from clear.

The first successful Monte Carlo method for simulating radiative transfer was Fleck and Cummings' Implicit Monte Carlo (IMC) method [23, 21], which is still widely used

today [24]. Through the mathematical process of linearization, it approximates the nonlinear terms in the TRT equations with linear terms over a short period of time. The linearization essentially models the process of absorption and black body reëmission[2] of photons as isotropic "pseudo-scattering." The resulting linear transport equation in each time step is solved with Monte Carlo to calculate the end-of-time-step radiation intensity.

Unlike linear MC methods, IMC does not limit to the exact solution with increasing number of particles. In addition to the statistical error incurred by the finite particle count, the linearization of the physics requires the imposition of both a temporal and a spatial grid, which leads to truncation errors in time and space. A further complication arises because the space and time grids must be properly correlated: for example, a fine spatial grid with a large time step will produce the unphysical artifact known as a violation of the maximum principle [26]. Additionally, to limit the statistical error (which typically shows up as random "noise" in the solution), the number of particles per space-time region must remain roughly constant. Finally, unlike linear Monte Carlo methods, which only need to accumulate "tallies," IMC requires that the full state of the radiation intensity be stored in computer memory. Therefore, generating an accurate fine-mesh solution with IMC requires an exceedingly large amount of computer time and memory.

Other Monte Carlo methods [27, 28, 29, 30] have been developed to simulate TRT, but they will not be discussed here.

Even though the IMC method is approximate, it is generally accepted to give accurate answers, and is thus used as the primary benchmark tool in our numerical experiments.

1.2.2 Deterministic transport

Rather than using a "stochastic" Monte Carlo interpretation of the physical process of radiation transport, "deterministic" transport methods approximate the partial differential equation itself. Deterministic methods make mathematical approximations to the transport equation, replacing the continuous nature of the variables with discrete unknowns that can be represented on a computer. The result is a large system of linear equations that can be solved, typically in an iterative process.

The most popular deterministic method is the discrete ordinates (S_N) transport method [31], which approximates the angular variable $\mathbf{\Omega}$ as a quadrature set of discrete directions. There are numerous ways to discretize the time and space variables, each of which adds the penalty of discretization error to the solution. These discrete approximations limit the accuracy of the S_N method as compared to a low-variance Monte Carlo

[2] For an in-depth discussion of the diæresis, refer to R. McClarren's seminal work on the inclusion of faux pretentious footnotes in a dissertation [25, p.18].

solution, but the discrete ordinates method is typically less computationally expensive.

To use S_N for thermal radiative transfer problems, a linearization process similar to IMC's is performed; it too leads to a pseudo-scattering term. For purely absorbing steady-state problems, calculating an S_N solution is relatively inexpensive. (We shall take advantage of this property in our anisotropic diffusion approximation.) However, because of the pseudoscattering term, S_N solutions for TRT problems can converge very slowly.

Like IMC, the S_N method requires the full solution of the radiation intensity I to be stored at the end of each time step. It is computationally intensive and requires large amounts of storage. In fact, high-fidelity transport solutions to some realistic 3-D problems are beyond the capability of even today's computers. Accurate but less computationally expensive approximations to transport are needed.

1.2.3 The diffusion approximation

If true transport methods are out of reach, it becomes necessary to make coarser approximations to the transport equation. The most common course of action is to entirely eliminate the angular variable from the transport equation, greatly reducing both the computational difficulty and required storage.

The diffusion approximation has been a mainstay of reactor analysis and TRT alike since the days of the Manhattan project. In systems whose intensity (or neutron flux in the case of nuclear reactors) change very slowly as a function of space, time, and angle, it is possible to show [32, 33] that the transport solution satisfies a relationship known as Fick's law. This "law" states that the flow of particles is only a function of the gradient of their density: particles diffuse from areas of high concentration to low concentration.

Diffusion is often used far outside its theoretical range of applicability and can lead to physically inaccurate answers. A particular artifact of the diffusion approximation is that, in time-dependent transport, energy can move faster than the speed of light. One effective but *ad hoc* means to counter this nonphysical effect is to use a "flux limiter." Flux-limited diffusion (FLD) can provide qualitatively accurate answers to certain TRT problems [18], and computationally it is relatively inexpensive, so it a common means of approximating thermal radiative transfer.

1.3 Contribution of this work

The different approximations to TRT are represented qualitatively in Fig. 1.1. The two predominant transport methods—IMC and S_N—are accurate but slow; flux-limited diffusion is fast but potentially inaccurate. No method yet provides a middle ground that balances accuracy and speed.

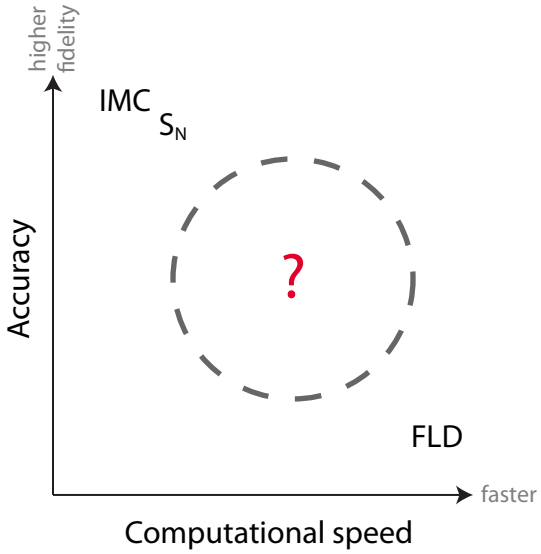

Figure 1.1: Figurative representation of existing TRT methods, showing the trade-off between accuracy and speed.

With our development of anisotropic diffusion and its application to TRT, we hope to provide a new solution process that is much less expensive than full-fledged transport but more theoretically robust than standard diffusion or FLD. Such a method would fit near the question mark in Fig. 1.1.

1.4 Synopsis

The remainder of this thesis is organized into the following chapters.

Chapter 2: Background to Thermal Radiative Transfer

The assertions about the difficulty of computational modeling of thermal radiative transfer are explained by presenting the equations themselves. We give a brief overview of existing approximations to the TRT equations and discuss how those approximations are used in our work. Particular emphasis is given to the semi-implicit treatment, which allows the nonlinear problem to be approximated by a system of linear equations.

Chapter 3: Anisotropic Diffusion

With the transport equation in hand, we derive a new approximation to radiation transport, anisotropic diffusion. The derivation accounts for both time dependence and boundary conditions. We then discuss some of the properties of the AD method and make predictions for its range of applicability.

Chapter 4: Anisotropic P_1

The derivation of the time-dependent AD equations assumed that the solution changes slowly in time, which can be a poor approximation when applied to TRT: it can actually lead to the nonphysical transfer of energy faster than the speed of light. This chapter addresses that shortcoming by modifying the ansatz used in deriving the anisotropic diffusion equations, leading to a new "anisotropic P_1" method.

Chapter 5: Low-order Discretization Schemes

The leakage terms for anisotropic diffusion are more complex than standard diffusion: rather than a scalar diffusion coefficient, AD has a diffusion tensor. This necessitates unusual discretization schemes in all but the simplest of problems. We present new discretization schemes for Cartesian x–y geometry that can account for the transverse leakage induced by the anisotropic diffusion tensor.

Chapter 6: Flatland geometry

As mentioned earlier, the "flatland" geometry has recently proven to be a valuable test bed for new transport methods because of its smaller phase space and correspondingly easier solution. This chapter gives a thorough overview of the differences between flatland and true 3-D geometries, with a focus on implementing flatland solvers. We also explore diffusion in flatland, not only deriving the prior result that the diffusion coefficient is different but also formulating correct diffusion boundary conditions. Finally, we present the AD equations in flatland geometry.

Chapter 7: Numerical Results: Linear Test Problems

Before applying the anisotropic approximations to full nonlinear transport in multi-dimensional geometries, it is important that we test individual components of the derivation. We detail several steady-state problems that test the discretization schemes, flatland diffusion boundary conditions, and anisotropic diffusion boundary conditions. We also

test some simple linear transport problems.

Chapter 8: Numerical Results: Thermal Radiative Transfer

Finally, we test the applicability of the anisotropic methods to the nonlinear TRT equations. To begin, we examine a few simple test problems in 1-D, where the anisotropic methods merely "smear" the diffusion coefficients spatially. This provides a test bed for determining the robustness of the nonlinear treatment. Then we move to more complicated flatland problems that simulate radiation flow through an optically thin channel. (This is the qualitative configuration of the CRASH problem.) Additionally, we apply the AD method to some difficult 2-D problems in the literature that feature optically thick obstacles rather than optically thin streaming channels.

Chapter 9: Conclusions

The final chapter summarizes the new theory, applications, and results developed in this thesis. We discuss potential refinements to the new methods and other future work.

Chapter 2

Background to Thermal Radiative Transfer

To elucidate the derivation of the anisotropic diffusion approximation, it is necessary to delve into the physical process of radiation transport. As discussed in the introduction, thermal radiative transfer is the physical process of energy transfer via high-energy photons in hot materials. Because the TRT equations and approximations have been probed and reviewed in other works [13, 12, 20, 21], our aim is a concise explanation of the physics relevant to the anisotropic diffusion approximation and its immediate application, rather than a thorough overview of the extensive field of radiation hydrodynamics. We also review the derivation of competing solution methods and discuss their advantages and shortcomings.

2.1 Nonlinear radiation transport

Thermal radiative transfer describes the motion of high-energy photons in a very hot material, such as the interior of a star or the target of a laser fusion experiment. The equations that model TRT are time-dependent, contain strong nonlinearities, and reside in a large phase space. A full representation of the physics in the high-energy-density regime often includes the consideration of moving relativistic materials, different electron and ion temperatures, photon scattering, and thermal conduction in the material [13]. However, much work in the methods development field neglects these complex phenomena by

- working in a fixed medium, disregarding material advection;
- assuming local thermodynamic equilibrium (LTE), which uses a single material temperature;
- neglecting photon scattering, which tends to be small;
- neglecting thermal conduction, since energy transfer is dominated by radiation at high temperatures;
- applying the “gray” (monoenergetic) approximation to the frequency dependence

by integrating the full transport equation over all ν, averaging the opacities with a suitable *a priori* weighting function [33].

For the purposes of discussion and the later AD derivation, we consider a general, 3-D universe, in which the spatial coordinates x, y, and z define a spatial point

$$\boldsymbol{x} = x\boldsymbol{i} + y\boldsymbol{j} + z\boldsymbol{k},$$

and the angular coordinates μ and θ define an arbitrary unit vector denoting the direction of flight:

$$\boldsymbol{\Omega} = \mu\boldsymbol{i} + \sqrt{1-\mu^2}\cos\theta\,\boldsymbol{j} + \sqrt{1-\mu^2}\sin\theta\,\boldsymbol{k}.$$

These angular coordinates reside in the domain $-1 \le \mu \le 1$, $0 \le \theta < 2\pi$; we use $\boldsymbol{\Omega} \in 4\pi$ as a shorthand denoting the entire unit sphere. See Refs. [34, 35] for a more complete discussion of the spatial and angular coordinate systems.

2.1.1 Equations of transfer

After the simplifications described above, the thermal radiative transfer process in the interior of a problem (away from the initial time and from boundaries) can be described [12] by the gray radiative transfer equation,

$$\frac{1}{c}\frac{\partial I}{\partial t} + \boldsymbol{\Omega}\cdot\boldsymbol{\nabla} I + \sigma I = \frac{\sigma acT^4}{4\pi} + \frac{q_r}{4\pi}, \tag{2.1a}$$

and the material energy balance equation,

$$c_v\frac{\partial T}{\partial t} = \sigma\int_{4\pi} I\,\mathrm{d}\Omega - \sigma acT^4 + q_m. \tag{2.1b}$$

The notation and omitted parameters in Eqs. (2.1) are:

$I = I(\boldsymbol{x},\boldsymbol{\Omega},t)$ = the angular radiation intensity,
$T = T(\boldsymbol{x},t)$ = the material temperature,
$\sigma = \sigma(\boldsymbol{x},T)$ = the absorption opacity,
$q_r = q_r(\boldsymbol{x},t)$ = an extraneous isotropic radiation energy source,
$q_m = q_m(\boldsymbol{x},t)$ = an energy source in the material,
$c_v = c_v(\boldsymbol{x},T)$ = the specific heat capacity of the material,
a = the radiation constant, and

c = the speed of light.

The intensity I and the temperature T are the primary unknowns: they describe the state of energy in the radiation and in the material. Each of the terms that depends on T implicitly depends on the time t. The explicit dependence of c_v and σ on $\boldsymbol{x}$ accounts for different materials in different parts of the problem.

Equation (2.1a) is a transport equation for I. The first two terms describe how photons "stream" in time and space: if the other terms were zero, Eq. (2.1a) would reduce to a wave equation with a wave speed of c. However, because the photons move through a material, there is a chance they will collide with its electrons, hence the *collision* term σI. The first term on the right-hand side represents particles emitted via the isotropic temperature-dependent process of *black body emission*. (The quantity $\frac{acT^4}{4\pi}$ is the frequency-integrated Planck function $B(\nu, T)$.) The additional term q_r is an extraneous isotropic radiation source that emits with an energy density (energy per volume per time) of q_r.

The material equation (2.1b) describes an energy balance in the material. The left-hand side is the time rate of change in the material energy density. The first term on the right-hand side exactly mirrors the collision term in the radiation equation: it is a "gain" term corresponding to photons that collided with (were absorbed by) the material. The second term describes the loss of energy from the material when it emits black body radiation. The material energy source, or electron source, is sometimes used in numerical test problems to emulate heating by a hydrodynamic shock wave [36].

The physical properties σ and c_v are often approximated by simplistic models in the methods development literature. The heat capacity c_v of an ideal gas is a constant, giving the material energy a linear proportionality to the material temperature T. A much-used model [11, 21] of the gray opacity is $\sigma \propto T^{-3}$. Many of our numerical test problems will use both of these idealized representations of the physical constants.

The nonlinear coupling between Eqs. (2.1a) and (2.1b) via T^4 emission and T^{-3} absorption make the TRT equations extremely "stiff" as a function of time [37] and therefore even more difficult to solve than the standard linear transport equation. In this work, we will not attempt to provide any new solutions to treat the nonlinearities, but we will formulate our time-dependent anisotropic diffusion approximations to be compatible with multiple solution techniques.

2.1.2 The radiation intensity

The state of the photons in a system is described by the radiation *photon density*,

$$N(\boldsymbol{x}, \boldsymbol{\Omega}, \nu, t)\,\mathrm{d}V\,\mathrm{d}\Omega = \text{the number of photons inside the differential volume } \mathrm{d}V \text{ about } \boldsymbol{x}\text{, traveling in the directions } \Omega \text{ about } \boldsymbol{\Omega}\text{, inside the frequencies } \mathrm{d}\nu \text{ about } \nu\text{, at time } t.$$

However, because the photon energy $h\nu$ determines the energy density of the radiation, and because the reaction rate with the material depends on the photons' speed c, the radiation field is almost always written as the *radiative intensity*,

$$I(\boldsymbol{x}, \boldsymbol{\Omega}, \nu, t) = ch\nu N(\boldsymbol{x}, \boldsymbol{\Omega}, \nu, t)\,.$$

The frequency-dependent intensity I is an energy-weighted radiation path length density, similar to the angular flux ψ in reactor physics.[1]

Integrating over all energy gives the gray intensity, which we use from this point forward:

$$I(\boldsymbol{x}, \boldsymbol{\Omega}, t) = c\int_0^\infty h\nu N(\boldsymbol{x}, \boldsymbol{\Omega}, \nu, t)\,\mathrm{d}\nu\,.$$

Additionally, integrating over all angles (i.e. taking the zeroth angular moment) yields the *scalar intensity*

$$\phi(\boldsymbol{x}, t) \equiv \int_{4\pi} I(\boldsymbol{x}, \boldsymbol{\Omega}, t)\,\mathrm{d}\Omega \tag{2.2}$$

$$= c\int_{4\pi}\int_0^\infty h\nu N(\boldsymbol{x}, \boldsymbol{\Omega}, \nu, t)\,\mathrm{d}\nu\,\mathrm{d}\Omega \tag{2.3}$$

which is directly proportional to the *radiation energy density*:

$$\frac{1}{c}\phi(\boldsymbol{x}, t)\,\mathrm{d}V = \text{the amount of energy in the radiation field inside the differential volume } \mathrm{d}V \text{ about } \boldsymbol{x}\text{, at time } t.$$

For our work, it is usually more convenient to refer to ϕ than to the radiation energy density (compare, for example, Ref. [38] to Ref. [39]). In fact, since our numerical model-experiments use the scaled system of variables $c = a = 1$, our later results can use "scalar intensity" and "radiation energy density" interchangeably.

[1] Note that ψ is not weighted by energy, because neutrons' energy primarily determines their interaction cross section; photons in contrast are the means of energy transfer in the regimes considered in this thesis.

The radiation temperature, defined as

$$T_{\text{rad}} = \left(\frac{\phi}{ac}\right)^{1/4}, \tag{2.4}$$

is often used in lieu of the radiation energy density (or scalar intensity) in TRT problem analysis, as it can be more closely compared against the material temperature T. At thermal equilibrium (where the time rate of change, streaming, and extraneous source terms in Eqs. (2.1) are set to zero), the frequency-dependent intensity is equal to the Planckian function, $I = B$, and the radiation temperature satisfies $T_{\text{rad}} = T$.

The first angular moment of the intensity also has physical significance. The *radiation flux* is defined as

$$\boldsymbol{F}(\boldsymbol{x}, t) \equiv \int_{4\pi} \boldsymbol{\Omega} I(\boldsymbol{x}, \boldsymbol{\Omega}, t)\, \mathrm{d}\Omega\,. \tag{2.5}$$

Analogous to the "neutron current" $\boldsymbol{J}$ in reactor physics, the radiation flux is the net rate and direction of energy flowing through a point.

At any particular point in space and time, the radiation intensity I is generally a complicated function of angle. For example, at the edge of a radiation shock wave, the distribution is highly peaked in the directions pointed away from the hot region, because that is the source of the photons. In parts of the problem where the system is closer to an equilibrium state, the intensity is nearly isotropic (almost uniform in angle).

2.2 Semi-implicit linearization

The anisotropic diffusion approximation is best implemented as a deterministic method. It is therefore necessary to discuss *discretization* schemes, in which the continuous unknowns in Eqs. (2.1) are approximated with discrete unknowns. In this section, we discuss the discretization of the time variable in the context of *linearization*, which approximates the nonlinear aspects of the TRT equations to allow a linear algebraic representation of the system of unknowns, facilitating their solution on a computer.

The common "semi-implicit" scheme uses operator splitting to decouple the radiation and material equations inside a time step; the remaining time-dependent unknowns are treated with the backward Euler discretization [39, 40, 41]. Like Fleck and Cummings' IMC method [23], this technique yields a linear transport equation with a pseudo-scattering term. Because of the extensive use of this nonlinear treatment in our implementations of anisotropic diffusion and the other tested methods, and because the semi-implicit scheme for radiation transport is usually glossed over in other works, we derive it here in

a practical level of detail. Existing derivations also omit the material source term q_m.

For the semi-implicit discretization, it is convenient to write Eqs. (2.1) in a slightly altered form:

$$\frac{1}{c}\frac{\partial I}{\partial t} + \mathbf{\Omega}\cdot\boldsymbol{\nabla} I + \sigma I = \frac{\sigma c U_r}{4\pi} + \frac{c q_r}{4\pi}\,, \tag{2.6a}$$

and the material energy balance equation,

$$\frac{\partial U_m}{\partial t} = \sigma\phi - \sigma c U_r + q_m\,. \tag{2.6b}$$

Here, we have defined the *material energy density*, which is a function of the material's temperature and specific heat capacity c_v:

$$U_m(T) = \int_0^T c_v(T')\,\mathrm{d}T'\,, \tag{2.7}$$

and the *equilibrium radiation energy density* of a material, which is a scaled integral of the Planckian emission function:

$$U_r(T) \equiv aT^4 = \frac{1}{c}\int_{4\pi}\int_0^\infty B(\nu, T)\,\mathrm{d}\nu\,\mathrm{d}\Omega\,. \tag{2.8}$$

The physical relevance of U_r is that, when the radiation field and material reach an equilibrium, the radiation intensity becomes the Planck function $I = B$, and the radiation energy density ϕ/c is equal to U_r. The quantity U_r is *not* equal to the energy stored in the material, U_m.

Note here that Eqs. (2.6) are two equations with three unknowns: I, U_r, and U_m. However, U_r and U_m are both properties of the material—explicit functions of the material temperature T—so there are only two underlying unknowns: one describing the radiation state (intensity), and the other describing the material state (temperature).

2.2.1 Linearizing the material energy equation

To proceed, we define a parameter β as a function of Eqs. (2.7) and (2.8):

$$\beta(\boldsymbol{x}, T) \equiv \frac{\partial U_r}{\partial U_m} = \frac{\partial U_r}{\partial T}\bigg/\frac{\partial U_m}{\partial T} = \frac{4aT^3}{c_v(\boldsymbol{x}, T)}\,. \tag{2.9}$$

The chain rule allows the left hand side of Eq. (2.6b) to be expressed without approximation in terms of the equilibrium radiation energy density U_r:

$$\frac{\partial U_m}{\partial t} = \frac{\partial U_m}{\partial U_r}\frac{\partial U_r}{\partial t} = \frac{1}{\beta(T)}\frac{\partial U_r}{\partial t} = \sigma\phi - \sigma c U_r + q_m\,.$$

The first approximation is to "freeze" the parameter β at the beginning-of-time-step temperature T^n:

$$\beta[\boldsymbol{x}, T(\boldsymbol{x}, t)] \approx \beta[\boldsymbol{x}, T(\boldsymbol{x}, t^n)] = \beta(\boldsymbol{x}, T^n) \equiv \beta^n(\boldsymbol{x}),$$

so Eq. (2.6b) becomes for $t^n < t < t^{n+1}$

$$\frac{1}{\beta^n}\frac{\partial U_r}{\partial t} \approx \sigma\phi - \sigma c U_r. \tag{2.10}$$

The process of freezing β is equivalent to approximating the material energy term using two first-order Taylor series:

$$\begin{aligned}
U_m(t^{n+1}) &\approx U_m(t^n) + (t^{n+1} - t^n)\frac{\partial U_m}{\partial t}\bigg|_{t^n} + O((t^{n+1} - t^n)^2) \\
U_m^{n+1} &= U_m^n + \Delta_t \frac{\partial U_m}{\partial U_r}\bigg|_{t^n}\frac{\partial U_r}{\partial t}\bigg|_{t^n} + O(\Delta_t^2) \\
U_m^{n+1} &= U_m^n + \Delta_t \frac{1}{\beta^n}\left[\frac{U_r^{n+1} - U_r^n}{\Delta_t} + O(\Delta_t)\right] + O(\Delta_t^2) \\
U_m^{n+1} &= U_m^n + \frac{U_r^{n+1} - U_r^n}{\beta^n} + O(\Delta_t^2) \\
U_m^{n+1} &\approx U_m^n + \frac{U_r^{n+1} - U_r^n}{\beta^n}.
\end{aligned} \tag{2.11}$$

Because the freezing of β approximates the rate of change in material energy, Eq. (2.10) no longer conserves the system's total energy. To enforce conservation of energy over a time step, we use Eq. (2.11).

The next approximation explicitly freezes the opacity σ in Eq. (2.10):

$$\frac{1}{\beta^n}\frac{\partial U_r}{\partial t} \approx \sigma^n\phi - \sigma^n c U_r + q_m.$$

Now we average the material equation in time to express it in terms of two simple unknowns. Operating by $\frac{1}{\Delta_t^n}\int_{t_n}^{t^{n+1}}(\cdot)\,\mathrm{d}t$, we obtain

$$\frac{1}{\beta^n}\frac{U_r^{n+1} - U_r^n}{\Delta_t^n} = \sigma^n\left[\frac{1}{\Delta_t^n}\int_{t_n}^{t^{n+1}}\phi\,\mathrm{d}t\right] - \sigma^n c\left[\frac{1}{\Delta_t^n}\int_{t_n}^{t^{n+1}}U_r\,\mathrm{d}t\right] + \frac{1}{4\pi}\left[\frac{1}{\Delta_t^n}\int_{t_n}^{t^{n+1}}q_m\,\mathrm{d}t\right].$$

Next, we apply the implicit Euler discretization[2] to $U_r(\boldsymbol{x}, \boldsymbol{\Omega}, t)$ and $\phi(\boldsymbol{x}, \boldsymbol{\Omega}, t)$ by approx-

[2]Note that the IMC method only applies the implicit approximation to U_r, allowing the continuous-in-time treatment of the intensity.

imating their time-averaged values with their values at the end of the time step t^{n+1}:

$$\frac{1}{\beta^n(\boldsymbol{x})}\frac{U_r^{n+1}(\boldsymbol{x})-U_r^n(\boldsymbol{x})}{\Delta_t^n}=\sigma^n(\boldsymbol{x})\phi^{n+1}(\boldsymbol{x})-c\sigma^n(\boldsymbol{x})U_r^{n+1}(\boldsymbol{x})+q_m^n. \tag{2.12}$$

(The material source q_m is known, so q_m^n is its pre-calculated time-averaged value.)

We solve Eq. (2.12) for U_r^{n+1} in order to eliminate the implicit dependence of the transport equation on the material energy equation.

$$\begin{aligned}
U_r^{n+1}[1+c\beta^n\Delta_t^n\sigma^n] &= \beta^n\Delta_t^n\sigma^n\phi^{n+1}+U_r^n+\beta^n\Delta_t^n q_m^n \\
U_r^{n+1} &= \frac{c\beta^n\Delta_t^n\sigma^n}{1+c\beta^n\Delta_t^n\sigma^n}\frac{1}{c}\phi^{n+1}+\frac{1}{1+c\beta^n\Delta_t^n\sigma^n}U_r^n+\frac{c\beta^n\Delta_t^n\sigma^n}{1+c\beta^n\Delta_t^n\sigma^n}\frac{1}{c\sigma^n}q_m^n \\
U_r^{n+1} &= \left(1-f^n\right)\frac{1}{c}\phi^{n+1}+f^nU_r^n+\left(1-f^n\right)\frac{1}{c\sigma^n}q_m^n,
\end{aligned} \tag{2.13}$$

where we have defined the Fleck factor [23] as

$$f^n=f^n(\boldsymbol{x})\equiv\left[1+\beta^nc\Delta_t^n\sigma^n\right]^{-1}. \tag{2.14}$$

Substituting Eq. (2.13) into (2.11) and rearranging, we obtain an energy balance equation using the linearized terms, the initial state, and the final radiation state:

$$U_m^{n+1}=U_m^n+f^n\sigma^n\Delta_t^n\left[\phi^{n+1}-cU_r^n\right]+f^n\Delta_t^nq_m^n. \tag{2.15}$$

2.2.2 Linearizing the transport equation

Next, we apply the same approximations to the nonlinear radiation transport equation (2.6a). As with the material equation, the opacities are "frozen" at their beginning-of-time-step values σ^n, and the equation is time-averaged:

$$\begin{aligned}
\frac{1}{c}\frac{I^{n+1}-I^n}{\Delta_t^n}+\boldsymbol{\Omega}\cdot\boldsymbol{\nabla}\left[\frac{1}{\Delta_t^n}\int_{t_n}^{t^{n+1}}I\,\mathrm{d}t\right]+\sigma^n\left[\frac{1}{\Delta_t^n}\int_{t_n}^{t^{n+1}}I\,\mathrm{d}t\right] \\
=\frac{\sigma^nc}{4\pi}\left[\frac{1}{\Delta_t^n}\int_{t_n}^{t^{n+1}}U_r\,\mathrm{d}t\right]+\frac{1}{4\pi}\left[\frac{1}{\Delta_t^n}\int_{t_n}^{t^{n+1}}q_r\,\mathrm{d}t\right].
\end{aligned}$$

We again apply the implicit backward Euler approximation to the radiation and material unknowns, I and U_r:

$$\frac{1}{c}\frac{I^{n+1}-I^n}{\Delta_t^n}+\boldsymbol{\Omega}\cdot\boldsymbol{\nabla}I^{n+1}+\sigma^nI^{n+1}=\frac{\sigma^nc}{4\pi}U_r^{n+1}+\frac{1}{4\pi}q_r^n.$$

(The extraneous energy source q_r is known *a priori*, so no approximation is made if q_r^n is its time-averaged value.) Finally, we substitute U_r^{n+1} from Eq. (2.13), which was derived from the material equation Eq. (2.6b):

$$\frac{1}{c}\frac{I^{n+1}-I^n}{\Delta_t^n}+\mathbf{\Omega}\cdot\nabla I^{n+1}+\sigma^n I^{n+1}=\frac{\sigma^n c}{4\pi}\left[\left(1-f^n\right)\frac{1}{c}\phi^{n+1}+f^n U_r^n+\left(1-f^n\right)\frac{1}{c\sigma^n}q_m^n\right]+\frac{1}{4\pi}q_r^n\,,$$

or, rearranged,

$$\begin{aligned}\frac{1}{c}\frac{I^{n+1}-I^n}{\Delta_t^n}+\mathbf{\Omega}\cdot\nabla I^{n+1}+\sigma^n I^{n+1}&\\ =\left(1-f^n\right)\sigma^n\frac{1}{4\pi}\phi^{n+1}+\frac{1}{4\pi}f^n\sigma^n cU_r^n+\frac{1}{4\pi}\left[q_r^n+\left(1-f^n\right)q_m^n\right]\,.&\end{aligned}\quad(2.16)$$

2.2.3 Comments

If we compare Eq. (2.16) to a temporally implicit discretization of a monoenergetic linear transport problem with isotropic scattering,

$$\frac{1}{v}\frac{\psi^{n+1}-\psi^n}{\Delta_t^n}+\mathbf{\Omega}\cdot\nabla\psi^{n+1}+\Sigma_t\psi^{n+1}=\frac{1}{4\pi}\Sigma_s\int_{4\pi}\psi^{n+1}\,\mathrm{d}\Omega+\frac{1}{4\pi}q\,,$$

we find equivalences between the two:

$$\begin{aligned}I\leftrightarrow\psi\ &=\text{the angular flux,}\\ \sigma^n\leftrightarrow\Sigma_t&=\text{the total cross section,}\\ \left(1-f^n\right)\sigma^n\leftrightarrow\Sigma_s&=\text{the scattering cross section,}\\ f^n\sigma^n cU_r^n+q_r^n+\left(1-f^n\right)q_m^n\leftrightarrow q\ &=\text{the isotropic source for time step } n,\\ v\leftrightarrow c\ &=\text{the particle speed.}\end{aligned}$$

Even though the original radiation transport equation was purely absorbing, the linearization scheme created a "pseudo-scattering" term that essentially emulates the absorption and isotropic reëmission of radiation during a time step. The IMC literature often refers to the "effective scattering opacity," $\sigma_{\mathrm{es}}^n\equiv\left(1-f^n\right)\sigma^n$. If we take the zeroth angular moment of Eq. (2.16), then we obtain the radiation energy conservation equation over the time step:

$$\frac{1}{c}\frac{\phi^{n+1}-\phi^n}{\Delta_t^n}+\nabla\cdot\boldsymbol{F}^{n+1}+\sigma_{\mathrm{ea}}^n\phi^{n+1}=\sigma_{\mathrm{ea}}^n cU_r^n+q_r^n+\left(1-f^n\right)q_m^n\,,\quad(2.17)$$

where $\sigma_{\mathrm{ea}}^n\equiv f^n\sigma^n$ is known as the "effective absorption opacity."

This effective absorption term also appears in the material energy update equation (2.15):

$$U_m^{n+1} = U_m^n + \sigma_{\text{ea}}^n \Delta_t^n \left[\phi^{n+1} - cU_r^n\right] + f^n \Delta_t^n q_m^n .$$

The energy transferred from the radiation to the material in the SI scheme is the time-integrated *effective* absorption rate.

2.2.4 Summary

The semi-implicit linearization decouples the material energy and radiation transport equations inside a time step, yielding a linear transport equation (2.16) with pseudo-scattering:

$$\frac{1}{c}\frac{I^{n+1} - I^n}{\Delta_t^n} + \mathbf{\Omega}\cdot\boldsymbol{\nabla} I^{n+1} + \sigma^n I^{n+1} = \left(1 - f^n\right)\sigma^n \frac{1}{4\pi}\phi^{n+1} + \frac{1}{4\pi} f^n \sigma^n c U_r^n + \frac{1}{4\pi} q_r^n ,$$

and a material energy update equation (2.15):

$$U_m^{n+1} = U_m^n + f^n \sigma^n \Delta_t^n \left[\phi^{n+1} - cU_r^n\right] + f^n \Delta_t^n q_m^n .$$

For the nth time step, given the initial radiation field I^n and the initial material energy density U_m^n, the solution process follows.

1. *Compute the linearized values.* Calculate the starting temperature T^n from the stored material energy density U_m^n by inverting the integral in Eq. (2.7). Using the temperature, calculate the frozen σ^n and β^n in each spatial cell. Use Eq. (2.14) to calculate f^n, which in turn is used to calculate the linearized isotropic source $f^n\sigma^n cU_r^n + q_r^n$ and the effective scattering cross section $\left(1 - f^n\right)\sigma^n$. If using a diffusion method to approximate the transport solution, the absorption cross sections and diffusion coefficients must be recalculated. This is a computationally inexpensive step.
2. *Solve the linear transport problem for* $\psi^{n+1} = I^{n+1}$. With the implicit discretization, this solution uses the stored value of the radiation field at the end of the time step, I^n.
3. *Update the material energy* U_m^{n+1}. Because of the linearization of β, the linearized estimate of the new material emission term in Eq. (2.13) is not directly related to the temperature: $U_r^{n+1} \neq a(T^{n+1})^4$. Instead, the material energy must be calculated using Eq. (2.15).

Figure 2.1 shows how the problem physics and the linearized quantities relate. The flow chart is useful when implementing the linearization scheme programmatically.

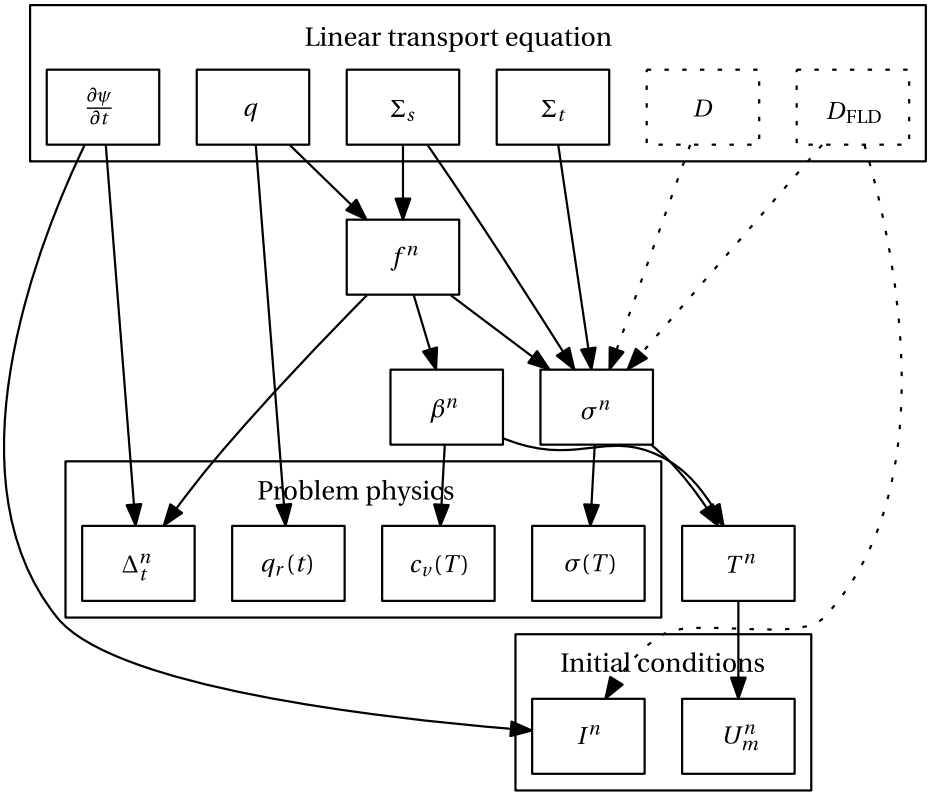

Figure 2.1: Dependency graph of quantities in the semi-implicit discretization. Arrows indicate a "depends on" relationship.

2.3 Deterministic radiation transport approximations

In this section, we briefly review several existing deterministic radiation transport methods, which discretize all unknowns in the TRT equations.

The salient difference among these methods is their treatment of the angular dependence of the intensity. Additionally, each method tends to have its own set of spatial discretizations that are effective and efficient for the given angular treatment. The choice of temporal discretization is usually independent of the method used.

Each approximation applied to the transport equation introduces an error. The angular approximations to I introduce errors that are particularly difficult to assess. Asymptotic analysis can be used to describe quantitative regimes of applicability of most methods [33, 42, 43], but we will confine our discussion here to some of the qualitative unphysical behavior introduced by the angular approximations.

Myriad spatial discretization schemes exist. Typically, a spatial discretization will introduce a local error into the solution with some relation to the grid size. In the diffusion (and anisotropic diffusion) methods, finite difference schemes are commonly used [44].

Furthermore, the treatment of the time dependence of the TRT equations is a lengthy topic [41]. As in other partial differential equations, the approximation made to the $\partial I/\partial t$ term (or to the time average of the other terms) incurs a discretization error of $O(\Delta_t)$ in the case of backward Euler. Because of the stiff nature of the TRT equations [37], unstable explicit methods such as forward Euler are practically unusable in this application. Furthermore, the operator split in the semi-implicit treatment produces an $O(\Delta_t)$ linearization error. Typically, then, higher-order [$O(\epsilon^2)$] methods require not only complex discretization schemes but also iteration on the nonlinearities (or the application of Jacobi-free Newton–Krylov techniques). In our work, we will use only the simple semi-implicit linearization with the backward Euler implicit time discretization. Thus, in our discussion of the methods in this section, we represent the transport equation in the linearized form

$$\frac{1}{c}\frac{I^{n+1}-I^n}{\Delta_t^n} + \mathbf{\Omega}\cdot\boldsymbol{\nabla} I^{n+1} + \sigma^n I^{n+1} = \frac{1}{4\pi}\sigma_{\text{es}}^n \phi^{n+1} + \frac{1}{4\pi}Q^n\,. \tag{2.18}$$

2.3.1 Discrete ordinates

The discrete ordinates (S_N) method enforces the transport equation (2.18) only for a "quadrature set" of M unit directions $\mathbf{\Omega}_m$, giving M equations

$$\frac{I_m^{n+1}-I_m^n}{c\Delta_t^n} + \mathbf{\Omega}_m\cdot\boldsymbol{\nabla} I_m^{n+1} + \sigma^n I^{n+1} = \frac{1}{4\pi}\sigma_{\text{es}}^n \phi^{n+1} + \frac{1}{4\pi}Q^n\,, \tag{2.19}$$

where each angle of the discrete intensity is defined as

$$I(\boldsymbol{x},\mathbf{\Omega}_m,t) = I_m(\boldsymbol{x},t)\,.$$

The equations for each ordinate are coupled at every point in space through the scalar intensity in the scattering term:

$$\phi^{n+1} = \sum_{m=1}^{M} I_m^{n+1} w_m\,,$$

where w_m is the quadrature weight corresponding to the direction $\mathbf{\Omega}_m$. The discrete equations can also be coupled at the boundaries of a problem, e.g. via specular reflection.

To interpret Eq. (2.19) as a linear algebraic expression, we rearrange it slightly:

$$\left(\mathbf{\Omega}_m\cdot\boldsymbol{\nabla} + \frac{1}{c\Delta_t^n} + \sigma^n\right) I_m^{n+1} = \frac{1}{c\Delta_t^n} I_m^n + \frac{1}{4\pi}\sigma_{\text{es}}^n \phi^{n+1} + \frac{1}{4\pi}Q^n\,,$$

or, combining all M equations into abstract linear operators (similar to that given in Ref. [45]),

$$L\psi = S\psi + q\,.$$

Here L is the operator representing "streaming plus collision" on the left hand side, S represents the isotropic redistribution of photons via scattering, ψ is the vector of unknown angular intensity at the new time step, and q is the isotropic source plus the initial condition. At every time step, the S_N equations can be solved iteratively with Richardson iteration (or "source iteration") [46],

$$\psi^{(k+1)} = L^{-1}(S\psi^{(k)} + q)\,.$$

Every application of L^{-1} to the unknowns is known as a "transport sweep," as it is normally implemented not as an explicit matrix of unknowns but rather in an algorithm that sweeps across a mesh, progressively inverting the transport equation in each cell to solve for the exiting angular intensity. In the absence of scattering ($\sigma_{\text{es}}^n = 0$) and with specified incident boundaries, the S_N equations can be solved in only one sweep. This feature is particularly advantageous for the anisotropic diffusion solution process.

In highly scattering systems, S_N can take an arbitrarily large number of iterations to converge using pure source iteration. Means of overcoming this—including diffusion synthetic acceleration, multigrid treatments, and Krylov methods—exist, but these are outside the scope of this background chapter. (Our primary use of the S_N method is to calculate anisotropic diffusion coefficients.)

The grid error incurred by the spatial discretization can lead to surprisingly inaccurate answers for optically thick, highly scattering cells [42, 47].

2.3.2 Spherical harmonics

The spherical harmonics (P_N) method takes a very different approach to approximating the angular dependence of the intensity. It expresses the intensity as a truncated series of angular moments,

$$\begin{aligned} I(\boldsymbol{x},\boldsymbol{\Omega},t) &\approx \sum_{l=0}^{L}\sum_{m=-l}^{l} Y_{l,m}(\boldsymbol{\Omega})\left[\int_{4\pi} Y_{l,m}^{*}(\boldsymbol{\Omega}')\,I(\boldsymbol{x},\boldsymbol{\Omega}',t)\,\mathrm{d}\Omega'\right] \\ &= \frac{1}{4\pi}\phi(\boldsymbol{x},t) + \frac{3}{4\pi}\boldsymbol{\Omega}\cdot\boldsymbol{F}(\boldsymbol{x},t) + \cdots, \end{aligned}$$

where $Y_{l,m}(\boldsymbol{\Omega})$ and $Y_{l,m}^{*}(\boldsymbol{\Omega})$ are the spherical harmonic functions and their complex conjugates [48, 34].

The full spherical harmonic equations [25] are lengthy, complicated, and largely irrelevant to our work. However, the P_1 equations, which result from taking $L = 1$, are indeed relevant. The first step in their derivation is to take the zeroth and first angular moments of Eq. (2.18). The zeroth angular moment of the linearized transport equation is

$$\frac{\phi^{n+1} - \phi^n}{c\Delta_t} + \boldsymbol{\nabla} \cdot \boldsymbol{F} + \sigma_{\text{ea}}^n \phi^{n+1} = Q^n \,, \tag{2.20}$$

and the first moment is the vector equation

$$\frac{\boldsymbol{F}^{n+1} - \boldsymbol{F}^n}{c\Delta_t} + \boldsymbol{\nabla} \cdot \int_{4\pi} \boldsymbol{\Omega}\boldsymbol{\Omega} I^{n+1} \, \mathrm{d}\Omega + \sigma^n \boldsymbol{F}^{n+1} = 0 \,. \tag{2.21}$$

The P_1 approximation provides a closure for Eq. (2.21) by approximating the intensity as

$$I^{n+1}(\boldsymbol{x}, \boldsymbol{\Omega}) \approx \frac{1}{4\pi} \phi^{n+1}(\boldsymbol{x}) + \frac{3}{4\pi} \boldsymbol{\Omega} \cdot \boldsymbol{F}^{n+1}(\boldsymbol{x}) \,. \tag{2.22}$$

Thus, the second angular moment is

$$\int_{4\pi} \boldsymbol{\Omega}\boldsymbol{\Omega} I^{n+1} \, \mathrm{d}\Omega \approx \frac{1}{4\pi} \phi^{n+1} \int_{4\pi} \boldsymbol{\Omega}\boldsymbol{\Omega} \, \mathrm{d}\Omega + 0 = \frac{1}{3} \mathbf{I} \phi^{n+1} \,,$$

where $\mathbf{I}$ is the identity matrix (the unit dyad). Equation (2.21) becomes

$$\frac{\boldsymbol{F}^{n+1} - \boldsymbol{F}^n}{c\Delta_t} + \frac{1}{3} \boldsymbol{\nabla} \phi^{n+1} + \sigma^n \boldsymbol{F}^{n+1} = 0 \,. \tag{2.23}$$

Rather than the M unknowns per spatial coordinate of the S_N method, the P_1 has four (or, in 2-D space, three). It is therefore easier to solve and store in computer memory. Unfortunately, the disadvantages of P_1 are pronounced. First, most obviously, the linear-in-angle approximation is not generally valid, so the solution will usually lag in accuracy compared to a transport method. Second, it happens that the approximation in Eq. (2.23) yields a plane wave propagation speed of $c/\sqrt{3}$ rather than the physical c [13, 49]. (When combined, Eqs. (2.20) and (2.21) yield the "telegrapher's equation," a hyperbolic differential equation with wave speed $c/\sqrt{3}$.) Even worse, the P_1 equation and in fact the entire P_N family can produce negative solutions for ϕ^{n+1} in the presence of steep gradients [19, 25, 48]. This is a significant problem in TRT applications because a negative ϕ can lead to a negative material temperature and the catastrophic failure of a simulation.

An alternative to using the linear-in-angle approximation in the closure for the second

angular moment $\int_{4\pi} \mathbf{\Omega\Omega} I^{n+1}\,\mathrm{d}\Omega$ is to define an Eddington tensor [50, 18] as

$$\mathbf{E} \equiv \frac{\int_{4\pi} \mathbf{\Omega\Omega} I^{n+1}\,\mathrm{d}\Omega}{\int_{4\pi} I^{n+1}\,\mathrm{d}\Omega},$$

so that Eq. (2.21) becomes

$$\frac{\boldsymbol{F}^{n+1} - \boldsymbol{F}^{n}}{c\Delta_t} + \boldsymbol{\nabla} \cdot \left(\mathbf{E}\phi^{n+1}\right) + \sigma^{n} \boldsymbol{F}^{n+1} = 0\,.$$

Typically, **E** is calculated via a transport problem or some *a priori* estimated relationship between ϕ and its gradient. The variable Eddington factor, or quasidiffusion, family of methods can be much more accurate than the P_1 equations, but the nonlinear closure for **E** can lead to nonphysical shocks and numerical instabilities [18].

2.3.3 Diffusion

After the P_1 approximation is applied to the first angular moment of the transport equation, Eq. (2.22), one further simplification leads to the very common diffusion approximation. The "quasi-static" [14] approximation is to discard the time derivative term in the first angular moment, Eq. (2.21), simplifying the expression and allowing for an explicit solution of $\boldsymbol{F}^{n+1}$ to yield Fick's law:

$$\boldsymbol{F}^{n+1} = -\frac{1}{3\sigma^{n}} \boldsymbol{\nabla} \phi^{n+1}\,.$$

This simple expression approximates the entire angular distribution of the intensity I using a single unknown, yielding a very small memory footprint and a typically very fast solution.

However, Fick's law is only a coarse approximation, and it is not necessarily accurate. An asymptotic analysis [32, 33] shows that the diffusion approximation indeed is a leading order solution of the transport equation given certain conditions—namely, that the material properties vary slowly in space, and that the system be highly scattering. However, for problems that have a fast time scale or contain strongly absorbing materials, the diffusion approximation will not yield transport-quality answers.

Furthermore, the time-dependent diffusion approximation yields a parabolic equation for ϕ, allowing energy to be transferred faster than the speed of light. This often severe shortcoming is addressed in a method known as *flux-limited diffusion*, which is discussed next.

2.3.4 Flux-limited diffusion

The exact radiation intensity satisfies the mathematical identity $\|F\| \leq \phi$, essentially limiting the leakage of radiation at a point to the radiation energy at that point. The identity can be shown using the triangle inequality:

$$\begin{aligned} \|\boldsymbol{F}\| &= \left\| \int_{4\pi} \boldsymbol{\Omega} I \, \mathrm{d}\Omega \right\| \\ &\leq \int_{4\pi} \|\boldsymbol{\Omega}\| \, |I| \, \mathrm{d}\Omega \\ &\leq \int_{4\pi} [1] I \, \mathrm{d}\Omega \end{aligned} \tag{2.24}$$

$$\|\boldsymbol{F}\| \leq \phi \,. \tag{2.25}$$

Substituting Fick's law for $\boldsymbol{F}$ gives a condition that shows when the diffusion coefficient satisfies this limit:

$$\begin{aligned} \left\| -D \boldsymbol{\nabla} \phi \right\| &\leq \phi \\ D &\leq \frac{\phi}{\left\| \boldsymbol{\nabla} \phi \right\|} \,. \end{aligned} \tag{2.26}$$

In an optically thin region, $\sigma \approx 0$, $D \to \infty$, and this condition will usually be violated. Additionally, the large radiation energy gradient at a wavefront can lead to a violation of the limit.

A *flux limiter* is designed to combat these problems by enforcing Eq. (2.26) through an *ad hoc* modification to the definition of D. Although certain flux limiters [51] are based on idealized models that the radiation intensity might take in an optically thin region, the usual approach is more straightforward. The flux-limited diffusion (FLD) coefficient should approach the standard diffusion coefficient $1/(3\sigma)$ when the spatial gradients are weak, but it should satisfy Eq. (2.25) when the gradients are strong. A standard formulation [18] is

$$D = \left[(3\sigma)^m + \left(\frac{\left\| \boldsymbol{\nabla} \phi \right\|}{\phi} \right)^m \right]^{-1/m} \,. \tag{2.27}$$

The "sum" limiter at $m = 1$ due to Wilson [43] leads to inaccuracies at the diffusion limit, but using the "square-root" limiter at $m = 2$ (as suggested by Larsen [18]) is accurate to

leading order. Taking $m \to \infty$ leads to the "max" limiter,

$$D = \max\left(3\sigma, \frac{\|\nabla\phi\|}{\phi}\right)^{-1}, \tag{2.28}$$

which is also accurate in the diffusion limit but has discontinuous derivatives.

Typically, Eq. (2.27) is evaluated explicitly or "lagged" because of its inherent nonlinearity, giving the following FLD version of Fick's law:

$$\boldsymbol{F}^{n+1} \approx -\left[(3\sigma)^m + \left(\frac{\|\nabla\phi^n\|}{\phi^n}\right)^m\right]^{-1/m} \nabla\phi^{n+1}.$$

The discretization of the normalized gradient in Eq. (2.27) is an additional consideration when using FLD. The implementation used in this thesis takes a geometric average of the normalized gradient on the face of a computational cell as suggested by [52]:

$$\frac{1}{\phi}\frac{\partial\phi}{\partial x} \approx \sqrt{\left|\left(\frac{1}{(\phi_{i+1}+\phi_i)/2}\frac{\phi_{i+1}-\phi_i}{(\Delta_{x,i+1}/2+\Delta_{x,i}/2)}\right)\left(\frac{1}{(\phi_i+\phi_{i-1})/2}\frac{\phi_i-\phi_{i-1}}{(\Delta_{x,i}/2+\Delta_{x,i-1}/2)}\right)\right|} \times \operatorname{sgn}(\phi_{i+1}-\phi_{i-1}),$$

rather than the arithmetic average

$$\frac{1}{\phi}\frac{\partial\phi}{\partial x} \approx \frac{1}{\phi_i}\frac{\phi_{i+1}-\phi_{i-1}}{(\Delta_{x,i+1}/2+\Delta_{x,i}+\Delta_{x,i-1}/2)}.$$

This choice reduces the sensitivity of the flux limiter to the mesh grid size.

2.4 Summary

This chapter provides an overview of the equations underlying thermal radiative transfer, as well as some existing techniques for solving these equations. We have discussed some of the strengths and weaknesses of several deterministic methods that will compete with the new anisotropic diffusion approximation method, which is discussed next.

Chapter 3
Anisotropic Diffusion

The common radiation transport methods presented in the last chapter approximate the angular dependence of the intensity each in a different way. The crudest of these methods, diffusion, has only one unknown ϕ at each point in space and time; the more complex such as S_N have many unknowns, leading to greater accuracy but greater computer run time and memory usage. In this chapter, we derive a new anisotropic diffusion method which approximates the intensity in such a way as to retain an arbitrary amount of anisotropy (like a true transport method), while solving for a single unknown (like a diffusion method).

The previous work in anisotropic diffusion has only considered steady-state, linear problems in an infinite medium [2, 4]. The novel work presented in this chapter provides a theoretical basis for using AD in time-dependent, nonlinear problems, and it also addresses boundary conditions for the AD method.

3.1 Derivation

In this section, we use an asymptotic analysis to derive the anisotropic diffusion approximation in a linear, time-dependent, finite problem. We will later demonstrate this analysis' applicability to nonlinear thermal radiative transfer.

The linear, time-dependent transport equation with isotropic scattering is

$$\frac{1}{c}\frac{\partial I}{\partial t}(\boldsymbol{x},\boldsymbol{\Omega},t)+\boldsymbol{\Omega}\cdot\boldsymbol{\nabla} I(\boldsymbol{x},\boldsymbol{\Omega},t)+\sigma(\boldsymbol{x})I(\boldsymbol{x},\boldsymbol{\Omega},t) = \frac{\sigma_s(\boldsymbol{x})}{4\pi}\int_{4\pi} I(\boldsymbol{x},\boldsymbol{\Omega}',t)\,\mathrm{d}\Omega'+\frac{q(\boldsymbol{x},t)}{4\pi}, \quad \boldsymbol{x}\in V,\ \boldsymbol{\Omega}\in 4\pi,\ t\geq 0. \tag{3.1a}$$

The boundary condition is specified for incident directions:

$$I(\boldsymbol{x},\boldsymbol{\Omega},t)=I^b(\boldsymbol{x},\boldsymbol{\Omega},t), \quad \boldsymbol{x}\in\partial V,\ \boldsymbol{\Omega}\cdot\boldsymbol{n}<0,\ t>0, \tag{3.1b}$$

and the initial condition is

$$I(\boldsymbol{x}, \boldsymbol{\Omega}, 0) = I^i(\boldsymbol{x}, \boldsymbol{\Omega}), \quad \boldsymbol{x} \in V, \ \boldsymbol{\Omega} \in 4\pi. \tag{3.1c}$$

For consistency with the rest of this thesis, we retain the nomenclature of radiative transfer rather than neutron transport.[1]

Because this transport equation is linear, we can write its solution as the linear superposition of three distinct transport solutions:

$$I(\boldsymbol{x}, \boldsymbol{\Omega}, t) \equiv I_{\mathrm{v}}(\boldsymbol{x}, \boldsymbol{\Omega}, t) + I_{\mathrm{bl}}(\boldsymbol{x}, \boldsymbol{\Omega}, t) + I_{\mathrm{il}}(\boldsymbol{x}, \boldsymbol{\Omega}, t). \tag{3.2}$$

Here, I_{v} is an "interior" solution, valid several mean free paths away from the exterior problem boundary and several free times away from $t = 0$; I_{bl} is a "boundary layer" solution that decays rapidly away from the exterior boundary; and I_{il} is an "initial layer" that decays rapidly away from $t = 0$. Figure 3.1 represents these three regimes graphically. In the interior, spatial and temporal variations are small; in the boundary layer, spatial variations normal to the boundary are large; and in the initial layer, the temporal variations are large.

Our goal is first to develop an approximation to I_{v} that satisfies the transport equation in some asymptotic limit, and then to use the boundary and initial layer equations to "match" the interior solution to the transport solution on the boundary and at the initial time. This procedure follows prior work in the field, e.g. the asymptotic derivation of the diffusion equation with transport-matched boundary conditions [53].

3.1.1 Interior solution

The transport equation for the interior accounts for the extraneous source term, but it has no initial or boundary conditions, as it is only valid away from the boundary and initial layer:

$$\frac{1}{c}\frac{\partial I_{\mathrm{v}}}{\partial t}(\boldsymbol{x}, \boldsymbol{\Omega}, t) + \boldsymbol{\Omega} \cdot \boldsymbol{\nabla} I_{\mathrm{v}}(\boldsymbol{x}, \boldsymbol{\Omega}, t) + \sigma(\boldsymbol{x}) I_{\mathrm{v}}(\boldsymbol{x}, \boldsymbol{\Omega}, t) = \frac{\sigma_s(\boldsymbol{x})}{4\pi}\phi(\boldsymbol{x}, t) + \frac{q(\boldsymbol{x}, t)}{4\pi}. \tag{3.3}$$

Here, we have defined

$$\phi(\boldsymbol{x}, t) \equiv \int_{4\pi} I_{\mathrm{v}}(\boldsymbol{x}, \boldsymbol{\Omega}, t)\, \mathrm{d}\Omega, \tag{3.4}$$

[1] To enumerate the differences: we refer to the "radiative intensity" I rather than the "angular flux" ψ, the "scalar intensity" rather than the "scalar flux", the "radiation flux" $\boldsymbol{F}$ rather than the "neutron current" $\boldsymbol{J}$, the "opacity" σ rather than the "total cross section" Σ_t, and so on.

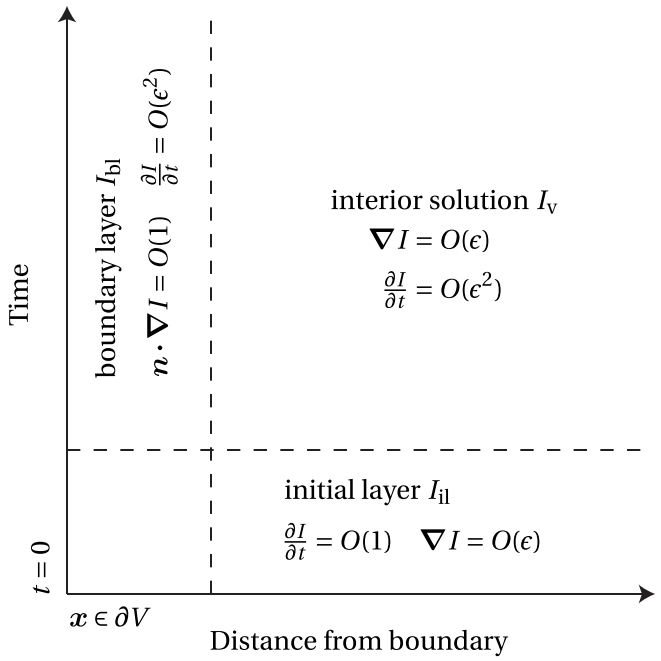

Figure 3.1: Depiction of interior, boundary layer, and initial layer of a transport problem.

which is the *interior* scalar intensity. We write Eq. (3.3) as

$$\left[\frac{1}{c}\frac{\partial}{\partial t} + \boldsymbol{\Omega}\cdot\boldsymbol{\nabla} + \sigma\right] I_{\text{v}} = \frac{\sigma_s}{4\pi}\phi + \frac{q}{4\pi}\,.$$

Taking the zeroth angular moment of Eq. (3.3) gives a *conservation equation* in the interior,

$$\frac{1}{c}\frac{\partial\phi}{\partial t}(\boldsymbol{x},t) + \boldsymbol{\nabla}\cdot\boldsymbol{F}(\boldsymbol{x},t) + \sigma(\boldsymbol{x})\phi(\boldsymbol{x},t) = \sigma_s(\boldsymbol{x})\phi(\boldsymbol{x},t) + q(\boldsymbol{x},t)\,. \tag{3.5}$$

Here we have defined the *interior* radiation flux:

$$\boldsymbol{F} \equiv \int_{4\pi} \boldsymbol{\Omega} I_{\text{v}}(\boldsymbol{x},\boldsymbol{\Omega},t)\,\mathrm{d}\Omega\,, \tag{3.6}$$

the first angular moment of the *interior* solution.

Adding $\boldsymbol{\Omega}\cdot\boldsymbol{\nabla}\phi$ to both sides of Eq. (3.5) and multiplying the resulting equation by $\frac{1}{4\pi}$, we obtain

$$\left[\frac{1}{c}\frac{\partial}{\partial t} + \boldsymbol{\Omega}\cdot\boldsymbol{\nabla} + \sigma\right]\left(\frac{1}{4\pi}\phi\right) = \frac{\sigma_s}{4\pi}\phi + \frac{q}{4\pi} - \frac{1}{4\pi}\boldsymbol{\nabla}\cdot\boldsymbol{F} + \frac{1}{4\pi}\boldsymbol{\Omega}\cdot\boldsymbol{\nabla}\phi\,.$$

Subtracting this equation from Eq. (3.3) cancels the isotropic source and scattering term on the right-hand side, yielding the following equation:

$$\left[\frac{1}{c}\frac{\partial}{\partial t} + \boldsymbol{\Omega}\cdot\boldsymbol{\nabla} + \sigma\right]\left(I_{\mathrm{v}} - \frac{1}{4\pi}\phi\right) = \frac{1}{4\pi}\boldsymbol{\nabla}\cdot\boldsymbol{F} - \frac{1}{4\pi}\boldsymbol{\Omega}\cdot\boldsymbol{\nabla}\phi\,. \tag{3.7}$$

At this point, we apply an asymptotic scaling typical of a diffusive regime. We make an ansatz that the spatial gradient of the solution is weak, the time derivative is very small, and the solution is mildly (but not necessarily linearly) anisotropic:

$$\sigma = O(1), \qquad I = O(1), \qquad \int_{4\pi} \boldsymbol{\Omega} I \,\mathrm{d}\Omega = O(\epsilon), \qquad \boldsymbol{\nabla} I = O(\epsilon), \qquad \frac{\partial I}{\partial t} = O(\epsilon^2)\,. \tag{3.8}$$

These scalings are the same as in an asymptotic derivation of the standard diffusion equation [32, 43]. With the scalings applied, Eq. (3.7) is written with the asymptotically small terms lumped together:

$$\left[\boldsymbol{\Omega}\cdot\boldsymbol{\nabla} + \sigma + O(\epsilon^2)\right]\left(I_{\mathrm{v}} - \frac{1}{4\pi}\phi\right) = -\frac{1}{4\pi}\boldsymbol{\Omega}\cdot\boldsymbol{\nabla}\phi + O(\epsilon^2)\,.$$

Neglecting the high-order $O(\epsilon^2)$ terms, we make the first approximation yet, obtaining:

$$\left[\boldsymbol{\Omega}\cdot\boldsymbol{\nabla} + \sigma\right]\left(I_{\mathrm{v}} - \frac{1}{4\pi}\phi\right) = -\frac{1}{4\pi}\boldsymbol{\Omega}\cdot\boldsymbol{\nabla}\phi\,. \tag{3.9}$$

Formally inverting the bracketed operator on the left-hand side, we obtain an approximate expression for the intensity in the interior:

$$I_{\mathrm{v}} = \frac{1}{4\pi}\phi - \left[\boldsymbol{\Omega}\cdot\boldsymbol{\nabla} + \sigma\right]^{-1}\left(\frac{1}{4\pi}\boldsymbol{\Omega}\cdot\boldsymbol{\nabla}\phi\right). \tag{3.10}$$

The inverted differential operator is an integral transport operator [35]:

$$\left[\boldsymbol{\Omega}\cdot\boldsymbol{\nabla} + \sigma\right]^{-1}\hat{Q}(\boldsymbol{x},\boldsymbol{\Omega},t) = \int_0^\infty \hat{Q}(\boldsymbol{x} - s\boldsymbol{\Omega},\boldsymbol{\Omega},t)\,\mathrm{e}^{-\tau(\boldsymbol{x},\boldsymbol{x}-s\boldsymbol{\Omega})}\,\mathrm{d}s\,. \tag{3.11a}$$

Here we have used the optical distance between points $\boldsymbol{x}$ and $\boldsymbol{x}'$ along the direction $\boldsymbol{\Omega} = (\boldsymbol{x}' - \boldsymbol{x})/\left\|\boldsymbol{x}' - \boldsymbol{x}\right\|$:

$$\tau(\boldsymbol{x},\boldsymbol{x}') = \int_0^{\|\boldsymbol{x}-\boldsymbol{x}'\|} \sigma(\boldsymbol{x} - s\boldsymbol{\Omega})\,\mathrm{d}s\,. \tag{3.11b}$$

Thus Eq. (3.10) for the interior intensity is a function of the nonlocal, unknown scalar

intensity:

$$I_{\mathrm{v}}(\boldsymbol{x},\boldsymbol{\Omega},t)=\frac{1}{4\pi}\phi(\boldsymbol{x},t)-\int_0^\infty\frac{1}{4\pi}\boldsymbol{\Omega}\cdot\boldsymbol{\nabla}\phi(\boldsymbol{x}-s\boldsymbol{\Omega},t)\,\mathrm{e}^{-\tau(\boldsymbol{x},\boldsymbol{x}-s\boldsymbol{\Omega})}\,\mathrm{d}s\,. \tag{3.12}$$

To simplify, we use the assumption from Eq. (3.8) that spatial gradients are weak to expand ϕ in a Taylor series about the local point:

$$\phi(\boldsymbol{x}-s\boldsymbol{\Omega},t)=\phi(\boldsymbol{x},t)-s\boldsymbol{\Omega}\cdot\boldsymbol{\nabla}\phi(\boldsymbol{x},t)+O(\epsilon^2)=\phi(\boldsymbol{x},t)+O(\epsilon)\,. \tag{3.13}$$

Applying the truncated Taylor expansion to the gradient in Eq. (3.12), we obtain

$$\boldsymbol{\nabla}\phi(\boldsymbol{x}-s\boldsymbol{\Omega},t)=\boldsymbol{\nabla}\phi(\boldsymbol{x},t)+O(\epsilon^2)\,.$$

Thus, Eq. (3.12) becomes

$$\begin{aligned}
I_{\mathrm{v}}(\boldsymbol{x},\boldsymbol{\Omega},t)&\approx\frac{1}{4\pi}\phi(\boldsymbol{x},t)-\int_0^\infty\frac{1}{4\pi}\boldsymbol{\Omega}\cdot\boldsymbol{\nabla}\phi(\boldsymbol{x}-s\boldsymbol{\Omega},t)\,\mathrm{e}^{-\tau(\boldsymbol{x},\boldsymbol{x}-s\boldsymbol{\Omega})}\,\mathrm{d}s\\
&=\frac{1}{4\pi}\phi(\boldsymbol{x},t)-\int_0^\infty\left[\frac{1}{4\pi}\boldsymbol{\Omega}\cdot\boldsymbol{\nabla}\phi(\boldsymbol{x},t)+O(\epsilon^2)\right]\mathrm{e}^{-\tau(\boldsymbol{x},\boldsymbol{x}-s\boldsymbol{\Omega})}\,\mathrm{d}s\\
&=\frac{1}{4\pi}\phi(\boldsymbol{x},t)-\left(\int_0^\infty\left[\frac{1}{4\pi}\right]\mathrm{e}^{-\tau(\boldsymbol{x},\boldsymbol{x}-s\boldsymbol{\Omega})}\,\mathrm{d}s\right)\boldsymbol{\Omega}\cdot\boldsymbol{\nabla}\phi(\boldsymbol{x},t)\\
&=\frac{1}{4\pi}\phi-\left[(\boldsymbol{\Omega}\cdot\boldsymbol{\nabla}+\sigma)^{-1}\frac{1}{4\pi}\right]\left(\boldsymbol{\Omega}\cdot\boldsymbol{\nabla}\phi\right).
\end{aligned}$$

We write this equation as

$$I_{\mathrm{v}}(\boldsymbol{x},\boldsymbol{\Omega},t)=\frac{1}{4\pi}\phi(\boldsymbol{x},t)-\left[f(\boldsymbol{x},\boldsymbol{\Omega})\right]\boldsymbol{\Omega}\cdot\boldsymbol{\nabla}\phi(\boldsymbol{x},t)\,, \tag{3.14}$$

where

$$f(\boldsymbol{x},\boldsymbol{\Omega})=(\boldsymbol{\Omega}\cdot\boldsymbol{\nabla}+\sigma)^{-1}\frac{1}{4\pi}$$

is the solution to the following differential transport equation:

$$\boldsymbol{\Omega}\cdot\boldsymbol{\nabla}f(\boldsymbol{x},\boldsymbol{\Omega})+\sigma(\boldsymbol{x})f(\boldsymbol{x},\boldsymbol{\Omega})=\frac{1}{4\pi}\,. \tag{3.15}$$

Taking the first angular moment of Eq. (3.14) gives the approximate radiation flux in the interior:

$$\begin{aligned}\boldsymbol{F}(\boldsymbol{x},t) &= \int_{4\pi} \boldsymbol{\Omega} I_{\mathrm{v}}(\boldsymbol{x},\boldsymbol{\Omega},t)\,\mathrm{d}\Omega \\ &= -\left[\int_{4\pi} \boldsymbol{\Omega}\boldsymbol{\Omega} f(\boldsymbol{x},\boldsymbol{\Omega})\,\mathrm{d}\Omega\right]\cdot\boldsymbol{\nabla}\phi(\boldsymbol{x},t) \\ &= -\mathbf{D}(\boldsymbol{x})\cdot\boldsymbol{\nabla}\phi(\boldsymbol{x},t)\,. \end{aligned} \tag{3.16}$$

This resembles "Fick's law," but instead of a scalar diffusion *coefficient*, the anisotropic diffusion method has a diffusion *tensor*, $\mathbf{D}$, the second angular moment of f:

$$\mathbf{D}(\boldsymbol{x}) \equiv \int_{4\pi} \boldsymbol{\Omega}\boldsymbol{\Omega} f(\boldsymbol{x},\boldsymbol{\Omega})\,\mathrm{d}\Omega\,. \tag{3.17}$$

In a homogeneous medium, $f \to \frac{1}{4\pi\sigma}$ and $\mathbf{D} \to \frac{1}{3\sigma}\mathbf{I}$: this reproduces Fick's law.

Because of the approximations made in developing Eq. (3.14), ϕ no longer satisfies the exact transport solution. Instead, like Fick's law, the first-order accurate approximation to the radiation flux is substituted into the low-order conservation equation (3.5) to yield an anisotropic diffusion equation that ϕ satisfies in the interior:

$$\frac{1}{c}\frac{\partial\phi}{\partial t}(\boldsymbol{x},t) - \boldsymbol{\nabla}\cdot\mathbf{D}(\boldsymbol{x})\cdot\boldsymbol{\nabla}\phi(\boldsymbol{x},t) + \sigma_a(\boldsymbol{x})\phi(\boldsymbol{x},t) = q(\boldsymbol{x},t)\,. \tag{3.18}$$

Here we use the absorption opacity $\sigma_a = \sigma - \sigma_s$.

The anisotropic diffusion approximation to the interior solution I_{v} comprises *(i)* the transport equation (3.15) for f, *(ii)* the definition in Eq. (3.17) of the diffusion tensor $\mathbf{D}$, and *(iii)* the anisotropic diffusion equation (3.18). We note that the transport equation (3.15) for f is very simple—it has no scattering. Thus, it is much less costly to solve than the original transport problem.

3.1.2 Initial layer solution

The initial layer solution accounts for the transition between the initial condition and the interior solution, using Eq. (3.2). It is significant only near the initial time $t = 0$, at which point the time derivatives are not assumed to be $O(\epsilon^2)$ but rather $O(1)$. The initial layer problem is defined in the spatial interior of the problem, where spatial gradients are $O(\epsilon)$, and the boundary layer solution has decayed to zero. (See Fig. 3.1 for a depiction of the initial layer in relation to the boundary layer and interior solution.) We shall use the diffusion scaling that the absorption is very small: $\sigma_a = \sigma - \sigma_s = O(\epsilon^2)$.

The transport problem for the initial layer complements the interior transport equation (3.3), so it has no extraneous source term:

$$\frac{1}{c}\frac{\partial I_{\mathrm{il}}}{\partial t}(\boldsymbol{x},\boldsymbol{\Omega},t)+\epsilon\boldsymbol{\Omega}\cdot\boldsymbol{\nabla}I_{\mathrm{il}}(\boldsymbol{x},\boldsymbol{\Omega},t)+\sigma(\boldsymbol{x})I_{\mathrm{il}}(\boldsymbol{x},\boldsymbol{\Omega},t)=\frac{\sigma(\boldsymbol{x})-\epsilon^2\sigma_a(\boldsymbol{x})}{4\pi}\phi_{\mathrm{il}}(\boldsymbol{x},t)\,. \tag{3.19a}$$

Here we have defined the zeroth angular moment of the initial layer solution to be

$$\phi_{\mathrm{il}}(\boldsymbol{x},t)\equiv\int_{4\pi}I_{\mathrm{il}}(\boldsymbol{x},\boldsymbol{\Omega},t)\,\mathrm{d}\Omega\,.$$

The initial layer accounts for the original transport initial condition in Eq. (3.1c) via the superposition equation (3.2):

$$I_{\mathrm{v}}(\boldsymbol{x},\boldsymbol{\Omega},0)+I_{\mathrm{il}}(\boldsymbol{x},\boldsymbol{\Omega},0)=I^{i}(\boldsymbol{x},\boldsymbol{\Omega})\,. \tag{3.19b}$$

(The I_{bl} term is not present because, in the spatial interior, the boundary layer solution has decayed away.) By construction we demand that its solution rapidly tend to zero for increasing t:

$$\lim_{t\to\infty}I_{\mathrm{il}}(\boldsymbol{x},\boldsymbol{\Omega},t)=0\,. \tag{3.19c}$$

The technique of asymptotic matching, which has previously applied to diffusion in Ref. [53, 54], uses this special transport problem to determine the initial value of the approximate interior solution ϕ.

The asymptotic analysis begins by expanding I_{il} in powers of ϵ,

$$I_{\mathrm{il}}(\boldsymbol{x},\boldsymbol{\Omega},t)\sim I_{\mathrm{il}}^{(0)}(\boldsymbol{x},\boldsymbol{\Omega},t)+\epsilon I_{\mathrm{il}}^{(1)}(\boldsymbol{x},\boldsymbol{\Omega},t)+\epsilon^2 I_{\mathrm{il}}^{(2)}(\boldsymbol{x},\boldsymbol{\Omega},t)+\cdots\,.$$

The zeroth moment of the initial layer solution is also written as a series expansion:

$$\phi_{\mathrm{il}}(\boldsymbol{x},t)\sim\phi_{\mathrm{il}}^{(0)}(\boldsymbol{x},t)+\epsilon\phi_{\mathrm{il}}^{(1)}(\boldsymbol{x},t)+\epsilon^2\phi_{\mathrm{il}}^{(2)}(\boldsymbol{x},t)+\cdots\,.$$

The expansions are substituted into the scaled transport equation (3.19a):

$$\begin{aligned}\frac{1}{c}\frac{\partial}{\partial t}\left[I_{\mathrm{il}}^{(0)}+\epsilon I_{\mathrm{il}}^{(1)}+\epsilon^2 I_{\mathrm{il}}^{(2)}\right]+\epsilon\boldsymbol{\Omega}\cdot\boldsymbol{\nabla}\left[I_{\mathrm{il}}^{(0)}\right]+\sigma(\boldsymbol{x})\left[I_{\mathrm{il}}^{(0)}+\epsilon I_{\mathrm{il}}^{(1)}+\epsilon^2 I_{\mathrm{il}}^{(2)}\right]\\ =\frac{\sigma(\boldsymbol{x})}{4\pi}\left[\phi_{\mathrm{il}}^{(0)}+\epsilon\phi_{\mathrm{il}}^{(1)}+\epsilon^2\phi_{\mathrm{il}}^{(2)}\right]-\frac{\epsilon^2\sigma_a(\boldsymbol{x})}{4\pi}\left[\phi_{\mathrm{il}}^{(0)}\right]+O(\epsilon^3)\,.\end{aligned} \tag{3.20}$$

To satisfy this equation, we equate the coefficients of each order of ϵ. Matching the $O(1)$

terms gives the following equation:

$$\frac{1}{c}\frac{\partial I_{\text{il}}^{(0)}}{\partial t} + \sigma I_{\text{il}}^{(0)} = \frac{\sigma}{4\pi}\phi_{\text{il}}^{(0)}, \tag{3.21a}$$

and matching the $O(\epsilon)$ terms gives another equation:

$$\frac{1}{c}\frac{\partial I_{\text{il}}^{(1)}}{\partial t} + \boldsymbol{\Omega}\cdot\boldsymbol{\nabla} I_{\text{il}}^{(0)} + \sigma I_{\text{il}}^{(1)} = \frac{\sigma}{4\pi}\phi_{\text{il}}^{(1)}. \tag{3.21b}$$

We ignore terms of $O(\epsilon^2)$ because the anisotropic diffusion approximation in the interior is only accurate to $O(\epsilon^2)$.

Next, we write the interior solution I_{v} by expanding the interior solution in powers of ϵ:

$$\phi(\boldsymbol{x}, t) \sim \phi^{(0)}(\boldsymbol{x}, t) + \epsilon\phi^{(1)}(\boldsymbol{x}, t) + \cdots.$$

Replacing $\boldsymbol{\Omega}\cdot\boldsymbol{\nabla}$ with $\epsilon\boldsymbol{\Omega}\cdot\boldsymbol{\nabla}$, the anisotropic diffusion approximation in the interior, Eq. (3.14), is:

$$\begin{aligned} I_{\text{v}} &= \frac{1}{4\pi}\left(\phi^{(0)} + \epsilon\phi^{(1)} + \cdots\right) - \epsilon f\boldsymbol{\Omega}\cdot\boldsymbol{\nabla}\left(\phi^{(0)} + \epsilon\phi^{(1)} + \cdots\right) \\ &= \frac{1}{4\pi}\phi^{(0)} + \epsilon\left[\frac{1}{4\pi}\phi^{(1)} - f\boldsymbol{\Omega}\cdot\boldsymbol{\nabla}\phi^{(0)}\right] + O(\epsilon^2). \end{aligned}$$

Thus the initial condition for the initial layer, Eq. (3.19b), becomes

$$\frac{1}{4\pi}\phi^{(0)}(0) + \epsilon\left[\frac{1}{4\pi}\phi^{(1)}(0) - f\boldsymbol{\Omega}\cdot\boldsymbol{\nabla}\phi^{(0)}(0)\right] + I_{\text{il}}^{(0)}(0) + \epsilon I_{\text{il}}^{(1)}(0) + O(\epsilon^2) = I^i(\boldsymbol{x}, \boldsymbol{\Omega}). \tag{3.22}$$

Matching powers of ϵ, we obtain the $O(1)$ equation:

$$\frac{1}{4\pi}\phi^{(0)}(0) + I_{\text{il}}^{(0)}(0) = I^i(\boldsymbol{x}, \boldsymbol{\Omega}), \tag{3.23a}$$

and the $O(\epsilon)$ equation:

$$\frac{1}{4\pi}\phi^{(1)}(0) + f\boldsymbol{\Omega}\cdot\boldsymbol{\nabla}\phi^{(0)}(0) + I_{\text{il}}^{(1)}(0) = 0. \tag{3.23b}$$

To satisfy Eq. (3.19c), each expanded term of the initial layer solution must rapidly tend to zero. We begin with the $O(1)$ terms in the initial layer equation, Eq. (3.21a):

$$\frac{1}{c}\frac{\partial I_{\text{il}}^{(0)}}{\partial t} + \sigma I_{\text{il}}^{(0)} = \frac{\sigma}{4\pi}\phi_{\text{il}}^{(0)}.$$

Taking the zeroth moment of this equation, we find that the number of particles in the leading term of the initial layer is constant:

$$\frac{1}{c}\frac{\partial \phi_{\text{il}}^{(0)}}{\partial t} = 0\,. \tag{3.24}$$

Thus to satisfy Eq. (3.19c), $\phi_{\text{il}}^{(0)}$ must be zero at the initial time:

$$\phi_{\text{il}}^{(0)}(0) = 0\,.$$

To use this fact, we take the leading order terms of the initial condition, Eq. (3.23a):

$$\frac{1}{4\pi}\phi^{(0)}(0) + I_{\text{il}}^{(0)}(0) = I^i(\boldsymbol{x}, \boldsymbol{\Omega})\,,$$

and integrate over all angles to obtain

$$\phi^{(0)}(0) + \phi_{\text{il}}^{(0)}(0) = \phi^i\,,$$

where

$$\phi^i(\boldsymbol{x}) = \int_{4\pi} I^i(\boldsymbol{x}, \boldsymbol{\Omega})\,\mathrm{d}\Omega\,.$$

Setting $\phi_{\text{il}}^{(0)}(0) = 0$, we obtain the desired relation between the leading order scalar intensity in the interior and the zeroth moment of the transport initial condition:

$$\phi^{(0)}(\boldsymbol{x}, 0) = \phi^i(\boldsymbol{x})\,. \tag{3.25}$$

This gives the initial condition to leading order. Because the anisotropic diffusion solution is $O(\epsilon^2)$-accurate in the interior of a diffusive problem, we desire an initial condition that has an additional order of accuracy.

The first step in solving for the $O(\epsilon^2)$-accurate initial condition is to exactly solve for the $O(1)$ component of I_{il} in Eq. (3.21a) for all times, using the fact that $\phi_{\text{il}}^{(0)} = 0$:

$$\frac{1}{c}\frac{\partial I_{\text{il}}^{(0)}}{\partial t} + \sigma I_{\text{il}}^{(0)} = 0 \quad \Longrightarrow \quad I_{\text{il}}^{(0)}(t) = I_{\text{il}}^{(0)}(0)\,\mathrm{e}^{-\sigma c t}\,.$$

We solve for $I_{\text{il}}^{(0)}(0)$ in Eq. (3.24) to find

$$I_{\text{il}}^{(0)}(t) = \left[I^i - \frac{\phi^i}{4\pi}\right]\mathrm{e}^{-\sigma c t}\,.$$

Now we turn to the $O(\epsilon)$ component of the initial layer equation:

$$\frac{1}{c}\frac{\partial I_{\text{il}}^{(1)}}{\partial t} + \boldsymbol{\Omega}\cdot\boldsymbol{\nabla} I_{\text{il}}^{(0)} + \sigma I_{\text{il}}^{(1)} = \frac{\sigma}{4\pi}\phi_{\text{il}}^{(1)}\,.$$

Substituting the solution $I_{\text{il}}^{(0)}$, we obtain

$$\frac{1}{c}\frac{\partial I_{\text{il}}^{(1)}}{\partial t} + \sigma I_{\text{il}}^{(1)} = \frac{\sigma}{4\pi}\phi_{\text{il}}^{(1)} - \boldsymbol{\Omega}\cdot\boldsymbol{\nabla}\left[\left(I^i - \frac{\phi^i}{4\pi}\right)\mathrm{e}^{-\sigma c t}\right].$$

Integrating this equation over angle eliminates the absorption term, we obtain a simple differential equation:

$$\frac{1}{c}\frac{\partial \phi_{\text{il}}^{(1)}}{\partial t} = -\boldsymbol{\nabla}\cdot\left[\boldsymbol{F}^i\,\mathrm{e}^{-\sigma c t}\right],$$

where the initial radiation flux is

$$\boldsymbol{F}^i = \int_{4\pi}\boldsymbol{\Omega} I^i(\boldsymbol{x},\boldsymbol{\Omega})\,\mathrm{d}\Omega\,.$$

We solve the differential equation for $\phi_{\text{il}}^{(1)}(t)$:

$$\phi_{\text{il}}^{(1)}(t) = \phi_{\text{il}}^{(1)}(0) - \boldsymbol{\nabla}\cdot\left[\frac{\boldsymbol{F}^i}{\sigma}\left(1-\mathrm{e}^{-\sigma c t}\right)\right].$$

Taking the limit as $t\to\infty$ and demanding that it satisfy Eq. (3.19c), we obtain a relation that the first-order initial layer must satisfy:

$$0 = \phi_{\text{il}}^{(1)}(0) - \boldsymbol{\nabla}\cdot\left[\frac{\boldsymbol{F}^i}{\sigma}\right]. \tag{3.26}$$

The first-order terms of the initial condition, Eq. (3.22), are:

$$\frac{1}{4\pi}\phi^{(1)}(0) + f\boldsymbol{\Omega}\cdot\boldsymbol{\nabla}\phi^{(0)}(0) + I_{\text{il}}^{(1)}(0) = 0\,.$$

The zeroth angular moment of this equation is:

$$\phi^{(1)}(0) + \int_{4\pi}\boldsymbol{\Omega} f\,\mathrm{d}\Omega\cdot\boldsymbol{\nabla}\phi^{(0)}(0) + \phi_{\text{il}}^{(1)}(0) = 0\,.$$

Applying the known $\phi^{(0)}(0)$ from Eq. (3.25), and the condition on the first-order initial

layer from Eq. (3.26), we obtain:

$$\phi^{(1)}(0) = -\int_{4\pi} \mathbf{\Omega} f \, \mathrm{d}\Omega \cdot \boldsymbol{\nabla} \phi^i - \boldsymbol{\nabla} \cdot \left(\frac{\boldsymbol{F}^i}{\sigma} \right). \tag{3.27}$$

Combining Eqs. (3.25) and (3.27) give the transport-matched initial condition for the interior to first order accuracy in ϵ:

$$\phi(\boldsymbol{x}, 0) = \phi^i(\boldsymbol{x}) - \epsilon \left[\int_{4\pi} \mathbf{\Omega} f \, \mathrm{d}\Omega \cdot \boldsymbol{\nabla} \phi^i(\boldsymbol{x}) + \boldsymbol{\nabla} \cdot \left(\frac{\boldsymbol{F}^i(\boldsymbol{x})}{\sigma(\boldsymbol{x})} \right) \right]. \tag{3.28}$$

In an infinite homogeneous medium, f is isotropic and $\int_{4\pi} \mathbf{\Omega} f \, \mathrm{d}\Omega = 0$. The resulting equation is the standard diffusion result [53],

$$\phi(0) = \phi^i - \epsilon \boldsymbol{\nabla} \cdot \left[\frac{\boldsymbol{F}^i}{\sigma} \right].$$

To summarize: the initial condition on ϕ that preserves the leading-order component of the transport solution is:

$$\phi(\boldsymbol{x}, 0) = \phi^i(\boldsymbol{x}) \equiv \phi^i(\boldsymbol{x}) = \int_{4\pi} I^i(\boldsymbol{x}, \mathbf{\Omega}) \, \mathrm{d}\Omega.$$

To match the transport solution and interior solution to *first* order accuracy in ϵ, the potentially nonconservative Eq. (3.28) should be used. However, in the rest of this work, we shall only use the leading-order accurate equation for the following reasons:

- In the truly diffusive problems to which this initial layer analysis is applicable, f is isotropic to leading order, so the second term of Eq. (3.28) may be discarded while retaining $O(\epsilon^2)$ accuracy.
- When the initial condition is isotropic, $\boldsymbol{F}^i = 0$, and the third term on the right side of Eq. (3.28) is identically zero.
- Using the nonconservative form in a radiation transport problem may violate the conservation of energy.
- The nonconservative $O(\epsilon)$-accurate form is not commonly used in practice.

3.1.3 Boundary layer solution

Near the exterior problem boundary, away from the initial time, the transport solution rapidly transitions to the interior solution in the *boundary layer*. (Figure 3.1 graphically depicts the relationship of the boundary layer to the interior solution.) The spatial gradient normal to the boundary is $O(1)$, and the time derivative is $O(\epsilon^2)$. The transport

equation for the boundary layer is source-free:

$$\frac{1}{c}\frac{\partial}{\partial t} I_{\mathrm{bl}}(\boldsymbol{x},\boldsymbol{\Omega},t) + \boldsymbol{\Omega}\cdot\boldsymbol{\nabla} I_{\mathrm{bl}}(\boldsymbol{x},\boldsymbol{\Omega},t) + \sigma(\boldsymbol{x}) I_{\mathrm{bl}}(\boldsymbol{x},\boldsymbol{\Omega},t) = \frac{\sigma_s(\boldsymbol{x})}{4\pi}\int_{4\pi} I_{\mathrm{bl}}(\boldsymbol{x},\boldsymbol{\Omega}',t)\,\mathrm{d}\Omega'\,. \quad (3.29a)$$

This equation accounts for the transport boundary condition, Eq. (3.1b), using the superposition relation of Eq. (3.2):

$$I_{\mathrm{v}}(\boldsymbol{x},\boldsymbol{\Omega},t) + I_{\mathrm{bl}}(\boldsymbol{x},\boldsymbol{\Omega},t) = I^b(\boldsymbol{x},\boldsymbol{\Omega},t)\,, \quad \boldsymbol{x}\in\partial V,\ \boldsymbol{\Omega}\cdot\boldsymbol{n}<0\,, \quad (3.29b)$$

(Here we have used $I_{\mathrm{il}}=0$ because the initial layer solution has decayed away, as the boundary layer is defined away from $t=0$.) We demand that the boundary layer solution rapidly tend to zero with increasing distance s from the boundary along the direction $-\boldsymbol{\Omega}$:

$$\lim_{s\to\infty} I_{\mathrm{bl}}(\boldsymbol{x},\boldsymbol{\Omega},t) = 0\,. \quad (3.29c)$$

If the boundary condition I^b varies slowly in space, and the radius of curvature of the exterior is large, then it can be shown [53] that the condition that satisfies Eqs. (3.29) to leading order is:

$$\int_{\boldsymbol{\Omega}\cdot\boldsymbol{n}<0} W(|\boldsymbol{\Omega}\cdot\boldsymbol{n}|)\, I_{\mathrm{bl}}(\boldsymbol{x},\boldsymbol{\Omega},t)\,\mathrm{d}\Omega = 0\,, \quad \boldsymbol{x}\in\partial V,\ \boldsymbol{\Omega}\cdot\boldsymbol{n}<0\,. \quad (3.30)$$

Here, W is related to Chandrasekhar's H-function [55]:

$$W(\mu) = \frac{\sqrt{3}}{2}\mu H(\mu) \approx \mu + \tfrac{3}{2}\mu^2\,, \quad 0<\mu\le 1\,. \quad (3.31)$$

The polynomial approximation is derived variationally [53] and is accurate to second order when used inside the integral in Eq. (3.30). The Marshak boundary condition uses $W(\mu)\approx 2\mu$.

Multiplying Eq. (3.29b) by $W(\mu)$, integrating over incident directions on the exterior boundary, and substituting Eq. (3.30) to demand that the boundary layer vanish in the interior, we obtain the following relation:

$$\int_{\boldsymbol{\Omega}\cdot\boldsymbol{n}<0} W(|\boldsymbol{\Omega}\cdot\boldsymbol{n}|)\, I_{\mathrm{v}}(\boldsymbol{x},\boldsymbol{\Omega},t)\,\mathrm{d}\Omega + 0 = \int_{\boldsymbol{\Omega}\cdot\boldsymbol{n}<0} W(|\boldsymbol{\Omega}\cdot\boldsymbol{n}|)\, I^b(\boldsymbol{x},\boldsymbol{\Omega},t)\,\mathrm{d}\Omega\,.$$

Substituting the interior approximation of Eq. (3.14), we find:

$$\begin{aligned}
&\int_{\boldsymbol{\Omega}\cdot\boldsymbol{n}<0} W(|\boldsymbol{\Omega}\cdot\boldsymbol{n}|)\, I^b(\boldsymbol{x},\boldsymbol{\Omega},t)\,\mathrm{d}\Omega \\
&\quad = \int_{\boldsymbol{\Omega}\cdot\boldsymbol{n}<0} W(|\boldsymbol{\Omega}\cdot\boldsymbol{n}|)\left[\frac{1}{4\pi}\phi(\boldsymbol{x},t) - f(\boldsymbol{x},\boldsymbol{\Omega})\boldsymbol{\Omega}\cdot\boldsymbol{\nabla}\phi(\boldsymbol{x},t)\right]\mathrm{d}\Omega \\
&\quad = \frac{1}{4\pi}\phi(\boldsymbol{x},t)\int_{\boldsymbol{\Omega}\cdot\boldsymbol{n}<0} W(|\boldsymbol{\Omega}\cdot\boldsymbol{n}|)\,\mathrm{d}\Omega - \left[\int_{\boldsymbol{\Omega}\cdot\boldsymbol{n}<0} W(|\boldsymbol{\Omega}\cdot\boldsymbol{n}|) f(\boldsymbol{x},\boldsymbol{\Omega})\boldsymbol{\Omega}\,\mathrm{d}\Omega\right]\cdot\boldsymbol{\nabla}\phi(\boldsymbol{x},t) \\
&\quad = \frac{1}{2}\phi(\boldsymbol{x},t) - \left[\int_{\boldsymbol{\Omega}\cdot\boldsymbol{n}<0} W(|\boldsymbol{\Omega}\cdot\boldsymbol{n}|)\boldsymbol{\Omega} f(\boldsymbol{x},\boldsymbol{\Omega})\,\mathrm{d}\Omega\right]\cdot\boldsymbol{\nabla}\phi(\boldsymbol{x},t)\,.
\end{aligned}$$

Multiplying by two, we arrive at the low-order boundary condition for the anisotropic diffusion approximation:

$$2\int_{\boldsymbol{\Omega}\cdot\boldsymbol{n}<0} W(|\boldsymbol{\Omega}\cdot\boldsymbol{n}|)\, I^b(\boldsymbol{x},\boldsymbol{\Omega},t)\,\mathrm{d}\Omega = \phi(\boldsymbol{x},t) + 2\left[-\int_{\boldsymbol{\Omega}\cdot\boldsymbol{n}<0} W(|\boldsymbol{\Omega}\cdot\boldsymbol{n}|)\boldsymbol{\Omega} f(\boldsymbol{x},\boldsymbol{\Omega})\,\mathrm{d}\Omega\right]\cdot\boldsymbol{\nabla}\phi(\boldsymbol{x},t)\,.$$

To make this equation clearer, we define the bracketed vector term to be

$$\boldsymbol{d}(\boldsymbol{x}) = -\int_{\boldsymbol{\Omega}\cdot\boldsymbol{n}<0} W(|\boldsymbol{\Omega}\cdot\boldsymbol{n}|)\boldsymbol{\Omega} f(\boldsymbol{x},\boldsymbol{\Omega})\,\mathrm{d}\Omega\,, \tag{3.32}$$

so that the boundary condition on ϕ becomes

$$2\int_{\boldsymbol{\Omega}\cdot\boldsymbol{n}<0} W(|\boldsymbol{\Omega}\cdot\boldsymbol{n}|)\, I^b(\boldsymbol{x},\boldsymbol{\Omega},t)\,\mathrm{d}\Omega = \phi(\boldsymbol{x},t) + 2\boldsymbol{d}(\boldsymbol{x})\cdot\boldsymbol{\nabla}\phi(\boldsymbol{x},t)\,. \tag{3.33}$$

Here, $\boldsymbol{d}$ is a vector defined on the boundary, $\boldsymbol{x}\in\partial V$, that is calculated from the incident values of the purely absorbing transport solution f.

The boundary condition is at this point incomplete, because the transport solution for f has only been defined for points away from the boundary: the prescription of f for incident directions on the boundary is unknown. We return to the definition of ϕ in Eq. (3.4) and substitute the approximated interior intensity from Eq. (3.14):

$$\begin{aligned}
\phi(\boldsymbol{x},t) &= \int_{4\pi}\left[\frac{1}{4\pi}\phi(\boldsymbol{x},t) - f(\boldsymbol{x},\boldsymbol{\Omega})\boldsymbol{\Omega}\cdot\boldsymbol{\nabla}\phi(\boldsymbol{x},t)\right]\mathrm{d}\Omega \\
\phi(\boldsymbol{x},t) &= \phi(\boldsymbol{x},t) - \int_{4\pi} f(\boldsymbol{x},\boldsymbol{\Omega})\boldsymbol{\Omega}\,\mathrm{d}\Omega\cdot\boldsymbol{\nabla}\phi(\boldsymbol{x},t) \\
0 &= -\left[\int_{4\pi} f(\boldsymbol{x},\boldsymbol{\Omega})\boldsymbol{\Omega}\,\mathrm{d}\Omega\right]\cdot\boldsymbol{\nabla}\phi(\boldsymbol{x},t)\,.
\end{aligned}$$

The above equation is not generally satisfied. It does hold true when f is an "even" function of $\boldsymbol{\Omega}$, e.g. in an optically thick, homogeneous material, where f is isotropic. At material boundaries, f can be strongly anisotropic, and the above relation does not hold. By

requiring $\int_{4\pi} I_\mathrm{v}\,\mathrm{d}\Omega = \phi$ at exterior boundaries, we obtain a relationship between the known outgoing values of f and the unknown incoming values:

$$0 = \int_{\boldsymbol{\Omega}\cdot\boldsymbol{n}>0} \boldsymbol{\Omega} f(\boldsymbol{x},\boldsymbol{\Omega})\,\mathrm{d}\Omega + \int_{\boldsymbol{\Omega}\cdot\boldsymbol{n}<0} \boldsymbol{\Omega} f(\boldsymbol{x},\boldsymbol{\Omega})\,\mathrm{d}\Omega\,.$$

If the opacity varies slowly along the boundary (which is a prerequisite for the analogous standard diffusion boundary condition), then to leading order, f is azimuthally symmetric about the outward normal at the boundary. The above relation is then equivalent to the following:

$$\int_{\boldsymbol{\Omega}\cdot\boldsymbol{n}>0} (\boldsymbol{\Omega}\cdot\boldsymbol{n}) f(\boldsymbol{x},\boldsymbol{\Omega})\,\mathrm{d}\Omega = \int_{\boldsymbol{\Omega}\cdot\boldsymbol{n}<0} |\boldsymbol{\Omega}\cdot\boldsymbol{n}|\, f(\boldsymbol{x},\boldsymbol{\Omega})\,\mathrm{d}\Omega\,. \tag{3.34}$$

Thus, the transport equation for f should have boundary conditions that enforce this relationship. Both specularly reflecting and "white" boundary conditions satisfy Eq. (3.34). The above condition does not *define* the boundary condition for f; it is only a restriction that preserves Eq. (3.4).

In the case when f is azimuthally symmetric about the outward normal, Eq. (3.32) can be written:

$$\boldsymbol{d}(\boldsymbol{x}) = -\int_{\boldsymbol{\Omega}\cdot\boldsymbol{n}<0} W(|\boldsymbol{\Omega}\cdot\boldsymbol{n}|)(-|\boldsymbol{\Omega}\cdot\boldsymbol{n}|\,\boldsymbol{n}) f(\boldsymbol{x},\boldsymbol{\Omega})\,\mathrm{d}\Omega\,,$$

thereby simplifying to the following expression:

$$\boldsymbol{d}(\boldsymbol{x}) = \left[\int_{\boldsymbol{\Omega}\cdot\boldsymbol{n}<0} |\boldsymbol{\Omega}\cdot\boldsymbol{n}|\, W(|\boldsymbol{\Omega}\cdot\boldsymbol{n}|) f(\boldsymbol{x},\boldsymbol{\Omega})\,\mathrm{d}\Omega\right]\boldsymbol{n}\,. \tag{3.35}$$

Thus the vector quantity $\boldsymbol{d}$ lives on the boundary, points along the outward normal, and has a positive magnitude that depends on the incident distribution of f. If f is isotropic and equal to the infinite medium value $1/(4\pi\sigma)$, then $\|\boldsymbol{d}\|$ reduces to $z_0/(2\sigma)$, where z_0 is the transport-corrected extrapolation distance for diffusion, and Eq. (3.33) becomes the transport-corrected standard diffusion boundary condition with transport extrapolation distance.

Marshak-like boundary condition

One distribution for the incident f that satisfies Eq. (3.34) is a specularly reflecting boundary:

$$f(\boldsymbol{x},\boldsymbol{\Omega}) = f(\boldsymbol{x},\boldsymbol{\Omega}_r)\,, \quad \boldsymbol{x}\in\partial V,\ \boldsymbol{\Omega}\cdot\boldsymbol{n}<0\,. \tag{3.36}$$

Here, $\boldsymbol{\Omega}_r$ is the reflected angle on a boundary surface with outward normal $\boldsymbol{n}$:

$$\boldsymbol{\Omega}_r = \boldsymbol{\Omega} - 2(\boldsymbol{\Omega}\cdot\boldsymbol{n})\boldsymbol{n}\,. \tag{3.37}$$

The choice of a reflecting boundary has a particular advantage if we use the "Marshak" approximation that $W(\mu) \approx 2\mu$. Equation (3.33) becomes

$$2\int_{\boldsymbol{\Omega}\cdot\boldsymbol{n}<0} (2\,|\boldsymbol{\Omega}\cdot\boldsymbol{n}|)\, I^b(\boldsymbol{\Omega})\,\mathrm{d}\Omega = \phi + 2\boldsymbol{d}\cdot\boldsymbol{\nabla}\phi,$$

or:

$$4F^- = \phi + 2\boldsymbol{d}\cdot\boldsymbol{\nabla}\phi.$$

With the Marshak approximation to $W(\mu)$, the expression for $\boldsymbol{d}$ simplifies greatly. Equation (3.32), becomes

$$\begin{aligned}\boldsymbol{d} &= -\int_{\boldsymbol{\Omega}\cdot\boldsymbol{n}<0} 2\,|\boldsymbol{\Omega}\cdot\boldsymbol{n}|\,\boldsymbol{\Omega} f\,\mathrm{d}\Omega \\ &= 2\boldsymbol{n}\cdot\int_{\boldsymbol{\Omega}\cdot\boldsymbol{n}<0} \boldsymbol{\Omega}\boldsymbol{\Omega} f\,\mathrm{d}\Omega.\end{aligned}$$

Because our chosen boundary condition of f gives $f(\boldsymbol{\Omega}) = f(-\boldsymbol{\Omega})$ if f is azimuthally symmetric, the integrand is an even function of $\boldsymbol{\Omega}$:

$$\boldsymbol{d} = \boldsymbol{n}\cdot\int_{4\pi} \boldsymbol{\Omega}\boldsymbol{\Omega} f\,\mathrm{d}\Omega.$$

The integral on the right hand side is the anisotropic diffusion tensor from Eq. (3.16):

$$\boldsymbol{d} = \boldsymbol{n}\cdot\mathbf{D}.$$

Thus Marshak-like boundary approximation for anisotropic diffusion is:

$$4F^-(\boldsymbol{x},t) = \phi(\boldsymbol{x},t) + 2\boldsymbol{n}\cdot\mathbf{D}(\boldsymbol{x})\cdot\boldsymbol{\nabla}\phi(\boldsymbol{x},t). \tag{3.38}$$

This is analogous to the standard diffusion Marshak boundary condition,

$$4F^-(\boldsymbol{x},t) = \phi(\boldsymbol{x},t) + 2D(\boldsymbol{x})\boldsymbol{n}\cdot\boldsymbol{\nabla}\phi(\boldsymbol{x},t).$$

3.1.4 Summary

We have now derived a full description of the time-dependent anisotropic diffusion equations in a finite medium.

The anisotropic diffusion method approximates the transport equations (3.1) with a set of low-order equations for the scalar intensity ϕ that use a diffusion tensor calculated from a simple high-order transport equation.

The low order equation is the result of substituting the approximate Fick's law, Eq. (3.16), into the conservation equation (3.5):

$$\frac{1}{c}\frac{\partial\phi}{\partial t}(\boldsymbol{x},t) - \boldsymbol{\nabla}\cdot\mathbf{D}(\boldsymbol{x})\cdot\boldsymbol{\nabla}\phi(\boldsymbol{x},t) + \sigma(\boldsymbol{x})\phi(\boldsymbol{x},t) = q(\boldsymbol{x},t)\,, \quad \boldsymbol{x}\in V,\ t>0\,.$$

From the initial layer analysis, the initial condition is to leading order:

$$\phi(\boldsymbol{x},0) = \int_{4\pi} I^i(\boldsymbol{x},\boldsymbol{\Omega})\,\mathrm{d}\Omega\,, \quad \boldsymbol{x}\in V\,.$$

The incident source boundary condition with the simpler Marshak-like approximation from Eq. (3.38) is

$$4F^-(\boldsymbol{x},t) = \phi(\boldsymbol{x},t) + 2\boldsymbol{n}\cdot\mathbf{D}(\boldsymbol{x})\cdot\boldsymbol{\nabla}\phi(\boldsymbol{x},t)\,, \quad \boldsymbol{x}\in\partial V,\ t>0\,.$$

The anisotropic diffusion tensor is defined in Eq. (3.17),

$$\mathbf{D}(\boldsymbol{x}) \equiv \int_{4\pi} \boldsymbol{\Omega}\boldsymbol{\Omega} f(\boldsymbol{x},\boldsymbol{\Omega})\,\mathrm{d}\Omega\,,$$

where f is the solution of the steady-state, purely absorbing transport equation described by Eq. (3.15):

$$\boldsymbol{\Omega}\cdot\boldsymbol{\nabla} f(\boldsymbol{x},\boldsymbol{\Omega}) + \sigma(\boldsymbol{x}) f(\boldsymbol{x},\boldsymbol{\Omega}) = \frac{1}{4\pi}\,, \quad x\in V,\ \boldsymbol{\Omega}\in 4\pi\,. \tag{3.39a}$$

In conjunction with the Marshak boundary condition, f should be reflecting on the problem boundary:

$$f(\boldsymbol{x},\boldsymbol{\Omega}) = f(\boldsymbol{x},\boldsymbol{\Omega}_r)\,, \quad \boldsymbol{x}\in\partial V,\ \boldsymbol{\Omega}\cdot\boldsymbol{n}<0\,. \tag{3.39b}$$

In the more general case when Eq. (3.33) is used, f only needs to satisfy the relation given in Eq. (3.34):

$$\int_{\boldsymbol{\Omega}\cdot\boldsymbol{n}>0} (\boldsymbol{\Omega}\cdot\boldsymbol{n}) f(\boldsymbol{x},\boldsymbol{\Omega})\,\mathrm{d}\Omega = \int_{\boldsymbol{\Omega}\cdot\boldsymbol{n}<0} |\boldsymbol{\Omega}\cdot\boldsymbol{n}|\, f(\boldsymbol{x},\boldsymbol{\Omega})\,\mathrm{d}\Omega\,.$$

The corresponding (and more accurate) transport-matched low-order boundary condition from Eq. (3.33) is:

$$2\int_{\boldsymbol{\Omega}\cdot\boldsymbol{n}<0} W(|\boldsymbol{\Omega}\cdot\boldsymbol{n}|)\, I^b(\boldsymbol{x},\boldsymbol{\Omega},t)\,\mathrm{d}\Omega = \phi(\boldsymbol{x},t) + 2\boldsymbol{d}(\boldsymbol{x})\cdot\boldsymbol{\nabla}\phi(\boldsymbol{x},t)\,,$$

where $\boldsymbol{d}$ is defined in Eq. (3.32) as a function of the incident values for f, written here under the assumption that f is rotationally invariant about the outward normal at the boundary:

$$\boldsymbol{d}(\boldsymbol{x}) = \left[\int_{\boldsymbol{\Omega}\cdot\boldsymbol{n}<0} |\boldsymbol{\Omega}\cdot\boldsymbol{n}|\, W(|\boldsymbol{\Omega}\cdot\boldsymbol{n}|)\, f(\boldsymbol{x},\boldsymbol{\Omega})\, \mathrm{d}\Omega \right] \boldsymbol{n}\,.$$

3.2 Discussion

Even without numerical results for the anisotropic diffusion equations, a number of interesting and beneficial properties can be deduced from the low-order AD equations and the transport equations for f.

3.2.1 Application to nonlinear radiation transport

In §3.1, the asymptotic analysis was performed only for linear time-dependent transport equation rather than to the nonlinear system of TRT equations. (For a rigorous asymptotic analysis of the TRT equations, see Ref. [33].) To apply our results to TRT, we appeal to two facts.

First, the implementation of the TRT equations in this thesis uses the semi-implicit linearization from §2.2. In that form, the TRT equations over a time step are reduced to a linear transport equation with an isotropic scattering term. Thus the linear asymptotic analysis presented here is applicable to that linearized radiation equation.

Second, if the standard diffusion scaling is taken, the anisotropic diffusion equations yield the standard diffusion result to first order. To see this, we apply the scaling $\boldsymbol{\Omega}\cdot\boldsymbol{\nabla} \to \epsilon\boldsymbol{\Omega}\cdot\boldsymbol{\nabla}$ to the transport equation for f in Eq. (3.39a):

$$\epsilon\boldsymbol{\Omega}\cdot\boldsymbol{\nabla} f(\boldsymbol{x},\boldsymbol{\Omega},t) + \sigma(\boldsymbol{x},t) f(\boldsymbol{x},\boldsymbol{\Omega},t) = \frac{1}{4\pi}\,.$$

Here, we have assumed a time-dependent opacity; resultantly, f depends on time as a parameter (not a variable). Solving for f as a series expansion in ϵ, we find:

$$f(\boldsymbol{x},\boldsymbol{\Omega},t) \sim \frac{1}{4\pi\sigma} - \epsilon\frac{1}{\sigma}\boldsymbol{\Omega}\cdot\boldsymbol{\nabla}\frac{1}{4\pi\sigma} + O(\epsilon^2)\,.$$

Taking the second angular moment, we obtain a diffusion tensor isotropic to first order:

$$\mathbf{D}(\boldsymbol{x},t) = \frac{1}{3\sigma}\mathbf{I} - 0 + O(\epsilon^2)\,.$$

Substituting this into the anisotropic Fick's law yields the standard Fick's law:

$$\boldsymbol{F}(\boldsymbol{x},t) = -\frac{1}{3\sigma(\boldsymbol{x},t)}\boldsymbol{\nabla}\phi(\boldsymbol{x},t)\,.$$

In other words, in the conventional diffusion limit, anisotropic diffusion limits to conventional diffusion to first order.

We therefore assert that the anisotropic diffusion method will satisfy the conventional diffusive limit of the transport equation for thermal radiative transport.

The low-order anisotropic diffusion equation for TRT is

$$\frac{1}{c}\frac{\partial\phi}{\partial t}(\boldsymbol{x},t) - \boldsymbol{\nabla}\cdot\mathbf{D}(\boldsymbol{x},t)\cdot\boldsymbol{\nabla}\phi(\boldsymbol{x},t) + \sigma(\boldsymbol{x},T[\boldsymbol{x},t])\phi(\boldsymbol{x},t) = \sigma(\boldsymbol{x})ac[T(\boldsymbol{x},t)]^4 + q_r(\boldsymbol{x},t)\,,$$

where the anisotropic diffusion tensor depends on the temperature-dependent opacity σ via the transport equation for f:

$$\boldsymbol{\Omega}\cdot\boldsymbol{\nabla}f(\boldsymbol{x},\boldsymbol{\Omega},t) + \sigma(\boldsymbol{x},T[\boldsymbol{x},t])f(\boldsymbol{x},\boldsymbol{\Omega},t) = \frac{1}{4\pi}\,.$$

In this transport problem for f, the time t is merely a parameter: the time dependence of f is due entirely to the time-dependence of σ. When the semi-implicit approximation is made that freezes σ at the beginning of the time step, there is no feedback between ϕ and f during a time step.

3.2.2 Transport calculation for f

The anisotropic diffusion tensor is calculated from f, the solution to the purely absorbing transport problem in Eqs. (3.39) with a unit isotropic source, "conservative" boundary conditions, and the same opacities as the physical problem being simulated. This is a steady-state transport problem, although a time-dependent σ necessitates a recalculation of f at each time step.

In an infinite medium problem, a discrete ordinates (S_N) solution for f takes only one transport sweep to complete, because there is no scattering source to converge. However, for a finite problem, because the boundary conditions rely on exiting values of f, in practice more than one source iteration (SI) will be required. The larger the optical thickness between boundaries, the faster the convergence will be. Conversely, if two opposing boundaries are separated by only a fraction of a mean free path (e.g. in the case of a voided channel), an SI solution may require many iterations to converge, especially if a very fine angular quadrature set is used (one with ordinates that are nearly

perpendicular to the boundary). If reflecting boundaries are used in the calculation of f, the solution of $f(\boldsymbol{x},\boldsymbol{\Omega})$, where $\boldsymbol{x}$ is inside a voided channel and $\boldsymbol{\Omega}$ is parallel to the channel's walls, will be nearly singular. Source iteration will require a correspondingly large number of transport sweeps.

The convergence problem can be obviated somewhat by taking advantage of the flexibility in Eq. (3.34), which allows for other angular shapes on the boundary. For example, rather than using a reflecting boundary on the offending surface, the user could select a white boundary in the transport calculation for f. The "averaging" effect of the white boundary leads to a solution along the voided region is no longer singular, and source iteration will converge more quickly.

For time-dependent problems in which σ remains constant from one time step to the next, the calculation for f needs only to be run once. For nonlinear problems in which σ is a function of time, storing f on the outer boundaries of the problem (which is already necessary for reflecting boundary conditions) will greatly speed up the recalculation of f. After the first time step, a good guess for f on the boundary means that only large changes in σ near the boundary will cause source iteration to require more than one sweep to converge.

Another desirable property of f is that, because it is a steady-state quantity, and only its second angular moment is required, the full angle-dependent solution does not need to be stored. The second angular moment $\mathbf{D}$ can merely be *accumulated* during the transport sweep, as is done with steady-state S_N transport. This is a distinct advantage over traditional time-dependent transport methods, which require the memory-intensive storage of the full solution $I(\boldsymbol{x},\boldsymbol{\Omega},t)$.

If the problem is homogeneous, then the interior solution for the purely absorbing transport problem is an isotropic, constant $f = 1/(4\pi\sigma)$. Taking the second moment of f then yields

$$\mathbf{D} = \frac{1}{4\pi\sigma}\int_{4\pi}\boldsymbol{\Omega}\boldsymbol{\Omega}\,\mathrm{d}\Omega = \frac{1}{3\sigma}\mathbf{I}.$$

Substituting this into the *anisotropic* Fick's law, Eq. (3.16), we reproduce the *standard* Fick's law:

$$\boldsymbol{F} = -\frac{1}{3\sigma}\boldsymbol{\nabla}\phi.$$

Thus, for a homogeneous medium, the anisotropic diffusion method reduces to the standard diffusion method. In a finite problem, either a specular reflecting or a white boundary will produce an isotropic incident $f = 1/(4\pi\sigma)$, which reproduces the standard diffusion coefficient near the boundaries.[2]

[2]The choice of a non-isotropic incident distribution for f will introduce a boundary layer, which is

Even in an inhomogeneous medium, if the transport equation for f is scaled as

$$\epsilon \boldsymbol{\Omega} \cdot \boldsymbol{\nabla} f(\boldsymbol{x}, \boldsymbol{\Omega}) + \sigma(\boldsymbol{x}) f(\boldsymbol{x}, \boldsymbol{\Omega}) = \frac{1}{4\pi},$$

then as $\epsilon \to 0$,

$$f(\boldsymbol{x}, \boldsymbol{\Omega}) \to \frac{1}{4\pi\sigma(\boldsymbol{x})} \quad \Longrightarrow \quad \mathbf{D}(\boldsymbol{x}) \to \frac{1}{3\sigma(\boldsymbol{x})}\mathbf{I},$$

which is the standard diffusion coefficient. The selection $\epsilon = 1$ yields the anisotropic diffusion tensor.

3.2.3 Properties of the anisotropic diffusion tensor

The diffusion tensor is defined in Eq. (3.17) to be

$$\mathbf{D}(\boldsymbol{x}) \equiv \int_{4\pi} \boldsymbol{\Omega}\boldsymbol{\Omega} f(\boldsymbol{x}, \boldsymbol{\Omega}) \, \mathrm{d}\Omega \,.$$

Equivalently, the component in row i, column j of $\mathbf{D}$ is

$$D^{ij} = \int_{4\pi} \Omega^i \Omega^j f(\boldsymbol{x}, \boldsymbol{\Omega}) \, \mathrm{d}\Omega \,, \tag{3.40}$$

where Ω^i is the ith component of the angular vector $\boldsymbol{\Omega}$ (e.g., $i = 1$ corresponds to the polar cosine angle μ).

Fick's law

Fick's law for diffusion states that a gradient in ϕ will induce particles to flow from the area of higher density to lower density along the gradient:

$$\boldsymbol{F}(\boldsymbol{x}, t) = -D(\boldsymbol{x}) \boldsymbol{\nabla} \phi(\boldsymbol{x}, t) \,.$$

The anisotropic diffusion tensor has a twist: a gradient in ϕ can induce particle flow in a direction *other than the direction of the gradient*. In 2-D, the anisotropic Fick's law has the form

$$\boldsymbol{F} = -\mathbf{D} \cdot \boldsymbol{\nabla} \phi \quad \Longrightarrow \quad \begin{bmatrix} F^x \\ F^y \end{bmatrix} = - \begin{bmatrix} D^{xx} & D^{yx} \\ D^{xy} & D^{yy} \end{bmatrix} \begin{bmatrix} \partial\phi/\partial x \\ \partial\phi/\partial y \end{bmatrix} .$$

If we calculate the "leakage" $\boldsymbol{n} \cdot \boldsymbol{F}$ averaged over a planar surface normal to $\boldsymbol{n}$, standard diffusion only depends on the gradient *normal* to the surface. For example, on a surface

undesirable as it does not preserve the standard diffusion solution near the problem's external boundary.

normal to the x axis, standard diffusion gives the leakage term

$$F^x = -D\frac{\partial\phi}{\partial x}.$$

However, anisotropic diffusion has the following leakage term:

$$F^x = -D^{xx}\frac{\partial\phi}{\partial x} - D^{yx}\frac{\partial\phi}{\partial y}.$$

We refer to the leakage normal to the face, $-D^{xx}\frac{\partial\phi}{\partial x}$, as "normal" leakage; the leakage along the face, $-D^{yx}\frac{\partial\phi}{\partial y}$, we use the term "transverse" leakage.[3] In Chapter 5, we show that the transverse leakage adds a layer of complexity to anisotropic diffusion discretization schemes that is not present in standard diffusion discretizations.

Behavior in voids

The diffusion model for neutrons and radiative transfer is often used far outside its realm of strict asymptotic applicability. In the case of radiation transport, a particularly egregious failure occurs near voided regions, where the true solution has strong spatial and temporal gradients (see §2.3.4). Standard diffusion fails in regions where $\sigma = 0$, particularly for problems with long voided channels along which the true ϕ can vary significantly. In contrast, anisotropic diffusion gracefully yields a qualitatively realistic approximation to the behavior of particles in a void.

The standard diffusion coefficient is defined as

$$D(\boldsymbol{x}) = \frac{1}{3\sigma(\boldsymbol{x})}.$$

As $\sigma \to 0$ locally, $D \to \infty$. An infinite diffusion coefficient in a region gives a spatially constant ϕ, which is almost always an unphysical result.[4]

In contrast to standard diffusion, the anisotropic diffusion approximation has a *non-local* dependence on σ through $f(\boldsymbol{x},\boldsymbol{\Omega})$. Since f remains bounded, even when $\sigma = 0$ at some point, $\mathbf{D}$ will also remain bounded. Furthermore, the behavior of the anisotropic Fick's law in a voided region benefits from the transport-calculated information embedded in the anisotropic diffusion tensor $\mathbf{D}$ that the standard diffusion's isotropic tensor D lacks. Because $f(\boldsymbol{x},\boldsymbol{\Omega})$ is larger for directions $\boldsymbol{\Omega}$ parallel to a voided channel

[3] These terms are compatible with the form of anisotropic diffusion used in geology and fluid flow. In the field of magneto-hydrodynamics, the terms "perpendicular" and "parallel" replace "normal" and "transverse," respectively.

[4] One exception is that in a 1-D slab configuration, a voided region truly does have a constant solution.

than perpendicular to it, the second angular moment **D** has a stronger action along that direction. In other words, particles in a channel prefer to travel along a voided channel than across it.

Linear algebraic properties

From Eq. (3.40), **D** is clearly symmetric: $D^{ij} = D^{ji}$. Yet **D** is also symmetric positive definite (SPD): this property follows from the fact that **D** is the second moment of a nonnegative density on a unit sphere, just like an Eddington tensor [51].

However, unlike the Eddington tensor used in quasidiffusion (see §2.3.2), which approximates the radiation flux using

$$\frac{1}{c}\frac{\partial \boldsymbol{F}}{\partial t} + \boldsymbol{\nabla}\cdot\mathbf{E}\phi + \sigma \boldsymbol{F} = 0\,,$$

the diffusion tensor is outside of the gradient operator:

$$\mathbf{D}\cdot\boldsymbol{\nabla}\phi + \boldsymbol{F} = 0\,.$$

The anisotropic Fick's law is therefore a self-adjoint equation. Consequently, many reasonable discretizations of the anisotropic diffusion equations will be SPD as well, allowing solution by the conjugate gradient (CG) method [56]. This is in contrast to quasidiffusion methods, which require a more computationally expensive solver such as GMRES [57].

Additionally, the principle eigenvector of the diffusion tensor (the direction on which **D** has the greatest action) can sometimes be deduced by the physics of the problem. We first note that **D** depends only on the transport solution f, and f depends only on the total opacity σ. Therefore, if at point $\boldsymbol{x}$ the opacity σ is invariant about some unit direction $\boldsymbol{n}$, then the solution f will be rotationally invariant about $\boldsymbol{n}$. As discussed in Ref. [51], the action of **D** upon $\boldsymbol{n}$ must therefore be invariant under the rotational transformation, and is therefore an eigenvector of **D**:

$$\mathbf{D}\cdot\boldsymbol{n} \equiv \int_{4\pi} \boldsymbol{\Omega\Omega}\cdot\boldsymbol{n} f \,\mathrm{d}\Omega = \chi\boldsymbol{n}\,.$$

Because the diffusion tensor is SPD, its eigenvectors are orthogonal. The implication is that if σ in a 2-D problem varies only along the x axis, then both the x and y unit vectors are eigenvectors of **D**, i.e., the diffusion tensor has only components along the diagonal, and there is no transverse leakage on any Cartesian face in the problem. As we will discuss in Chapter 5, it is numerically advantageous to have only normal leakage.

To exemplify the usefulness of knowing the eigenvectors, we consider the 2-D VHTR problem in Ref. [2], which features a total cross section that varied only in the x direction. From the discussion above, we know *a priori* that, even though the physical problem is two-dimensional, the diffusion tensor has principle eigenvectors oriented along the Cartesian axes, yielding $D^{xy} = D^{yx} = 0$ and allowing the use of a simple spatial discretization.

Smoothness

The standard diffusion coefficient, $1/3\sigma$, is discontinuous at material interfaces. Such is not the case with anisotropic diffusion. Recall that f is the solution of a transport equation with a unit source: the solution is continuous and positive. Thus the second angular moment of f, the anisotropic diffusion tensor, is also a continuous function of position.

The consequence of a discontinuity in the diffusion coefficient is a "kink" in the scalar intensity—a continuous value for ϕ but a discontinuous first derivative. From standard diffusion, this may be discerned from Fick's law, which we consider in 1-D for simplicity:

$$F(x) = -D(x)\frac{\partial \phi}{\partial x}(x)\,.$$

Particle conservation demands that F be continuous: a discontinuity in D must necessarily be balanced by a discontinuity in $\partial\phi/\partial x$. Likewise, if $D(x)$ is continuous, as is the case for anisotropic diffusion, the first derivative of ϕ must necessarily be continuous. The smooth transition of the anisotropic diffusion tensor $\mathbf{D}$ at a material discontinuity produces a boundary layer between the materials. Standard diffusion has no boundary layer.

The true transport solution contains both a boundary layer *and* a kink in the scalar intensity. Anisotropic diffusion contains the former; standard diffusion, the latter.

The smoothness of the interior solution ϕ for anisotropic diffusion is compatible with the derivation of the anisotropic diffusion approximation, the starting assumption that the derivatives of ϕ are small.

A possible implication of a smooth diffusion coefficient is that a spatially coarse approximation to $\mathbf{D}$ may yield nearly as accurate an answer as a fine-mesh calculation of $\mathbf{D}$. Because even the simple transport sweep used to calculate f will likely be far more computationally expensive than a diffusion solve, this could result in a significant speedup for AD calculations.

3.3 Flux-limited anisotropic diffusion

Like standard diffusion, the time-dependent anisotropic diffusion equation is parabolic [50, 18], allowing radiation energy to unphysically propagate faster than the speed of light. This undesirable property results from the assumption that the time derivative of the intensity varied slowly in time, $\frac{1}{c}\frac{\partial I}{\partial t} = O(\epsilon^2)$, effectively the same quasi-static approximation as standard diffusion. To overcome this defect, we apply a flux limiter (see §2.3.4) to the anisotropic diffusion approximation.

To recapitulate, a flux limiter enforces the following property of the true intensity:

$$\|\boldsymbol{F}\| \leq \phi\,. \tag{3.41}$$

This is accomplished by modifying the approximation to $\boldsymbol{F}$, which in standard diffusion is the standard Fick's law that relates the radiation flux to the gradient of the intensity. In the presence of steep gradients, the diffusion coefficient D is modified so that Eq. (3.41) is satisfied:

$$\left\|-D\boldsymbol{\nabla}\phi\right\| = D\left\|\boldsymbol{\nabla}\phi\right\| \leq \phi\,.$$

Like the standard diffusion Fick's law, the new "anisotropic" Fick's law, Eq. (3.16), can violate Eq. (3.41):

$$\left\|-\mathbf{D}\cdot\boldsymbol{\nabla}\phi\right\| \stackrel{?}{\leq} \phi\,.$$

The left hand side can exceed the right if either $\mathbf{D}$ or $\boldsymbol{\nabla}\phi$ is "large", which may occur in optically thin regions or in a radiation shock wave. Flux-limited anisotropic diffusion (FLAD) modifies the transport-calculated anisotropic diffusion tensor to preserve Eq. (3.41) in the presence of large gradients.

Constructing a flux limiter for anisotropic diffusion is less straightforward than for standard diffusion. The scalar diffusion coefficient D may simply be moved outside the magnitude operator $\|\cdot\|$, but the anisotropic diffusion *tensor* $\mathbf{D}$ cannot be treated that way. However, a "max" limiter for anisotropic diffusion is easily formulated. A semi-implicit implementation of this limiter is

$$\mathbf{D}^{n+1/2} = \mathbf{D}^n \times \max\left(1, \left\|\mathbf{D}^n \cdot \frac{\boldsymbol{\nabla}\phi^n}{\phi^n}\right\|\right)^{-1}. \tag{3.42}$$

Effectively, the limiter tests whether an estimate of $\boldsymbol{F}^{n+1}$ (using the previous time step's solution) exceeds the flux limit; if it does, then it uniformly scales the diffusion tensor to satisfy the estimated limit.

Flux limiting is an admittedly *ad hoc* correction, but it restores a qualitative behavior

of the true intensity when the assumptions that led to anisotropic diffusion break down. However, because the magnitude of the anisotropic diffusion tensor is always smaller than the corresponding standard diffusion coefficient in an optically thin region (see §3.2.3), the flux limiting relationship of Eq. (3.41) will not be violated as often. We expect that anisotropic diffusion flux limiter will therefore be used less often.

3.4 Summary

To derive the anisotropic diffusion method, we manipulated the transport equation in the interior of the physical system under certain asymptotic assumptions: primarily, that the spatial and temporal gradients of the intensity are weak. From boundary and initial layer analyses we determined transport-matched boundary and initial conditions.

The procedure resulted in two straightforward sets of equations. The first set is a simple transport equation for f, whose second angular moment is the anisotropic diffusion tensor $\mathbf{D}$. The second set of equations are the low-order equations for ϕ that use $\mathbf{D}$ to approximate the flow of radiation inside a time step.

These equations limit to the standard diffusion approximation in a homogeneous medium, but they do not make the diffusion approximation that the radiation intensity be linear in angle. We therefore expect the AD method to yield more accurate solutions for problems in which the intensity is a complex function of angle. Chapters 7 and 8 will put this expectation to the test.

Chapter 4

Anisotropic P_1

The anisotropic diffusion method was derived under the assumptions that the intensity has weak spatial gradients, mild anisotropy, and very slow time dependence. By reducing the asymptotic smallness of the time derivative, we derive a new "anisotropic" method, which we name *anisotropic* P_1 (AP_1). In the steady-state case, it reduces to the anisotropic diffusion approximation; in the homogeneous-medium case, it reduces to the standard P_1 (spherical harmonic) approximation.

4.1 Derivation

We begin with the linear, time-dependent transport equation with isotropic scattering. By omitting the complication of material–radiation coupling and nonlinearities, we derive the AP_1 equations with a straightforward linear asymptotic analysis. We then show how the results may be applied to the thermal radiative transfer equations.

The linear transport equation, given in Chapter 3 and repeated here, comprise the Boltzmann equation,

$$\frac{1}{c}\frac{\partial I}{\partial t}(\boldsymbol{x},\boldsymbol{\Omega},t)+\boldsymbol{\Omega}\cdot\boldsymbol{\nabla} I(\boldsymbol{x},\boldsymbol{\Omega},t)+\sigma(\boldsymbol{x})I(\boldsymbol{x},\boldsymbol{\Omega},t) = \frac{\sigma_s(\boldsymbol{x})}{4\pi}\int_{4\pi} I(\boldsymbol{x},\boldsymbol{\Omega}',t)\,\mathrm{d}\Omega'+\frac{q(\boldsymbol{x},t)}{4\pi}, \quad \boldsymbol{x}\in V,\ \boldsymbol{\Omega}\in 4\pi,\ t\geq 0; \tag{4.1}$$

the boundary condition,

$$I(\boldsymbol{x},\boldsymbol{\Omega},t)=I^b(\boldsymbol{x},\boldsymbol{\Omega},t), \quad \boldsymbol{x}\in\partial V,\ \boldsymbol{\Omega}\cdot\boldsymbol{n}<0,\ t>0; \tag{4.2}$$

and the initial condition,

$$I(\boldsymbol{x},\boldsymbol{\Omega},0)=I^i(\boldsymbol{x},\boldsymbol{\Omega}), \quad \boldsymbol{x}\in V,\ \boldsymbol{\Omega}\in 4\pi. \tag{4.3}$$

To perform the asymptotic analysis, we again consider the intensity as the linear

superposition of three distinct transport solutions:

$$I(\boldsymbol{x},\boldsymbol{\Omega},t) \equiv I_{\mathrm{v}}(\boldsymbol{x},\boldsymbol{\Omega},t) + I_{\mathrm{bl}}(\boldsymbol{x},\boldsymbol{\Omega},t) + I_{\mathrm{il}}(\boldsymbol{x},\boldsymbol{\Omega},t)\,. \tag{4.4}$$

Here, I_{v} is an "interior" solution, I_{bl} is a "boundary layer" solution, and I_{il} is an "initial layer" solution. For a more detailed description of these, see §3.1 and Fig. 3.1.

We shall approximate the interior solution I_{v} using a slightly different set of assumptions than were used to arrive at the anisotropic diffusion approximation. As before, the boundary and initial layer solutions are used to match the resulting interior result to the transport solution at the boundary and initial time.

4.1.1 Interior solution

The interior transport equation is valid several mean free paths away from the outer boundary, and several mean free times after the initial time. It is identical to the interior equation in §3.1.1, and the first steps in developing the AP_1 approximation strongly resemble those for the AD approximation. The derivation differs because the AP_1 assumptions do not allow the time derivative to be discarded: we instead "split" the transport operator into a component that depends on angle and a component that depends on time. The result is an interior approximation I_{v} that requires the storage of both ϕ and $\boldsymbol{F}$.

The interior transport equation is

$$\frac{1}{c}\frac{\partial I_{\mathrm{v}}}{\partial t}(\boldsymbol{x},\boldsymbol{\Omega},t) + \boldsymbol{\Omega}\cdot\boldsymbol{\nabla} I_{\mathrm{v}}(\boldsymbol{x},\boldsymbol{\Omega},t) + \sigma(\boldsymbol{x}) I_{\mathrm{v}}(\boldsymbol{x},\boldsymbol{\Omega},t) = \frac{\sigma_s(\boldsymbol{x})}{4\pi}\phi(\boldsymbol{x},t) + \frac{q(\boldsymbol{x},t)}{4\pi}\,, \tag{4.5}$$

with the *interior* scalar intensity defined as

$$\phi(\boldsymbol{x}) \equiv \int_{4\pi} I_{\mathrm{v}}(\boldsymbol{x},\boldsymbol{\Omega},t)\,\mathrm{d}\Omega\,. \tag{4.6}$$

The zeroth angular moment of the interior transport equation is the following conservation equation:

$$\frac{1}{c}\frac{\partial \phi}{\partial t}(\boldsymbol{x},t) + \boldsymbol{\nabla}\cdot\boldsymbol{F}(\boldsymbol{x},t) + \sigma(\boldsymbol{x})\phi(\boldsymbol{x},t) = \sigma_s(\boldsymbol{x})\phi(\boldsymbol{x},t) + q(\boldsymbol{x},t)\,, \tag{4.7}$$

with the *interior* radiation flux defined as

$$\boldsymbol{F} \equiv \int_{4\pi} \boldsymbol{\Omega} I_{\mathrm{v}}(\boldsymbol{x},\boldsymbol{\Omega},t)\,\mathrm{d}\Omega\,. \tag{4.8}$$

By combining Eqs. (4.5) and (4.7) (see §3.1.1), we eliminate the isotropic scattering

and extraneous sources on the right-hand side of the transport equation to obtain

$$\left[\frac{1}{c}\frac{\partial}{\partial t}+\mathbf{\Omega}\cdot\boldsymbol{\nabla}+\sigma\right]\left(I_{\mathrm{v}}-\frac{1}{4\pi}\phi\right)=\frac{1}{4\pi}\boldsymbol{\nabla}\cdot\boldsymbol{F}-\frac{1}{4\pi}\mathbf{\Omega}\cdot\boldsymbol{\nabla}\phi\,. \tag{4.9}$$

Next, we approximate Eq. (4.9) by making an asymptotic ansatz about the behavior of I and then discarding "small" terms. Here the derivation diverges from anisotropic diffusion: rather than assuming $\partial I/\partial t = O(\epsilon^2)$, we take the scaling $\partial I/\partial t = O(\epsilon)$. Thus the assumed magnitude of the intensity, its derivatives, and its anisotropy are:

$$\sigma = O(1), \qquad I = O(1), \qquad \int_{4\pi}\mathbf{\Omega} I\,\mathrm{d}\Omega = O(\epsilon), \qquad \boldsymbol{\nabla} I = O(\epsilon), \qquad \frac{\partial I}{\partial t} = O(\epsilon)\,. \tag{4.10}$$

The stronger assumed magnitude of $\partial I/\partial t$ requires that the time derivative in Eq. (4.9) must be retained to preserving $O(\epsilon^2)$ accuracy. (This differs from anisotropic diffusion, in which the term was discarded.) The only asymptotically small term is $\boldsymbol{\nabla}\cdot\boldsymbol{F} = O(\epsilon^2)$, which we discard. Equation (4.9) is then

$$\left[\frac{1}{c}\frac{\partial}{\partial t}+\mathbf{\Omega}\cdot\boldsymbol{\nabla}+\sigma\right]\left(I_{\mathrm{v}}-\frac{1}{4\pi}\phi\right)=-\frac{1}{4\pi}\mathbf{\Omega}\cdot\boldsymbol{\nabla}\phi\,.$$

Now we decompose the "time + leakage + collision" operator on the left-hand side into an $(\boldsymbol{x}, t)$-dependent operator, an $(\boldsymbol{x}, \mathbf{\Omega})$-dependent operator, and an asymptotically small remainder:

$$\frac{1}{c}\frac{\partial}{\partial t}+\mathbf{\Omega}\cdot\boldsymbol{\nabla}+\sigma=(\mathbf{\Omega}\cdot\boldsymbol{\nabla}+\sigma)\left(\frac{1}{\sigma}\frac{1}{c}\frac{\partial}{\partial t}+1\right)-\mathbf{\Omega}\cdot\boldsymbol{\nabla}\frac{1}{\sigma}\frac{1}{c}\frac{\partial}{\partial t}\,.$$

Formally, the rightmost term is $O(\epsilon^2)$: σ is $O(1)$, $\mathbf{\Omega}\cdot\boldsymbol{\nabla}$ is $O(\epsilon)$, and $\frac{1}{c}\frac{\partial}{\partial t}$ is $O(\epsilon)$. Thus the previous equation can be written with $O(\epsilon^2)$ error as:

$$(\mathbf{\Omega}\cdot\boldsymbol{\nabla}+\sigma)\left(\frac{1}{\sigma}\frac{1}{c}\frac{\partial}{\partial t}+1\right)\left(I_{\mathrm{v}}-\frac{1}{4\pi}\phi\right)=-\frac{1}{4\pi}\mathbf{\Omega}\cdot\boldsymbol{\nabla}\phi\,.$$

By making the definition

$$\Psi(\boldsymbol{x},\mathbf{\Omega},t)\equiv\left(\frac{1}{\sigma(\boldsymbol{x})}\frac{1}{c}\frac{\partial}{\partial t}+1\right)\left(I_{\mathrm{v}}(\boldsymbol{x},\mathbf{\Omega},t)-\frac{1}{4\pi}\phi(\boldsymbol{x},t)\right), \tag{4.11}$$

we obtain the following "steady-state" equation:

$$\left[\mathbf{\Omega}\cdot\boldsymbol{\nabla}+\sigma(\boldsymbol{x})\right]\Psi(\boldsymbol{x},\mathbf{\Omega},t)=-\frac{1}{4\pi}\mathbf{\Omega}\cdot\boldsymbol{\nabla}\phi(\boldsymbol{x},t)\,. \tag{4.12}$$

Here, time is a parameter, not a variable: if $\phi(\boldsymbol{x}, t)$ is known, $\Psi(\boldsymbol{x}, \boldsymbol{\Omega}, t)$ can be calculated without knowledge of any prior ϕ or Ψ.

Equation (4.12) is very similar to Eq. (3.9) of the AD derivation. As we did there, we formally invert the streaming + collision operator on the left, interpreting the inverse as an integral transport operator:

$$\begin{aligned}\Psi &= [\boldsymbol{\Omega}\cdot\boldsymbol{\nabla}+\sigma]^{-1}\left(-\frac{1}{4\pi}\boldsymbol{\Omega}\cdot\boldsymbol{\nabla}\phi\right)\\ &= -\int_0^\infty \left(\frac{1}{4\pi}\boldsymbol{\Omega}\cdot\boldsymbol{\nabla}\phi(\boldsymbol{x}-s\boldsymbol{\Omega}, t)\right)\mathrm{e}^{-\tau(\boldsymbol{x},\boldsymbol{x}-s\boldsymbol{\Omega})}\,\mathrm{d}s\,.\end{aligned}$$

Taylor-expanding the non-local ϕ about the local point $\boldsymbol{x}$, and recalling the assumption that $\boldsymbol{\nabla}\phi = O(\epsilon)$, we move ϕ outside the operator to obtain the following:

$$\begin{aligned}\Psi(\boldsymbol{x}, \boldsymbol{\Omega}, t) &= -\left[\int_0^\infty \frac{1}{4\pi}\,\mathrm{e}^{-\tau(\boldsymbol{x},\boldsymbol{x}-s\boldsymbol{\Omega})}\,\mathrm{d}s\right]\boldsymbol{\Omega}\cdot\boldsymbol{\nabla}\phi(\boldsymbol{x}, t) + O(\epsilon^2)\\ &= -\left[(\boldsymbol{\Omega}\cdot\boldsymbol{\nabla}+\sigma)^{-1}\,\frac{1}{4\pi}\right]\boldsymbol{\Omega}\cdot\boldsymbol{\nabla}\phi(\boldsymbol{x}, t)\\ &= -\left[f(\boldsymbol{x}, \boldsymbol{\Omega})\right]\boldsymbol{\Omega}\cdot\boldsymbol{\nabla}\phi(\boldsymbol{x}, t)\,.\end{aligned} \tag{4.13}$$

Here, f is the solution to the same purely absorbing, steady-state transport problem as in §3.1.1:

$$\boldsymbol{\Omega}\cdot\boldsymbol{\nabla} f(\boldsymbol{x}, \boldsymbol{\Omega}) + \sigma(\boldsymbol{x}) f(\boldsymbol{x}, \boldsymbol{\Omega}) = \frac{1}{4\pi}\,. \tag{4.14}$$

We substitute the $O(\epsilon^2)$-accurate expression for Ψ, Eq. (4.13), into Eq. (4.11):

$$\left(\frac{1}{\sigma(\boldsymbol{x})}\frac{1}{c}\frac{\partial}{\partial t}+1\right)\left(I_\mathrm{v}(\boldsymbol{x}, \boldsymbol{\Omega}, t) - \frac{1}{4\pi}\phi(\boldsymbol{x}, t)\right) = -f(\boldsymbol{x}, \boldsymbol{\Omega})\boldsymbol{\Omega}\cdot\boldsymbol{\nabla}\phi(\boldsymbol{x}, t)\,. \tag{4.15}$$

Taking the first angular moment of this equation eliminates ϕ on the left-hand side to yield the following equation:

$$\left(\frac{1}{\sigma(\boldsymbol{x})}\frac{1}{c}\frac{\partial}{\partial t}+1\right)\boldsymbol{F}(\boldsymbol{x}, t) = -\int_{4\pi}\boldsymbol{\Omega} f(\boldsymbol{x}, \boldsymbol{\Omega})\boldsymbol{\Omega}\,\mathrm{d}\Omega\cdot\boldsymbol{\nabla}\phi(\boldsymbol{x}, t)\,. \tag{4.16}$$

Multiplying through by σ and rearranging, we get:

$$\frac{1}{c}\frac{\partial \boldsymbol{F}}{\partial t}(\boldsymbol{x}, t) + \sigma(\boldsymbol{x})\mathbf{D}(\boldsymbol{x})\cdot\boldsymbol{\nabla}\phi(\boldsymbol{x}, t) + \sigma(\boldsymbol{x})\boldsymbol{F}(\boldsymbol{x}, t) = 0\,, \tag{4.17}$$

where we have used the definition of the anisotropic diffusion tensor from Chapter 3,

$$\mathbf{D}(\boldsymbol{x}) \equiv \int_{4\pi} \boldsymbol{\Omega}\boldsymbol{\Omega} f(\boldsymbol{x}, \boldsymbol{\Omega})\, \mathrm{d}\Omega\,. \tag{4.18}$$

Equation (4.17) is our first attempt at an "anisotropic P_1" equation. It approximates the radiation using the scalar unknown ϕ and the vector unknown $\boldsymbol{F}$ in tandem with the calculated anisotropic diffusion tensor $\mathbf{D}$.

In a homogeneous medium, $\mathbf{D}$ limits to $\mathbf{I}/(3\sigma)$, so Eq. (4.17) becomes:

$$\frac{1}{c}\frac{\partial \boldsymbol{F}}{\partial t}(\boldsymbol{x}, t) - \frac{1}{3}\boldsymbol{\nabla}\phi(\boldsymbol{x}, t) + \sigma \boldsymbol{F}(\boldsymbol{x}, t) = 0\,,$$

which is the standard P_1 equation.

An important substitution

In a voided region, $\sigma \approx 0$, Eq. (4.17) has a serious deficiency. The nonlocal dependence of f on σ (see §3.2.3) prevents $\mathbf{D}$ from "blowing up," but in the AP_1 equation, the local $\sigma = 0$ eliminates two of the terms. In a void, Eq. (4.17) becomes the unphysical

$$\frac{1}{c}\frac{\partial \boldsymbol{F}}{\partial t}(\boldsymbol{x}, t) = 0\,.$$

(Preliminary numerical tests rightly demonstrated this to be a fatal shortcoming in any problem with optically thin regions.)

To understand this behavior, we show how a similar procedure yields the standard P_1 equation,

$$\frac{1}{c}\frac{\partial \boldsymbol{F}}{\partial t}(\boldsymbol{x}, t) - \frac{1}{3}\boldsymbol{\nabla}\phi(\boldsymbol{x}, t) + \sigma \boldsymbol{F} = 0\,.$$

We return to Equation (4.12), just after we split the time and angle operators with an asymptotic error of $O(\epsilon^2)$:

$$\Psi(\boldsymbol{x}, \boldsymbol{\Omega}, t) = -\left[\boldsymbol{\Omega}\cdot\boldsymbol{\nabla} + \sigma(\boldsymbol{x})\right]^{-1} \frac{1}{4\pi}\boldsymbol{\Omega}\cdot\boldsymbol{\nabla}\phi(\boldsymbol{x}, t)\,.$$

The term in brackets can be asymptotically expanded as

$$\left[\epsilon\boldsymbol{\Omega}\cdot\boldsymbol{\nabla} + \sigma\right]^{-1} \sim \frac{1}{\sigma}\left(1 - \epsilon\frac{1}{\sigma}\boldsymbol{\Omega}\cdot\boldsymbol{\nabla} + O(\epsilon^2)\right).$$

Substituting into Eq. (4.13) gives

$$\left(\frac{1}{\sigma(\boldsymbol{x})}\frac{1}{c}\frac{\partial}{\partial t}+1\right)\left(I_{\mathrm{v}}(\boldsymbol{x},\boldsymbol{\Omega},t)-\frac{1}{4\pi}\phi(\boldsymbol{x},t)\right)=-\frac{1}{\sigma(\boldsymbol{x})}\left(1-\frac{1}{\sigma}\boldsymbol{\Omega}\cdot\boldsymbol{\nabla}\right)\frac{1}{4\pi}\boldsymbol{\Omega}\cdot\boldsymbol{\nabla}\phi(\boldsymbol{x},t)\,.$$

The first angular moment of this equation is:

$$\frac{1}{\sigma}\frac{1}{c}\frac{\partial \boldsymbol{F}}{\partial t}+\boldsymbol{F}=-\frac{1}{3}\frac{1}{\sigma}\boldsymbol{\nabla}\phi\,.$$

Multiplying by σ gives the P_1 equation:

$$\frac{1}{c}\frac{\partial \boldsymbol{F}}{\partial t}+\frac{1}{3}\frac{1}{\sigma}\boldsymbol{\nabla}\phi+\sigma\boldsymbol{F}=0\,.$$

The asymptotic expansion used in the derivation of the P_1 equation used a local approximation to σ that corresponded to the local σ in the split operator. In contrast, the derivation of the "anisotropic" equation (4.17) uses both a local σ and a nonlocal f. To rectify this imbalance, we wish to replace the $1/\sigma$ in Eq. (4.16) with a quantity that does not blow up as $\sigma\to 0$ but which approaches $1/\sigma$ in the diffusive limit.

We make the following substitution, which is accurate to $O(\epsilon^2)$ in the diffusive limit (in which the opacity has weak spatial derivatives):

$$\begin{aligned}\frac{1}{\sigma(\boldsymbol{x})} &\approx \int_{4\pi} f(\boldsymbol{x},\boldsymbol{\Omega})\,\mathrm{d}\Omega\\ &= \int_{4\pi}(\boldsymbol{\Omega}\cdot\boldsymbol{\nabla}+\sigma(\boldsymbol{x}))^{-1}\frac{1}{4\pi}\,\mathrm{d}\Omega\\ &= \int_{4\pi}\left(\frac{1}{\sigma}\boldsymbol{\Omega}\cdot\boldsymbol{\nabla}+1\right)^{-1}\frac{1}{4\pi\sigma}\,\mathrm{d}\Omega\\ &\sim \int_{4\pi}\left(1-\frac{1}{\sigma}\boldsymbol{\Omega}\cdot\boldsymbol{\nabla}+O(\epsilon^2)\right)\frac{1}{4\pi\sigma}\,\mathrm{d}\Omega\\ &\sim \frac{1}{\sigma}+O(\epsilon^2)\,.\end{aligned}$$

The resulting AP_1 approximation is:

$$\frac{1}{\varsigma(\boldsymbol{x})}\frac{\partial \boldsymbol{F}}{\partial t}(\boldsymbol{x},t)+\boldsymbol{F}(\boldsymbol{x},t)=-\mathbf{D}(\boldsymbol{x})\cdot\boldsymbol{\nabla}\phi\,,$$

where we have defined

$$\frac{1}{\varsigma(\boldsymbol{x})}\equiv\int_{4\pi} f(\boldsymbol{x},\boldsymbol{\Omega})\,\mathrm{d}\Omega\sim\frac{1}{\sigma(\boldsymbol{x})}+O(\epsilon^2)\,. \tag{4.19}$$

Now Eq. (4.17) is replaced by the new anisotropic P_1 equation:

$$\frac{1}{c}\frac{\partial \boldsymbol{F}}{\partial t}(\boldsymbol{x},t)+\varsigma(\boldsymbol{x})\mathbf{D}(\boldsymbol{x})\cdot\boldsymbol{\nabla}\phi(\boldsymbol{x},t)+\varsigma(\boldsymbol{x})\boldsymbol{F}(\boldsymbol{x},t)=0\,. \tag{4.20}$$

This is a closure for the unknown $\boldsymbol{F}$ in the conservation equation (4.7); I_v in the interior is thus approximated by the unknowns ϕ and $\boldsymbol{F}$ using the coefficients ς and $\mathbf{D}$ calculated from the purely absorbing transport equation for f.

The interior approximate intensity

We return to Eq. (4.15) and replace σ with ς as discussed in the previous section:

$$\left(\frac{1}{\varsigma(\boldsymbol{x})}\frac{1}{c}\frac{\partial}{\partial t}+1\right)\left(I_\mathrm{v}(\boldsymbol{x},\boldsymbol{\Omega},t)-\frac{1}{4\pi}\phi(\boldsymbol{x},t)\right)=-f(\boldsymbol{x},\boldsymbol{\Omega})\boldsymbol{\Omega}\cdot\boldsymbol{\nabla}\phi(\boldsymbol{x},t)\,.$$

Formally inverting the operator on the left-hand side, we obtain an expression for the AP_1 approximation to the radiation intensity:

$$I_\mathrm{v}(\boldsymbol{x},\boldsymbol{\Omega},t)=\frac{1}{4\pi}\phi(\boldsymbol{x},t)-f(\boldsymbol{x},\boldsymbol{\Omega})\boldsymbol{\Omega}\cdot\left(\frac{1}{\varsigma(\boldsymbol{x})}\frac{1}{c}\frac{\partial}{\partial t}+1\right)^{-1}\boldsymbol{\nabla}\phi(\boldsymbol{x},t)\,. \tag{4.21}$$

This expression is unwieldy. We therefore rewrite it as a function of the known f and its second moment $\mathbf{D}$, and of the unknown ϕ and $\boldsymbol{F}$ that are solved using the conservation equation (4.7) and the AP_1 equation (4.20).

The first angular moment of Eq. (4.21) is a restatement of Eq. (4.20):

$$\boldsymbol{F}(\boldsymbol{x},t)=-\mathbf{D}(\boldsymbol{x})\cdot\left(\frac{1}{\varsigma(\boldsymbol{x})}\frac{1}{c}\frac{\partial}{\partial t}+1\right)^{-1}\boldsymbol{\nabla}\phi(\boldsymbol{x},t)\,.$$

Left-multiplying by the matrix inverse of $\mathbf{D}$, we obtain:

$$\mathbf{D}^{-1}(\boldsymbol{x})\cdot\boldsymbol{F}(\boldsymbol{x},t)=-\left(\frac{1}{\varsigma(\boldsymbol{x})}\frac{1}{c}\frac{\partial}{\partial t}+1\right)^{-1}\boldsymbol{\nabla}\phi(\boldsymbol{x},t)\,.$$

The right-hand side of this equation is present in Eq. (4.21). We substitute it for the left-hand side to obtain the anisotropic P_1 approximation to the radiation intensity:

$$I_\mathrm{v}(\boldsymbol{x},\boldsymbol{\Omega},t)=\frac{1}{4\pi}\phi(\boldsymbol{x},t)+f(\boldsymbol{x},\boldsymbol{\Omega})\boldsymbol{\Omega}\cdot\mathbf{D}^{-1}(\boldsymbol{x})\cdot\boldsymbol{F}(\boldsymbol{x},t)\,. \tag{4.22}$$

Here, ϕ and $\boldsymbol{F}$ are the solutions of Eqs. (4.7) and Eq. (4.20).

In a steady-state problem, $\boldsymbol{F}=-\mathbf{D}\cdot\boldsymbol{\nabla}\phi$, and the above equation reduces to the aniso-

tropic diffusion approximation to I_{v}.

4.1.2 Initial layer

Formally, as shown in Chapter 3, the initial layer solution matches the transport initial condition, Eq. (4.3), to the interior approximation of the radiation intensity, which in the case of AP_1 is Eq. (4.22). From Eq. (4.4), the initial conditions of the original transport equation, the interior approximation, and the initial layer satisfy:

$$I^i(\boldsymbol{x},\boldsymbol{\Omega}) = I_{\mathrm{v}}(\boldsymbol{x},\boldsymbol{\Omega},0) + I_{\mathrm{il}}(\boldsymbol{x},\boldsymbol{\Omega},0)\,,$$

and I_{il} must rapidly diminish as $t \to \infty$.

In the case of anisotropic P_1, which uses two unknowns ϕ and $\boldsymbol{F}$, the asymptotic matching procedure for the initial condition is not as clear as with anisotropic diffusion, which has the single unknown ϕ. (We are also not aware of any asymptotic procedure to derive the standard P_1 equations or match them to initial conditions.)

We therefore take the sensible approach of approximating $I_{\mathrm{il}} \approx 0$, and setting the zeroth and first moments of the AP_1 initial condition to the zeroth and first moments of the transport initial condition:

$$\phi(\boldsymbol{x},0) = \phi^i(\boldsymbol{x})\,, \qquad \text{and} \qquad \boldsymbol{F}(\boldsymbol{x},0) = \boldsymbol{F}^i(\boldsymbol{x})\,. \tag{4.23}$$

4.1.3 Boundary layer

The boundary layer describes the transition from the transport boundary condition to the interior solution. The boundary layer solution decays to zero rapidly in the spatial interior, and it satisfies the superposition equation (4.4):

$$I^b(\boldsymbol{x},\boldsymbol{\Omega},t) = I_{\mathrm{v}}(\boldsymbol{x},\boldsymbol{\Omega},t) + I_{\mathrm{bl}}(\boldsymbol{x},\boldsymbol{\Omega},t)\,, \quad \boldsymbol{x} \in \partial V, \boldsymbol{\Omega}\cdot\boldsymbol{n} < 0\,.$$

As described in §3.1.3, the condition that causes the boundary layer solution to vanish in the interior is

$$\int_{\boldsymbol{\Omega}\cdot\boldsymbol{n}<0} W(|\boldsymbol{\Omega}\cdot\boldsymbol{n}|)\, I_{\mathrm{bl}}(\boldsymbol{x},\boldsymbol{\Omega},t)\,\mathrm{d}\Omega = 0\,, \quad \boldsymbol{x} \in \partial V,\ \boldsymbol{\Omega}\cdot\boldsymbol{n} < 0. \tag{4.24}$$

(The function W is related to the Chandrasekhar function, $W(\mu) \approx \mu + \frac{3}{2}\mu^2$.)

Operating by $\int_{\boldsymbol{\Omega}\cdot\boldsymbol{n}<0} W(|\boldsymbol{\Omega}\cdot\boldsymbol{n}|)(\cdot)\,\mathrm{d}\Omega$ on the superposition equation at the boundary, and substituting the AP_1 approximation in the interior from Eq. (4.22), we obtain the

following relation:

$$\begin{aligned}
&\int_{\boldsymbol{\Omega}\cdot\boldsymbol{n}<0} W(|\boldsymbol{\Omega}\cdot\boldsymbol{n}|)\, I^b(\boldsymbol{x},\boldsymbol{\Omega},t)\,\mathrm{d}\Omega \\
&\quad = \int_{\boldsymbol{\Omega}\cdot\boldsymbol{n}<0} W(|\boldsymbol{\Omega}\cdot\boldsymbol{n}|)\left[\frac{1}{4\pi}\phi(\boldsymbol{x},t) + f(\boldsymbol{x},\boldsymbol{\Omega})\boldsymbol{\Omega}\cdot\mathbf{D}^{-1}(\boldsymbol{x})\cdot\boldsymbol{F}(\boldsymbol{x},t)\right]\mathrm{d}\Omega \\
&\quad = \frac{1}{2}\phi(\boldsymbol{x},t) - \left[-\int_{\boldsymbol{\Omega}\cdot\boldsymbol{n}<0} W(|\boldsymbol{\Omega}\cdot\boldsymbol{n}|)\boldsymbol{\Omega} f(\boldsymbol{x},\boldsymbol{\Omega})\,\mathrm{d}\Omega\right]\mathbf{D}^{-1}(\boldsymbol{x})\cdot\boldsymbol{F}(\boldsymbol{x},t)\,.
\end{aligned}$$

The quantity in brackets is the same vector $\boldsymbol{d}$ as in the anisotropic diffusion approximation,

$$\boldsymbol{d}(\boldsymbol{x}) = -\int_{\boldsymbol{\Omega}\cdot\boldsymbol{n}<0} W(|\boldsymbol{\Omega}\cdot\boldsymbol{n}|)\boldsymbol{\Omega} f(\boldsymbol{x},\boldsymbol{\Omega})\,\mathrm{d}\Omega\,. \tag{4.25}$$

Substituting this into the previous equation and multiplying by 2, we obtain the anisotropic P_1 boundary condition:

$$2\int_{\boldsymbol{\Omega}\cdot\boldsymbol{n}<0} W(|\boldsymbol{\Omega}\cdot\boldsymbol{n}|)\, I^b(\boldsymbol{x},\boldsymbol{\Omega},t)\,\mathrm{d}\Omega = \phi(\boldsymbol{x},t) - 2\boldsymbol{d}(\boldsymbol{x})\cdot\mathbf{D}^{-1}(\boldsymbol{x})\cdot\boldsymbol{F}(\boldsymbol{x},t)\,. \tag{4.26}$$

If the problem is steady-state, $\boldsymbol{F} = -\mathbf{D}\cdot\boldsymbol{\nabla}\phi$, and the boundary condition reduces to the anisotropic diffusion boundary condition from Chapter 3.

The boundary condition for f can, as with anisotropic diffusion, be derived by demanding that Eq. (4.6) hold on the boundary:

$$\phi(\boldsymbol{x},t) = \int_{4\pi} I_{\mathrm{V}}(\boldsymbol{x},\boldsymbol{\Omega},t)\,\mathrm{d}\Omega = \int_{4\pi}\left(\frac{1}{4\pi}\phi(\boldsymbol{x},t) + f(\boldsymbol{x},\boldsymbol{\Omega})\boldsymbol{\Omega}\cdot\mathbf{D}^{-1}(\boldsymbol{x})\cdot\boldsymbol{F}(\boldsymbol{x},t)\right).$$

The result is the same as Eq. (3.34):

$$\int_{\boldsymbol{\Omega}\cdot\boldsymbol{n}>0} (\boldsymbol{\Omega}\cdot\boldsymbol{n}) f(\boldsymbol{x},\boldsymbol{\Omega})\,\mathrm{d}\Omega = \int_{\boldsymbol{\Omega}\cdot\boldsymbol{n}<0} |\boldsymbol{\Omega}\cdot\boldsymbol{n}|\, f(\boldsymbol{x},\boldsymbol{\Omega})\,\mathrm{d}\Omega\,, \tag{4.27}$$

which can be satisfied by a white or a reflecting boundary on f.

Recall that under the assumption that f is rotationally invariant about $\boldsymbol{n}$ at the boundary, and if the Marshak approximation $W(\mu)\approx 2\mu$ is used, then $\boldsymbol{d} = \boldsymbol{n}\cdot\mathbf{D}$, canceling $\mathbf{D}^{-1}$ in the above expression to yield the standard Marshak boundary condition:

$$4F^-(\boldsymbol{x},t) = \phi(\boldsymbol{x},t) - 2\boldsymbol{n}\cdot\boldsymbol{F}(\boldsymbol{x},t)\,,$$

where $\boldsymbol{F}$ satisfies the anisotropic P_1 equation (4.20) rather than Fick's law.

4.1.4 Summary

By making several asymptotically valid approximations and substitutions, we have derived a new "anisotropic P_1" approximation to time-dependent radiation transport. Like the anisotropic diffusion approximation, it uses a simple, transport-calculated diffusion tensor in conjunction with a low-order conservation equation. Yet, like the P_1 method, the low-order unknowns now comprise not only ϕ but also $\boldsymbol{F}$, the zeroth and first moments of the radiation field, rather than merely the zeroth.

The low-order conservation equation (4.7) is:

$$\frac{1}{c}\frac{\partial \phi}{\partial t}(\boldsymbol{x},t) + \boldsymbol{\nabla}\cdot\boldsymbol{F}(\boldsymbol{x},t) + \sigma(\boldsymbol{x})\phi(\boldsymbol{x},t) = q(\boldsymbol{x},t)\,, \quad \boldsymbol{x}\in V,\ t>0\,.$$

This is coupled with Eq. (4.20), which acts as a replacement to Fick's law by relating the radiation flux $\boldsymbol{F}$ to the scalar intensity ϕ:

$$\frac{1}{c}\frac{\partial \boldsymbol{F}}{\partial t}(\boldsymbol{x},t) + \varsigma(\boldsymbol{x})\mathbf{D}(\boldsymbol{x})\cdot\boldsymbol{\nabla}\phi(\boldsymbol{x},t) + \varsigma(\boldsymbol{x})\boldsymbol{F}(\boldsymbol{x},t) = 0\,.$$

In this equation are embedded two moments of the simple transport solution f: the zeroth moment from Eq. (4.19),

$$\varsigma(\boldsymbol{x}) = \left[\int_{4\pi} f(\boldsymbol{x},\boldsymbol{\Omega})\,\mathrm{d}\Omega\right]^{-1},$$

and the second moment from Eq. (4.18),

$$\mathbf{D}(\boldsymbol{x}) \equiv \int_{4\pi} \boldsymbol{\Omega}\boldsymbol{\Omega} f(\boldsymbol{x},\boldsymbol{\Omega})\,\mathrm{d}\Omega\,.$$

The general boundary condition for the low-order equation is given in Eq. (4.26):

$$2\int_{\boldsymbol{\Omega}\cdot\boldsymbol{n}<0} W(|\boldsymbol{\Omega}\cdot\boldsymbol{n}|)\,I^b(\boldsymbol{x},\boldsymbol{\Omega},t)\,\mathrm{d}\Omega = \phi(\boldsymbol{x},t) - 2\boldsymbol{d}(\boldsymbol{x})\cdot\mathbf{D}^{-1}(\boldsymbol{x})\cdot\boldsymbol{F}(\boldsymbol{x},t)\,,$$

where $\boldsymbol{d}$, from Eq. (3.32), is a particular angular moment of the transport solution f, evaluated at the boundary for incident angles:

$$\boldsymbol{d}(\boldsymbol{x}) = \left[-\int_{\boldsymbol{\Omega}\cdot\boldsymbol{n}<0} |\boldsymbol{\Omega}\cdot\boldsymbol{n}|\,W(|\boldsymbol{\Omega}\cdot\boldsymbol{n}|)\,f(\boldsymbol{x},\boldsymbol{\Omega})\,\mathrm{d}\Omega\right]\boldsymbol{n}\,.$$

(This equation is written under the assumption that f is rotationally invariant about $\boldsymbol{n}$ at the boundary.)

The transport problem for f is the same as in standard anisotropic diffusion: a steady-

state, purely absorbing transport equation described by Eq. (4.14):

$$\boldsymbol{\Omega}\cdot\boldsymbol{\nabla} f(\boldsymbol{x},\boldsymbol{\Omega}) + \sigma(\boldsymbol{x}) f(\boldsymbol{x},\boldsymbol{\Omega}) = \frac{1}{4\pi}, \quad x \in V,\ \boldsymbol{\Omega} \in 4\pi,$$

with boundary conditions, usually taken to be reflecting, that satisfy Eq. (4.27):

$$\int_{\boldsymbol{\Omega}\cdot\boldsymbol{n}>0} (\boldsymbol{\Omega}\cdot\boldsymbol{n}) f(\boldsymbol{x},\boldsymbol{\Omega})\,\mathrm{d}\Omega = \int_{\boldsymbol{\Omega}\cdot\boldsymbol{n}<0} |\boldsymbol{\Omega}\cdot\boldsymbol{n}|\, f(\boldsymbol{x},\boldsymbol{\Omega})\,\mathrm{d}\Omega.$$

4.2 Discussion

Because the transport equation for f in anisotropic P_1 is the same as in anisotropic diffusion, the diffusion tensor $\mathbf{D}$ is also the same, and much of the discussion there also applies here. The transport calculation for f has no scattering source to converge; the anisotropic diffusion tensor $\mathbf{D}$ is therefore computationally inexpensive to compute. The diffusion tensor $\mathbf{D}$ and the nonlocal opacity ς are both angular moments of f, so no extra transport calculation is needed in AP_1 as compared to AD.

4.2.1 Steady-state limit

Just as the P_1 method limits to standard diffusion as $\partial I/\partial t \to 0$, the AP_1 method limits to the anisotropic diffusion method. We return to Eq. (4.20):

$$\frac{1}{c}\frac{\partial \boldsymbol{F}}{\partial t}(\boldsymbol{x},t) + \varsigma(\boldsymbol{x})\mathbf{D}(\boldsymbol{x})\cdot\boldsymbol{\nabla}\phi(\boldsymbol{x},t) + \varsigma(\boldsymbol{x})\boldsymbol{F}(\boldsymbol{x},t) = 0.$$

Letting $\frac{1}{c}\frac{\partial \boldsymbol{F}}{\partial t} \to 0$,

$$\varsigma(\boldsymbol{x})\boldsymbol{F}(\boldsymbol{x},t) = -\varsigma(\boldsymbol{x})\mathbf{D}(\boldsymbol{x})\cdot\boldsymbol{\nabla}\phi(\boldsymbol{x},t).$$

Dividing through by ς, which is strictly positive, we obtain the anisotropic Fick's law of Eq. (3.16):

$$\boldsymbol{F}(\boldsymbol{x},t) = -\mathbf{D}(\boldsymbol{x})\cdot\boldsymbol{\nabla}\phi(\boldsymbol{x},t).$$

4.2.2 Homogeneous medium limit

In a homogeneous medium, the AP_1 equation (4.20) limits to the P_1 equation. When σ is constant, the purely absorbing transport problem for f has the constant solution

$f = 1/(4\pi\sigma)$. The nonlocal opacity, ς from Eq. (4.19), becomes

$$\varsigma = \left[\int_{4\pi} f \,\mathrm{d}\Omega\right]^{-1} = \left[\int_{4\pi} \frac{1}{4\pi\sigma} \,\mathrm{d}\Omega\right]^{-1} = \sigma\,.$$

The anisotropic diffusion tensor likewise simplifies to

$$\mathbf{D} = \int_{4\pi} \boldsymbol{\Omega}\boldsymbol{\Omega} f \,\mathrm{d}\Omega = \frac{1}{3\sigma}\mathbf{I}\,.$$

Substituting these into the AP_1 equation (4.20), we obtain

$$\frac{1}{c}\frac{\partial \boldsymbol{F}}{\partial t}(\boldsymbol{x},t) + \sigma\left[\frac{1}{3\sigma}\mathbf{I}\right]\cdot\boldsymbol{\nabla}\phi(\boldsymbol{x},t) + \sigma\boldsymbol{F}(\boldsymbol{x},t) = 0\,,$$

which is the conventional P_1 approximation:

$$\frac{1}{c}\frac{\partial \boldsymbol{F}}{\partial t}(\boldsymbol{x},t) + \frac{1}{3}\boldsymbol{\nabla}\phi + \sigma\boldsymbol{F}(\boldsymbol{x},t) = 0\,.$$

4.2.3 Application to nonlinear radiation transport

As with the anisotropic diffusion approximation in Chapter 3, the AP_1 method was derived for a linear, time-dependent transport problem with isotropic scattering. We again argue that it has the proper behavior in the diffusive limit of nonlinear radiation transport. We note that the semi-implicit linearization of the TRT equations result in a linear transport equation with isotropic scattering, the subject of the asymptotic analysis in this section. Furthermore, in the diffusive limit, $\mathbf{D} \to \frac{1}{3\sigma} + O(\epsilon^2)$, and the AP_1 equation reduces to the P_1 equation. From Ref. [43], the P_1 approximation has the correct asymptotic behavior in the diffusive limit; we therefore assert that the AP_1 approximation does as well.

4.3 Summary

The anisotropic P_1 approximation was derived using the same procedure as time-dependent anisotropic diffusion. The assumption of a stronger time dependence of the radiative intensity led to a larger unknown space—now the zeroth *and* first moments of I—and we therefore expect this method to be more accurate than AD in problems with rapid transient behavior.

Chapter 5
Low-order Discretization Schemes

Tensor diffusion—the diffusion of particles through anisotropic media—has many applications outside of radiation transport, including the fields of geology, magnetohydrodynamics, and image reconstruction. Numerous tensor diffusion schemes have been developed, but many of these are more general than is needed in our work. The anisotropic diffusion tensor derived in Chapter 3 is relatively well behaved: it is a smooth function in space, it tends toward isotropy in optically thick problems, it is SPD, and it is diagonally dominant. Additionally, our test problems are executed in a structured two-dimensional Cartesian "brick" mesh, a simple testbed environment in which all cells are quadrilaterals, each interior cell is connected to four adjacent cells through four faces, and each face is perpendicular to one of the coordinate system axes.

Because of these simplifying properties, we need not use the more complex discretization schemes, which have more unknowns per spatial cell and are therefore more costly to solve. (An example is the Support Operators Method [58, 59], with roughly three unknowns per cell.) Instead, we derive some simple, second-order, conservative difference schemes for anisotropic diffusion. Because the boundary conditions for our AD method are distinct from standard diffusion boundary conditions, we also present a second-order-accurate discretization of these.

The "Anisotropic P_1" scheme is entirely new, so we develop a discretization scheme for it by making a minor modification to the traditional P_1 discretization. It uses a "staggered mesh," in which the scalar intensity ϕ is cell-centered and the exiting radiation flux $\boldsymbol{F} \cdot \boldsymbol{n}$ is edge-centered [57].

Each discretization derived in this chapter simplifies to the standard five-point finite difference diffusion scheme in the case of an *isotropic* diffusion tensor and a steady-state problem. We admit the possibility that, because of the simplicity of these discretizations, they were developed independently decades ago, but an extensive literature search did not unearth any previously formulated schemes equivalent to ours.

5.1 Introduction

Because the semi-implicit gray TRT formulation of the particle conservation equation can be expressed as a steady-state transport equation (see §2.2), for the sake of simplicity we will present the anisotropic diffusion discretizations without time dependence.

5.1.1 Conservation equation

The steady-state particle conservation equation is

$$\boldsymbol{\nabla} \cdot \boldsymbol{F}(\boldsymbol{x}) + \sigma_a(\boldsymbol{x})\phi(\boldsymbol{x}) = Q(\boldsymbol{x}), \qquad \boldsymbol{x} \in V. \tag{5.1}$$

(In an implicitly discretized time-dependent problem, $\boldsymbol{F} = \boldsymbol{F}(t^{n+1})$, $\phi = \phi(t^{n+1})$, σ_a is the absorption opacity plus the constant $\frac{1}{c\Delta_t}$, and the source Q contains an additional $\frac{\phi(t^n)}{c\Delta_t}$.)

The first step in deriving our finite difference schemes is to assume that the unknown—in this case, ϕ—is constant over a single cell, represented in Fig. 5.1. We also assume that the effective absorption opacity σ_a and source Q are constant over the cell, which in TRT problems means approximating the material temperature as constant over a cell. Integrating Eq. (5.1) over cell i, j and applying the divergence theorem gives the following equation:

$$\Delta_{x,i}\left(F_T^y - F_B^y\right) + \Delta_{y,j}\left(F_R^x - F_L^x\right) + \Delta_{x,i}\Delta_{y,j}\sigma_{a,i,j}\phi_{i,j} = \Delta_{x,i}\Delta_{y,j}q_{i,j}. \tag{5.2}$$

The unknown face-averaged radiation flux F—also known as the *leakage*—and the unknown cell-averaged scalar intensity are diagrammed in Fig. 5.2.

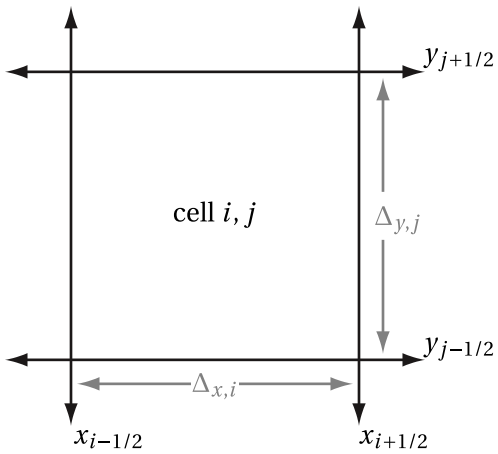

Figure 5.1: Diagram of cell i, j.

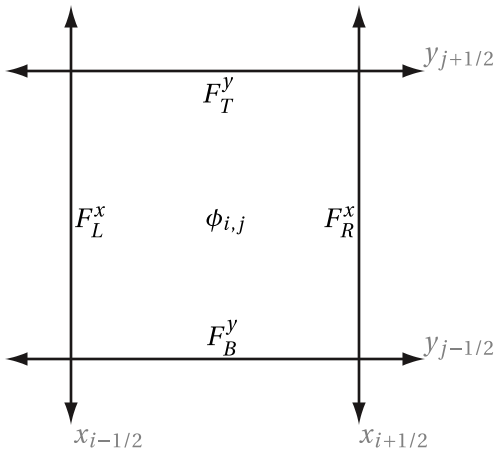

Figure 5.2: Unknowns in cell i, j.

In all discretizations of the conservation equation, it is essential that $\boldsymbol{F}$ be continuous at cell interfaces: e.g., F_T^y in cell i, j must be equal to $-F_B^y$ in cell $i, j+1$. Otherwise, the difference scheme is not conservative.

5.1.2 Anisotropic closure equations

The radiation flux $\boldsymbol{F}$ and scalar intensity ϕ are related, in the case of anisotropic diffusion, by the anisotropic Fick's law of Eq. (3.16):

$$\boldsymbol{F}(\boldsymbol{x}) = -\mathbf{D}(\boldsymbol{x}) \cdot \boldsymbol{\nabla}\phi(\boldsymbol{x}) \,.$$

The anisotropic P_1 approximation, given in Eq. (4.20), contains an additional term that accounts for stronger time dependence:

$$\frac{1}{c}\frac{\partial \boldsymbol{F}}{\partial t}(\boldsymbol{x}, t) + \varsigma(\boldsymbol{x})\mathbf{D}(\boldsymbol{x}) \cdot \boldsymbol{\nabla}\phi(\boldsymbol{x}, t) + \varsigma(\boldsymbol{x})\boldsymbol{F}(\boldsymbol{x}, t) = 0 \,.$$

We discretize this equation implicitly in time in accordance with the semi-implicit approximation. Applying the backward Euler approximation to ϕ and $\boldsymbol{F}$, then solving for $\boldsymbol{F}$, we obtain:

$$\boldsymbol{F}(\boldsymbol{x}) = -[1-\eta(\boldsymbol{x})]\mathbf{D}(\boldsymbol{x}) \cdot \boldsymbol{\nabla}\phi(\boldsymbol{x}) + \eta(\boldsymbol{x})\hat{\boldsymbol{F}}(\boldsymbol{x}) \,, \tag{5.3a}$$

where $\boldsymbol{F}(\boldsymbol{x}) = \boldsymbol{F}(\boldsymbol{x}, t^{n+1})$, $\hat{\boldsymbol{F}}(\boldsymbol{x}) = \boldsymbol{F}(\boldsymbol{x}, t^n)$, and

$$\eta(\boldsymbol{x}) \equiv \frac{1}{1+\varsigma(\boldsymbol{x})c\Delta_t} \,. \tag{5.3b}$$

Setting $\eta = 0$ reduces this equation to Eq. (5.5). (We will use this fact to simplify the derivation of boundary conditions

Equation (5.3a) in 2-D comprises two equations in vector form:

$$\begin{aligned}\begin{bmatrix} F^x \\ F^y \end{bmatrix} &= -(1-\eta)\begin{bmatrix} D^{xx} & D^{yx} \\ D^{xy} & D^{yy} \end{bmatrix}\begin{bmatrix} \partial\phi/\partial x \\ \partial\phi/\partial y \end{bmatrix} + \eta\begin{bmatrix} \hat{F}^x \\ \hat{F}^y \end{bmatrix} \\ &= \begin{bmatrix} -(1-\eta)D^{xx}\partial\phi/\partial x - (1-\eta)D^{yx}\partial\phi/\partial y + \eta\hat{F}^x \\ -(1-\eta)D^{yy}\partial\phi/\partial y - (1-\eta)D^{xy}\partial\phi/\partial x + \eta\hat{F}^x \end{bmatrix}.\end{aligned} \tag{5.4}$$

The diagonal components of **D** contribute to "normal" leakage; and the off-diagonal components D^{xy} contribute to "transverse" leakage, particle movement *across* the face due to a gradient *along* the face. Note that since the anisotropic diffusion tensor is symmetric, $D^{yx} = D^{xy}$.

Setting $\eta = 0$ in Eq. (5.4) reduces the AP_1 equation to the anisotropic Fick's law:

$$\begin{bmatrix} F^x \\ F^y \end{bmatrix} = -\begin{bmatrix} D^{xx} & D^{yx} \\ D^{xy} & D^{yy} \end{bmatrix}\begin{bmatrix} \partial\phi/\partial x \\ \partial\phi/\partial y \end{bmatrix} = \begin{bmatrix} -D^{xx}\partial\phi/\partial x - D^{yx}\partial\phi/\partial y \\ -D^{yy}\partial\phi/\partial y - D^{xy}\partial\phi/\partial x \end{bmatrix}. \tag{5.5}$$

The finite difference schemes presented in this chapter approximate these equations for F^x and F^y on cell edges. These approximations are then used to relate the cell-centered ϕ from the conservation equation (5.1).

5.2 Neglecting transverse diffusion

Under a simplifying assumption about the structure of the anisotropic diffusion tensor, very simple existing centered difference schemes can be applied to AD and AP_1. The conservative cell-centered diffusion scheme is derived in Ref. [14]; the AP_1 difference scheme is a minor extension [57].

In the structured Cartesian geometry we consider, the simplifying assumption is to neglect the off-diagonal terms of the diffusion tensor that cause transverse leakage. In certain simple problems, however, this is not an approximation. If the opacity is invariant with respect to one of the Cartesian coordinate system's axes (see §3.2.3), the off-diagonal terms of **D** are identically zero. For problems in which transverse leakage is non-negligible, the discretization scheme in this chapter must be used with caution: it is not truly consistent with the underlying mixed-derivative partial differential equation. Even as the grid size approaches zero, the off-diagonal diffusion components are still neglected.

The simple "diagonal-only" centered difference scheme is also useful as an instructive tool, because we later develop a more complex difference scheme that uses the same principles.

5.2.1 Anisotropic diffusion

The discretization scheme for anisotropic diffusion presented here is only a slight modification of common cell-centered diffusion scheme: the orientation of the faces determines which component of the anisotropic diffusion tensor is used. This centered difference scheme was used in the earliest work on the anisotropic diffusion approximation [2].

Setting $D^{yx} = D^{xy} = 0$ simplifies Eq. (5.5) to:

$$\begin{bmatrix} F^x \\ F^y \end{bmatrix} = - \begin{bmatrix} D^{xx} & 0 \\ 0 & D^{yy} \end{bmatrix} \begin{bmatrix} \partial\phi/\partial x \\ \partial\phi/\partial y \end{bmatrix} = \begin{bmatrix} -D^{xx}\partial\phi/\partial x \\ -D^{yy}\partial\phi/\partial y \end{bmatrix}.$$

Without loss of generality, we evaluate the face-averaged flux from cell i, j through its right face, which has an outer normal along the $+x$ axis, $\boldsymbol{n}_R = [1, 0]$:

$$F_R^x \equiv \frac{1}{\Delta_{y,j}} \int_{y_{j-1/2}}^{y_{j+1/2}} \boldsymbol{F}(x_{i+1/2}, y) \cdot \boldsymbol{n}_R \, \mathrm{d}y.$$

Substituting the anisotropic Fick's law, we obtain

$$F_R^x = -\frac{1}{\Delta_{y,j}} \int_{y_{j-1/2}}^{y_{j+1/2}} D_{i,j}^{xx} \frac{\partial\phi}{\partial x} \, \mathrm{d}y.$$

Now we introduce a temporary value ϕ_* on the edge of the cell to approximate the partial derivative using a second-order finite difference stencil:

$$F_R^x \approx -D_{i,j}^{xx} \frac{\phi_* - \phi_{i,j}}{\Delta_{x,i}/2}. \tag{5.6}$$

To be conservative, this term must be equal to F_L^x from the cell to the right. Evaluating the flux across the same face in the $+x$ direction from the perspective of cell $i+1, j$, and approximating the derivative using the same edge-centered ϕ_*, we obtain

$$F_{L,i+1,j}^x \approx -D_{i+1,j}^{xx} \frac{\phi_{i+1,j} - \phi_*}{\Delta_{x,i+1}/2}. \tag{5.7}$$

Scaling Eqs. (5.6) and (5.7) by $\Delta_x/(2D^{xx})$ and adding them, we eliminate ϕ_*:

$$\frac{\Delta_{x,i}/2}{D^{xx}_{i,j}}F^x_R + \frac{\Delta_{x,i+1}/2}{D^{xx}_{i+1,j}}F^x_{L,i+1,j} = \left[-(\phi_* - \phi_i)\right] + \left[-(\phi_{i+1,j} - \phi_*)\right] = -\left(\phi_{i+1,j} - \phi_{i,j}\right).$$

We enforce particle conservation by setting $F^x_{L,i+1,j} = F^x_R$, and we solve for F^x_R. This gives the following expression for the net leakage through the right face of cell i,j:

$$F^x_R = -\frac{D^{xx}_{i+1/2,j}}{\Delta_{x,i+1/2}}\left(\phi_{i+1,j} - \phi_{i,j}\right). \tag{5.8}$$

Here we have defined a harmonically averaged cell-edge diffusion coefficient:

$$\frac{D^{xx}_{i+1/2,j}}{\Delta_{x,i+1/2}} \equiv \left[\frac{1}{2}\left(\frac{D^{xx}_{i,j}}{\Delta_{x,i}}\right)^{-1} + \frac{1}{2}\left(\frac{D^{xx}_{i+1,j}}{\Delta_{x,i+1}}\right)^{-1}\right]^{-1}. \tag{5.9}$$

This is the standard relation between neighboring cells in the cell-centered discretization scheme [14], except that in anisotropic diffusion, leakage across the face normal to the x axis takes the D^{xx} component of the diffusion tensor.

The same procedure yields similar for the three other faces of cell i,j:

$$\begin{aligned}
F^x_L &= -\frac{D^{xx}_{i-1/2,j}}{\Delta_{x,i-1/2}}\left(\phi_{i,j} - \phi_{i-1,j}\right),\\
F^y_T &= -\frac{D^{yy}_{i,j+1/2}}{\Delta_{y,j+1/2}}\left(\phi_{i,j+1} - \phi_{i,j}\right),\\
F^y_B &= -\frac{D^{yy}_{i,j-1/2}}{\Delta_{y,j-1/2}}\left(\phi_{i,j} - \phi_{i,j-1}\right).
\end{aligned}$$

These terms, substituted into Eq. (5.2), relate the cell-centered values of ϕ in the interior of the system:

$$\begin{aligned}
&\Delta_{x,i}\left(-\frac{D^{yy}_{i,j+1/2}}{\Delta_{y,j+1/2}}\left(\phi_{i,j+1} - \phi_{i,j}\right) + \frac{D^{yy}_{i,j-1/2}}{\Delta_{y,j-1/2}}\left(\phi_{i,j} - \phi_{i,j-1}\right)\right)\\
+\Delta_{y,j}&\left(-\frac{D^{xx}_{i+1/2,j}}{\Delta_{x,i+1/2}}\left(\phi_{i+1,j} - \phi_{i,j}\right) + \frac{D^{xx}_{i-1/2,j}}{\Delta_{x,i-1/2}}\left(\phi_{i,j} - \phi_{i-1,j}\right)\right)\\
&+\Delta_{x,i}\Delta_{y,j}\sigma_{a,i,j}\phi_{i,j} = \Delta_{x,i}\Delta_{y,j}q_{i,j}.
\end{aligned} \tag{5.10}$$

Rearranging shows the leakage terms to be part of a discretized Laplacian operator. In fact, if $\Delta_x = \Delta_y = h$, and $\mathbf{D}(\boldsymbol{x}) = D\mathbf{I}$, then Eq. (5.10) reduces to a well-known five-point

stencil:

$$-\frac{D}{h^2}\left(\phi_{i+1,j}+\phi_{i,j+1}+\phi_{i-1,j}+\phi_{i,j-1}-4\phi_{i,j}\right)+\sigma_a = q\,.$$

When a cell has one or more faces on an exterior boundary, the above relations for $\boldsymbol{n}\cdot\boldsymbol{F}$ are replaced by a discretized form of the boundary condition, which we shall derive presently.

5.2.2 Anisotropic P_1

The time-dependent P_1 and anisotropic P_1 methods have as unknowns the radiation flux $\boldsymbol{F}$ in addition to the scalar intensity ϕ. Using the same finite differencing procedure as performed above for anisotropic diffusion, we obtain a discretization for AP_1 that stores ϕ in cell centers and $\boldsymbol{F}$ on cell edges. In the steady-state case, the edge-centered $\boldsymbol{F}$ terms can be eliminated algebraically, and this discretization reduces to the above anisotropic diffusion discretization.

We evaluate the 2-D anisotropic P_1 equation (5.4) on the right face of cell i,j, set $D^{yx}=0$, and introduce the temporary edge-centered ϕ_* to approximate the derivative normal to the face:

$$F^x_{i+1/2,j} = -(1-\eta_{i,j})D^{xx}_{i,j}\frac{\phi_*-\phi_{i,j}}{\Delta_{x,i}/2}+\eta_{i,j}\hat{F}^x_{i+1/2,j}\,.$$

Evaluating the leakage on same face from cell $i+1,j$, we obtain:

$$F^x_{i+1/2,j} = -(1-\eta_{i+1,j})D^{xx}_{i+1,j}\frac{\phi_{i+1,j}-\phi_*}{\Delta_{x,i+1}/2}+\eta_{i+1,j}\hat{F}^x_{i+1/2,j}\,.$$

Multiplying the equations by $(\Delta_x/2)/[(1-\eta)D^{xx}]$, we eliminate the temporary ϕ_* to arrive at the following conservative equation:

$$\left[\frac{\Delta_{x,i}/2}{(1-\eta_{i,j})D^{xx}_{i,j}}+\frac{\Delta_{x,i+1}/2}{(1-\eta_{i+1,j})D^{xx}_{i+1,j}}\right]F^x_{i+1/2,j} = \phi_{i,j}-\phi_{i+1,j}+\left[\frac{\eta_{i,j}\Delta_{x,i}/2}{(1-\eta_{i,j})D^{xx}_{i,j}}+\frac{\eta_{i+1,j}\Delta_{x,i+1}/2}{(1-\eta_{i+1,j})D^{xx}_{i+1,j}}\right]\hat{F}^x_{i+1/2,j}\,. \quad (5.11a)$$

For faces normal to the y axis, the corresponding equation uses the D^{yy} component of the diffusion tensor:

$$\left[\frac{\Delta_{y,j}/2}{(1-\eta_{i,j})D^{yy}_{i,j}} + \frac{\Delta_{y,j+1}/2}{(1-\eta_{i,j+1})D^{yy}_{i,j+1}}\right] F^{y}_{i,j+1/2}$$
$$= \phi_{i,j} - \phi_{i,j+1} + \left[\frac{\eta_{i,j}\Delta_{y,j}/2}{(1-\eta_{i,j})D^{yy}_{i,j}} + \frac{\eta_{i,j+1}\Delta_{y,j+1}/2}{(1-\eta_{i,j+1})D^{yy}_{i,j+1}}\right] \hat{F}^{y}_{i,j+1/2}. \quad (5.11b)$$

Equations (5.11) relate the flux at a face with the scalar intensity in the adjacent cells. They provide one equation for each interior face; the conservation equation (5.2) provides an equation for each cell; and a discretization of the anisotropic P_1 boundary conditions (described next) provides an equation for each boundary face.

5.2.3 Boundary conditions

The specified incident boundary condition for anisotropic diffusion is given in Eq. (3.33):

$$2\int_{\boldsymbol{\Omega}\cdot\boldsymbol{n}<0} W(|\boldsymbol{\Omega}\cdot\boldsymbol{n}|)\, I^b \,\mathrm{d}\Omega = \phi + 2\boldsymbol{d}\cdot\boldsymbol{\nabla}\phi,$$

where the transport-calculated boundary coefficient is given in Eq. (3.32):

$$\boldsymbol{d} = -\int_{\boldsymbol{\Omega}\cdot\boldsymbol{n}<0} W(|\boldsymbol{\Omega}\cdot\boldsymbol{n}|)\boldsymbol{\Omega} f \,\mathrm{d}\Omega.$$

The anisotropic P_1 boundary condition, Eq. (4.26), is similar:

$$2\int_{\boldsymbol{\Omega}\cdot\boldsymbol{n}<0} W(|\boldsymbol{\Omega}\cdot\boldsymbol{n}|)\, I^b \,\mathrm{d}\Omega = \phi - 2\boldsymbol{d}\cdot\mathbf{D}^{-1}\cdot\boldsymbol{F},$$

where $\boldsymbol{d}$ is the same as in anisotropic diffusion. In fact, by substituting the time-discretized $\boldsymbol{F}$ from Eq. (5.3a), we obtain a general boundary condition that reduces to the anisotropic diffusion boundary condition by setting $\eta = 0$:

$$2\int_{\boldsymbol{\Omega}\cdot\boldsymbol{n}<0} W(|\boldsymbol{\Omega}\cdot\boldsymbol{n}|)\, I^b \,\mathrm{d}\Omega = \phi - 2\boldsymbol{d}\cdot\mathbf{D}^{-1}\cdot\left[-(1-\eta)\mathbf{D}\cdot\boldsymbol{\nabla}\phi + \eta\hat{\boldsymbol{F}}\right]$$
$$= \phi + 2(1-\eta)\boldsymbol{d}\cdot\boldsymbol{\nabla}\phi - 2\eta\boldsymbol{d}\cdot\mathbf{D}^{-1}\cdot\hat{\boldsymbol{F}}.$$

Looking ahead to using flatland geometry (Chapter 6) in addition to standard 2-D geometry, we write this AD/AP_1 boundary condition in a more general form:

$$q = \phi + r(1-\eta)\boldsymbol{d}\cdot\boldsymbol{\nabla}\phi - r\eta\boldsymbol{d}\cdot\mathbf{D}^{-1}\cdot\hat{\boldsymbol{F}}, \quad (5.12)$$

where q, r, $\boldsymbol{d}$, and $\mathbf{D}$ all depend upon the chosen geometry. The values q and r are given in Table 5.1.

	q	r
1-D/2-D/3-D	$2\int_{\boldsymbol{\Omega}\cdot\boldsymbol{n}<0} W(\lvert\boldsymbol{\Omega}\cdot\boldsymbol{n}\rvert) I^b \,\mathrm{d}\Omega$	2
Flatland	$2\pi\int_{\boldsymbol{\Omega}\cdot\boldsymbol{n}<0} V(\lvert\boldsymbol{\Omega}\cdot\boldsymbol{n}\rvert) I^b \,\mathrm{d}\Omega$	$\pi/2$

Table 5.1: Coefficients for the discretized boundary conditions. The flatland values and the function V are discussed in Chapter 6.

At this point, Eq. (5.12) applies to arbitrary geometries, both anisotropic methods, and problems in which $D^{xy} \neq 0$. Now we make the analysis slightly less general by demanding that η be azimuthally symmetric about the outward normal of the boundary face. (Equivalently, we discard the $D^{yx} = D^{xy}$ terms if the boundary face is along one of the coordinate axes.) With this assumption, as discussed in §3.2.3, the normal vector $\boldsymbol{n}$ of the boundary face is an eigenvector of $\mathbf{D}$:

$$\mathbf{D} \to D\boldsymbol{n}\boldsymbol{n},$$

and the boundary coefficient is pointed along the outward normal:

$$\boldsymbol{d} \to d\boldsymbol{n}.$$

Under this assumption, Eq. (5.12) simplifies (using the fact that $\boldsymbol{n}$ is a unit vector):

$$\begin{aligned} q &= \phi + r(1-\eta)\,[d\boldsymbol{n}]\cdot\boldsymbol{\nabla}\phi - r\eta\,[d\boldsymbol{n}]\cdot[D\boldsymbol{n}\boldsymbol{n}]\cdot\hat{\boldsymbol{F}}, \\ q &= \phi + (1-\eta)\,dr\,\boldsymbol{n}\cdot\boldsymbol{\nabla}\phi - \frac{\eta dr}{D}\hat{F}. \end{aligned} \tag{5.13}$$

Here we have defined the outward component of the radiation flux at the beginning of the time step (t^n):

$$\hat{F} \equiv \boldsymbol{n}\cdot\hat{\boldsymbol{F}} = \boldsymbol{n}\cdot\boldsymbol{F}(t^n).$$

In both the case of anisotropic diffusion and anisotropic P_1, we seek the exiting radiation flux on the boundary face, the dot product of the outward normal $\boldsymbol{n}$ and Eq. (5.3a):

$$\begin{aligned} \boldsymbol{n}\cdot\boldsymbol{F} &= -[1-\eta]\,\boldsymbol{n}\cdot[D\boldsymbol{n}\boldsymbol{n}]\cdot\boldsymbol{\nabla}\phi + \eta\,\boldsymbol{n}\cdot\hat{\boldsymbol{F}} \\ F &= -[1-\eta]\,D\boldsymbol{n}\cdot\boldsymbol{\nabla}\phi + \eta\hat{F}, \end{aligned} \tag{5.14}$$

where

$$F \equiv \boldsymbol{n} \cdot \boldsymbol{F}.$$

Both Eqs. (5.13) and (5.14) are evaluated at the exterior boundary face. In our discretization schemes, F is located on the boundary, but ϕ is stored at cell centers. To obtain a boundary discretization accurate to $O(\Delta_x^2)$, we cannot approximate the cell-edge value of ϕ with the cell-center value of ϕ. Instead, we introduce a temporary edge-centered ϕ_*, approximating the directional derivative in the two equations with:

$$\boldsymbol{n} \cdot \boldsymbol{\nabla} \phi(\boldsymbol{x}_b) \approx \frac{\phi_* - \phi}{\Delta/2},$$

where ϕ is the cell-centered scalar intensity, and Δ is the width of the cell along direction normal to the boundary. Equations (5.13) and (5.14) then become:

$$q = \phi + (1-\eta) dr \frac{\phi_* - \phi}{\Delta/2} - \frac{\eta dr}{D} \hat{F}, \tag{5.15a}$$

and

$$F = -[1-\eta] D \frac{\phi_* - \phi}{\Delta/2} + \eta \hat{F}. \tag{5.15b}$$

Eliminating ϕ_* in Eqs. (5.15), we obtain an equation for the exiting radiation flux on the boundary for the AP_1 approximation:

$$F = \left[\frac{\Delta/2}{1-\eta} + dr \right]^{-1} \left[D\phi - Dq - \eta dr \hat{F} \right] + \eta \hat{F}. \tag{5.16}$$

Setting $\eta = 0$ gives the discretized anisotropic diffusion boundary condition:

$$F = [\Delta/2 + dr]^{-1} \left[D\phi - Dq \right]. \tag{5.17}$$

If the 2-D Marshak approximation is used for the geometry and coefficients, then $q = 4F^-$, $r = 2$, and $d = D$; and Eq. (5.17) resultantly reduces to the discretized standard diffusion boundary condition:

$$F = [\Delta/2 + 2D]^{-1} \left[D\phi - 4DF^- \right].$$

5.3 Quasidiffusion-like discretization

The discretization in §5.2 relies on discarding the components of the diffusion tensor that lead to transverse leakage. If those components are non-negligible, i.e. in a problem with opacities that vary strongly along both the x and y axes, we would like a more accurate discretization scheme that preserves those components.

One scheme is an adaptation an existing difference method for quasidiffusion (QD) that is attributed to Fryazinov [60], used by Aksenov and Gol'din [61], and implemented in several contemporary theses on the topic of QD [62, 63]. The discretization scheme is straightforward to derive and implement using the following procedure:

1. Let the unknown ϕ live at both the cell centers and the cell edges.[1]
2. Integrate $\boldsymbol{F}\cdot\boldsymbol{n}$ over half of a cell, approximating it as a constant in that domain.
3. Use particle conservation to relate adjacent cells.

Applying this procedure to anisotropic diffusion does not yield the same result as given in Ref. [62]. This is because, even though AD and QD both contain tensors in their approximations to the radiation flux, the placement of the gradient operator $\boldsymbol{\nabla}$ differs. Steady-state AD uses the approximation

$$\boldsymbol{F} = -\mathbf{D}\cdot\boldsymbol{\nabla}\phi$$

whereas steady-state QD uses the approximation

$$\boldsymbol{F} = -\frac{1}{\sigma}\boldsymbol{\nabla}\cdot\mathbf{E}\phi\,.$$

To apply the QD discretization to the anisotropic diffusion equation, we integrate the Anisotropic Fick's law, Eq. (5.5), over the right half of cell i,j as represented in Fig. 5.3.

Integrating the anisotropic Fick's law, Eq. (5.5), over the right half of cell i,j, as represented in Fig. 5.3, gives an approximate expression for the flux exiting the right face $F_R^x = \boldsymbol{F}\cdot\boldsymbol{n}_R$:

$$\int_{y_{j-1/2}}^{y_{j+1/2}}\int_{x_i}^{x_{i+1/2}} \boldsymbol{n}_R\cdot\boldsymbol{F}\,\mathrm{d}x\,\mathrm{d}y = \int_{y_{j-1/2}}^{y_{j+1/2}}\int_{x_i}^{x_{i+1/2}} -\boldsymbol{n}_R\cdot\mathbf{D}\cdot\boldsymbol{\nabla}\phi\,\mathrm{d}x\,\mathrm{d}y$$

$$F_R^x\frac{\Delta_{x,i}\Delta_{y,j}}{2} = -\begin{bmatrix}1 & 0\end{bmatrix}\begin{bmatrix}D_{i,j}^{xx} & D_{i,j}^{yx}\\ D_{i,j}^{xy} & D_{i,j}^{yy}\end{bmatrix}\int_{y_{j-1/2}}^{y_{j+1/2}}\int_{x_i}^{x_{i+1/2}}\begin{bmatrix}\partial\phi/\partial x\\ \partial\phi/\partial y\end{bmatrix}\mathrm{d}x\,\mathrm{d}y$$

[1] For an $M\times N$ Cartesian grid, this means MN cell-centered ϕ and $2MN+M+N$ edge-centered ϕ, roughly treble the number of unknowns in the simple cell-centered difference scheme of §5.2.

$$F_R^x \frac{\Delta_{x,i}\Delta_{y,j}}{2} = -\begin{bmatrix} D_{i,j}^{xx} & D_{i,j}^{yx} \end{bmatrix} \begin{bmatrix} (\phi_R - \phi_{i,j})\,\Delta_{y,j} \\ (\phi_T - \phi_B)\,\Delta_{x,i}/2 \end{bmatrix}$$

$$F_R^x = -D_{i,j}^{xx} \frac{\phi_R - \phi_{i,j}}{\Delta_{x,i}/2} - D_{i,j}^{yx} \frac{\phi_T - \phi_B}{\Delta_{y,j}} \,.$$

Performing the same procedure for the left side, we obtain

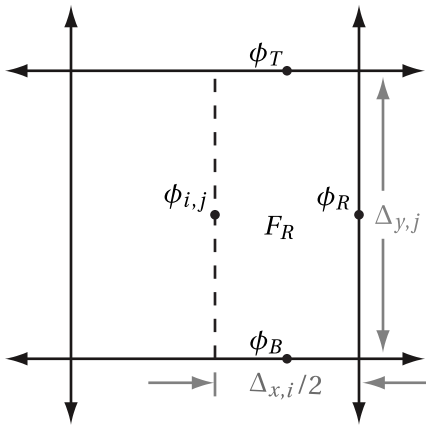

Figure 5.3: The right half of cell i, j.

$$\int_{y_{j-1/2}}^{y_{j+1/2}} \int_{x_{i-1/2}}^{x_i} \boldsymbol{n}_L \cdot \boldsymbol{F}\, \mathrm{d}x\, \mathrm{d}y = \int_{y_{j-1/2}}^{y_{j+1/2}} \int_{x_{i-1/2}}^{x_i} -\boldsymbol{n}_L \cdot \mathbf{D} \cdot \boldsymbol{\nabla}\phi\, \mathrm{d}x\, \mathrm{d}y$$

$$-F_L^x \frac{\Delta_{x,i}\Delta_{y,j}}{2} = -\begin{bmatrix} -1 & 0 \end{bmatrix} \begin{bmatrix} D_{i,j}^{xx} & D_{i,j}^{yx} \\ D_{i,j}^{xy} & D_{i,j}^{yy} \end{bmatrix} \int_{y_{j-1/2}}^{y_{j+1/2}} \int_{x_{i-1/2}}^{x_i} \begin{bmatrix} \partial\phi/\partial x \\ \partial\phi/\partial y \end{bmatrix} \mathrm{d}x\, \mathrm{d}y$$

$$F_L^x \frac{\Delta_{x,i}\Delta_{y,j}}{2} = -\begin{bmatrix} D_{i,j}^{xx} & D_{i,j}^{yx} \end{bmatrix} \begin{bmatrix} (\phi_{i,j} - \phi_L)\,\Delta_{y,j} \\ (\phi_T - \phi_B)\,\Delta_{x,i}/2 \end{bmatrix} \mathrm{d}x\, \mathrm{d}y$$

$$F_L^x = -D_{i,j}^{xx} \frac{\phi_{i,j} - \phi_L}{\Delta_{x,i}/2} - D_{i,j}^{yx} \frac{\phi_T - \phi_B}{\Delta_{y,j}} \,.$$

Rotating the coordinate system by swapping $x \leftrightarrow y$, $T \leftrightarrow R$, $B \leftrightarrow L$, and $i \leftrightarrow j$, we obtain analogous equations for the top and bottom leakage terms:

$$F_T^y = -D_{i,j}^{yy} \frac{\phi_T - \phi_{i,j}}{\Delta_{y,j}/2} - D_{i,j}^{xy} \frac{\phi_R - \phi_L}{\Delta_{x,i}} \,,$$

$$F_B^y = -D_{i,j}^{yy} \frac{\phi_{i,j} - \phi_B}{\Delta_{y,j}/2} - D_{i,j}^{xy} \frac{\phi_R - \phi_L}{\Delta_{x,i}} \,.$$

At each interior face, we demand that the scalar intensity ϕ be continuous, i.e.,

$$\phi_{R,i,j} = \phi_{L,i+1,j} \equiv \phi_{i+1/2,j} \,.$$

Substituting these definitions and the net leakage expressions into the conservation equation (5.2), we obtain:

$$
\begin{aligned}
&-\Delta_{x,i} D^{yy}_{i,j} \frac{\phi_{i,j+1/2} - \phi_{i,j}}{\Delta_{y,j}/2} - \Delta_{x,i} D^{xy}_{i,j} \frac{\phi_{i+1/2,j} - \phi_{i-1/2,j}}{\Delta_{x,i}} + \Delta_{x,i} D^{yy}_{i,j} \frac{\phi_{i,j} - \phi_{i,j-1/2}}{\Delta_{y,j}/2} \\
&+ \Delta_{x,i} D^{xy}_{i,j} \frac{\phi_{i+1/2,j} - \phi_{i-1/2,j}}{\Delta_{x,i}} - \Delta_{y,j} D^{xx}_{i,j} \frac{\phi_{i+1/2,j} - \phi_{i,j}}{\Delta_{x,i}/2} - \Delta_{y,j} D^{yx}_{i,j} \frac{\phi_{i,j+1/2} - \phi_{i,j-1/2}}{\Delta_{y,j}} \\
&+ \Delta_{y,j} D^{xx}_{i,j} \frac{\phi_{i,j} - \phi_{i-1/2,j}}{\Delta_{x,i}/2} + \Delta_{y,j} D^{yx}_{i,j} \frac{\phi_{i,j+1/2} - \phi_{i,j-1/2}}{\Delta_{y,j}} + \Delta_{x,i}\Delta_{y,j}\sigma_{a,i,j}\phi_{i,j} = \Delta_{x,i}\Delta_{y,j} q_{i,j} \,.
\end{aligned}
$$

The transverse leakage terms cancel, leaving a conservative relation between the cell-centered $\phi_{i,j}$ and the surrounding edge-centered ϕ:

$$
\begin{aligned}
\phi_{i,j} &\left(4D^{xx}_{i,j} \frac{\Delta_{y,j}}{\Delta_{x,i}} + 4D^{yy}_{i,j} \frac{\Delta_{x,i}}{\Delta_{y,j}} + \Delta_{x,i}\Delta_{y,j}\sigma_{a,i,j} \right) \\
&- 2D^{xx}_{i,j} \frac{\Delta_{y,j}}{\Delta_{x,i}} \left(\phi_{i+1/2,j} + \phi_{i-1/2,j} \right) - 2D^{yy}_{i,j} \frac{\Delta_{x,i}}{\Delta_{y,j}} \left(\phi_{i,j+1/2} + \phi_{i,j-1/2} \right) \\
&= \Delta_{x,i}\Delta_{y,j} q_{i,j} \,. \qquad \text{(5.18a)}
\end{aligned}
$$

To complete the equations for the QD-like discretization, we enforce continuity of the radiation flux on interior faces. On the top face, we set $F^y_{T,i,j} = F^y_{B,i,j+1}$ to obtain equations for horizontal cell edges in the interior:

$$
\begin{aligned}
&-D^{yy}_{i,j} \frac{\phi_{i,j+1/2} - \phi_{i,j}}{\Delta_{y,j}/2} - D^{xy}_{i,j} \frac{\phi_{i+1/2,j} - \phi_{i-1/2,j}}{\Delta_{x,i}} \\
&\qquad = -D^{yy}_{i,j+1} \frac{\phi_{i,j+1} - \phi_{i,j+1/2}}{\Delta_{y,j}/2} - D^{xy}_{i,j+1} \frac{\phi_{i+1/2,j+1} - \phi_{i-1/2,j+1}}{\Delta_{x,i}} \,. \qquad \text{(5.18b)}
\end{aligned}
$$

Setting $F^x_{R,i,j} = F^x_{L,i+1,j}$ yields equations for the interior vertical edges:

$$
\begin{aligned}
&-D^{xx}_{i,j} \frac{\phi_{i+1/2,j} - \phi_{i,j}}{\Delta_{x,i}/2} - D^{yx}_{i,j} \frac{\phi_{i,j+1/2} - \phi_{i,j-1/2}}{\Delta_{y,j}} \\
&\qquad = -D^{xx}_{i+1,j} \frac{\phi_{i+1,j} - \phi_{i,j}}{\Delta_{x,i}/2} - D^{yx}_{i+1,j} \frac{\phi_{i+1,j+1/2} - \phi_{i+1,j-1/2}}{\Delta_{y,j}} \,. \qquad \text{(5.18c)}
\end{aligned}
$$

If $D^{xy} = D^{yx} = 0$, the edge-centered ϕ can be algebraically eliminated without approximation, and the QD-like method reduces to the simple cell-centered difference scheme of §5.2.

Equations (5.18) give one relation for each cell and interior edge. The boundary conditions for this discretization are simpler to derive than those in §5.2: because the

edge-centered ϕ are actual unknowns, there is no need to solve for F and algebraically eliminate the edge values in Eqs. (5.15). Only Eq. (5.13) by itself is necessary.

The greater number of unknowns inherent to this discretization are undesirable. However, unlike the "diagonal-only" discretization from §5.2, it does not make any approximations to the transverse leakage terms. We have used this Gol'din discretization in our internal testing to verify the discretizations presented in the next section, but we will not use it in our final numerical experiments.

5.4 Nine-point stencil

Because the QD-like method uses three times as many unknowns as the simple cell-centered difference method given in §5.2, it is computationally more expensive to solve. We desire a discretization scheme that incorporates transverse leakage but has only MN unknowns on an $M \times N$ structured Cartesian mesh. One way is to develop a stencil in which the transverse leakage is approximated using both the adjacent cell and cells along the diagonal, as depicted in Fig. 5.4.

We begin by evaluating the face-averaged normal component of the flux, $F^x_{i+1/2,j} \equiv \int_{y_{j-1/2}}^{y_{j+1/2}} \boldsymbol{F}\cdot\boldsymbol{n}\,\mathrm{d}y$. We approximate the derivative normal to the face by introducing an edge-centered ϕ_*, using the same second-order difference as in §5.2, and demanding that

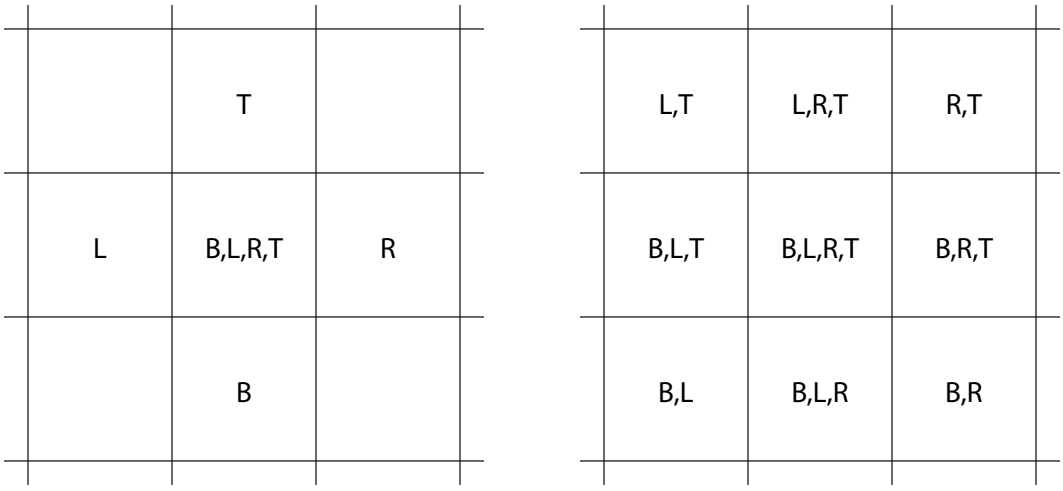

(a) Transverse terms neglected **(b)** Nine-point stencil

Figure 5.4: Stencils for $-\boldsymbol{\nabla}\cdot\mathbf{D}\boldsymbol{\nabla}\phi$. The leakage from each face B, L, R, T depends on the values of ϕ in each cell with the corresponding letter.

$F^x_{i+1/2,j}$ be the same when from both cell i,j and cell $i+1,j$. Solving for $F^x_{i+1/2,j}$ gives a more general version of Eq. (5.8):

$$F^x_{i+1/2,j} \approx -\frac{D^{xx}_{i+1/2,j}}{\Delta_{x,i+1/2}}\left[\left(\phi_{i+1,j}-\phi_{i,j}\right)+\frac{D^{xy}_{i,j}/D^{xx}_{i,j}}{2/\Delta_{x,i}}\left.\frac{\partial\phi}{\partial y}\right|_{x^-_{i+1/2}}+\frac{D^{xy}_{i+1,j}/D^{xx}_{i+1,j}}{2/\Delta_{x,i+1}}\left.\frac{\partial\phi}{\partial y}\right|_{x^+_{i+1/2}}\right], \tag{5.19}$$

where $\partial\phi/\partial y|_{x^-_{i+1/2}}$ is the transverse derivative of ϕ on the left side of the face, and $\partial\phi/\partial y|_{x^+_{i+1/2}}$ is the transverse derivative as viewed from the right side of the face. The harmonically averaged diffusion coefficient is the same as in Eq. (5.9):

$$\frac{D^{xx}_{i+1/2,j}}{\Delta_{x,i+1/2}} \equiv \left[\frac{1}{2}\left(\frac{D^{xx}_{i,j}}{\Delta_{x,i}}\right)^{-1}+\frac{1}{2}\left(\frac{D^{xx}_{i+1,j}}{\Delta_{x,i+1}}\right)^{-1}\right]^{-1}.$$

Figure 5.5 shows the net leakage from cell i,j through the right face, and the surrounding cell-centered unknowns. Our goal is to approximate Eq. (5.19) using only these cell-centered values, without introducing extra unknowns.

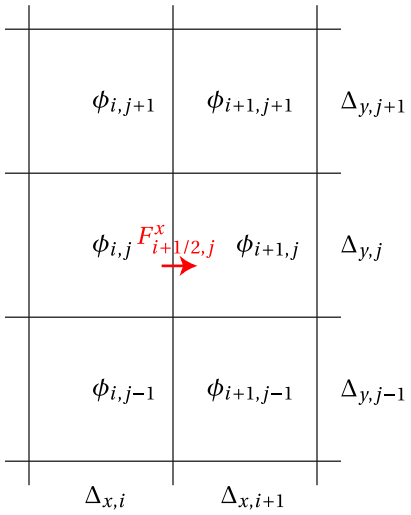

Figure 5.5: Diagram showing the radiation exiting interior cell i,j through the right face.

5.4.1 Stencil A

One approximation to the transverse derivative in Eq. (5.19) is the following second-order-accurate centered difference:

$$\left.\frac{\partial\phi}{\partial y}\right|_{x^-_{i+1/2}} \approx \frac{\phi_{i,j+1}-\phi_{i,j-1}}{\frac{1}{2}\Delta_{y,j+1}+\Delta_{y,j}+\frac{1}{2}\Delta_{y,j-1}}. \tag{5.20a}$$

The transverse derivative on the right-hand side of the face is:

$$\left.\frac{\partial\phi}{\partial y}\right|_{x^+_{i+1/2}} \approx \frac{\phi_{i+1,j+1}-\phi_{i+1,j-1}}{\frac{1}{2}\Delta_{y,j+1}+\Delta_{y,j}+\frac{1}{2}\Delta_{y,j-1}}. \tag{5.20b}$$

When cell i,j is adjacent to the boundary in the transverse direction, we use a backward difference stencil, given here in the case of evaluating the transverse leakage on the right face of cell i,j when it is on the top boundary:

$$\left.\frac{\partial\phi}{\partial y}\right|_{x^-_{i+1/2}} \approx \frac{\phi_{i,j}-\phi_{i,j-1}}{\frac{1}{2}\Delta_{y,j}+\frac{1}{2}\Delta_{y,j-1}}.$$

Though this stencil is only first-order accurate, it avoids the severe implementation penalty of involving the boundary conditions in the transverse direction.[2] If the cells adjacent to the boundary have no transverse leakage, this term is not used. (Indeed, the boundary conditions derived in §5.2.3 require that assumption.)

5.4.2 Stencil B

A different approximation to the transverse derivatives in Eq. (5.19) is to formulate some to-be-determined approximate edge centered ϕ:

$$\left.\frac{\partial\phi}{\partial y}\right|_{x^-_{i+1/2}} \approx \frac{\phi_{i,j+1/2}-\phi_{i,j-1/2}}{\Delta_{y,j}}, \tag{5.21a}$$

and

$$\left.\frac{\partial\phi}{\partial y}\right|_{x^+_{i+1/2}} \approx \frac{\phi_{i+1,j+1/2}-\phi_{i+1,j-1/2}}{\Delta_{y,j}}, \tag{5.21b}$$

or if the cell is not in the interior,

$$\left.\frac{\partial\phi}{\partial y}\right|_{x^-_{i+1/2}} \approx \frac{\phi_{i,j}-\phi_{i,j-1/2}}{\frac{1}{2}\Delta_{y,j}}. \tag{5.21c}$$

[2] If second-order accuracy for the transverse leakage on the boundary is *truly* needed, an effective alternative to direct boundary conditions might be the method of "ghost cells."

To derive an expression for $\phi_{i+1,j+1/2}$ that depends only on cells local to i, j, we consider the finite difference scheme of §5.2, in which we introduced a temporary cell-edge unknown and discarded the off-diagonal terms of the diffusion tensor. In evaluating Eq. (5.21a) for the transverse partial derivative in the y direction, let us apply the difference using conservation of energy, and discarding the transverse leakage terms of this secondary equation.

The finite difference approximations coupling cell $i, j \equiv B$ to cell $i, j+1 \equiv T$ via leakage through the top face, $F_{i,j+1/2} \equiv F$ are:

$$F = -D_B \frac{\phi_* - \phi_B}{\Delta_B/2} \qquad \text{and} \qquad F = -D_T \frac{\phi_T - \phi_*}{\Delta_T/2},$$

where $\phi_* \equiv \phi_{i+1,j+1/2}$. Before, we sought to eliminate ϕ_*. Now we wish to solve for it as an approximation to insert into Eq. (5.21a), which is then used in Eq. (5.19).

Multiplying the equation for the bottom face by Δ_B/D_B and for the top face by Δ_T/D_T, we obtain two equations:

$$-\frac{\Delta_B/2}{D_B} F = \phi_* - \phi_B \qquad \text{and} \qquad -\frac{\Delta_T/2}{D_T} F = \phi_T - \phi_* .$$

Adding them eliminates gives the standard finite-difference approximation for F, seen in §5.2:

$$F = -\left(\frac{\Delta_B/2}{D_B} + \frac{\Delta_T/2}{D_T}\right)^{-1} \left(\phi_T - \phi_B\right),$$

and subtracting the second from the first gives an equation from which to solve for ϕ_*:

$$-\frac{\Delta_B/2}{D_B} F + \frac{\Delta_T/2}{D_T} F = 2\phi_* - (\phi_B + \phi_T) .$$

Solving these two equations for ϕ_*, we obtain the following expression:

$$\phi_* = \frac{\Delta_B/D_B}{\Delta_T/D_T + \Delta_B/D_B} \phi_T + \frac{\Delta_T/D_T}{\Delta_T/D_T + \Delta_B/D_B} \phi_B . \tag{5.22}$$

This equation approximates the cell-edge ϕ in the transverse direction as:

$$\phi_{i,j+1/2} \approx \frac{D^{yy}_{i,j}/\Delta_{y,j}}{D^{yy}_{i,j+1}/\Delta_{y,j+1} + D^{yy}_{i,j}/\Delta_{y,j}} \phi_{i,j+1} + \frac{D^{yy}_{i,j+1}/\Delta_{y,j+1}}{D^{yy}_{i,j+1}/\Delta_{y,j+1} + D^{yy}_{i,j}/\Delta_{y,j}} \phi_{i,j} ,$$

and

$$\phi_{i,j-1/2} \approx \frac{D^{yy}_{i,j-1}/\Delta_{y,j-1}}{D^{yy}_{i,j}/\Delta_{y,j} + D^{yy}_{i,j-1}/\Delta_{y,j-1}}\phi_{i,j} + \frac{D^{yy}_{i,j}/\Delta_{y,j}}{D^{yy}_{i,j}/\Delta_{y,j} + D^{yy}_{i,j-1}/\Delta_{y,j-1}}\phi_{i,j-1}\,.$$

These edge values are then introduced into Eqs. (5.21) to approximate the transverse leakage through a face normal to the x axis. In the interior, then,

$$\begin{aligned}\left.\frac{\partial\phi}{\partial y}\right|_{x^-_{i+1/2}} &\approx \frac{\phi_{i,j+1/2} - \phi_{i,j-1/2}}{\Delta_{y,j}} \\ &= \frac{1}{\Delta_{y,j}}\left[\frac{D^{yy}_{i,j}/\Delta_{y,j}}{D^{yy}_{i,j+1}/\Delta_{y,j+1} + D^{yy}_{i,j}/\Delta_{y,j}}\phi_{i,j+1} + \frac{D^{yy}_{i,j+1}/\Delta_{y,j+1}}{D^{yy}_{i,j+1}/\Delta_{y,j+1} + D^{yy}_{i,j}/\Delta_{y,j}}\phi_{i,j}\right. \\ &\qquad \left. - \frac{D^{yy}_{i,j-1}/\Delta_{y,j-1}}{D^{yy}_{i,j}/\Delta_{y,j} + D^{yy}_{i,j-1}/\Delta_{y,j-1}}\phi_{i,j} - \frac{D^{yy}_{i,j}/\Delta_{y,j}}{D^{yy}_{i,j}/\Delta_{y,j} + D^{yy}_{i,j-1}/\Delta_{y,j-1}}\phi_{i,j-1}\right].\end{aligned}$$

If the anisotropic diffusion coefficients are homogeneous and the grid is uniform, Eq. (5.22) and Eqs. (5.21) simplify to Eqs. (5.20). The nine-point stencil for $-\boldsymbol{\nabla}\cdot\boldsymbol{\nabla}\phi$ becomes:

$$\begin{array}{ccc} \frac{1}{2}D^{xy}\phi_{i-1,j+1} & -D^{yy}\phi_{i,j+1} & -\frac{1}{2}D^{xy}\phi_{i+1,j+1} \\ -D^{yy}\phi_{i-1,j} & +\left(2D^{xx}+2D^{yy}\right)\phi_{i,j} & -D^{xx}\phi_{i+1,j} \\ -\frac{1}{2}D^{xy}\phi_{i-1,j-1} & -D^{yy}\phi_{i,j-1} & +\frac{1}{2}D^{xy}\phi_{i+1,j-1}\,. \end{array}$$

5.5 Summary

We have derived several discretizations of the anisotropic diffusion and anisotropic P_1 equations. The first simple discretization, in which transverse leakage is neglected, is a minor modification of existing cell-centered difference schemes. The second quasi-diffusion-like scheme is a new application of an existing methodology, but it undesirably introduces additional unknowns. (We have used this scheme internally to compare against other discretizations, but we will not employ it further.) The final discretization scheme is, as far as we are aware, a novel extension of standard cell differencing. It accounts for the "transverse leakage" introduced by the off-diagonal components of the diffusion tensor, yet it retains the compact unknown space of simple cell-centered finite difference methods.

Chapter 6
Flatland geometry

"Flatland" is a fictional two-dimensional universe where particles are constrained to exist and travel in a 2-D plane [6]. Because the flatland phase space is (x, y, ω) with *one* angular variable (the azimuthal ω), rather than the standard 2-D (x, y, μ, ω) with *two* angular variables (the polar cosine μ and the azimuthal ω), flatland is a computationally simpler testing ground that retains the complexity of multidimensional geometry. For this reason, flatland has recently been used in the development and testing of multi-D transport methods, including the new anisotropic diffusion method [2, 64, 9, 3].

Previous work has shown that the 3-D diffusion coefficient $\frac{1}{3\sigma}$ differs from the flatland diffusion coefficient $\frac{1}{2\sigma}$, but accurate boundary conditions for the flatland diffusion equations have not been derived. An accurate diffusion boundary condition is needed for benchmarking new transport methods, such as anisotropic diffusion, against diffusion solutions. Thus, in this chapter we derive "Marshak" and "variational" boundary conditions for the flatland diffusion equation. We also present Monte Carlo sampling algorithms tailored to flatland geometry, as well as a description of how 2-D S_N transport can be easily adapted to flatland.

These methods are implemented in flatland primarily for the purpose of comparison with the new anisotropic diffusion methods. We briefly derive the AD approximation in flatland geometry for use in our benchmark problems.

6.1 Transport

To briefly illustrate the difference between flatland and 2-D geometry, we view an infinite gap between two materials. The flatland problem and the two-dimensional cross section are identical, shown in Fig. 6.1. However, in the 2-D case, the figure is merely a slice of a three-dimensional problem in which the two gray rectangles and the gap are infinite in extent (Fig. 6.2). In the flatland case, the polar angle θ is effectively fixed at $\theta = \pi/2$, i.e., $\mu = \cos\theta = 0$.

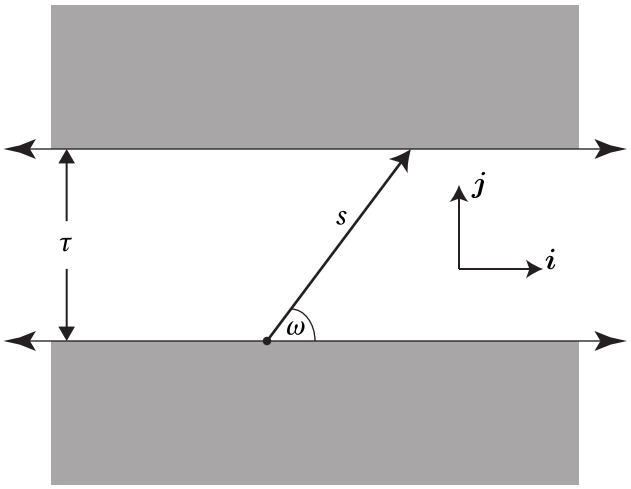

Figure 6.1: The infinite gap as represented on paper. The gap is a distance τ across, ω is the azimuthal angle, and s is the distance across the gap.

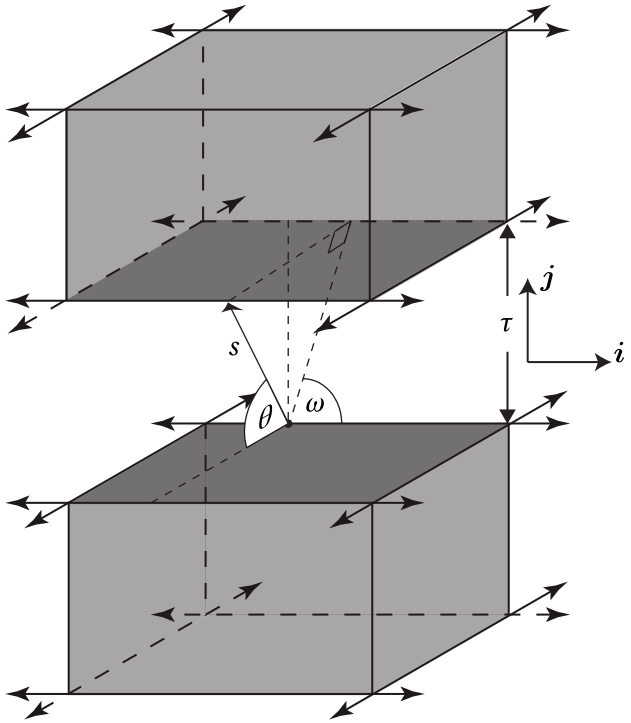

Figure 6.2: A 3-D view of the "2-D" infinite gap. The polar angle cosine is $\mu = \cos\theta$, and the azimuthal angle is ω.

Because the time-dependent and nonlinear terms of thermal radiative transfer are not affected by the choice of geometry, we constrain our discussion in this section to steady-state transport. Our application of the flatland transport equation has only isotropic emission (and "pseudo-scattering" if the linearized transport equation is used), so we limit our study to the case of isotropic scattering.

To begin, we write the steady-state transport equation with isotropic scattering in a "general geometry" form valid both for flatland and real space (1-D, 2-D, and 3-D):

$$\boldsymbol{\Omega}\cdot\boldsymbol{\nabla} I(\boldsymbol{x},\boldsymbol{\Omega}) + \sigma(\boldsymbol{x}) I(\boldsymbol{x},\boldsymbol{\Omega}) = \frac{c(\boldsymbol{x})\sigma(\boldsymbol{x})}{\gamma_0}\phi(\boldsymbol{x}) + \frac{1}{\gamma_0} q(\boldsymbol{x}), \quad \boldsymbol{x}\in V,\ \boldsymbol{\Omega}\in S. \tag{6.1a}$$

Here, we use the following definitions:

$I(\boldsymbol{x},\boldsymbol{\Omega})$ = the steady-state angular intensity,

$\boldsymbol{\Omega}$ = the unit direction vector,

S = the domain of the direction vector (the "unit sphere"),

γ_n = the nth angular moment,

$c(\boldsymbol{x})$ = the scattering ratio, and

$\phi(\boldsymbol{x})$ = the scalar intensity, i.e. the zeroth angular moment of I.

The direction vectors $\boldsymbol{\Omega}$ and domains S are presented in Table 6.1, and the moments γ_0 are evaluated in Table 6.2. The transport equation has a specified incident radiation boundary:

$$I(\boldsymbol{x},\boldsymbol{\Omega}) = I^b(\boldsymbol{x},\boldsymbol{\Omega}) \quad \boldsymbol{x}\in\partial V,\ \boldsymbol{\Omega}\cdot\boldsymbol{n} < 0. \tag{6.1b}$$

The "unit sphere"—the domain of the unit direction $\boldsymbol{\Omega}$—differs among the geometries. In 3-D, the direction variable is a unit vector, $\|\boldsymbol{\Omega}\| = 1$, so valid angles lie on the surface of a sphere of unit radius. In 2-D, those angles are projected onto a slice through the sphere's middle, so that $\|\boldsymbol{\Omega}\| \le 1$: valid angles are on a unit disc. Angles on the edge of the disc—the unit circle—represent particles traveling along the slice, and angles inside the unit circle are the projection of 3-D angles traveling with a non-zero polar angle cosine. Flatland geometry allows only angles on the unit circle, $\|\boldsymbol{\Omega}\| = 1$.

Geometry	$\boldsymbol{\Omega}$	Domain S	$\mathrm{d}\Omega$
1-D	μ	$-1 \le \mu \le 1$	$\mathrm{d}\mu$
2-D	$\sqrt{1-\mu^2}\cos\omega\boldsymbol{i} + \sqrt{1-\mu^2}\sin\omega\boldsymbol{j}$	$-1 \le \mu \le 1,\ 0 \le \omega < 2\pi$	$\mathrm{d}\mu\,\mathrm{d}\omega$
Flatland	$\cos\omega\boldsymbol{i} + \sin\omega\boldsymbol{j}$	$0 \le \omega < 2\pi$	$\mathrm{d}\omega$
3-D	$\mu\boldsymbol{i} + \sqrt{1-\mu^2}\cos\omega\boldsymbol{j} + \sqrt{1-\mu^2}\sin\omega\boldsymbol{k}$	$-1 \le \mu \le 1,\ 0 \le \omega < 2\pi$	$\mathrm{d}\mu\,\mathrm{d}\omega$

Table 6.1: Angular variables in the various geometries.

Geometry	$\gamma_0 \equiv \int_S \mathrm{d}\Omega$	$\gamma_1 \equiv \int_S \lvert\boldsymbol{\Omega}\cdot\boldsymbol{i}\rvert\,\mathrm{d}\Omega$	$\gamma_2 \equiv \int_S (\boldsymbol{\Omega}\cdot\boldsymbol{i})^2\,\mathrm{d}\Omega$
1-D	2	1	$\frac{2}{3}$
2-D	4π	2π	$\frac{4\pi}{3}$
Flatland	2π	4	π
3-D	4π	2π	$\frac{4\pi}{3}$

Table 6.2: Angular moments in each geometry.

6.1.1 Monte Carlo sampling

In numerically testing the anisotropic diffusion approximation, we use Monte Carlo methods (with a very large number of particles) to generate the reference solutions. The Monte Carlo method approximates the transport equation by tracking the random histories of statistically large numbers of particles as they traverse a problem. The behavior during their lifetime depends on probability distribution functions (PDFs) that describe how they are born, how far they travel without a collision, how they behave when they collide, and others [46, 22].

In this section, we form and discuss the probability distributions particular to flatland geometry. We briefly derive those PDFs, integrate them to get cumulative distribution functions (CDFs), and use the direct inversion method to show how a uniformly sampled pseudo-random number $\xi \in [0,1)$ may be used to determine particle behavior in flatland. Because the geometry tracking routines of steady state Monte Carlo and Fleck and Cummings' IMC are identical, the results in this section are applicable to any flatland Monte Carlo implementation.

Isotropic volume source

A particle emitted from an isotropic internal source, whether an extraneous radiation source or an indirect isotropic scattering event, has an equal probability of entering any angle. In any geometry, the normalized PDF that represents this process is

$$f(\boldsymbol{\Omega})\,\mathrm{d}\Omega = \alpha\,\mathrm{d}\Omega\,, \quad \boldsymbol{\Omega} \in S\,,$$

where S is the angular domain of the geometry (see Table 6.1), and α is a normalization constant. Requiring the PDF to integrate to unity over its domain gives the following value for α in any geometry:

$$1 = \int_S f(\boldsymbol{\Omega})\,\mathrm{d}\Omega = \alpha \int_S \mathrm{d}\Omega = \alpha\gamma_0 \quad \Longrightarrow \quad \alpha = \frac{1}{\gamma_0}\,.$$

Thus, the angular distribution of an isotropic volume source is

$$f(\mathbf{\Omega})\,\mathrm{d}\Omega = \frac{\mathrm{d}\Omega}{\gamma_0}, \quad \mathbf{\Omega} \in S. \tag{6.2}$$

In 2-D, using the identities from Tables 6.1 and 6.2, Eq. (6.2) evaluates to the familiar

$$f(\mu,\omega)\,\mathrm{d}\mu\,\mathrm{d}\omega = \frac{\mathrm{d}\mu\,\mathrm{d}\omega}{4\pi} = \frac{\mathrm{d}\mu}{2}\frac{\mathrm{d}\omega}{2\pi}, \quad -1 \le \mu \le 1,\ 0 \le \omega < 2\pi,$$

which, integrated, yields the separable CDF

$$F(\mu,\omega) = F_1(\mu)F_2(\omega) = \frac{1+\mu}{2}\frac{\omega}{2\pi}, \quad -1 \le \mu \le 1,\ 0 \le \omega < 2\pi.$$

Setting two uniformly sampled random numbers $\xi_1 = F_1(\mu)$ and $\xi_2 = F_2(\omega)$, solving for μ and ω, and introducing them back into the 2-D representation of $\mathbf{\Omega}$, we obtain the new direction for an isotropically emitted particle in 2-D:

$$\begin{aligned}\mathbf{\Omega} &= \sqrt{1-\mu^2}\cos\omega\,\boldsymbol{i} + \sqrt{1-\mu^2}\sin\omega\,\boldsymbol{j} \\ &= \sqrt{1-(2\xi_1-1)^2}\cos(2\pi\xi_2)\,\boldsymbol{i} + \sqrt{1-(2\xi_1-1)^2}\sin(2\pi\xi_2)\,\boldsymbol{j}.\end{aligned}$$

In flatland, Eq. (6.2) becomes the simpler

$$f(\omega)\,\mathrm{d}\omega = \frac{\mathrm{d}\omega}{2\pi}, \quad 0 \le \omega < 2\pi,$$

yielding the CDF

$$F(\omega) = \frac{\omega}{2\pi}, \quad 0 \le \omega < 2\pi, \tag{6.3}$$

Setting $\xi_1 = F(\omega)$ and solving for $\omega = F^{-1}(\xi_1)$ gives the following simple relation between an isotropically sampled angle ω and a uniformly sampled random number ξ_1:

$$\omega = 2\pi\xi_1.$$

The flatland particle's new angle is therefore

$$\mathbf{\Omega} = \cos\omega\,\boldsymbol{i} + \sin\omega\,\boldsymbol{j} = \cos(2\pi\xi_1)\,\boldsymbol{i} + \sin(2\pi\xi_1)\,\boldsymbol{j}.$$

With only one independent variable that needs sampling, and the omission of the transcendental operation $\sqrt{1-\mu^2}$, the computational cost of a scattering event is less in flatland than in 2-D, leading to faster simulation times.

Isotropic surface source

Particles emitted from an isotropic surface source have a cosine distribution [65], in which the partial first moment in each differential angle is constant. The PDF for a surface source is

$$f(\boldsymbol{\Omega})\,\mathrm{d}\Omega = \alpha\,|\boldsymbol{\Omega}\cdot\boldsymbol{n}|\,\mathrm{d}\Omega\,, \quad \boldsymbol{\Omega}\cdot\boldsymbol{n} < 0\,,$$

where α is a normalization constant. We obtain α by integrating over the angular domain and substituting the angular moments from Table 6.2:

$$\begin{aligned} 1 &= \int_{\boldsymbol{\Omega}\cdot\boldsymbol{n}<0} [\alpha\,|\boldsymbol{\Omega}\cdot\boldsymbol{n}|]\,\mathrm{d}\Omega \\ 1 &= \frac{\alpha}{2}\int_S |\boldsymbol{\Omega}\cdot\boldsymbol{n}|\,\mathrm{d}\Omega \\ \alpha &= \frac{2}{\gamma_1}\,. \end{aligned}$$

Thus, the normalized PDF for an isotropic surface source is

$$f(\boldsymbol{\Omega})\,\mathrm{d}\Omega = \frac{2}{\gamma_1}\,|\boldsymbol{\Omega}\cdot\boldsymbol{n}|\,\mathrm{d}\Omega\,, \quad \boldsymbol{\Omega}\cdot\boldsymbol{n} < 0\,. \tag{6.4}$$

In 3-D, choosing $\boldsymbol{n} = \boldsymbol{i}$, the isotropic surface PDF is

$$f(\mu,\omega)\,\mathrm{d}\mu\,\mathrm{d}\omega = \frac{1}{\pi}\mu\,\mathrm{d}\mu\,\mathrm{d}\omega = (2\mu\,\mathrm{d}\mu)\frac{\mathrm{d}\omega}{2\pi}\,,$$

which gives the separable CDF

$$F(\mu,\omega) = \mu^2\,\frac{\omega}{2\pi}\,.$$

The sampled directions are thus $\mu = \sqrt{\xi_1}$ and $\omega = 2\pi\xi_2$.

In flatland, the surface source distribution is different. Let us choose $\boldsymbol{n} = -\boldsymbol{j}$ so that emitted particles have azimuthal angles in the range $\omega \in [0,\pi)$. Applying the flatland identities in Tables 6.1 and 6.2 to Eq. (6.4), we obtain the following surface source PDF for flatland:

$$f(\omega)\,\mathrm{d}\omega = \frac{2}{4}\,|-\sin\omega|\,\mathrm{d}\omega = \frac{1}{2}\sin\omega\,\mathrm{d}\omega\,, \quad 0 \le \omega < \pi\,.$$

The corresponding CDF is

$$F(\omega) = \frac{1}{2}\,(1-\cos\omega)\,, \quad 0 \le \omega < \pi\,. \tag{6.5}$$

Solving for $\omega = F^{-1}(\xi_1)$ gives the sampled azimuthal angle for a surface source in flatland:

$$\omega = \cos^{-1}(1-2\xi_1)\,.$$

Finally, we insert this sampled angle into the flatland direction vector $\mathbf{\Omega}$ and use the identity $\cos^2\omega + \sin^2\omega = 1$ to obviate the trigonometric functions. Thus the sampled direction of a particle from an isotropic surface source is:

$$\begin{aligned}\mathbf{\Omega} &= \cos\omega\,\boldsymbol{i} + \sin\omega\,\boldsymbol{j} \\ &= \cos[\cos^{-1}(1-2\xi_1)]\,\boldsymbol{i} + \sin[\cos^{-1}(1-2\xi_1)]\,\boldsymbol{j} \\ &= (1-2\xi_1)\,\boldsymbol{i} + \sqrt{1-(1-2\xi_1)^2}\,\boldsymbol{j}\,.\end{aligned}$$

6.1.2 Discrete ordinates quadrature

A standard practice in two-dimensional discrete ordinates (S_N) solvers is to create a quadrature set with polar angles that encompass only the top half of a unit sphere, $\mu > 0$, and to modify the ordinate weights so that they sum to 4π [66]. Well-constructed quadrature sets will also correctly integrate the spherical harmonic functions [67] over the unit sphere. The odd spherical harmonic functions will automatically integrate to zero, and the even functions are linear combinations of the even angular moments of Table 6.2:

$$\gamma_n = \sum_{m=1}^{M} |\mathbf{\Omega}_m \cdot \boldsymbol{i}|^n\, w_m = \int_S |\mathbf{\Omega}\cdot\boldsymbol{i}|^n \,\mathrm{d}\Omega\,, \quad n \text{ even.}$$

Most quadrature sets do not exactly integrate partial odd moments.

The most straightforward way to implement a *flatland* S_N code with only isotropic scattering is to use an existing 2-D S_N code with a special quadrature set consisting of ordinates that have a single polar angle $\mu = 0$. Using a Chebyshev–Gauss quadrature of the first kind [68] for the azimuthal angles will preserve the flatland angular moments,

$$\gamma_n = \sum_{m=1}^{M} \sin^n\theta_m\, w_m = \int_{2\pi} \sin^n\theta\,\mathrm{d}\theta\,, \quad n \text{ even}\,.$$

A quadrature set with $2M$ total ordinates (i.e., M per two octants, the standard nomenclature for discrete ordinates quadratures) will exactly integrate the first $2M-1$ polynomials of $\sin\theta$. The procedure to calculate a Chebyshev quadrature set for the first quadrant is:

1. Solve for the roots of an M-order Chebyshev polynomial of the first kind on $[-1,1]$. Discard the negative roots.

2. Take the inverse sine of the positive roots. These $M/2$ roots are the ordinate directions θ_m in the first quadrant.
3. Assign the uniform weight $w_m = \frac{\pi}{M}$.

For ease of implementation, we normalized the quadrature weights so that they sum to 4π instead of 2π. This allows flatland quadrature sets to be used in an existing 2-D discrete ordinates code in which the scattering kernel expects the quadrature set to be normalized to 4π. Table 6.3 gives several orders of the Chebyshev quadrature set with sixteen digits of precision; a more extensive and computer-readable set of ordinates is available online at `https://github.com/sethrj/PyTRT/blob/master/tools/python/qs/cgvalues2.json`.

In order to demonstrate the effect of this weight renormalization, let us consider the calculation of the anisotropic diffusion tensor in a homogeneous medium. The purely absorbing flatland transport problem has the solution $f(\mathbf{\Omega}) = \frac{1}{2\pi\sigma}$, which yields the diffusion coefficient

$$\mathbf{D} = \int_0^{2\pi} \mathbf{\Omega}\mathbf{\Omega} f(\mathbf{\Omega})\,\mathrm{d}\omega = \frac{1}{2\sigma}\mathbf{I}.$$

In an S_N calculation implemented with modified quadrature weights, the transport solution for each angle m will yield $f_m = \frac{1}{4\pi\sigma}$, and the quadrature integration will yield

$$\mathbf{D} = \sum_{m=1}^{M} \mathbf{\Omega}_m \mathbf{\Omega}_m f_m w_m = \frac{1}{2\sigma}\mathbf{I}.$$

This implementation therefore will calculate correct low-order angular moments of the transport solution, but the apparent value of each f_m is one half the correct value. Thus, for example, visualizing the S_N solution by plotting f_m as a function of ω_m requires multiplying by a factor of two.

6.1.3 Thermal radiative transfer

To describe incident boundary conditions in thermal radiative transfer problems, the typical approach is to specify the *radiation temperature* [see Eq. (2.4)] on the boundary rather than the incident radiation flux. The boundary radiation temperature is equivalent to having an infinite homogeneous medium just outside the boundary with the blackbody scalar intensity $\phi = acT_{\mathrm{rad}}^4$. (A problem with these boundary conditions will be at thermal equilibrium when it has *(i)* a homogeneous material temperature T, *(ii)* a homogeneous radiation temperature $T_{\mathrm{rad}} = T$, *(iii)* a boundary radiation temperature $T_{\mathrm{rad}} = T$, and *(iv)* no extraneous sources. The amount of energy exiting the boundary is equal to the amount emitted into the problem by the radiation boundary.)

$M = 2,\ w = \pi$	
ω_0	$= 0.7853981633974483$

$M = 4,\ w = \pi/2$	
ω_0	$= 0.3926990816987241$
ω_1	$= 1.1780972450961724$

$M = 8,\ w = \pi/4$	
ω_0	$= 0.1963495408493621$
ω_1	$= 0.5890486225480862$
ω_2	$= 0.9817477042468103$
ω_3	$= 1.3744467859455345$

$M = 16,\ w = \pi/8$	
ω_0	$= 0.0981747704246810$
ω_1	$= 0.2945243112740431$
ω_2	$= 0.4908738521234052$
ω_3	$= 0.6872233929727672$
ω_4	$= 0.8835729338221293$
ω_5	$= 1.0799224746714915$
ω_6	$= 1.2762720155208536$
ω_7	$= 1.4726215563702156$

$M = 32,\ w = \pi/16$	
ω_0	$= 0.0490873852123405$
ω_1	$= 0.1472621556370216$
ω_2	$= 0.2454369260617026$
ω_3	$= 0.3436116964863836$
ω_4	$= 0.4417864669110647$
ω_5	$= 0.5399612373357457$
ω_6	$= 0.6381360077604268$
ω_7	$= 0.7363107781851078$
ω_8	$= 0.8344855486097889$
ω_9	$= 0.9326603190344699$
ω_{10}	$= 1.0308350894591509$
ω_{11}	$= 1.1290098598838318$
ω_{12}	$= 1.2271846303085130$
ω_{13}	$= 1.3253594007331939$
ω_{14}	$= 1.4235341711578751$
ω_{15}	$= 1.5217089415825562$

$M = 64,\ w = \pi/32$	
ω_0	$= 0.0245436926061703$
ω_1	$= 0.0736310778185108$
ω_2	$= 0.1227184630308513$
ω_3	$= 0.1718058482431918$
ω_4	$= 0.2208932334555323$
ω_5	$= 0.2699806186678729$
ω_6	$= 0.3190680038802134$
ω_7	$= 0.3681553890925539$
ω_8	$= 0.4172427743048944$
ω_9	$= 0.4663301595172349$
ω_{10}	$= 0.5154175447295755$
ω_{11}	$= 0.5645049299419159$
ω_{12}	$= 0.6135923151542565$
ω_{13}	$= 0.6626797003665970$
ω_{14}	$= 0.7117670855789375$
ω_{15}	$= 0.7608544707912781$
ω_{16}	$= 0.8099418560036186$
ω_{17}	$= 0.8590292412159591$
ω_{18}	$= 0.9081166264282996$
ω_{19}	$= 0.9572040116406402$
ω_{20}	$= 1.0062913968529807$
ω_{21}	$= 1.0553787820653211$
ω_{22}	$= 1.1044661672776617$
ω_{23}	$= 1.1535535524900022$
ω_{24}	$= 1.2026409377023428$
ω_{25}	$= 1.2517283229146832$
ω_{26}	$= 1.3008157081270237$
ω_{27}	$= 1.3499030933393643$
ω_{28}	$= 1.3989904785517049$
ω_{29}	$= 1.4480778637640452$
ω_{30}	$= 1.4971652489763858$
ω_{31}	$= 1.5462526341887264$

Table 6.3: Chebyshev–Gauss flatland quadrature sets. Orders 2, 4, 8, 16, 32, and 64 are given for the first quadrant. The weights in each order are equal and sum to 4π.

The equilibrium intensity is, using the notation of Table 6.2,

$$I(\boldsymbol{x}, \boldsymbol{\Omega}, t) = \frac{acT_{\text{rad}}^4}{\gamma_0}.$$

The incident black-body radiation flux is then

$$F^- = \int_{\boldsymbol{\Omega}\cdot\boldsymbol{n}<0} (\boldsymbol{\Omega}\cdot\boldsymbol{n}) \left[\frac{acT_{\text{rad}}^4}{\gamma_0}\right] \mathrm{d}\Omega = \frac{\gamma_1}{2}\frac{acT_{\text{rad}}^4}{\gamma_0}. \tag{6.6}$$

In 1-D, 2-D, and 3-D, this gives the physical incident rate of energy from a black body boundary source:

$$F^- = \frac{1}{4}acT_{\text{rad}}^4. \tag{6.7}$$

In flatland, Eq. (6.6) evaluates to a different incident rate:

$$F^- = \frac{1}{\pi}acT_{\text{rad}}^4. \tag{6.8}$$

6.2 Diffusion

An accurate flatland diffusion formulation is needed for benchmarking the anisotropic diffusion approximation against diffusion solutions. In the following section we derive "Marshak" and "variational" boundary conditions for the flatland diffusion equation. (A summary of this original work is published in Ref. [7].)

The difference between diffusion in flatland and 2-D results from the angular moments in the two geometries, which are defined (and evaluated in Table 6.2) as:

$$\gamma_n \equiv \int_S |\boldsymbol{\Omega}\cdot\boldsymbol{i}|^n \,\mathrm{d}\Omega.$$

These give rise not only to a different diffusion coefficient in the interior but also different boundary conditions.

6.2.1 Interior diffusion approximation

The diffusion approximation begins by assuming that I is linear in angle:

$$I(\boldsymbol{x}, \boldsymbol{\Omega}) \approx f(\boldsymbol{x}) + \boldsymbol{\Omega}\cdot\boldsymbol{g}(\boldsymbol{x}).$$

The zeroth angular moment of I determines f:

$$\phi = \int_S I \,\mathrm{d}\Omega = \int_S \left(f + \boldsymbol{\Omega}\cdot\boldsymbol{g}\right)\mathrm{d}\Omega = \int_S \mathrm{d}\Omega f + 0 = \gamma_0 f\,,$$

and the first moment of I determines g:

$$\boldsymbol{F} = \int_S \boldsymbol{\Omega} I \,\mathrm{d}\Omega = f\int_S \boldsymbol{\Omega}\,\mathrm{d}\Omega + \boldsymbol{g}\cdot\int_S \boldsymbol{\Omega}\boldsymbol{\Omega}\,\mathrm{d}\Omega = \gamma_2 \boldsymbol{g}\,.$$

This is the P_1 approximation to the radiation intensity:

$$I(\boldsymbol{x},\boldsymbol{\Omega}) \approx \frac{1}{\gamma_0}\phi(\boldsymbol{x}) + \frac{1}{\gamma_2}\boldsymbol{\Omega}\cdot\boldsymbol{F}(\boldsymbol{x})\,. \tag{6.9}$$

The diffusion approximation is a closure for the first angular moment of the transport equation. Operating on Eq. (6.1a) by $\int_S \boldsymbol{\Omega}(\cdot)\,\mathrm{d}\Omega$ and substituting the approximation in Eq. (6.9) reduces the first angular moment of the transport equation to the following:

$$\begin{aligned}
\boldsymbol{\nabla}\cdot\int_S \boldsymbol{\Omega}\boldsymbol{\Omega} I\,\mathrm{d}\Omega + \sigma\int_S \boldsymbol{\Omega} I\,\mathrm{d}\Omega &= \frac{c\sigma}{\gamma_0}\phi\int_S \boldsymbol{\Omega}\,\mathrm{d}\Omega + \frac{1}{\gamma_0}q\int_S \boldsymbol{\Omega}\,\mathrm{d}\Omega \\
\boldsymbol{\nabla}\cdot\int_S \boldsymbol{\Omega}\boldsymbol{\Omega}\left(\frac{1}{\gamma_0}\phi + \frac{1}{\gamma_2}\boldsymbol{\Omega}\cdot\boldsymbol{F}\right)\mathrm{d}\Omega + \sigma\boldsymbol{F} &= 0 \\
\frac{1}{\gamma_0}\boldsymbol{\nabla}\cdot\int_S \boldsymbol{\Omega}\boldsymbol{\Omega}\,\mathrm{d}\Omega\,\phi + \sigma\boldsymbol{F} &= 0 \\
\frac{\gamma_2}{\gamma_0}\boldsymbol{\nabla}\phi + \sigma\boldsymbol{F} &= 0\,.
\end{aligned}$$

Solving for $\boldsymbol{F}$ gives Fick's law, expressed in the general form:

$$\boldsymbol{F}(\boldsymbol{x}) = -\frac{\gamma_2}{\gamma_0}\frac{1}{\sigma(\boldsymbol{x})}\boldsymbol{\nabla}\phi(\boldsymbol{x}) \equiv -D(\boldsymbol{x})\boldsymbol{\nabla}\phi(\boldsymbol{x})\,. \tag{6.10}$$

In 2-D and 3-D, $\gamma_2/\gamma_0 = (4\pi/3)/(4\pi) = 1/3$; in flatland, $\gamma_2/\gamma_0 = \pi/(2\pi) = 1/2$. Thus, $D = \frac{1}{3\sigma}$ in 2-D but $D = \frac{1}{2\sigma}$ in flatland.

Substituting Fick's law into the linear-in-angle approximation, Eq. (6.9), we obtain the diffusion approximation to the angular intensity:

$$\begin{aligned}
I(\boldsymbol{x},\boldsymbol{\Omega}) &\approx \frac{1}{\gamma_0}\phi(\boldsymbol{x}) + \frac{1}{\gamma_2}\boldsymbol{\Omega}\cdot\left[-\frac{\gamma_2}{\gamma_0}\frac{1}{\sigma(\boldsymbol{x})}\boldsymbol{\nabla}\phi(\boldsymbol{x})\right] \\
I(\boldsymbol{x},\boldsymbol{\Omega}) &= \frac{1}{\gamma_0}\left[\phi(\boldsymbol{x}) - \frac{1}{\sigma(\boldsymbol{x})}\boldsymbol{\Omega}\cdot\boldsymbol{\nabla}\phi(\boldsymbol{x})\right]\,.
\end{aligned} \tag{6.11}$$

In physical geometry this is the standard diffusion approximation

$$I(\boldsymbol{x},\boldsymbol{\Omega}) = \frac{1}{4\pi}\left[\phi(\boldsymbol{x}) - \frac{1}{\sigma(\boldsymbol{x})}\boldsymbol{\Omega}\cdot\boldsymbol{\nabla}\phi(\boldsymbol{x})\right],$$

and in flatland, the diffusion approximation is

$$I(\boldsymbol{x},\boldsymbol{\Omega}) = \frac{1}{2\pi}\left[\phi(\boldsymbol{x}) - \frac{1}{\sigma(\boldsymbol{x})}\boldsymbol{\Omega}\cdot\boldsymbol{\nabla}\phi(\boldsymbol{x})\right]. \tag{6.12}$$

6.2.2 Marshak boundary condition

The Marshak boundary condition [69] preserves the incident radiation flux (the partial first moment for incoming directions) on the boundary. It is derived by substituting the approximate diffusion intensity from Eq. (6.11) into the boundary condition, Eq. (6.1b), multiplying by $|\boldsymbol{\Omega}\cdot\boldsymbol{n}|$, and integrating over incident directions:

$$\begin{aligned}
\int_{\boldsymbol{\Omega}\cdot\boldsymbol{n}<0} |\boldsymbol{\Omega}\cdot\boldsymbol{n}|\, I^b \,\mathrm{d}\Omega &= \int_{\boldsymbol{\Omega}\cdot\boldsymbol{n}<0} |\boldsymbol{\Omega}\cdot\boldsymbol{n}| \frac{1}{\gamma_0}\left[\phi - \frac{1}{\sigma}\boldsymbol{\Omega}\cdot\boldsymbol{\nabla}\phi\right]\mathrm{d}\Omega \\
F^- &= \frac{1}{\gamma_0}\phi\left(\int_{\boldsymbol{\Omega}\cdot\boldsymbol{n}<0} |\boldsymbol{\Omega}\cdot\boldsymbol{n}|\,\mathrm{d}\Omega\right) - \frac{1}{\gamma_0}\frac{1}{\sigma}\left(\int_{\boldsymbol{\Omega}\cdot\boldsymbol{n}<0} [-\boldsymbol{\Omega}\cdot\boldsymbol{n}]\boldsymbol{\Omega}\,\mathrm{d}\Omega\right)\cdot\boldsymbol{\nabla}\phi \\
F^- &= \frac{1}{\gamma_0}\phi\left(\frac{\gamma_1}{2}\right) + \frac{1}{\gamma_0}\frac{1}{\sigma}\left(\boldsymbol{n}\cdot\frac{\gamma_2}{2}\mathbf{I}\right)\cdot\boldsymbol{\nabla}\phi \\
F^- &= \frac{\gamma_1}{2\gamma_0}\phi + \frac{\gamma_2}{2\gamma_0}\frac{1}{\sigma}\boldsymbol{n}\cdot\boldsymbol{\nabla}\phi.
\end{aligned}$$

This is the Marshak diffusion boundary condition:

$$\frac{2\gamma_0}{\gamma_1}F^- = \phi + \frac{\gamma_2}{\gamma_1}\frac{1}{\sigma}\boldsymbol{n}\cdot\boldsymbol{\nabla}\phi. \tag{6.13}$$

The value

$$\frac{\gamma_2}{\gamma_1} = \begin{cases} \frac{2}{3} \approx 0.6667 & \text{in 1-D, 2-D, 3-D; and} \\ \frac{\pi}{4} \approx 0.7854 & \text{in flatland,} \end{cases}$$

is the Marshak extrapolation distance. The physical reason for the longer extrapolation distance in flatland is that in 2-D, a greater fraction of particles travel at a steep angle to the x,y-plane, yielding a steeper slope for ϕ on the boundary.

We can also rewrite the Marshak boundary condition in terms of the diffusion coefficient by substituting D from Eq. (6.10):

$$\frac{2\gamma_0}{\gamma_1}F^- = \phi + \frac{\gamma_0}{\gamma_1}D\boldsymbol{n}\cdot\boldsymbol{\nabla}\phi.$$

In 1-D, 2-D, and 3-D geometries, this is the standard Marshak boundary condition

$$4F^- = \phi + 2D\boldsymbol{n}\cdot\boldsymbol{\nabla}\phi\,.$$

In flatland, it is the following:

$$\pi F^- = \phi + \frac{\pi}{2} D\boldsymbol{n}\cdot\boldsymbol{\nabla}\phi\,. \tag{6.14}$$

6.2.3 Variational boundary condition

The Marshak boundary condition is heuristic: it attempts only to conserve the rate of energy entering through the boundary. A more accurate boundary condition recognizes that the diffusion approximation is an asymptotic limit of the transport equation and uses an asymptotic matched boundary layer analysis to relate the transport solution on the boundary to the diffusive solution in the interior. However, a simpler (than asymptotic) method of deriving a more accurate (than Marshak) boundary condition is to use a variational analysis [53]. A shorter but equivalent analysis, adapted to flatland geometry, follows.

We consider a homogeneous, source-free ($q = 0$), purely scattering ($c = 1$) transport problem in a semi-infinite flatland plane.[1] The transport equation (6.1a) becomes

$$\cos\omega\frac{\partial I}{\partial x} + \sin\omega\frac{\partial I}{\partial y} + \sigma I = \frac{\sigma}{2\pi}\int_0^{2\pi} I\,\mathrm{d}\omega'\,, \quad -\infty < x < \infty,\ 0 \le y < \infty,\ 0 \le \omega < 2\pi\,. \tag{6.15a}$$

It has a uniform incident boundary condition,

$$I(x,0,\omega) = I^b(\omega)\,, \quad -\infty < x < \infty,\ 0 \le \omega < \pi\,. \tag{6.15b}$$

Because neither the boundary condition nor σ varies in x, $\partial I/\partial x = 0$, and Eq. (6.15a) reduces to a one-dimensional flatland transport equation:

$$\sin\omega\frac{\partial}{\partial y} I(y,\omega) + \sigma I(y,\omega) = \frac{\sigma}{2\pi}\int_0^{2\pi} I(y,\omega')\,\mathrm{d}\omega'\,. \tag{6.16}$$

This is *not* the 1-D planar geometry transport equation.

[1] The justification for setting $c = 1$ and $q = 0$ relates to the asymptotic scaling used to derive diffusion from the transport equation: both q and $1 - c$ are $O(\epsilon^2)$ quantities [53].

We define the y components of the angular moments of I as

$$\phi_m(y) = \int_0^{2\pi} (\mathbf{\Omega}\cdot\boldsymbol{j})^m I(y,\omega)\,\mathrm{d}\omega = \int_0^{2\pi} (\sin\omega)^m I(y,\omega)\,\mathrm{d}\omega\,. \tag{6.17}$$

As $y\to\infty$, the intensity I approaches a constant $\varphi/2\pi$, which gives $\phi_0(\infty)=\phi(\infty)\equiv\varphi$. Concordantly, $\phi_1(\infty)=0$.

Operating on the transport equation by $\int_0^{2\pi}(\sin\omega)^m(\cdot)\,\mathrm{d}\omega$ gives the mth angular moment in the y direction:

$$\begin{aligned}\frac{\partial}{\partial y}\int_0^{2\pi}(\sin\omega)^{m+1} I\,\mathrm{d}\omega + \sigma\int_0^{2\pi}(\sin\omega)^m I\,\mathrm{d}\omega &= \frac{\sigma}{2\pi}\int_0^{2\pi} I\,\mathrm{d}\omega'\int_0^{2\pi}(\sin\omega)^m\,\mathrm{d}\omega\\ \frac{\partial\phi_{m+1}}{\partial y} + \sigma\phi_m &= \frac{\sigma}{2\pi}\phi_0\int_0^{2\pi}(\sin\omega)^m\,\mathrm{d}\omega\,.\end{aligned} \tag{6.18}$$

For $m=0$, the conservation equation, Eq. (6.18) evaluates to

$$\frac{\partial\phi_1}{\partial y} + \sigma\phi_0 = \frac{\sigma}{2\pi}\phi_0(2\pi) \quad\Longrightarrow\quad \frac{\partial\phi_1}{\partial y} = 0\,.$$

Thus, the radiation flux is a constant, and because $\phi_1(\infty)=0$, that constant is zero. Physically, $\phi_1=0$ means that at every point, the rate of energy being transferred away from the boundary is balanced by energy moving toward the boundary. This logically follows from the lack of absorption in the problem: at steady-state, the only means of energy loss is through exiting the boundary.

Evaluating Eq. (6.18) for $m=1$ and using the result that $\phi_1=0$, we obtain

$$\frac{\partial\phi_2}{\partial y} + \sigma\phi_1 = \frac{\sigma}{2\pi}\phi_0(0) \quad\Longrightarrow\quad \frac{\partial\phi_2}{\partial y} = 0\,.$$

Thus ϕ_2 is also a constant. At large distances from the boundary, $y\to\infty$, the radiation assumes an isotropic distribution, $I\to\varphi/2\pi$. From these two facts we relate the second angular moment throughout the problem to the equilibrium scalar intensity φ:

$$\phi_2 = \int_0^{2\pi}(\sin\omega)^2\frac{\varphi}{2\pi}\,\mathrm{d}\omega = \frac{1}{2}\varphi\,.$$

Since $\phi_1=0$, we can add $\alpha\phi_1$ to the previous equation for any α:

$$\begin{aligned}\alpha\phi_1 + \phi_2 &= \frac{\varphi}{2}\\ \int_0^{2\pi}(\alpha\sin\omega + \sin^2\omega)\,I(y,\omega)\,\mathrm{d}\omega &= \frac{\varphi}{2}\,.\end{aligned}$$

At the boundary $y = 0$, $I = I^b$ for incident angles $0 \le \omega < \pi$. The variational analysis in Ref. [53] reveals that certain trial functions allow an exiting angular distribution that is isotropic to second order accuracy, so we make the "variational" approximation that $I(0,\omega) = I^{\text{out}}$. The previous equation then becomes

$$\int_0^\pi (\alpha \sin\omega + \sin^2\omega) I^b(\omega)\,\mathrm{d}\omega + \int_\pi^{2\pi} (\alpha \sin\omega + \sin^2\omega)\,\mathrm{d}\omega\, I^{\text{out}} = \frac{\varphi}{2}.$$

The value $\alpha = \pi/4$ eliminates the integral over outgoing directions and gives the following relation between moments of the incident angular intensity and the magnitude of the intensity as $y \to \infty$:

$$\varphi = 2\int_0^\pi \left(\frac{\pi}{4}\sin\omega + \sin^2\omega\right) I^b(\omega)\,\mathrm{d}\omega. \tag{6.19}$$

We wish our boundary condition to preserve the value of φ when the diffusion method is used, so we substitute the diffusion approximation, Eq. (6.12):

$$\begin{aligned}
\varphi &= 2\int_0^\pi \left(\frac{\pi}{4}\sin\omega + \sin^2\omega\right) I^b(\omega)\,\mathrm{d}\omega \\
&= 2\int_0^\pi \left(\frac{\pi}{4}\sin\omega + \sin^2\omega\right)\left(\frac{1}{2\pi}\phi - \frac{1}{\sigma}\sin\omega\frac{\partial\phi}{\partial y}\right)\mathrm{d}\omega \\
&= \frac{1}{2\pi}\int_0^\pi \left(\frac{\pi}{2}\sin\omega + 2\sin^2\omega\right)\mathrm{d}\omega\,\phi - \frac{1}{2\pi}\int_0^\pi \left(\frac{\pi}{2}\sin^2\omega + 2\sin^3\omega\right)\mathrm{d}\omega\,\frac{1}{\sigma}\frac{\partial\phi}{\partial y} \\
&= \frac{1}{2\pi}\left(\frac{\pi}{2}[2] + 2\frac{\pi}{2}\right)\phi - \frac{1}{2\pi}\left(\frac{\pi}{2}\left[\frac{\pi}{2}\right] + 2\left[\frac{4}{3}\right]\right)\frac{1}{\sigma}\frac{\partial\phi}{\partial y} \\
&= \phi - \left(\frac{\pi}{8} + \frac{4}{3\pi}\right)\frac{1}{\sigma}\frac{\partial\phi}{\partial y}.
\end{aligned}$$

In this problem, the boundary surface outer normal is $\boldsymbol{n} = -\boldsymbol{j}$. Replacing $\sin\omega$ with $-\boldsymbol{\Omega}\cdot\boldsymbol{n}$, we obtain the following flatland variational boundary condition:

$$\int_{\boldsymbol{\Omega}\cdot\boldsymbol{n}<0} \left[\frac{\pi}{2}|\boldsymbol{\Omega}\cdot\boldsymbol{n}| + 2(\boldsymbol{\Omega}\cdot\boldsymbol{n})^2\right] I^b(\boldsymbol{x},\boldsymbol{\Omega})\,\mathrm{d}\Omega = \phi(\boldsymbol{x}) - \left(\frac{\pi}{8} + \frac{4}{3\pi}\right)\frac{1}{\sigma}\boldsymbol{n}\cdot\boldsymbol{\nabla}\phi(\boldsymbol{x}). \tag{6.20}$$

Compared to the flatland Marshak boundary condition, Eq. (6.14), the variational boundary condition not only yields a different extrapolation distance $\frac{\pi}{8} + \frac{4}{3\pi} \approx 0.8171$ but also uses a different angular moment of the incident boundary flux.

6.2.4 Generalization

We recall from the discussion of boundary conditions in Chapter 3 that to eliminate the boundary layer solution in the interior of a 3-D problem, the necessary condition is

$$\int_{\mathbf{\Omega}\cdot\boldsymbol{n}<0} W(|\mathbf{\Omega}\cdot\boldsymbol{n}|)\, I_{\mathrm{bl}}(\boldsymbol{x},\mathbf{\Omega})\,\mathrm{d}\Omega = 0\,, \quad \boldsymbol{x}\in\partial V,\ \mathbf{\Omega}\cdot\boldsymbol{n}<0\,, \tag{6.21}$$

where W is related to Chandrasekhar's H-function [55] and can be approximated by a variationally-derived polynomial W_2:

$$W(\mu) = \frac{\sqrt{3}}{2}\mu H(\mu) \approx W_2(\mu) \equiv \mu + \tfrac{3}{2}\mu^2\,, \quad 0<\mu\le 1\,. \tag{6.22}$$

The exact extrapolation distance is the first moment of W:

$$z_0 = \int_0^1 \mu W(\mu)\,\mathrm{d}\mu \approx 0.7104\,,$$

and the variational approximation gives the following extrapolation distance:

$$z_0 \approx \int_0^1 \mu W_2(\mu)\,\mathrm{d}\mu = \tfrac{17}{24} \approx 0.7083\,.$$

Similarly, the 3-D Marshak boundary condition uses

$$W(\mu) \approx W_1(\mu) \equiv 2\mu\,,$$

which gives the Marshak extrapolation distance

$$z_0 \approx \int_0^1 \mu W_1(\mu)\,\mathrm{d}\mu = \tfrac{2}{3} \approx 0.6667\,.$$

In our analysis of flatland boundary conditions, we have essentially investigated an equivalent of the W function for flatland. This new function, which we term "V", preserves the interior solution in a purely scattering *flatland* half-space:

$$\int_{\mathbf{\Omega}\cdot\boldsymbol{n}<0} V(|\mathbf{\Omega}\cdot\boldsymbol{n}|)\, I^b(\boldsymbol{x},\mathbf{\Omega})\,\mathrm{d}\Omega = \int_{\mathbf{\Omega}\cdot\boldsymbol{n}<0} V(|\mathbf{\Omega}\cdot\boldsymbol{n}|)\, I_{\mathrm{approx}}(\boldsymbol{x},\mathbf{\Omega})\,\mathrm{d}\Omega\,. \tag{6.23}$$

The "true" function V might be calculable, for example, by using a singular eigenvalue solution [70] of Eq. (6.16), but we instead used a "variational" analysis and the standard Marshak treatment to approximate V.

We define $V(\mu)$ on the domain $0<\mu\le 1$, where for our purposes $\mu = |\mathbf{\Omega}\cdot\boldsymbol{n}|$, and

normalize the function and its approximations so that in flatland geometry:

$$\int_{\mathbf{\Omega}\cdot\boldsymbol{n}<0} V(|\mathbf{\Omega}\cdot\boldsymbol{n}|)\,\mathrm{d}\Omega = \int_0^\pi V(\sin\omega)\,\mathrm{d}\omega = 1\,.$$

The approximations to V should also have this normalization. Analogous to the W function, the flatland extrapolation distance is the first moment of V:

$$z_0 = \int_{\mathbf{\Omega}\cdot\boldsymbol{n}<0} |\mathbf{\Omega}\cdot\boldsymbol{n}|\, V(|\mathbf{\Omega}\cdot\boldsymbol{n}|)\,\mathrm{d}\Omega = \int_0^\pi V(\sin\omega)\sin\omega\,\mathrm{d}\omega\,.$$

The flatland Marshak approximation uses only the first angular moment, which, after normalization, is:

$$V_1(\mu) \equiv \frac{1}{2}\mu\,, \quad 0<\mu\le 1\,, \tag{6.24}$$

giving the flatland Marshak extrapolation distance

$$z_0 = \int_0^\pi V_1(\sin\omega)\sin\omega\,\mathrm{d}\omega = \frac{\pi}{4} \approx 0.7854\,.$$

The variational analysis yielded the following two-term approximation to V:

$$V_2(\mu) \equiv \frac{1}{2}\mu + \frac{1}{\pi}\mu^2\,, \quad 0<\mu\le 1\,. \tag{6.25}$$

The resulting flatland variational extrapolation distance is:

$$z_0 = \int_0^\pi V_2(\sin\omega)\sin\omega\,\mathrm{d}\omega = \frac{\pi}{8} + \frac{4}{3\pi} \approx 0.8171\,.$$

Using the variational $V(\mu)\approx V_2(\mu)$ with the diffusion approximation, Eq. (6.12), we obtain Eq. (6.20). With the Marshak $V(\mu)\approx V_1(\mu)$, the result is the less accurate Eq. (6.14).

6.3 Anisotropic diffusion

The anisotropic diffusion method presented in Chapter 3 needs little modification to be formulated in the flatland geometry. The most notable change is in formulating the low-order boundary conditions, which use the flatland function "V" rather than the 3-D Chandrasekhar "W."

We begin with the time-dependent transport equation in the general-geometry form,

$$\frac{1}{c}\frac{\partial I}{\partial t}(\boldsymbol{x},\boldsymbol{\Omega},t)+\boldsymbol{\Omega}\cdot\boldsymbol{\nabla}I(\boldsymbol{x},\boldsymbol{\Omega},t)+\sigma(\boldsymbol{x})I(\boldsymbol{x},\boldsymbol{\Omega},t) = \frac{\sigma_s(\boldsymbol{x})}{\gamma_0}\int_S I(\boldsymbol{x},\boldsymbol{\Omega}',t)\,\mathrm{d}\Omega'+\frac{q(\boldsymbol{x},t)}{\gamma_0}, \quad \boldsymbol{x}\in V,\ \boldsymbol{\Omega}\in S,\ t\geq 0, \tag{6.26a}$$

with specified incident boundary conditions

$$I(\boldsymbol{x},\boldsymbol{\Omega},t)=I^b(\boldsymbol{x},\boldsymbol{\Omega},t), \quad \boldsymbol{x}\in\partial V,\ \boldsymbol{\Omega}\cdot\boldsymbol{n}<0,\ t>0, \tag{6.26b}$$

and the initial condition

$$I(\boldsymbol{x},\boldsymbol{\Omega},0)=I^i(\boldsymbol{x},\boldsymbol{\Omega}), \quad \boldsymbol{x}\in V,\ \boldsymbol{\Omega}\in S. \tag{6.26c}$$

In flatland, the unit sphere S is $0\leq\omega<2\pi$, $\boldsymbol{\Omega}$ lives on the unit circle, and $\gamma_0=2\pi$.

As before, we write the transport solution as a superposition of an interior solution (far from initial conditions and exterior boundaries), a boundary layer solution, and an initial layer solution.

$$I(\boldsymbol{x},\boldsymbol{\Omega},t)\equiv I_{\mathrm{v}}(\boldsymbol{x},\boldsymbol{\Omega},t)+I_{\mathrm{bl}}(\boldsymbol{x},\boldsymbol{\Omega},t)+I_{\mathrm{il}}(\boldsymbol{x},\boldsymbol{\Omega},t). \tag{6.27}$$

See §3.1 for a review of the relationship between the three transport equations.

6.3.1 Interior approximation

The interior transport equation is

$$\frac{1}{c}\frac{\partial I_{\mathrm{v}}}{\partial t}(\boldsymbol{x},\boldsymbol{\Omega},t)+\boldsymbol{\Omega}\cdot\boldsymbol{\nabla}I_{\mathrm{v}}(\boldsymbol{x},\boldsymbol{\Omega},t)+\sigma(\boldsymbol{x})I_{\mathrm{v}}(\boldsymbol{x},\boldsymbol{\Omega},t)=\frac{\sigma_s(\boldsymbol{x})}{\gamma_0}\int_S I_{\mathrm{v}}(\boldsymbol{x},\boldsymbol{\Omega}',t)\,\mathrm{d}\Omega'+\frac{q(\boldsymbol{x},t)}{2\pi}. \tag{6.28}$$

The zeroth moment, $\int_S(\cdot)\,\mathrm{d}\Omega$, is the conservation equation:

$$\frac{1}{c}\frac{\partial\phi}{\partial t}(\boldsymbol{x},t)+\boldsymbol{\nabla}\cdot\boldsymbol{F}(\boldsymbol{x},t)+\sigma(\boldsymbol{x})\phi(\boldsymbol{x},t)=\sigma_s(\boldsymbol{x})\phi(\boldsymbol{x},t)+q(\boldsymbol{x},t). \tag{6.29}$$

This equation is identical to the 3-D conservation equation in Eq. (3.5) because $\int_S \mathrm{d}\Omega = \gamma_0$.

Multiplying the conservation equation by $\frac{1}{\gamma_0}$ and subtracting from Eq. (6.28), we cancel the isotropic sources on the right-hand side to obtain

$$\left[\frac{1}{c}\frac{\partial}{\partial t} + \boldsymbol{\Omega}\cdot\boldsymbol{\nabla} + \sigma\right]\left(I_\mathrm{v} - \frac{1}{\gamma_0}\phi\right) = \frac{1}{\gamma_0}\boldsymbol{\nabla}\cdot\boldsymbol{F} - \frac{1}{\gamma_0}\boldsymbol{\Omega}\cdot\boldsymbol{\nabla}\phi\,.$$

As before, we take the scaling that, in the interior, the intensity has weak gradients in space, very weak gradients in time, and only mild anisotropy:

$$\sigma = O(1), \qquad I = O(1), \qquad \int_S \boldsymbol{\Omega} I\,\mathrm{d}\Omega = O(\epsilon), \qquad \boldsymbol{\nabla} I = O(\epsilon), \qquad \frac{\partial I}{\partial t} = O(\epsilon^2)\,. \tag{6.30}$$

With this scaling, the time derivative and $\boldsymbol{\nabla}\cdot\boldsymbol{F}$ are $O(\epsilon^2)$, and we discard them to obtain the following asymptotically valid approximation:

$$[\boldsymbol{\Omega}\cdot\boldsymbol{\nabla} + \sigma]\left(I_\mathrm{v} - \frac{1}{\gamma_0}\phi\right) = -\frac{1}{\gamma_0}\boldsymbol{\Omega}\cdot\boldsymbol{\nabla}\phi\,.$$

Formally inverting the left-hand side gives the approximate interior intensity:

$$I_\mathrm{v} = \frac{1}{\gamma_0}\phi - [\boldsymbol{\Omega}\cdot\boldsymbol{\nabla} + \sigma]^{-1}\left(\frac{1}{\gamma_0}\boldsymbol{\Omega}\cdot\boldsymbol{\nabla}\phi\right).$$

The inverse expression has the interpretation of an integral transport equation, given in Eqs. (3.11). It is independent of geometry, so we expand the nonlocal ϕ and discard the $O(\epsilon^2)$ and higher terms to obtain:

$$I_\mathrm{v} = \frac{1}{\gamma_0}\phi - \left([\boldsymbol{\Omega}\cdot\boldsymbol{\nabla} + \sigma]^{-1}\frac{1}{\gamma_0}\right)\boldsymbol{\Omega}\cdot\boldsymbol{\nabla}\phi\,.$$

We define the parenthesized quantity to be f, the solution of a purely absorbing transport equation with a unit, isotropic source:

$$\boldsymbol{\Omega}\cdot\boldsymbol{\nabla} f(\boldsymbol{x},\boldsymbol{\Omega}) + \sigma(\boldsymbol{x}) f(\boldsymbol{x},\boldsymbol{\Omega}) = \frac{1}{\gamma_0}, \quad \boldsymbol{\Omega}\in S\,. \tag{6.31}$$

Therefore, the anisotropic diffusion approximation in the interior is

$$I_\mathrm{v}(\boldsymbol{x},\boldsymbol{\Omega},t) = \frac{1}{\gamma_0}\phi(\boldsymbol{x},t) - f(\boldsymbol{x},\boldsymbol{\Omega})\boldsymbol{\Omega}\cdot\boldsymbol{\nabla}\phi(\boldsymbol{x},t)\,. \tag{6.32}$$

The first moment of Eq. (6.32) relates the radiation flux to the gradient of ϕ, the same

anisotropic Fick's law as in §3.1:

$$\boldsymbol{F}(\boldsymbol{x},t) = -\mathbf{D}(\boldsymbol{x}) \cdot \boldsymbol{\nabla}\phi(\boldsymbol{x},t)\,. \tag{6.33}$$

Here, $\mathbf{D}$ is a second-order tensor, the second moment of the transport solution f. In flatland, it is a 2×2 matrix.

In 3-D geometry, in a homogeneous medium, $f = 1/(4\pi\sigma)$ so $\mathbf{D} = 1/(3\sigma)$. In flatland, $f = 1/(2\pi\sigma)$, and its second moment is

$$\mathbf{D} = \frac{1}{2\pi\sigma}\int_S \boldsymbol{\Omega}\boldsymbol{\Omega}\,\mathrm{d}\Omega = \frac{1}{2\pi\sigma}\gamma_2\mathbf{I} = \frac{1}{2\sigma}\mathbf{I}.$$

This is the standard flatland diffusion coefficient.

6.3.2 Initial conditions

The initial conditions for flatland are the same as in 3-D. To match the interior solution to the transport initial condition,

$$\phi(\boldsymbol{x},0) = \int_0^{2\pi} I^i(\boldsymbol{x},\boldsymbol{\Omega})\,\mathrm{d}\omega\,.$$

6.3.3 Boundary conditions

To formulate boundary conditions for the flatland anisotropic diffusion equation, we return to §6.2.4, where we defined a function $V(\mu)$ that preserves the interior solution in a flatland problem when integrated over the boundary:

$$\int_{\boldsymbol{\Omega}\cdot\boldsymbol{n}<0} V(|\boldsymbol{\Omega}\cdot\boldsymbol{n}|)\,I^b(\boldsymbol{x},\boldsymbol{\Omega},t)\,\mathrm{d}\Omega = \int_{\boldsymbol{\Omega}\cdot\boldsymbol{n}<0} V(|\boldsymbol{\Omega}\cdot\boldsymbol{n}|)\,I_{\text{approx}}(\boldsymbol{x},\boldsymbol{\Omega},t)\,\mathrm{d}\Omega\,. \tag{6.23}$$

Substituting the flatland anisotropic diffusion approximation, Eq. (6.32), and evaluating, we obtain:

$$\begin{aligned}\int_{\boldsymbol{\Omega}\cdot\boldsymbol{n}<0} V(|\boldsymbol{\Omega}\cdot\boldsymbol{n}|)\,I^b(\boldsymbol{x},\boldsymbol{\Omega},t)\,\mathrm{d}\Omega &= \int_{\boldsymbol{\Omega}\cdot\boldsymbol{n}<0} V(|\boldsymbol{\Omega}\cdot\boldsymbol{n}|)\left[\frac{1}{2\pi}\phi(\boldsymbol{x},t) - f(\boldsymbol{x},\boldsymbol{\Omega})\boldsymbol{\Omega}\cdot\boldsymbol{\nabla}\phi(\boldsymbol{x},t)\right]\mathrm{d}\Omega \\ &= \frac{1}{2\pi}\phi(\boldsymbol{x},t) - \int_{\boldsymbol{\Omega}\cdot\boldsymbol{n}<0} V(|\boldsymbol{\Omega}\cdot\boldsymbol{n}|)\boldsymbol{\Omega}f(\boldsymbol{x},\boldsymbol{\Omega})\,\mathrm{d}\Omega\cdot\boldsymbol{\nabla}\phi(\boldsymbol{x},t)\,.\end{aligned}$$

Multiplying by 2π, we arrive at the flatland anisotropic diffusion boundary condition:

$$2\pi\int_{\boldsymbol{\Omega}\cdot\boldsymbol{n}<0} V(|\boldsymbol{\Omega}\cdot\boldsymbol{n}|)\,I^b(\boldsymbol{x},\boldsymbol{\Omega},t)\,\mathrm{d}\Omega = \phi(\boldsymbol{x},t) + \frac{\pi}{2}\boldsymbol{d}(\boldsymbol{x})\cdot\boldsymbol{\nabla}\phi(\boldsymbol{x},t)\,, \tag{6.34}$$

where we have defined the flatland equivalent of Eq. (3.32), the flatland anisotropic diffusion boundary condition, to be

$$\boldsymbol{d}(\boldsymbol{x}) = -4\int_{\boldsymbol{\Omega}\cdot\boldsymbol{n}<0} V(|\boldsymbol{\Omega}\cdot\boldsymbol{n}|)\boldsymbol{\Omega} f(\boldsymbol{x},\boldsymbol{\Omega})\,\mathrm{d}\Omega\,. \tag{6.35}$$

The incident boundary condition for f should preserve the identity

$$\phi(\boldsymbol{x},t) = \int_S I_{\mathrm{v}}(\boldsymbol{x},\boldsymbol{\Omega},t)\,\mathrm{d}\Omega = \phi(\boldsymbol{x},t) - \int_S \boldsymbol{\Omega} f(\boldsymbol{x},\boldsymbol{\Omega})\,\mathrm{d}\Omega\cdot\boldsymbol{\nabla}\phi(\boldsymbol{x},t)\,.$$

Under the assumption that f is rotationally invariant about the boundary normal, the above relationship reduces to Eq. (3.34)

$$\int_{\boldsymbol{\Omega}\cdot\boldsymbol{n}>0} (\boldsymbol{\Omega}\cdot\boldsymbol{n}) f(\boldsymbol{x},\boldsymbol{\Omega})\,\mathrm{d}\Omega = \int_{\boldsymbol{\Omega}\cdot\boldsymbol{n}<0} |\boldsymbol{\Omega}\cdot\boldsymbol{n}|\, f(\boldsymbol{x},\boldsymbol{\Omega})\,\mathrm{d}\Omega\,.$$

As discussed in §3.1.3, this is satisfied by a reflecting or white boundary condition. In flatland, "rotational invariance" has the interpretation not of a conical surface of angles but of two rays.

If f is isotropic, $1/(2\pi\sigma)$, then $\boldsymbol{d}$ simplifies:

$$\begin{aligned}\boldsymbol{d}(\boldsymbol{x}) &= -4\int_{\boldsymbol{\Omega}\cdot\boldsymbol{n}<0} V(|\boldsymbol{\Omega}\cdot\boldsymbol{n}|)\boldsymbol{\Omega}\frac{1}{2\pi\sigma}\,\mathrm{d}\Omega \\ &= \frac{2}{\pi\sigma}\left(\int_{\boldsymbol{\Omega}\cdot\boldsymbol{n}<0} V(|\boldsymbol{\Omega}\cdot\boldsymbol{n}|)\,|\boldsymbol{\Omega}\cdot\boldsymbol{n}|\,\mathrm{d}\Omega\right)\boldsymbol{n} \\ &= \frac{2}{\pi\sigma}(z_0)\,,\end{aligned}$$

and Eq. (6.34) reduces to the flatland diffusion boundary condition:

$$2\pi\int_{\boldsymbol{\Omega}\cdot\boldsymbol{n}<0} V(|\boldsymbol{\Omega}\cdot\boldsymbol{n}|)\,I^b(\boldsymbol{x},\boldsymbol{\Omega},t)\,\mathrm{d}\Omega = \phi(\boldsymbol{x},t) + \frac{z_0}{\sigma}\boldsymbol{n}\cdot\boldsymbol{\nabla}\phi(\boldsymbol{x},t)\,.$$

Here, of course, z_0 is the *flatland* extrapolation distance from §6.2.4, $z_0 \approx 0.8171$.

The Marshak-like approximation is $V_1(\mu) \approx \mu/2$. Substituting that into (6.34) gives

$$2\pi \int_{\mathbf{\Omega}\cdot\boldsymbol{n}<0} \left[\frac{1}{2}|\mathbf{\Omega}\cdot\boldsymbol{n}|\right] I^b(\boldsymbol{x},\mathbf{\Omega},t)\,\mathrm{d}\Omega = \phi(\boldsymbol{x},t) + \frac{\pi}{2}\boldsymbol{d}(\boldsymbol{x})\cdot\boldsymbol{\nabla}\phi(\boldsymbol{x},t)$$
$$F^-(\boldsymbol{x},t) = \phi(\boldsymbol{x},t) + \frac{\pi}{2}\boldsymbol{d}(\boldsymbol{x})\cdot\boldsymbol{\nabla}\phi(\boldsymbol{x},t)\,,$$

where the boundary coefficient is:

$$\begin{aligned}\boldsymbol{d}(\boldsymbol{x}) &= -4\int_{\mathbf{\Omega}\cdot\boldsymbol{n}<0}\left[\frac{1}{2}|\mathbf{\Omega}\cdot\boldsymbol{n}|\right]\mathbf{\Omega} f(\boldsymbol{x},\mathbf{\Omega})\,\mathrm{d}\Omega \\ &= 2\int_{\mathbf{\Omega}\cdot\boldsymbol{n}<0}(\mathbf{\Omega}\cdot\boldsymbol{n})\mathbf{\Omega} f(\boldsymbol{x},\mathbf{\Omega})\,\mathrm{d}\Omega \\ &= 2\boldsymbol{n}\cdot\int_{\mathbf{\Omega}\cdot\boldsymbol{n}<0}\mathbf{\Omega}\mathbf{\Omega} f(\boldsymbol{x},\mathbf{\Omega})\,\mathrm{d}\Omega\,.\end{aligned}$$

A reflecting boundary condition on f causes this integral to be an even function of $\mathbf{\Omega}$:

$$\begin{aligned}\boldsymbol{d}(\boldsymbol{x}) &= \boldsymbol{n}\cdot\int_S \mathbf{\Omega}\mathbf{\Omega} f(\boldsymbol{x},\mathbf{\Omega})\,\mathrm{d}\Omega \\ &= \boldsymbol{n}\cdot\mathbf{D}\,.\end{aligned}$$

Thus the Marshak-like boundary condition for flatland anisotropic diffusion is:

$$\pi F^-(\boldsymbol{x},t) = \phi(\boldsymbol{x},t) + \frac{\pi}{2}\boldsymbol{n}\cdot\mathbf{D}(\boldsymbol{x})\cdot\boldsymbol{\nabla}\phi(\boldsymbol{x},t)\,. \tag{6.36}$$

This is virtually identical to the standard flatland diffusion Marshak boundary, Eq. (6.14).

6.3.4 Review

Anisotropic diffusion in flatland is very similar to anisotropic diffusion in 3-D. The difference lies in the value of $\mathbf{D}$, its underlying transport formulation, and the boundary conditions.

The low-order equation results from substituting the anisotropic Fick's law, Eq. (6.33), into the flatland conservation equation, Eq. (6.29):

$$\frac{1}{c}\frac{\partial\phi}{\partial t}(\boldsymbol{x},t) - \boldsymbol{\nabla}\cdot\mathbf{D}(\boldsymbol{x})\cdot\boldsymbol{\nabla}\phi(\boldsymbol{x},t) + \sigma(\boldsymbol{x})\phi(\boldsymbol{x},t) = \sigma_s(\boldsymbol{x})\phi(\boldsymbol{x},t) + q(\boldsymbol{x},t)\,,\quad \boldsymbol{x}\in V\,, 0\le t<\infty\,.$$

This low-order equation is identical in form to its 3-D counterpart, but the value and size of the anisotropic diffusion tensor $\mathbf{D}$ will be different. (It is a 2×2 matrix, and it approaches $\frac{1}{2\sigma}\mathbf{I}$ away from material boundaries.) The initial condition for the low-order

unknown ϕ is the zeroth moment of the transport initial condition:

$$\phi(\boldsymbol{x},0) = \int_0^{2\pi} I^i(\boldsymbol{x},\boldsymbol{\Omega})\,\mathrm{d}\omega\,.$$

The Marshak boundary condition for flatland anisotropic diffusion, from Eq. (6.36), is:

$$\pi F^-(\boldsymbol{x},t) = \phi(\boldsymbol{x},t) + \frac{\pi}{2}\boldsymbol{n}\cdot\mathbf{D}(\boldsymbol{x})\cdot\boldsymbol{\nabla}\phi(\boldsymbol{x},t)\,.$$

The diffusion coefficient is the second angular moment of a purely absorbing flatland transport solution f:

$$\mathbf{D}(\boldsymbol{x}) \equiv \int_0^{2\pi} \boldsymbol{\Omega}\boldsymbol{\Omega} f(\boldsymbol{x},\boldsymbol{\Omega})\,\mathrm{d}\omega\,, \tag{6.37}$$

where f is given in Eq. (6.31) as:

$$\boldsymbol{\Omega}\cdot\boldsymbol{\nabla} f(\boldsymbol{x},\boldsymbol{\Omega}) + \sigma(\boldsymbol{x}) f(\boldsymbol{x},\boldsymbol{\Omega}) = \frac{1}{2\pi}\,, \quad \boldsymbol{x}\in V\,, 0\le\omega<2\pi\,.$$

The incident boundary condition for f satisfies Eq. (3.34),

$$\int_{\boldsymbol{\Omega}\cdot\boldsymbol{n}>0} (\boldsymbol{\Omega}\cdot\boldsymbol{n}) f(\boldsymbol{x},\boldsymbol{\Omega})\,\mathrm{d}\Omega = \int_{\boldsymbol{\Omega}\cdot\boldsymbol{n}<0} |\boldsymbol{\Omega}\cdot\boldsymbol{n}|\, f(\boldsymbol{x},\boldsymbol{\Omega})\,\mathrm{d}\Omega\,, \quad \boldsymbol{x}\in\partial V\,.$$

A more accurate low-order boundary condition (compared to the Marshak boundary condition above), given in Eq. (6.34), uses transport-calculated coefficients on the exiting boundary of the problem:

$$2\pi\int_{\boldsymbol{\Omega}\cdot\boldsymbol{n}<0} V(|\boldsymbol{\Omega}\cdot\boldsymbol{n}|)\, I^b(\boldsymbol{x},\boldsymbol{\Omega},t)\,\mathrm{d}\Omega = \phi(\boldsymbol{x},t) + \frac{\pi}{2}\boldsymbol{d}(\boldsymbol{x})\cdot\boldsymbol{\nabla}\phi(\boldsymbol{x},t)\,,$$

where

$$\boldsymbol{d}(\boldsymbol{x}) = -4\int_{\boldsymbol{\Omega}\cdot\boldsymbol{n}<0} V(|\boldsymbol{\Omega}\cdot\boldsymbol{n}|)\boldsymbol{\Omega} f(\boldsymbol{x},\boldsymbol{\Omega})\,\mathrm{d}\Omega\,, \tag{6.35}$$

and V is well-approximated by the variational form derived in §6.2.3:

$$V(\mu) \approx V_2(\mu) = \frac{1}{2}\mu + \frac{1}{\pi}\mu^2\,, \quad 0<\mu\le 1\,.$$

6.4 Summary

Compared to 2-D geometry, flatland is less computationally expensive to simulate because of its reduced phase space. In Monte Carlo implementations, fewer random numbers are sampled per event and fewer expensive transcendental functions are evaluated.

Additionally, the smaller phase space implies that fewer particles need be run to achieve a statistical accuracy comparable to a 2-D problem. In the discrete ordinates method, only one polar angle ($\mu = 0$) is needed in flatland. The correspondingly smaller quadrature set reduces the cost of a transport sweep and the computational memory burden.

We derived both Marshak and variational boundary conditions for flatland diffusion. The simpler Marshak boundary uses the first moment of the incident boundary source and gives an extrapolation distance of about 0.7854. The more accurate variational boundary condition given in Eq. (6.20) uses a more complex angular moment and results in an extrapolation distance of about 0.8171. The accuracy of these methods will be compared in Chapter 7.

The formulation of the flatland anisotropic diffusion method is virtually identical to that presented in Chapter 3. The only differences between flatland and 2-D are in the angular variable of the transport problem and the coefficients in the boundary condition.

With the flatland versions of anisotropic diffusion and the benchmark methods in hand, we will evaluate the performance of the AD approximations with numerical experiments.

Chapter 7
Numerical Results: Linear Test Problems

When the anisotropic diffusion equations are solved numerically, the solution is not just a function of the physical problem: it is also affected by the choice of low-order discretization scheme, the transport discretization used in calculating the AD coefficients, the transport convergence criteria, and many other parameters. Because our work is the first to use S_N-generated anisotropic diffusion coefficients, we need to ensure that the chosen parameters and discretizations give accurate answers in simple problems, before running complex problems with time dependence and nonlinear opacities.

Furthermore, because of the novelty of the flatland geometry, which we use extensively, it is also necessary to provide numerical validation for the flatland boundary conditions derived in Chapter 6.

In this chapter, we investigate the quality of the anisotropic diffusion (AD), flux-limited anisotropic diffusion (FLAD), and anisotropic P_1 (AP_1) methods by analyzing their behavior in relatively simple steady-state and time-dependent problems. Most of these problems emulate attributes of realistic thermal radiative transfer problems, viz. high scattering ratios and optically thin regions surrounded by optically thick regions.

Our numerical simulations are executed with several existing methods (discussed more thoroughly in Chapter 2), as well as the new anisotropic diffusion methods. All are implemented in the PyTRT research code [71]. Unless otherwise noted, we use the following solver parameters with each method.

The Monte Carlo method functions as the benchmark transport method. Our implementation uses stratified sampling of source regions, and weight windows that attempt to keep uniform the weight of particles both emitted from sources and transported through previous time steps. The solver runs 10^7 particles and uses path length–weighted tallies.

Standard diffusion in our implementation uses a cell-centered discretization [14]. We use "variational" [Eq. (6.20)] rather than the less accurate "Marshak" [Eq. (6.14)]

boundary conditions. As with the following diffusion-like methods, we explicitly construct a sparse matrix that is passed to the Trilinos library [72]. In steady-state problems with fewer than 50,000 unknowns, we use the KLU direct solver [72]; otherwise, we use the method of conjugate gradients (CG).

Time-dependent $\mathbf{P}_1$ uses the standard "staggered mesh" discretization, in which the unknowns are a cell-centered ϕ and a face-centered $\boldsymbol{F}$.

Flux-limited diffusion is implemented with the "square root" limiter and discretization scheme discussed in §2.3.4. The limiter is treated semi-implicitly; i.e., the nonlinear flux-limited diffusion coefficient is not converged. (This is common practice.) The unknowns and diffusion coefficients are stored as cell-centered data.

Anisotropic diffusion uses coefficients calculated with the diamond difference S_N method, performing up to 100 sweep iterations.[1] In flatland, we use a Chebyshev–Gauss quadrature set (see §6.1.2) with 64 ordinates (S_{32}). As with FLD, the opacities, diffusion coefficients, and unknowns are cell-centered. We use the nine-point stencil given in §5.4.1. The low-order boundary conditions [Eq. (3.33)] use the variational extrapolation distance.

Flux-limited anisotropic diffusion is implemented with the "max" limiter described in §3.3 using the flux limiter discretization of §2.3.4. Otherwise, it is treated identically to the above anisotropic diffusion method.

Anisotropic $\mathbf{P}_1$ uses the same "staggered mesh" discretization as P_1. In all other aspects, it is identical to the other anisotropic methods.

7.1 Analysis of non-analytic AD coefficients

In prior work, the anisotropic diffusion coefficients were calculated using analytic solutions of f [2]. However, in all but the simplest problems, such solutions are not available, so here we use an S_N transport solver to calculate the coefficients. Because S_N is only an approximation to the transport equation, discretization in both the spatial and angular variables will affect the calculated diffusion coefficients $\mathbf{D}$, which in turn affect the anisotropic diffusion solution ϕ.

[1] As a reminder, only one sweep is needed in the absence of boundaries because the transport problem is purely absorbing. Opposing reflecting boundaries may require many iterations to converge, so we have chosen a very large number of sweeps to ensure the AD coefficients are calculated accurately. A more realistic number of sweeps would be two or three if white boundaries are used and the problem is not minuscule in extent.

To assess the discrepancy in the solution incurred by using discrete transport, we compare the solutions of a simple test problem using S_N-calculated coefficients and analytically calculated coefficients. Furthermore, we compare the analytic and discrete solutions to a Monte Carlo reference solution, to see if the discrepancy in the diffusion coefficients affects the accuracy of the methods.

By varying the number of ordinates in the quadrature set, the spatial refinement in the S_N calculation, the S_N convergence criteria, and the choice of boundary conditions for the calculation of f (reflecting or white), we determine acceptable solver parameters for later, more complex problems. A voided channel surrounded by a diffusive, optically thick medium is representative of many of our later test problems.

7.1.1 Problem description

The prototypical anisotropic diffusion test problem, a flatland VHTR mock-up considered by Larsen and Trahan [2], consists of voided vertical channels in a diffusive medium. The diffusive region has $\sigma_d = 1$, the channel $\sigma_c = 0.01$. The scattering ratio is uniformly 0.99. We use a small portion of this problem (Fig. 7.1), a single channel of unit width, with diffusive regions on the left and right each with width 4. The left and lower boundaries are reflecting, and the right and upper boundaries are vacuum. The source is a Gaussian

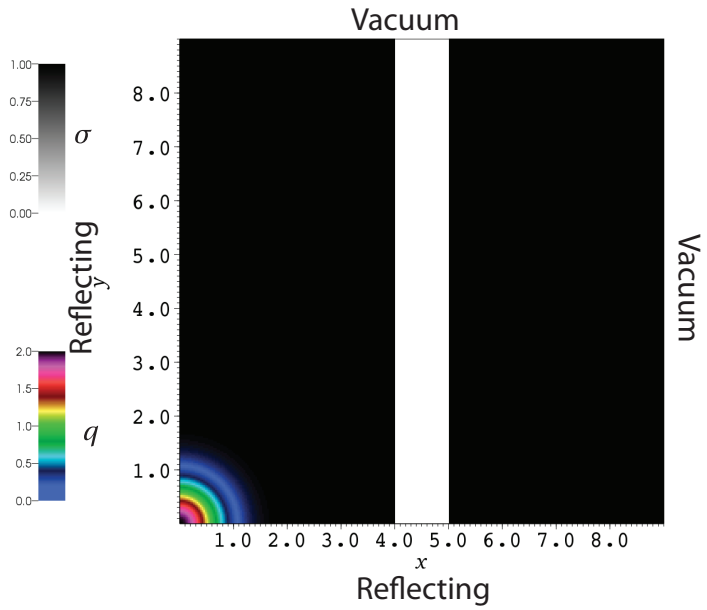

Figure 7.1: The single channel problem configuration. The total opacity is plotted in black and white, and the colored region in the lower left is the Gaussian source.

function peaked at $(0,0)$,

$$q(x,y) = 2\,\mathrm{e}^{-2(x^2+y^2)}\,.$$

The analytic solution of the purely absorbing transport solution for this problem is derived in Ref. [2] and restated here:

$$f(x,y,\omega) = \frac{1}{2\pi\sigma_d} + \frac{1}{2\pi}\left(\frac{1}{\sigma_c} - \frac{1}{\sigma_d}\right) \times g(x-4.5,\omega)\,, \tag{7.1}$$

where $g(x,\omega)$ is given in Table 7.1.

	Voided region ($\lvert x\rvert < W$)	Diffusive region ($\lvert x\rvert > W$)
$0 \le \omega < \frac{\pi}{2}$	$1 - \mathrm{e}^{-\sigma_c (W+x)/\cos\omega}$	$\mathrm{e}^{-\sigma_d (x-W)/\cos\omega} \times \left(1 - \mathrm{e}^{-\sigma_c (2W)/\cos\omega}\right)$
$\frac{\pi}{2} < \omega \le \pi$	$1 - \mathrm{e}^{-\sigma_c (W-x)/\lvert\cos\omega\rvert}$	0

Table 7.1: Component $g(x,\omega)$ of the analytic solution of f in the single-channel problem. Here, σ_c and σ_d are the total opacity in the channel and diffusive region, respectively; and $W = 0.5$ is the half-width of the channel. Because the problem is symmetric, $g(x,\omega) = g(x,2\pi-\omega)$ for $\omega < \pi \le 2\pi$.

This solution for f is based on the assumption that the channel is infinite in extent along the y axis, and that the diffusive regions are infinitely wide. We therefore expect reflecting boundaries on the S_N transport problem for f to produce answers closer to the analytic values. However, since the channel is *not* indeed infinite, reflecting boundaries will not necessarily produce more accurate answers compared to the reference transport solution.

Using the analytic solution for f given in Eq. (7.1), we calculate exact (to machine precision) solutions for the anisotropic diffusion coefficient $\mathbf{D}$ [from Eq. (6.37)]:

$$\mathbf{D}(x,y) \equiv \int_0^{2\pi} \mathbf{\Omega\Omega} f(x,y,\mathbf{\Omega})\,\mathrm{d}\omega\,,$$

as well as the boundary coefficient $\boldsymbol{d}$ [from Eq. (6.35)]:

$$\boldsymbol{d}(x,y) = -4 \int_{\mathbf{\Omega}\cdot\boldsymbol{n}<0} V(\lvert\mathbf{\Omega}\cdot\boldsymbol{n}\rvert)\mathbf{\Omega} f(x,y,\mathbf{\Omega})\,\mathrm{d}\Omega\,.$$

All of the diffusion solutions, even though they may use analytically-calculated coefficients, are solved using the standard five-point cell-centered diffusion scheme[2] using a uniform cell width of 0.0625.

[2] Because the opacity is symmetric about the x axis, $D^{xy} = 0$ throughout the problem; see §3.2.3.

7.1.2 Solution

The solution of the problem using four different methods is plotted in Fig. 7.2. The Monte Carlo solution is the reference solution. We have also shown the anisotropic diffusion solutions with both analytically calculated coefficients and S_N-calculated coefficients. The latter uses reflecting boundaries on the transport calculation for f with 10^4 source iterations. (Many sweeps are needed to fully converge the opposing reflecting boundaries. Our goal is to determine the error introduced by the S_N discretization itself, so we wish to reduce the additional error incurred by an incomplete S_N solution.) For comparative purposes, we also plot the standard diffusion solution.

Before exploring the parameter space of S_N solver options, we first point out some features in the solution characteristic of anisotropic diffusion. Unlike the Monte Carlo and diffusion solutions, which have discontinuous first derivatives at the boundary between channel and medium, the anisotropic diffusion solution is smooth. The AD solution is less accurate near the material boundaries, but along the centerline of the channel (Fig. 7.3) and a few mean free paths into the medium, it matches the reference solution very closely.

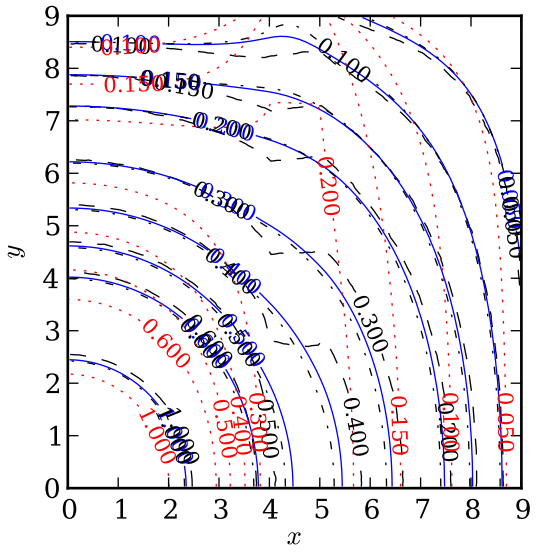

Figure 7.2: Contour plot of ϕ in the steady-state single channel problem. The dashed black line is the reference Monte Carlo solution; the dotted red line is standard diffusion; the broken black line is anisotropic diffusion with analytic coefficients; the solid blue line is anisotropic diffusion with coefficients calculated with an S_{32} transport sweep.

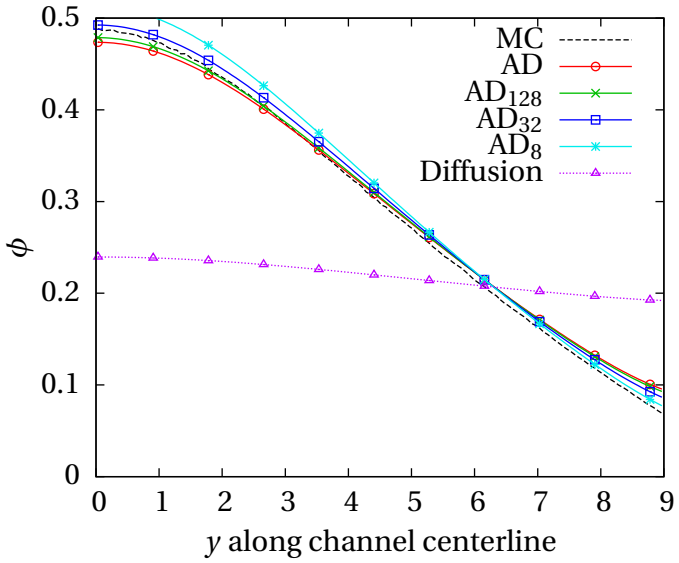

Figure 7.3: Scalar intensity along $x = 5.0$. The "AD" curve is the solution using analytic diffusion coefficients; the "AD_N" curves use S_N-calculated coefficients with reflecting boundaries.

7.1.3 S_N parameter convergence

Figure 7.4a plots the convergence of the solution ϕ against the solution with analytically-calculated AD coefficients, for four different combinations of S_N solver parameters, as a function of the number of source iterations (transport sweeps) in the calculation of f.

Likewise, figure 7.4b plots the convergence of the S_N solution with increasing number of ordinates. The black line shows that refining the quadrature brings the solution closer to the analytic value, but the red line demonstrates that it does *not* converge to the Monte Carlo transport solution. This is expected: the anisotropic diffusion method is only an approximation; based on assumptions about the problem's physics, asymptotically small terms were discarded (see §3.1.1). Yet in and around the channel region in this problem, the discarded terms are probably not asymptotically small. The true solution is strongly anisotropic and has strong gradients at the channel interface. The assumptions underlying diffusion also are not strictly valid at points in this problem. However, unlike diffusion, anisotropic diffusion yields reasonable answers in the presence of voids.

The convergence is calculated using a volume-weighted relative 2-norm:

$$\text{reported difference} = \left[\sum_{i \in \text{cells}} \left(\frac{\phi_i}{\phi_{i,\text{reference}}} - 1 \right)^2 (V_i)^2 \right]^{1/2}. \tag{7.2}$$

This is *not* the convergence of the transport solution f, which only affects ϕ indirectly.

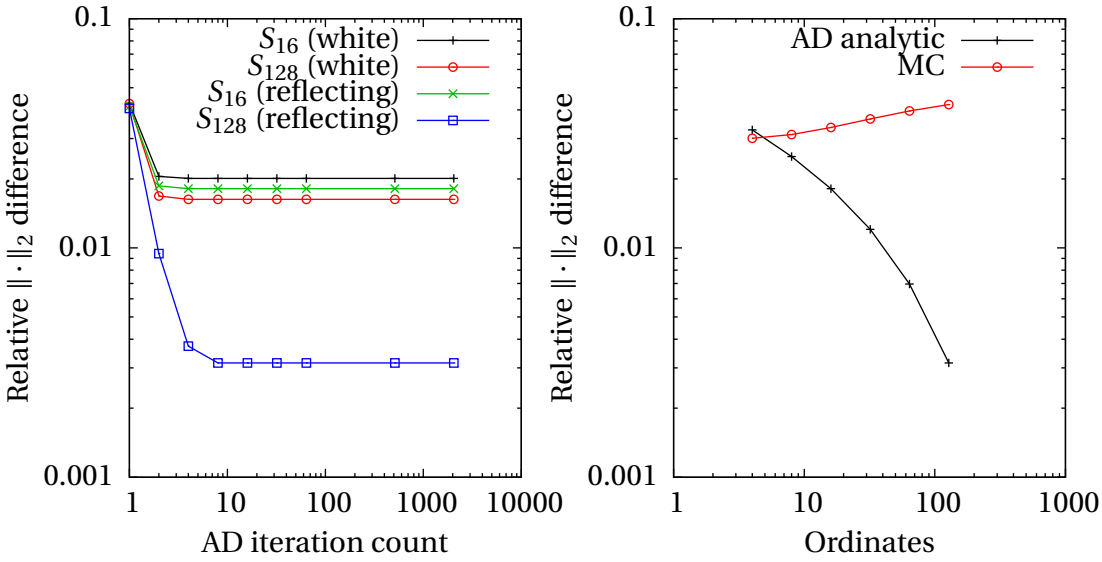

(a) Source iterations **(b)** Quadrature sets

Figure 7.4: Convergence of ϕ as a function of S_N parameters. The AD solution ϕ with S_N-calculated coefficients is compared against the solution with analytic coefficients using a volume-weighted 2-norm, as a function of increasing source iterations in the calculation of f. The red line in (b) shows convergence compared to the Monte Carlo solution.

Compared to the reference solution, AD (with analytic coefficients) has a 4.5% absolute error, and standard diffusion has a 19.8% error.

The data in Fig. 7.4a suggest that with a finite number of ordinates, which cannot exactly approximate the angular domain, there is little added benefit to using more than a few sweeps: the error introduced by the angular approximation exceeds that caused by the lack of convergence. But Fig. 7.4b shows that, since the analytic AD solution differs from the exact solution by 5%, even a coarse quadrature set can provide accuracy within the inherent limits of the method.

This conclusion may not hold for all problems, of course, but it suggests that a modest number of ordinates and sweeps are sufficient to yield solutions with close to the accuracy of an analytic anisotropic diffusion solution.

7.1.4 Coarse spatial grid calculation of D

In addition to investigating the sensitivity of the AD solution to the granularity of the angular variable in the solution of f, we test the discrepancy introduced by calculating f on a coarser spatial grid. As discussed in §3.2.3, the transport-calculated f is a smooth

function of space, and **D** likewise has no discontinuities. We have implemented the basic multigrid operations of prolongation and restriction in the PyTRT code [71] for quantities located at the center of cells (i.e., σ and **D**) and at the external problem boundary faces (i.e., $\boldsymbol{d}$).

We run the transport calculation for f on a coarse grid and prolongate the diffusion tensor **D** and boundary coefficient $\boldsymbol{d}$ back to the fine grid, in which ϕ is then solved. With this methodology, the spatial discretization error of the diffusion solve is unaffected; the only difference is that the diffusion coefficients are coarser functions of space. Figure 7.5 shows the resulting coarse anisotropic diffusion coefficients.

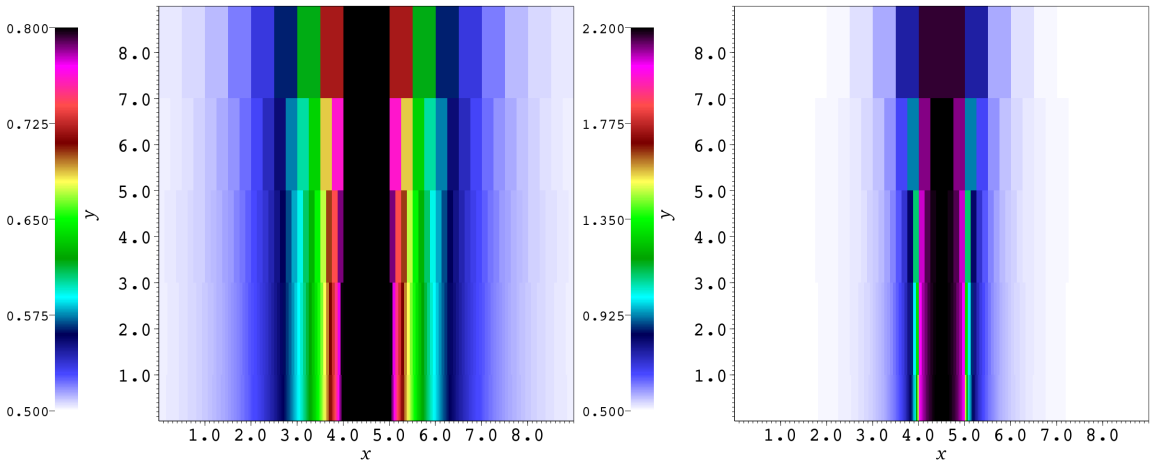

(a) D^{xx} **(b)** D^{yy}

Figure 7.5: Calculated diffusion coefficients for different grid coarseness. Every two units downward represents a factor of four refinement in the number of fine cells per coarse cell.

Figure 7.6 plots the error in ϕ introduced by using coarse approximations to the anisotropic diffusion coefficient. (In this problem, the grid and refinements were chosen so that in the coarsest case, each coarse cell was composed of a single material.) The rightmost data point in the figure has a coarse cell width of $\Delta_x = 0.5$, half the width of the channel. In this simple problem with well-defined material boundaries, the solution is relatively insensitive to using less spatially refined diffusion coefficients. This is perhaps not surprising, since the standard diffusion coefficient has no spatial variation inside a homogeneous material.

The implication of all these results is clear: high-fidelity transport calculations are *not* needed in calculation of the anisotropic diffusion coefficients. Because the cost of the transport calculation is roughly proportional to (the number of transport sweeps) ×

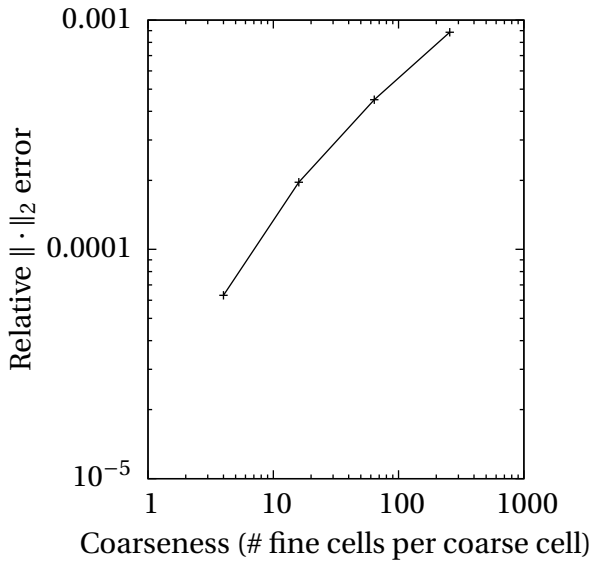

Figure 7.6: Error introduced by coarse spatial grids in calculating the AD coefficients.

(the number of ordinates) × (the number of spatial cells), using only a modest number of sweeps and a small quadrature set with a coarse-grid calculation can provide a substantial speedup when compared with a fine-grid calculation that might improve the answer only by a tenth of a percent. Because we do not expect the anisotropic diffusion approximation to yield exact transport solutions, and because a high-fidelity transport calculation requires far more computational effort than a diffusion solve, the small error incurred by using a coarse transport solution is justifiable in light of the performance gain.

7.2 Flatland boundary conditions

The flatland boundary conditions derived in Chapter 6 must, for the sake of completeness, be numerically verified. We compare the novel diffusion boundary conditions against a Monte Carlo reference solution in a simple, diffusive test problem.

We consider a homogeneous flatland problem (Fig. 7.7) with a total cross section $\sigma = 1$ and scattering ratio $c = 0.99$. The spatial domain is the rectangle $0 \le x \le 2$, $0 \le y \le 10$, with reflecting boundaries on the left, right, and top sides. The bottom side has a specified unit incident radiation flux; we consider three different angular distributions given in Table 7.2.[3]

[3]These distributions were chosen because of their prior use in a 1-D boundary matching analysis in Ref. [73].

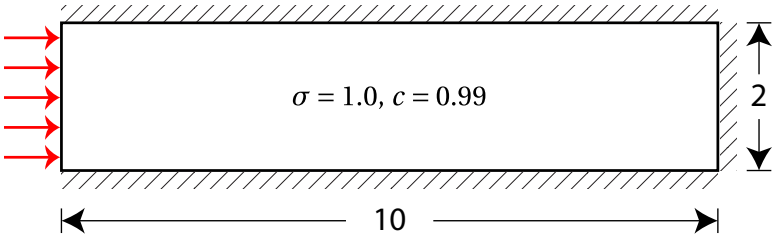

Figure 7.7: Problem description for the flatland boundary test.

Distribution	1-D	Flatland
Isotropic	$I(\mu) = \frac{1}{2}$	$I(\omega) = \frac{\pi}{2}$
Normal	$I(\mu) = \delta(\mu - 1)$	$I(\omega) = \delta(\omega - \pi/2)$
Grazing	$I(\mu) = \delta(\mu - 0.1)$	$I(\omega) = \delta(\omega - \sin^{-1}.1)$

Table 7.2: Angular distributions used in boundary condition tests.

Figure 7.8, a line-out of the scalar intensity ϕ_0 along $x = 1$ for the normally incident boundary, illustrates the differences between the methods. The diffusion approximation cannot reproduce the boundary layer that the true transport solution features, but the variational approximation to the flatland diffusion boundary condition allows the asymptotic diffusion solution to closely match the transport solution in the interior of the system. The Marshak boundary condition does not have this desirable property.

Figure 7.9 quantitatively compares both "variational" and "Marshak" diffusion boundary conditions against the transport solution for all three incident distributions. As with the variational boundary condition for 3-D geometry, the flatland variational boundary condition gives an interior scalar intensity accurate to within a few percent. The Marshak condition fails to limit to the transport solution except in the case of an isotropic boundary source, in which case only the extrapolation distance differs from the variational boundary condition.

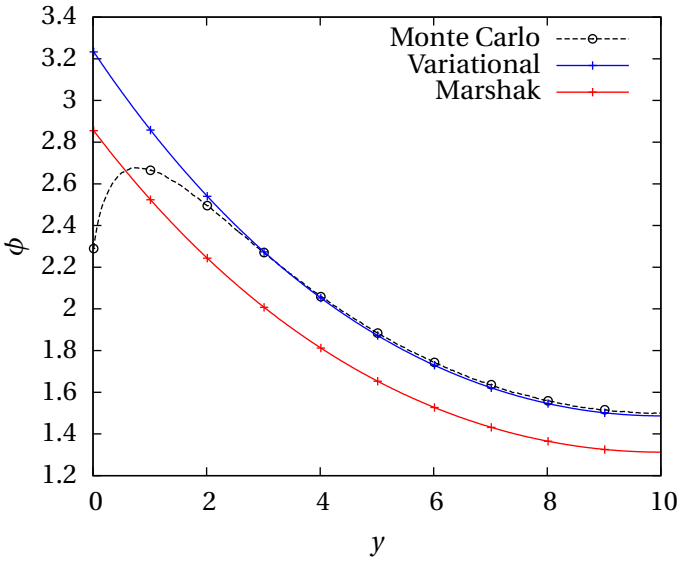

Figure 7.8: Scalar intensity with a normally incident boundary condition in a homogeneous flatland problem.

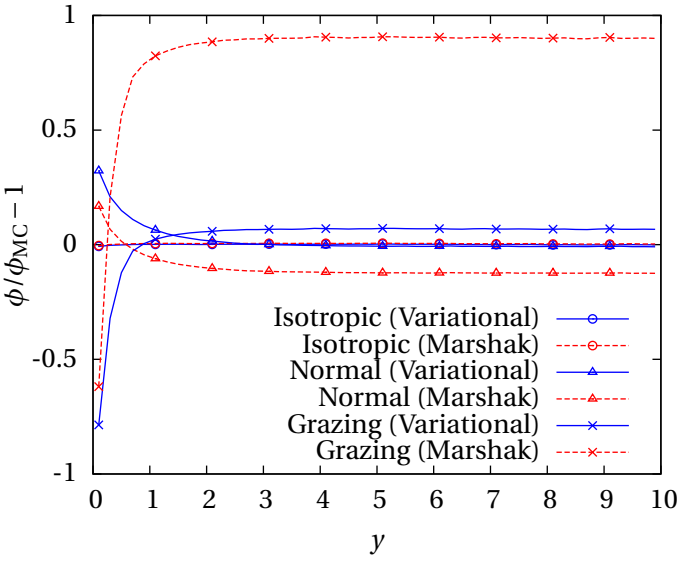

Figure 7.9: Relative errors ($\phi/\phi_{\mathrm{MC}} - 1$) of the three tested distributions.

7.3 Anisotropic diffusion boundary conditions

In Chapter 3, we derived boundary conditions for the anisotropic diffusion approximation. These boundary conditions reduce to the standard diffusion boundary condition in a homogeneous medium, but they were derived under a different set of asymptotic assumptions. We test the extent of their applicability using two steady-state flatland test problems similar to the previous voided channel test problem.

7.3.1 Interior source

The first test of the anisotropic diffusion boundary conditions is a highly scattering problem with a spatially smooth source in the interior. A vacuum boundary in the problem serves as the primary sink for particles in the problem; we therefore expect the global solution to be sensitive to the choice of boundary conditions.

Problem description

The test problem (Fig. 7.10) is similar to the above flatland boundary condition test

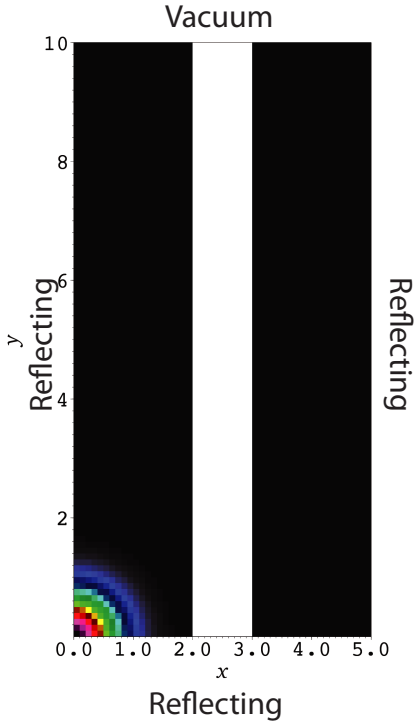

Figure 7.10: Steady-state AD boundary condition test problem. The black region is diffusive ($\sigma = 1$, $\sigma_s = 0.99$), the white region is optically thin ($\sigma = 0.01$, $\sigma_s = 0.0099$). The colored region in the lower-left is the Gaussian source.

problem. It features a diffusive medium in flatland on the domain $0 \le x \le 5$ and $0 \le y \le 10$, with a channel of unit width running vertically through the middle ($2.5 \le x \le 3.5$). The diffusive region has $\sigma = 1$ and $\sigma_s = 0.99$, and the channel has $\sigma = 0.01$ and $\sigma_s = 0.0099$. The bottom, left, and right boundaries are reflecting; the top is a vacuum boundary.

The source is an isotropic Gaussian-shaped radiation source in the lower-left corner:

$$q(x, y) = 2\,\mathrm{e}^{-2(x^2+y^2)}\,.$$

The spatial mesh has the grid spacing $\Delta_x = \Delta_y = 0.1$.

We compare a Monte Carlo solution, a diffusion solution, and three instances of anisotropic diffusion with different choices for the boundary condition on the vacuum boundary. Only two—the white and reflecting conditions—satisfy Eq. (3.34). The "naïve" boundary condition sets the incident values of f to zero and uses the Marshak diffusion boundary condition from Eq. (6.36). It serves to demonstrate the importance of using theoretically sound boundary conditions.

Results and discussion

First, we plot f (Fig. 7.11) at the top of the problem for the three alternative boundary conditions for the purely absorbing transport problem. (The polar plots of f are described in Fig. 7.12.) The effect of the boundary condition on f is straightforward: a reflecting boundary condition mirrors the angular distribution across the x axis, and a white boundary condition yields an isotropic distribution for incident angles. The naïve boundary condition is positive only for exiting angles. For the sake of comparison, the diffusion approximation $f(\boldsymbol{x}, \boldsymbol{\Omega}) = \frac{1}{2\pi\sigma(\boldsymbol{x})}$ could be plotted as a circle. (In Fig. 7.11a, it would be out of range of the plot.) Both the anisotropic diffusion tensor $\mathbf{D}$ and the boundary coefficient $\boldsymbol{d}$ change as a result of the boundary conditions.

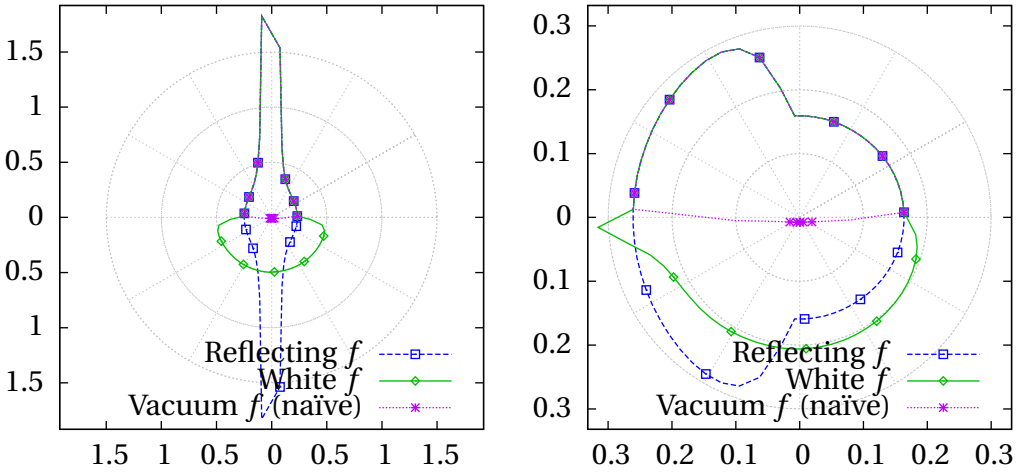

(a) $f(2.5, 10, \omega)$ **(b)** $f(1.5, 10, \omega)$

Figure 7.11: Polar plots of the purely absorbing transport solution at two points in at the end of the channel. The solution as a function of azimuthal angle ω is plotted (a) at the center of the channel (where f is the strongly anisotropic) and (b) further from material discontinuities (where f tends toward isotropy).

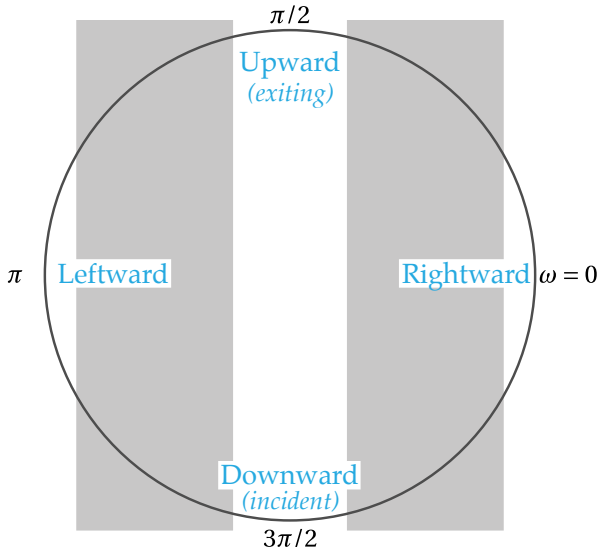

Figure 7.12: Cartoon describing the polar plots of f. The gray bars depict the location of the diffusive regions relative to the centerline of the channel. Directions near $\omega = \pi/2$ at $y = 10$ are exiting the problem; directions in $\pi \leq \omega < 2\pi$ are incident and therefore depend on the boundary conditions for f.

The different diffusion and boundary coefficients naturally cause the anisotropic diffusion solutions ϕ to differ. Figure 7.13 compares the three instances of anisotropic diffusion with the Monte Carlo reference solution and the diffusion solution.

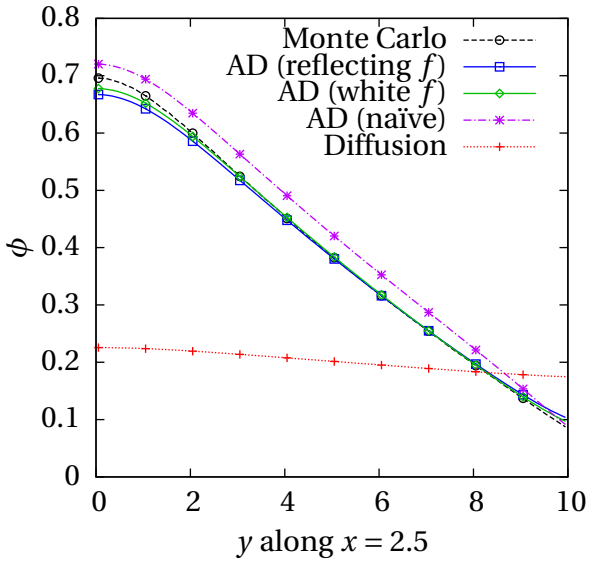

Figure 7.13: Scalar intensity in the steady-state interior source problem.

Clearly, anisotropic diffusion is superior to conventional diffusion for this problem: the solution differs from the reference solution by only a few percent globally. The two choices of boundary conditions for f consistent with Eq. (3.34), reflecting and white, produce very similar answers. In contrast, the inconsistent choice of a vacuum boundary for f introduces a significant global error, even many mean free paths away from the boundary.

To help understand the accuracy of anisotropic diffusion as compared to standard diffusion, we have plotted in Fig. 7.14 the angular intensity at several points in the problem as approximated by S_N, AD, and standard diffusion. Whereas standard diffusion approximates the radiation as linear in angle, anisotropic diffusion has much more *shape*, resulting from the (generally nonlinear) anisotropy in f. As we asserted in Chapter 3, this extra transport-derived information results in a more accurate approximation.

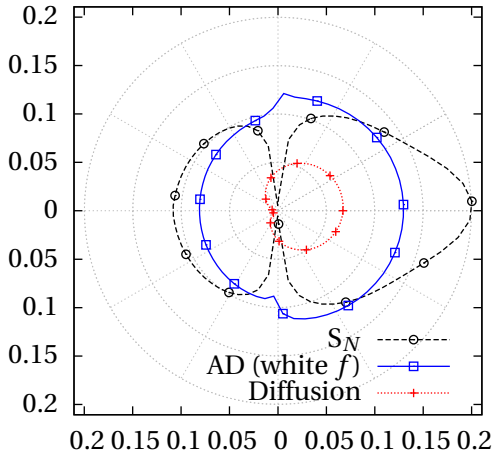

(a) $I(2.5, 0, \omega)$

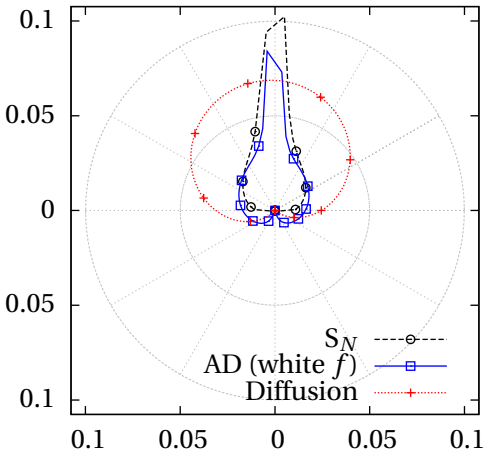

(b) $I(2.5, 10, \omega)$

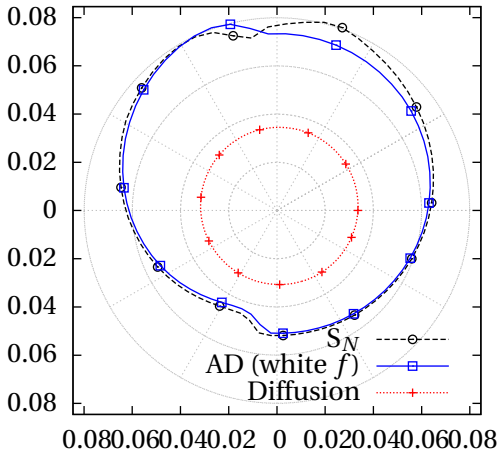

(c) $I(1.55, 5, \omega)$

Figure 7.14: Polar plots of the angular intensity in the channel. The intensity as a function of azimuthal angle ω is shown at (a) the bottom center, (b) the top center, and (c) the middle left edge.

7.3.2 Boundary source

The problems with an incident particle flux on the boundary potentially have strong gradients and anisotropy outside the applicable range of the anisotropic diffusion approximation. As an alternative test of the boundary conditions, we consider three boundary source–driven problems.

Problem description

This test problem has opacities identical to the previous problem: two diffusive regions surround an optically thin channel. However, rather than being driven by an extraneous source, the problem has an incident radiation flux on the bottom face. The top, left, and right sides are reflecting. We consider the same incident angular distributions as in §7.2, given in Table 7.2: an isotropic source, a normally-incident source, and a grazing source.

Results and Discussion

Figure 7.15 shows a line-out of the scalar intensity $\phi(2.5, y)$ along the center of the channel in the isotropic incident case. Standard diffusion fails because $\sigma = 0.01$ leads to a large diffusion coefficient, resulting in a nearly constant solution inside the channel. Anisotropic diffusion performs quite well, and the white boundary condition for f gives a more accurate result than the reflecting boundary condition. (The naïve boundary condition, as discussed in the previous test problem, is inaccurate.)

The AD approximation and its boundary conditions do have their limits. In the case of a strongly anisotropic boundary source, the ansatz that $\boldsymbol{F} = O(\epsilon)$ is violated in swaths of the problem, so the solutions for the normal and grazing boundary conditions have large errors (Fig. 7.16).

A visualization of the angular intensity for each method (replacing Monte Carlo with an S_N solution), Fig. 7.17a, helps explain the accuracy of the AD method and the difference between the reflecting and white boundary treatments. Even though AD cannot exactly model the peak of freely streaming photons in the channel (which the S_N angular intensity shows at $\omega = 3\pi/2$), it accurately approximates the shape driven by scattering from the diffusive region (the lobes on the left and right) in the isotropic incident case. In the strongly anisotropic (normal incident source) case, where uncollided particles from the boundary dominate the scattered particles, anisotropic diffusion cannot accurately approximate the particle distribution in the channel. The linear-in-angle diffusion approximation cannot represent any of these features.

The shape around $\omega = \pi/2$ gives insight into why the white boundary performs slightly

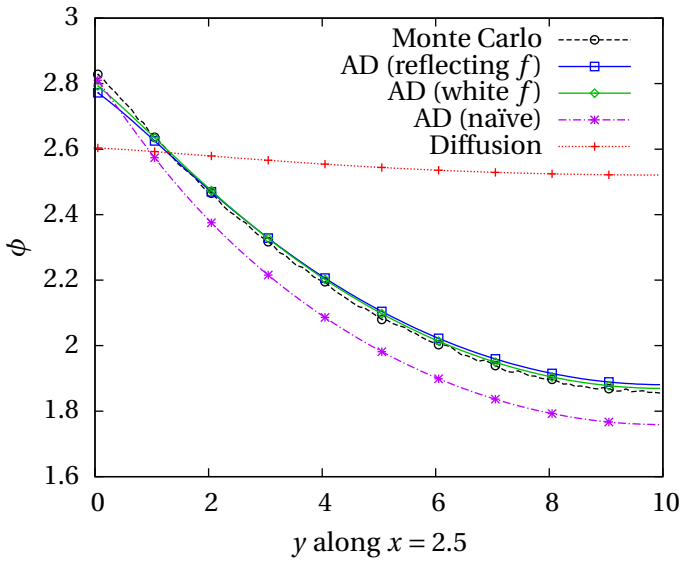

Figure 7.15: Scalar intensity along the centerline of the channel with an isotropic boundary condition at $y = 0$.

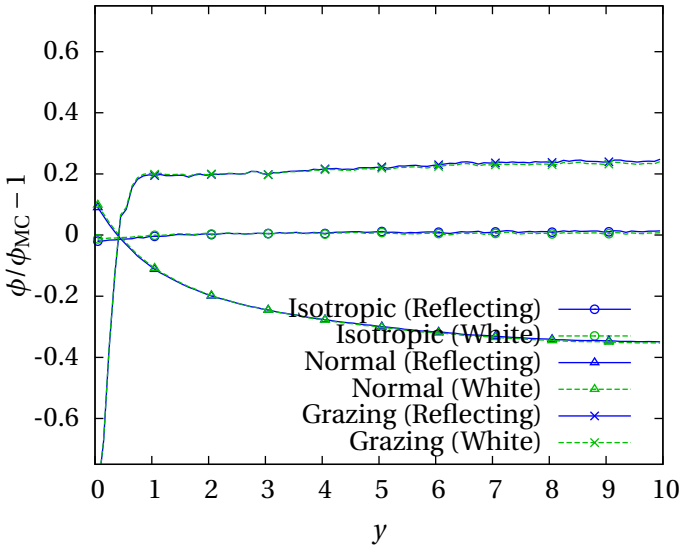

Figure 7.16: Relative errors along the centerline of the channel with the three different incident boundary conditions.

better in the case of an isotropic incident boundary condition: a reflecting boundary produces a peak in f along the channel, but a white boundary gives a more isotropic shape near that range, better matching the incident isotropic boundary condition. This suggests that the qualitatively best way to satisfy Eq. (3.34) may be to require the incident distribution of f to take the shape of the true boundary condition.

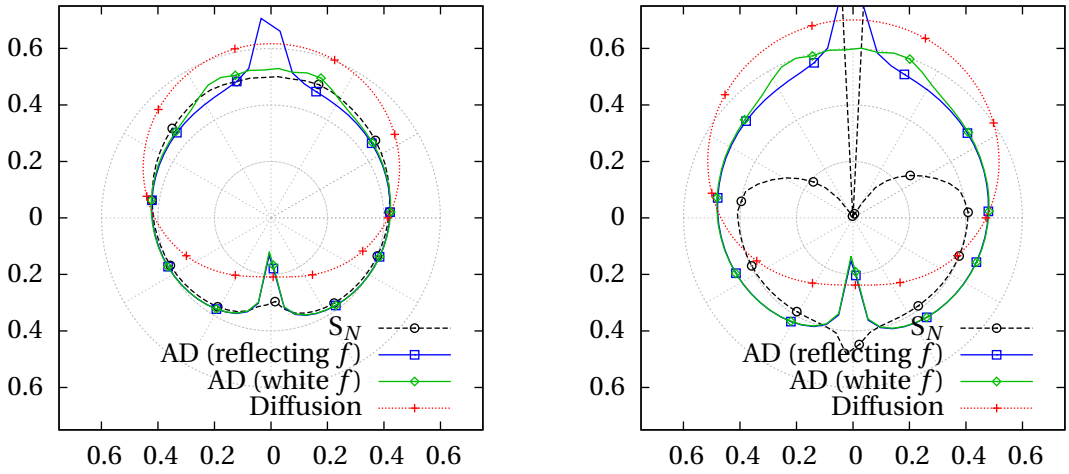

(a) Isotropic

(b) Normal

Figure 7.17: Angular intensity $I(2.5, 1, \omega)$ in the incident boundary source problem. The isotropic (a) and normal (b) incident cases are plotted in the centerline of the channel, one unit from the boundary.

7.4 Smooth time-dependent problem

Before testing the new time-dependent anisotropic diffusion methods in nonlinear thermal radiative transfer problems, we examine their behavior in a more simple situation: linear, time-dependent problems with time-independent opacities.

In this first time-dependent problem, we expect the temporal and spatial gradients to be moderate but significant enough to distinguish diffusion from transport.

7.4.1 Problem description

This smooth problem features a unit source in the bottom left corner of a highly scattering medium of width 2 with $\sigma = 1$ and $\sigma_s = 0.99$. A voided region with width 0.5, $\sigma = 0.01$, and $\sigma_s = 0.0099$ lies along the right edge of the problem. The bottom, left, and right boundaries are reflecting; the top of the problem has a vacuum boundary. The problem's initial condition is uniformly zero, and the particle speed is unity ($c = 1$).

Because this problem is time-dependent, it is the first test of the anisotropic P_1 method devised in Chapter 4. This method uses not only the anisotropic diffusion tensors $\mathbf{D}$ but also a nonlocal opacity ς, as formulated in (4.20):

$$\frac{1}{c}\frac{\partial \boldsymbol{F}}{\partial t}(\boldsymbol{x}, t) + \varsigma(\boldsymbol{x})\mathbf{D}(\boldsymbol{x}) \cdot \boldsymbol{\nabla}\phi(\boldsymbol{x}, t) + \varsigma(\boldsymbol{x})\boldsymbol{F}(\boldsymbol{x}, t) = 0\,.$$

Figure 7.18 overlays these transport-calculated coefficients on the problem's physical description.

In this figure, the anisotropic diffusion tensors are plotted as ellipses. Each ellipse's major axis lies along the principal eigenvector of $\mathbf{D}$, and the size along that axis is proportional to the corresponding eigenvalue. The minor axis is proportional to the second eigenvalue of the tensor. If f is isotropic, $\mathbf{D}$ is proportional to the identity tensor, and its two eigenvalues are equal: thus, in the interior, the anisotropic diffusion coefficients appear as circles whose sizes are proportional to $1/\sigma$. In the channel, where f is strongly anisotropic, the ellipses show that the primary action of the diffusion tensor is along the channel.

7.4.2 Results and Discussion

The large phase space of time-dependent transport forces us to carefully choose representative metrics. We use contour plots to compare select methods at select times, lineouts to compare more methods in greater detail, and wavefront plots to visualize the detailed time evolution of the problem.

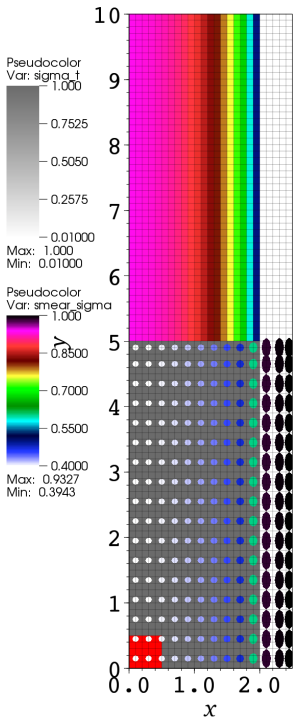

Figure 7.18: Time-dependent smooth problem properties. The source region is the red square in the lower-left; the grey and white area in the bottom half shows σ, the colored region above shows $\varsigma = 1/\int_S f \, \mathrm{d}\Omega$, and the ellipses are a visualization of the diffusion tensor $\mathbf{D} = \int_S \mathbf{\Omega\Omega} f \, \mathrm{d}\Omega$.

The behavior of ϕ along the center of the channel (i.e., at the right edge of the problem) is plotted in Fig. 7.19. Anisotropic diffusion and conventional diffusion, which both assume a quasi-static problem, are significantly less accurate and are not plotted in that figure. Their more accurate flux-limited counterparts, FLAD and FLD, are shown instead.

None of the low-order methods exactly reproduces the transport solution. Even with flux limiting, FLD and FLAD overestimate the rate of particles flowing into the void. However, as the problem tends toward steady-state, the anisotropic methods become relatively accurate. (We recall that both FLAD and AP_1 limit to the AD method when the solution varies slowly in time.)

As one diagnostic, we plot the "wavefront" positions—determined by the location at which $\phi = 0.001$ after applying a small amount of smoothing—for all of the methods in Fig. 7.20. These plots again show how FLAD and AD both overestimate the scalar

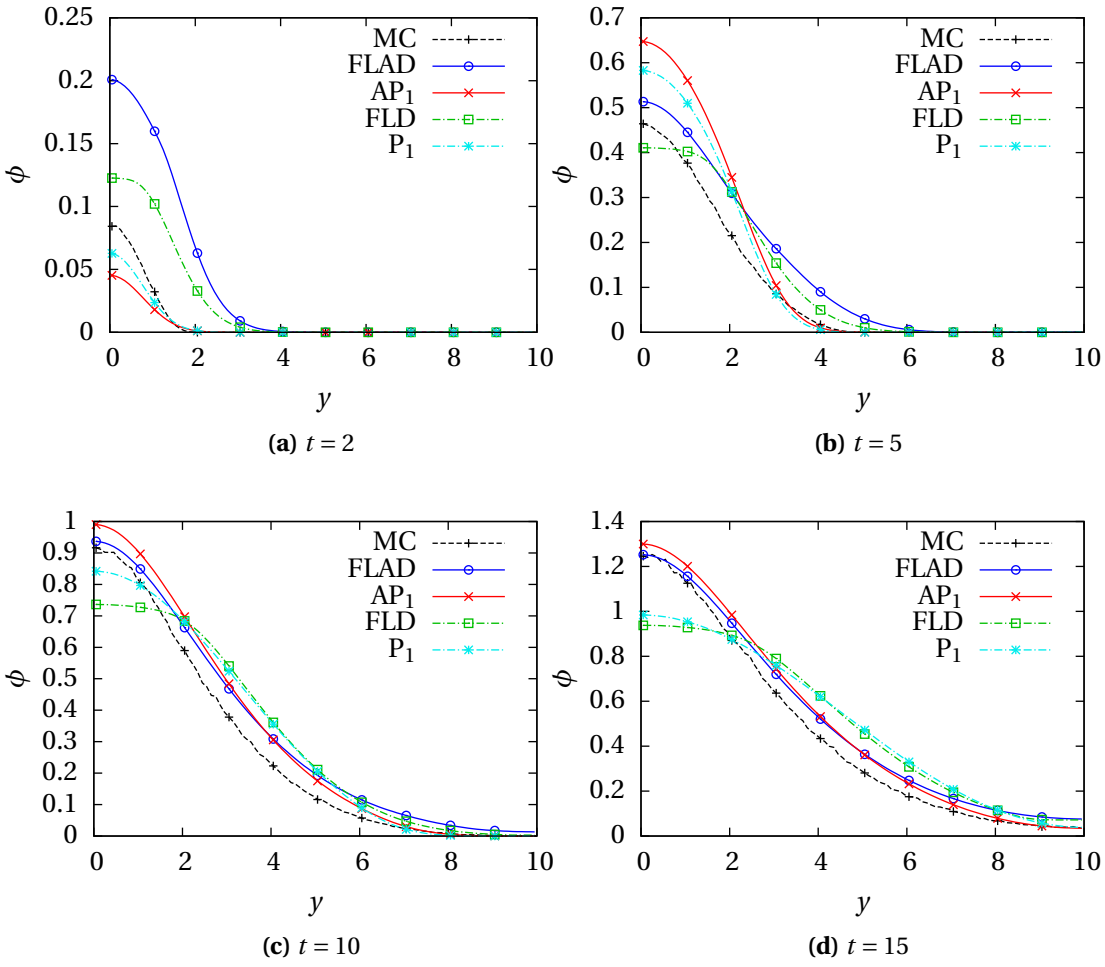

Figure 7.19: Scalar intensity ϕ along the centerline of the channel, $y = 2.5$.

intensity at early times, and they also point to an explanation. Because the flux limiters are not iterated upon, the solution of the first time step is the same as the standard diffusion solution. (In Fig. 7.20b, the flux-limited and standard diffusion methods share a starting point.) As a result, the flux-limited methods carry that artifact of non-flux-limited particles for all later time steps. To obviate this error, shorter initial time steps (in which the effective time absorption $1/c\Delta_t$ reduces the magnitude of the precursor) could be used. Alternatively, the nonlinear flux-limited diffusion coefficient could be converged.

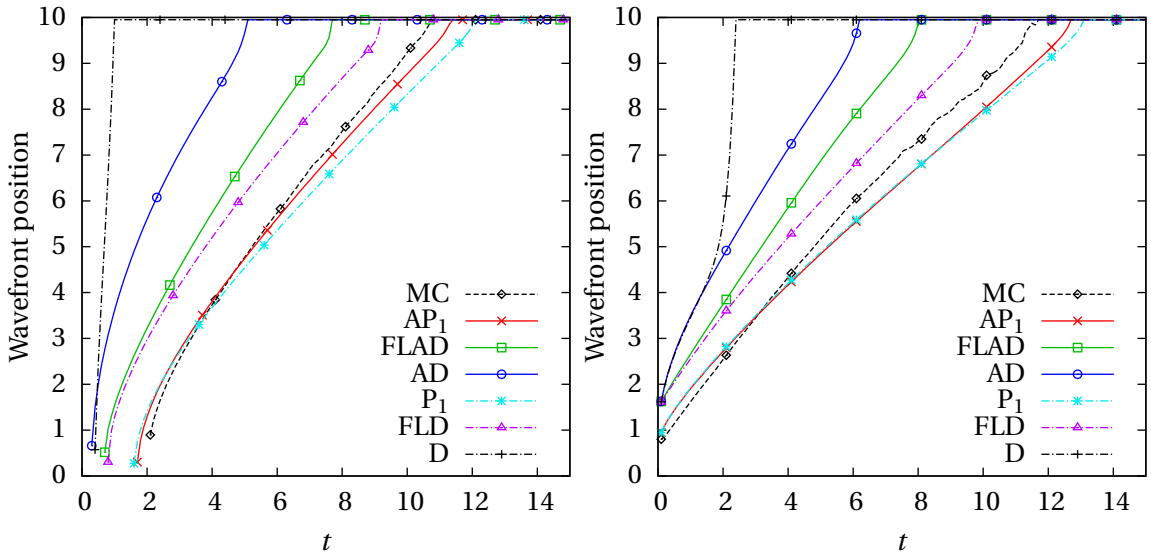

(a) Channel, $x = 2.5$ **(b)** Medium, $x = 0$

Figure 7.20: Wavefront position along the y axis.

A contour plot showing the difference between P_1 and AP_1 is given in Fig. 7.21. The AP_1 solution is generally more accurate than P_1. As the system evolves in time, it becomes like the steady-state channel problems analyzed earlier: diffusion (the steady-state limit of P_1) fails in these problems, so it is unsurprising that AP_1 outperforms P_1 at late times.

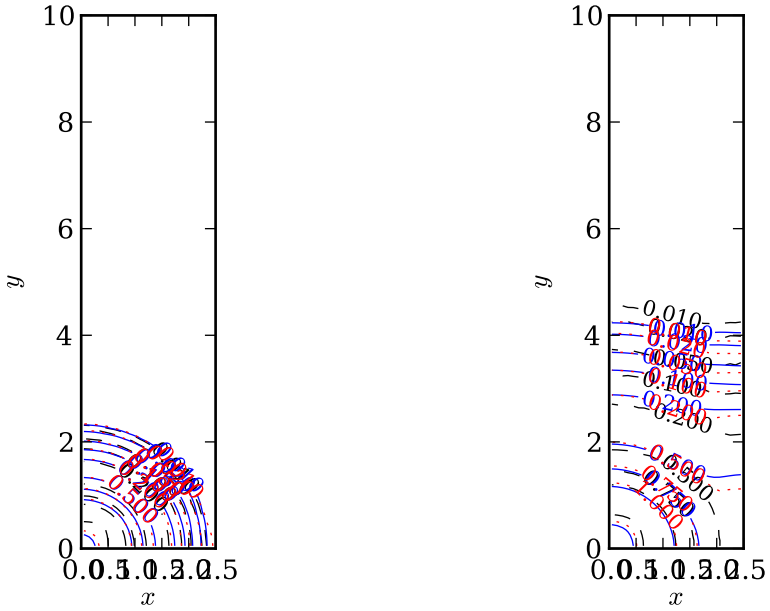

(a) $t = 2$

(b) $t = 5$

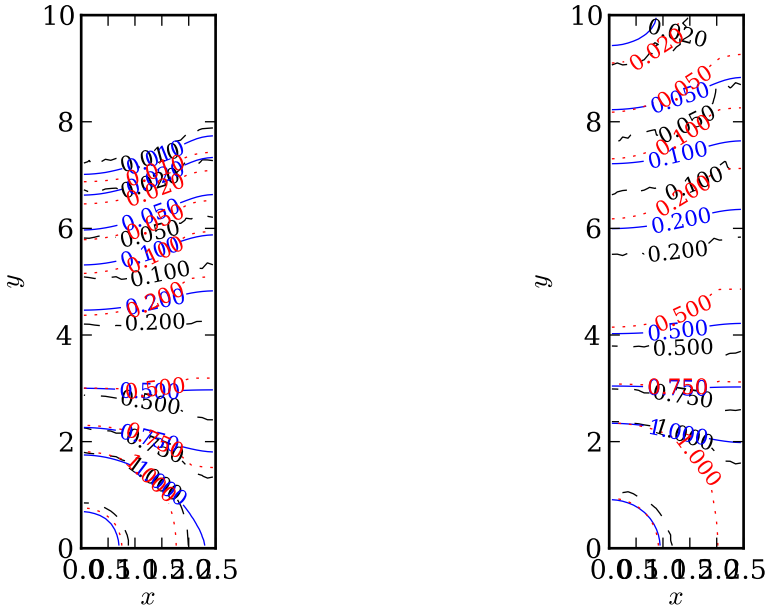

(c) $t = 10$

(d) $t = 15$

Figure 7.21: Contour plots of the scalar intensity at four times. The black dashed line is the Monte Carlo solution, the blue solid line is the AP_1 solution, and the red dotted line is the P_1 solution.

7.5 Time-dependent blast wave

Thermal radiative transfer problems often contain strong spatial and temporal gradients. We consider a more stressful test of the different anisotropic approximations to the transport equation.

7.5.1 Problem description

The "blast wave" test problem (Fig. 7.22) features a localized impulse of radiation; the magnitude of the coefficients and the initial condition is based on a recurrent test problem in the field of thermal radiative transfer [39, 40, 8, 52]. The domain of this problem is $0 \le x \le 3$ and $-1.1 \le y \le 1.1$. It features an optically thin channel with $\sigma = 1$ and $\sigma_s = 0.99$ inside $-.1 \le y \le .1$, with a diffusive region $\sigma = 10$ and $\sigma_s = 9.99$ outside it. All boundaries are specularly reflecting.

The initial condition is a local but smooth Gaussian function:

$$\phi^i(x,y) = 0.001 + 100\,\mathrm{e}^{-100(x^2+y^2)}\,.$$

We use a grid spacing of $\Delta_x = \Delta_y = 0.02$, and a uniform time step $\Delta_t = 0.02$. As in the previous problem, the particle speed is $c = 1$.

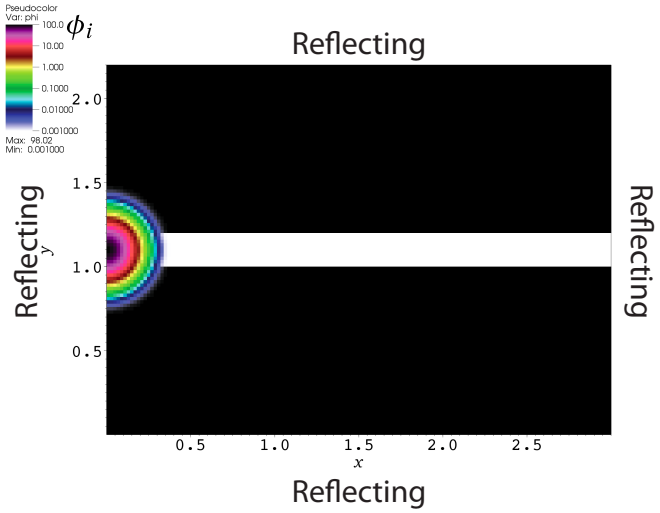

Figure 7.22: Opacities and initial condition for the blast wave problem. The colored region is the isotropic initial condition ϕ_i.

7.5.2 Results and Discussion

The isotropic initial condition is the only source of particles in this problem. Because a majority of them are born in the optically thin channel, those with directions close to the $+x$ axis will tend to stream down the channel uncollided. This is the *hyperbolic* behavior of the transport equation: when σ and sources are small, the Boltzmann equation reduces to a wave equation. Particles that enter the medium diffuse: this is *parabolic* behavior. The transport solution can be viewed as a combination of the hyperbolic and parabolic solutions.

The final state ($t = 3$) of the problem is plotted in Fig. 7.23. Several features characteristic of the methods are apparent. First, only the transport solution (Monte Carlo) contains the peak of uncollided particles at $x = 3$. Aside from that peak, the particles that have undergone multiple collisions, the anisotropic diffusion methods all match reasonably well. In this particular problem, flux-limited anisotropic diffusion is the most accurate. The P_1 method fails even to produce a positive solution: this is a known limitation of the method in multi-dimensional problems with strong spatial and temporal gradients. Interestingly, the AP_1 solution is markedly better. The smoothness of $\mathbf{D}$ and ς as compared to $1/3\sigma$ and σ presumably obviate the strain on the wavelike behavior of the problem.

The time-dependent behavior of the transport solution (MC) and flux-limited anisotropic diffusion (FLAD) is shown in Fig. 7.24. At longer times, the FLAD solution ap-

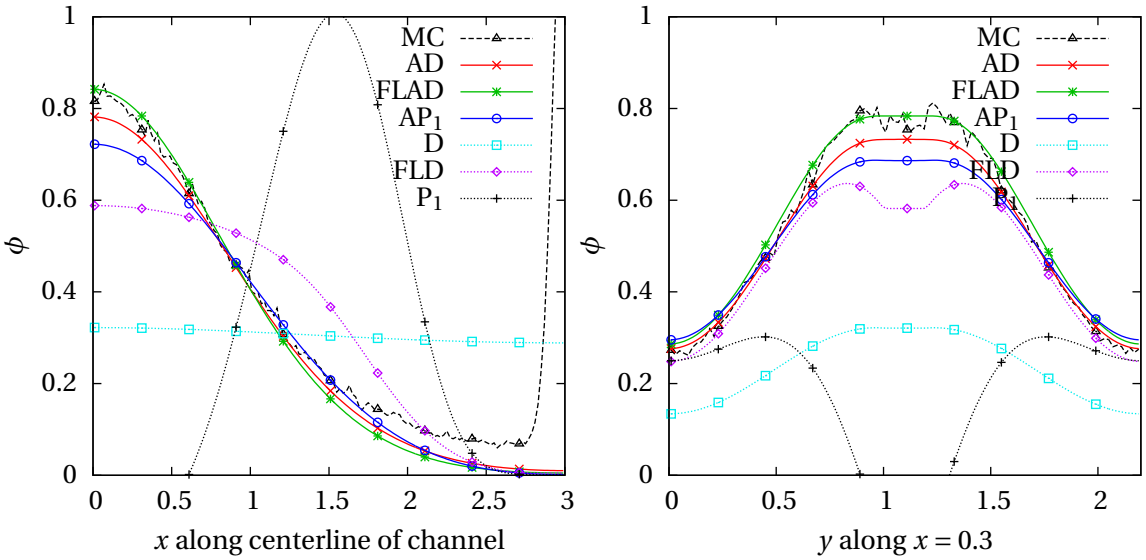

(a) Along center **(b)** Orthogonal view

Figure 7.23: Scalar intensity at $t = 3$ in the blast wave problem.

proaches the MC solution away from the uncollided pulse of particles.

Because the diffusion equations are inherently parabolic, they cannot capture the behavior of the uncollided particles seen in the Monte Carlo solution. However, the hyperbolic (diffusive) behavior is modeled more accurately with the AD methods than with conventional diffusion methods. As we have seen in the previous test problems, the linear-in-angle approximation of standard diffusion is wholly inadequate in the interior of the channel, leading to an inaccurate solution.

The timings for the blast wave problem, as run on a single core of a 2.4 GHz Intel Core 2 Duo chip, are presented in Table 7.3. These give a rough idea of the relative performance

	Wall time (s)
MC	790
AP_1	31
FLAD	40
AD	38
P_1	23
FLD	18
Diffusion	18

Table 7.3: Timing comparison for the blast wave problem.

of the standard diffusion methods, the anisotropic diffusion methods, and the transport method. The initial calculation of the anisotropic diffusion coefficients is amortized over

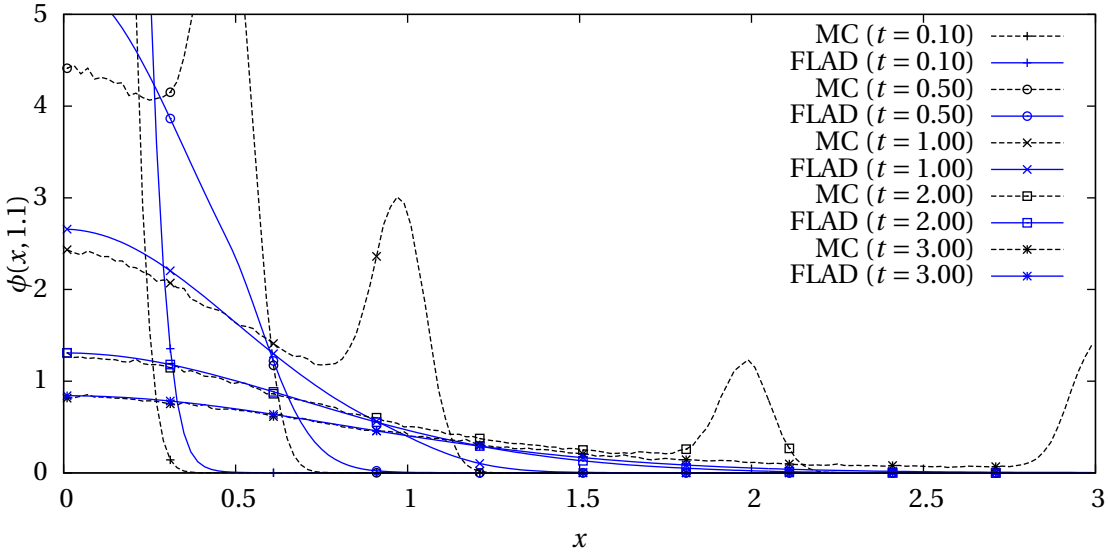

Figure 7.24: Comparison of Monte Carlo and flux-limited anisotropic diffusion at four times in the blast wave problem.

the subsequent time steps, so over longer times, the performance of the AD methods asymptotically approaches the performance of the standard diffusion methods.

7.5.3 Extended problem parameter space

To quantitatively verify that the positive results in this problem are not accidental, we parameterized the problem and extensively investigated the parameter space. Using Latin Hypercube Sampling [74], we sampled 40 instances of the above problem with the following parameters and corresponding distributions:

- the width of the diffusive region (uniform on $[0,2]$);
- the width of the channel region (uniform on $[0,1]$);
- the sharpness of the Gaussian (exponential with $\lambda = 100$);
- the value of σ in the diffusive region (uniform on $[1,20]$); and
- the value of σ in the channel region (exponential with $\lambda = 0.1$).

As a metric of error, we compared the volume-weighted 2-norm error (with the reference solution being a Monte Carlo simulation using 10^6 particles) along the channel centerline and a cross-section of the problem at $x = 0.3$ at the final problem time. (Other metrics yielded similar results.)

The error distributions are plotted in Fig. 7.25. Distributions more peaked toward the

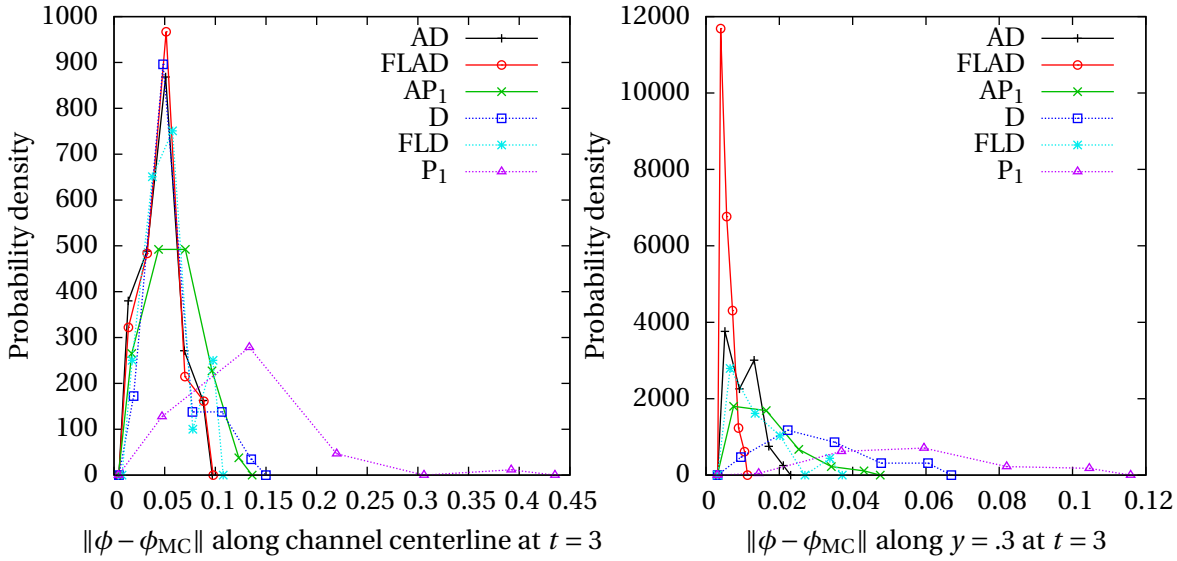

(a) Channel centerline

(b) Orthogonal line

Figure 7.25: Distributions of errors in the parameterized blast wave problem. The FLAD solutions are consistently accurate; the P_1 solutions are inaccurate with a wide range of inaccuracy.

left of the plot are more accurate, and wider distributions indicate a method inconsistent in its accuracy. As one might expect from the detailed discussion of one instance of the blast wave problem, flux-limited anisotropic diffusion is the most accurate, and P_1 is the least accurate.

7.6 Conclusions

We have established and tested some approximations that undergird the rest of our results. First, we ensured that non-analytic (discrete ordinates–calculated) AD coefficients do not compromise the accuracy of the method. We also demonstrated that the number of sweeps required to converge a transport-calculated f is small enough to make an AD solution competitive.

With the linear numerical experiments in this chapter, we have verified the theory developed in the previous chapters. The boundary conditions we proposed for anisotropic diffusion in Chapter 3 yield accurate answers for our test problems in which the radiation is not strongly anisotropic throughout the problem. The boundary conditions for flatland diffusion were also successfully tested.

Finally, we performed the first test of time-dependent anisotropic diffusion. In a wide variety of problems with optically thin channels, the anisotropic diffusion methods (particularly flux-limited anisotropic diffusion) outperformed their conventional counterparts.

With these encouraging results for linear, time-dependent problems, we move to more difficult nonlinear problems in Chapter 8.

Chapter 8

Numerical Results: Thermal Radiative Transfer

Thermal radiative transfer (TRT), as we discussed at length in Chapter 2, adds complexities beyond the already substantial difficulties of particle transport. The radiation source term is coupled to a material temperature unknown, and the material's changing temperature modifies the absorption opacity. These nonlinearities require special treatment (semi-implicit linearization, in our work), and they mean that the problem's physical properties are time-dependent. For the anisotropic diffusion methods, this imposes the extra requirement that the diffusion coefficients be recalculated at every time step.

In this chapter we test a wide range of TRT problems, beginning with diffusive 1-D problems that contain temperature-dependent opacities. In addition to testing multi-D problems with optically thin channels, we compare the performance of the anisotropic methods against conventional methods using standard 2-D TRT benchmark problems.

Most of the methods we compare are described at the start of Chapter 7, but the following methods need further discussion when applied to TRT.

Monte Carlo is replaced by Implicit Monte Carlo [23]. Our implementation uses implicit absorption, source tilting, census combing, and energy-weighted path length tallies [24]. Each problem uses roughly 10^7 particles per time step.

Anisotropic methods Because the opacity is a time-dependent quantity in TRT, the anisotropic diffusion coefficients must be recalculated at every time step. The first time step uses up to 100 source iteration sweeps[1] to calculate the coefficients, but each time step thereafter uses only one sweep to update them. (Because the transport problem for f is purely absorbing, one sweep is sufficient to converge the diffusion coefficients in the interior.)

P_1-like methods A known shortcoming of P_1 is that, in multidimensional geometry with steep gradients, the radiation can have a negative solution [48]. To prevent

[1] This is a *very* conservative number; as the previous chapter showed, two or three iterations are sufficient.

unphysical negative temperatures, we "fix" non-positive values for the radiation by setting them to 10^{-16}, violating conservation by adding energy to the problem.

8.1 1-D blast wave

We begin by testing a simple one-dimensional slab geometry problem on a refined spatial and temporal grid. The anisotropic diffusion approximation is less meaningful in 1-D: the rank-2 tensor becomes a scalar. Nevertheless, the AD coefficient is still nonlocal and distinct from the standard diffusion coefficient.

The classic Marshak wave [15] is a feature of radiative transfer at the boundaries between hot and cold materials. Because the cold material tends to be optically opaque, radiation emitted from the hot material penetrates only a short distance into the cold, rapidly heating it. As that layer of cold material heats up, it begins to emit into the adjacent cold layer: the result is a distinct radiation shock that looks like a wave. (Because the radiation behavior tends to be diffusive rather than streaming, this wave does not travel at the speed of light.)

This 1-D test problem does not create a "classic" Marshak wave: rather than a constant incident radiation boundary, it contains a large pulse of energy as an initial condition. Yet the resulting qualitative behavior strongly resembles a Marshak wave, since the pulse penetrates the colder material and heats it up progressively.

Higher-dimensional geometries also have Marshak wave–like behavior, so the features observed in this one-dimensional problem serves as a useful introduction to the behavior of the different methods tested.

8.1.1 Problem description

This "diffusive" test problem has been used to assess the performance of flux limiters and nonlinear convergence schemes [8, 52]. It features a smooth but localized energy peak as an initial condition in both the material and the radiation:

$$\phi(x,0) = [acT(x,0)]^4 = 0.001 + 100\,\mathrm{e}^{-100x^2}.$$

The material is uniform with a constant heat capacity $c_v = 1$ and a temperature-dependent opacity $\sigma(T) = T^{-3}$. We use a uniform spatial and temporal grid of $\Delta_x = \Delta_t = 0.01$. The boundaries at $x = 0$ and $x = 3$ are reflecting.

The problem uses a scaled unit system often seen in TRT methods development: $c = a = 1$. The anisotropic diffusion coefficients are calculated with a Gauss–Legendre

S_{16} quadrature set and the step characteristics method.

8.1.2 Results and discussion

The wavefront position (Fig. 8.1) provides an effective visualization of the problem's time evolution. The position is calculated at each point in time by taking the radiation temperature, convolving it with a weighted five-point kernel to smooth out potential noise in the solution, and using linear interpolation to find the point at which the radiation temperature is twice the initial temperature of the problem.

We note how Fig. 8.1 shows that, during the streaming-dominated early times, both standard diffusion and anisotropic diffusion display an unphysical wave speed. For these methods, the slope of the wavefront position near $t = 0$ exceeds $c = 1$: energy is transferred through the system faster than the speed of light. This shortcoming motivated the development of both flux-limited diffusion (§2.3.4) and our flux-limited anisotropic diffusion (§3.3). Both the standard P_1 and anisotropic P_1 are wave equations, but they have the incorrect wave speed of $c/\sqrt{3}$.

A detailed view of the radiation and material temperatures (Fig. 8.2) at $t = 3$ gives further insight into the differences between the methods. Both P_1-like methods share a characteristic, unphysical wavefront shape that results from the equations' hyperbolic nature. The radiation pulse at the beginning, with its steep spatial gradients, induces a wave-like pulse of particles that travel through the problem. The AP_1 approximation, because it uses a non-local ς [see Eq. (4.20)] rather than a local σ, is smoother: the

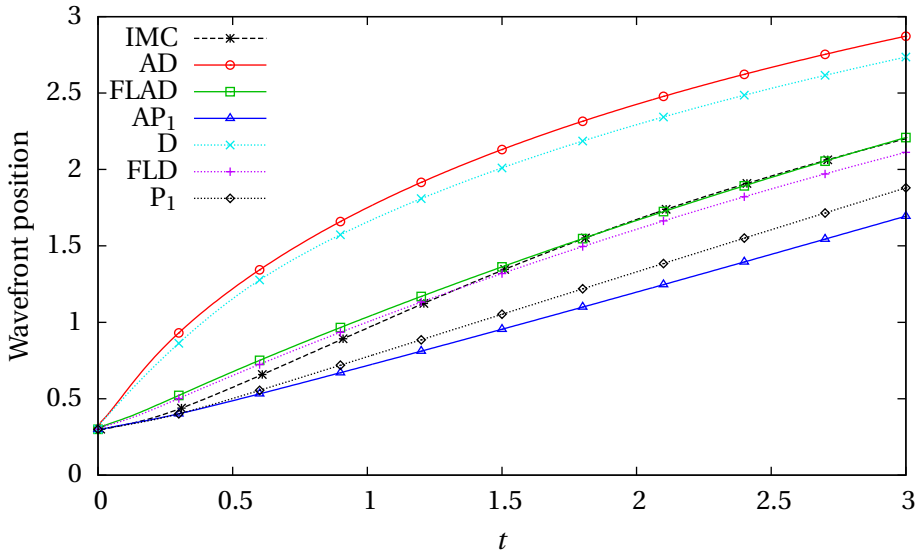

Figure 8.1: Wavefront position of ϕ in 1-D blast wave problem.

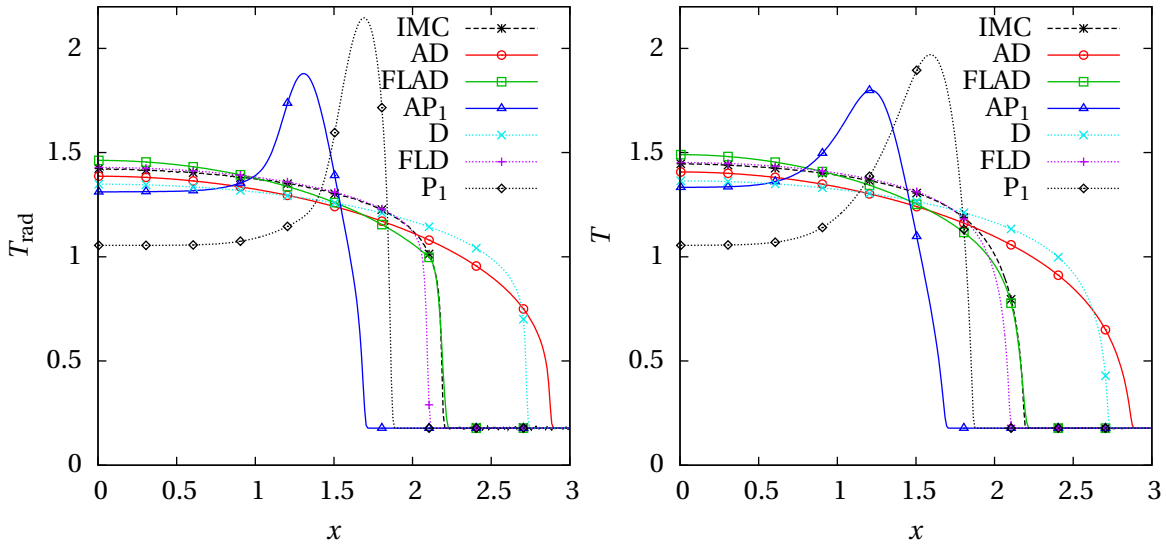

(a) Radiation temperature

(b) Material temperature

Figure 8.2: Solution at $t = 3$ in the 1-D blast wave problem.

wavefront's "hump" is not as peaked, but the larger ς slows the propagation of energy compared to P_1.

Flux-limited diffusion matches the transport solution very closely in this problem: the gradients in the interior are small, the radiation is predominantly isotropic, and the difficulties with streaming are overcome by the flux limiter. However, at later times, the wavefront drops off more abruptly than the transport solution because the limiter reduces the diffusion coefficient too far.

Flux-limited anisotropic diffusion better matches the wavefront position and shape of the transport solution. However, near $x = 0$, the temperature is too high: the AD coefficients are smaller than the diffusion coefficients because of their nonlocal nature, so the radiation behind the wavefront tends to be less homogeneous than in the standard FLD solution.

Overall, in this simple problem, the flux-limited methods match the transport solution most closely. (The problem was, after all, constructed to test the relative performance of flux-limited diffusion.) The standard diffusion and AD methods allow radiation to travel too quickly through the problem, resulting in wavefront positions unrealistically deep into the problem. The P_1-like methods fail to match even the qualitative shape of the solution.

8.2 Flatland pipe

For most transport approximations, the extension from one to multiple spatial dimensions is nontrivial. In the case of anisotropic diffusion, as we saw, the diffusion coefficient becomes a diffusion tensor, necessitating new discretization schemes. At the same time, the added complexity inherent to anisotropic diffusion gives it an advantage relative to standard diffusion.

The practical extension of flux-limited diffusion to multi-D is straightforward, but the theory is less sound: most flux limiters are derived under the assumption of 1-D radiation behavior. In multiple dimensions, the anisotropic diffusion methods may become more advantageous relative to FLD because their smaller diffusion coefficients reduce the necessity for flux limiting.

8.2.1 Problem description

Our first multi-D test problem for thermal radiative transfer is loosely based on the problem of interest to the Center for Radiative Shock Hydrodynamics (CRASH) program: radiation travels down an optically thin channel with optically thick walls. We use the same unit system as in the 1-D test problem, $c = a = 1$.

As represented in Fig. 8.3, this flatland problem consists of:

- a radiation source region (red) with an energy emission rate density $q_r = 25$, a constant opacity $\sigma = 0.5$, and a constant heat capacity $c_v = 0.5$;
- a small channel region (white) with $\sigma = T^{-3}$ and $c_v = 1.0$; and
- a diffusive region (gray) with $\sigma = 25T^{-3}$ and $c_v = 2.5$.

The physical properties of the channel are the same as those in the 1-D test problem.

The time step is piecewise linear: it increases from $\Delta_t = 0.002$ at $t = 0$ to $\Delta_t = 0.02$ at $t = 0.1$, and stays constant thereafter. (Keeping the time step small at the beginning is a technique used to improve the performance of the flux limiters and reduce the linearization error during the initial strong temperature gradients.) The mesh size used is $\Delta_x = \Delta_y = 0.02$. The initial condition is uniformly $\phi = T^4 = 0.001$, and the problem is run until time $t = 3$. The left problem boundary is reflecting, and the others are vacuum.

8.2.2 Results and discussion

The constant radiation source at the left end of the channel drives the problem. At the beginning, the entire domain is optically thick (even the channel has the initial opacity $\sigma = 0.001^{-4/3}$), but it quickly heats up as it absorbs radiation from the source. As the

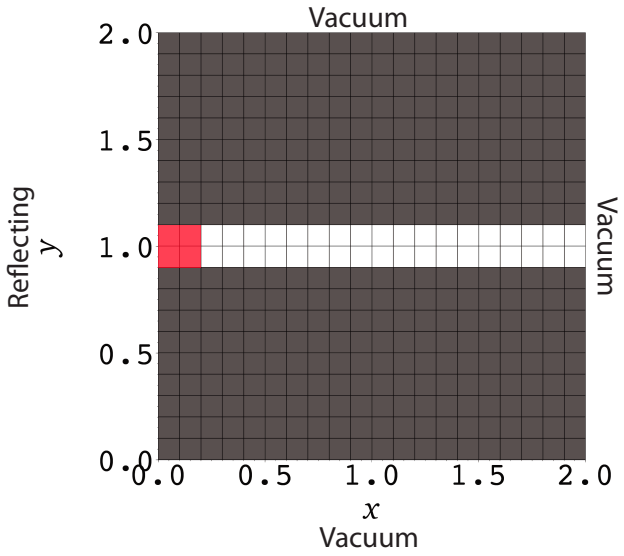

Figure 8.3: Materials, geometry, and grid spacing in the flatland pipe problem. Each "cell" shown on the grid encompasses 5×5 cells in the actual numerical simulation. The red zone is the radiation source, the white zone is the channel, and the gray zone is the diffusive region.

material's temperature rises, the material becomes optically thinner: the lower heat capacity and optical thinness of the channel cause it to become transparent more quickly than the surrounding region. Energy flows readily from the radiation source through the channel, and less readily from the channel into the diffusive region.

Two lineouts of the material temperatures at the final state are plotted in Fig. 8.4. The standard diffusion approximation performs poorly: like the previous 1-D problem, it allows energy to move too quickly. Yet, unlike in the 1-D problem, standard flux-limited diffusion also performs poorly. As seen by comparing the centerline (Fig. 8.4a) and orthogonal (Fig. 8.4b) views, flux-limited diffusion artificially constrains the movement of energy into the surrounding opaque materials, preferring instead to heat the channel and further propagate energy in that direction. This is not entirely unexpected: flux limiters cannot approximate the full angular dependence of the intensity; they only restrict the flow of energy *based on the local spatial gradients*. The gradient at the cold–hot material interface in the diffusive material is strong, so the flow of radiation is limited.

Compared to the conventional methods, the new anisotropic methods perform quite well. Their differing behavior can be better understood by viewing the magnitude of the diffusion coefficients and anisotropic diffusion tensor. Figure 8.5 shows the diffusion coefficients of FLAD, FLD, and standard diffusion at the final state. (The components of the FLAD tensor are plotted separately.) The anisotropic diffusion tensor remains consistently smaller than the diffusion coefficients, slowing down the radiative transfer

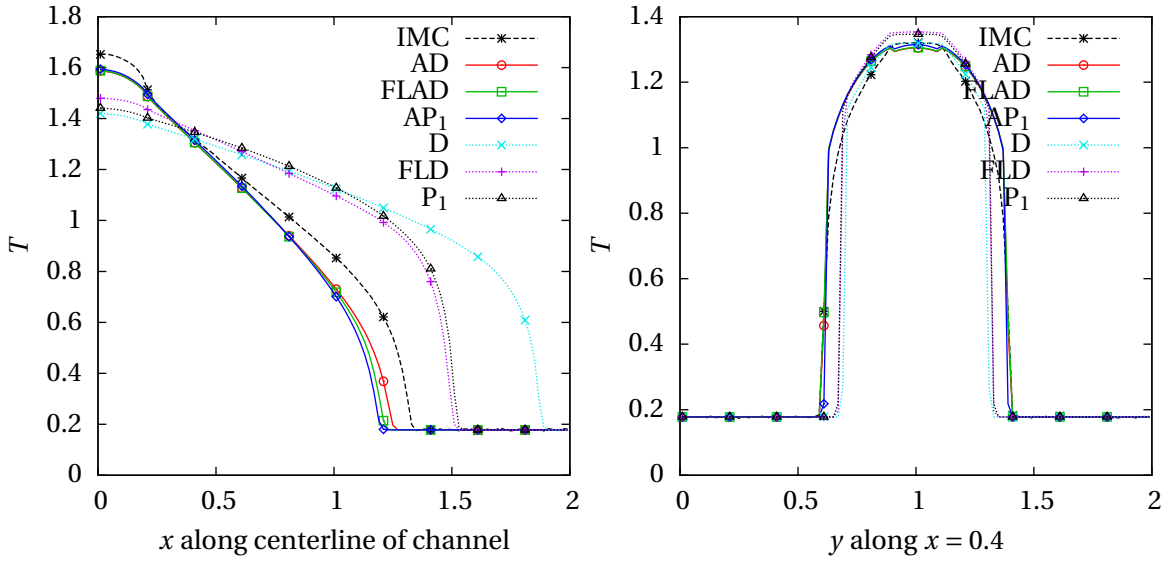

(a) Centerline view

(b) Orthogonal view

Figure 8.4: Material temperature at $t = 3$ in the flatland pipe problem.

even compared to flux-limited diffusion. We also note that in most of the problem, the off-diagonal component of the AD tensor D^{xy} is much smaller than the corresponding D^{xx} and D^{yy} components: the temperature-dependent opacity in the problem is nearly symmetric about the line $y = 1$, so this is not unexpected.

The anisotropy of the problem is plotted in Fig. 8.6. This metric is defined by:

$$\text{anisotropy} = \frac{|\lambda_1 - \lambda_2|}{\sqrt{\lambda_1^2 + \lambda_2^2}}, \tag{8.1}$$

where λ are the eigenvalues of the diffusion tensor $\mathbf{D}$. An isotropic diffusion tensor is proportional to the identity matrix, so its eigenvalues are equal, giving an anisotropy of zero. A tensor that only allows diffusion along one axis (i.e., $\lambda_2 = 0$) would have an anisotropy of unity. In this problem, the AD method produces strongly anisotropic coefficients in the channel.

Because the problem is driven by a constant spatial source rather than a pulsed initial condition, the gradients are smoother than in the 1-D Marshak wave problem, and the P_1 and AP_1 methods concordantly perform much better. In fact, the AP_1 and FLAD methods are qualitatively very close, as are the P_1 and FLD methods.

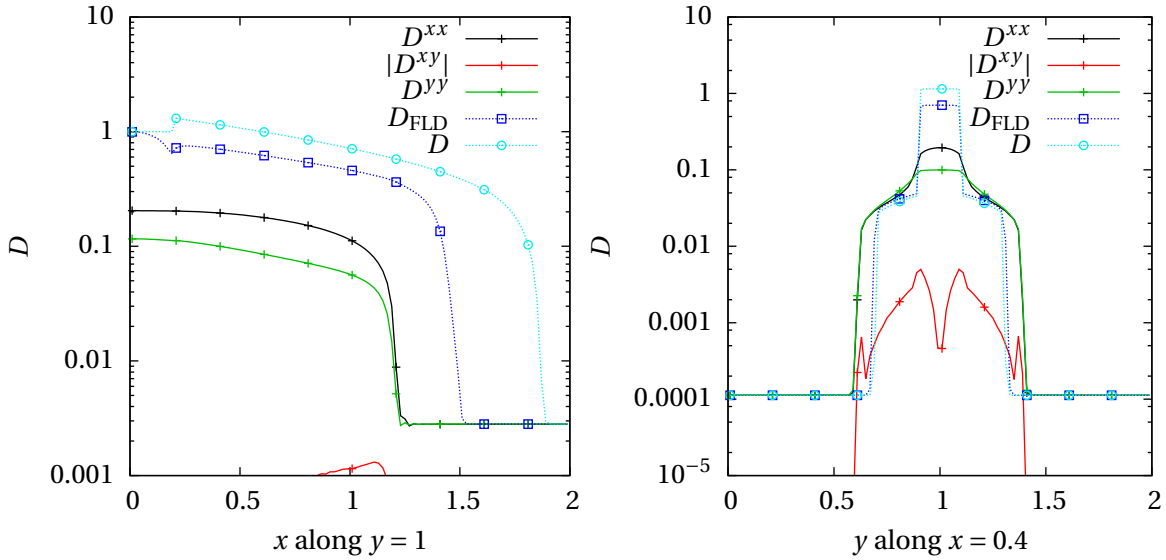

(a) Centerline view

(b) Orthogonal view

Figure 8.5: Diffusion coefficients at $t = 3$ in the flatland pipe problem. The three components of the FLAD tensor are plotted as solid lines; the flux-limited diffusion and standard diffusion coefficients are plotted for comparison.

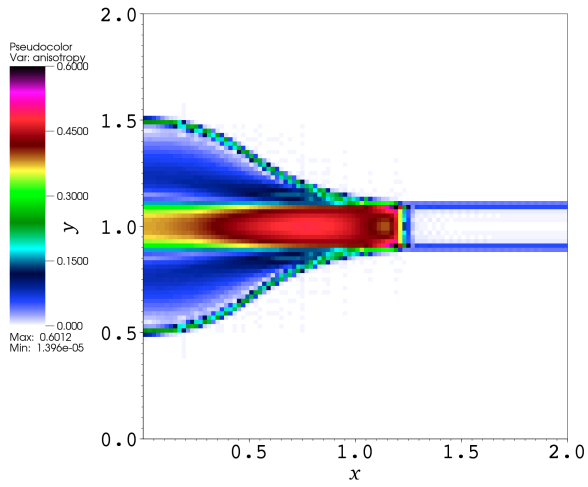

Figure 8.6: Anisotropy of the flatland pipe problem. In white regions, the FLAD tensor is isotropic, and in red regions, it is highly anisotropic.

Finally, a plot of the wavefront location along the channel centerline (Fig. 8.7) provides a comparison of the methods over a broader range of times. Both the diffusion and AD methods initially push energy too quickly into the channel, but the more moderate AD coefficients naturally limit the speed after that point. Only during the initial ~0.5 units of time are the slopes of the FLAD- and AD-calculated wavefront positions different, demonstrating that flux limiting is most important at the initial times and less so thereafter.

We more quantitatively test our expectation (see §3.3) that the more moderate AD coefficients require less flux-limiting than standard diffusion. Using this flatland pipe problem, we compare anisotropic diffusion to standard diffusion, with a "max" limiter modifying the coefficients of both. (The rest of our FLD problems use the "square root" limiter.) When the magnitude of the cell-average flux $\|\boldsymbol{F}\|$ exceeds the cell-average ϕ, the limiter not only modifies the diffusion coefficient/tensor but also increments a counter. In Fig. 8.8, we plot the fraction of cells that required limiting in each time step as a function of time. As a reminder, the relatively thin channel comprises 10% of the problem, and the problem contains 10 000 cells total. Both methods require the same amount of limiting during the initial transient, but flux limiting is active in far fewer cells at later times. Because flux limiting is an *ad hoc* fix-up, it is desirable for a method to use it as little as possible. The similarity between the AD and FLAD answers at later times are in accord with the very moderate use of flux limiting.

We note that this problem was also solved with the AD coefficients calculated on

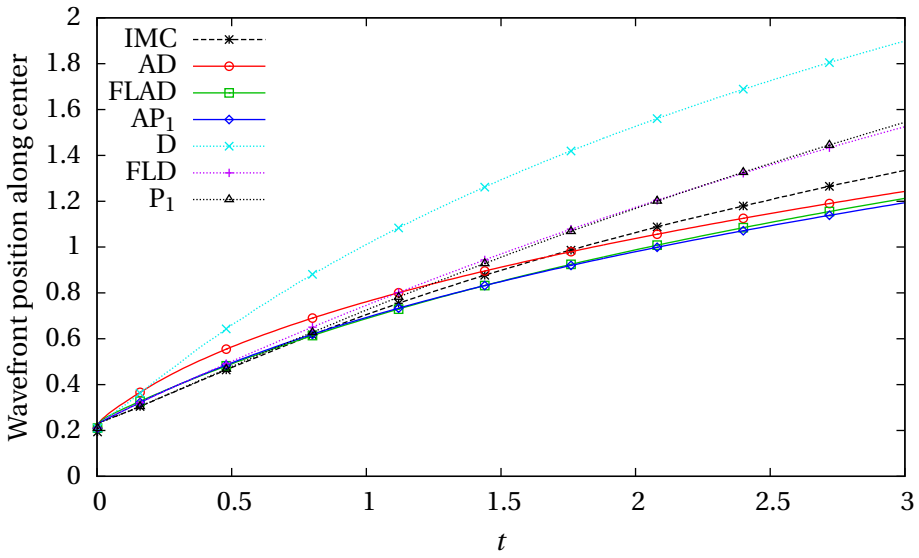

Figure 8.7: Wavefront position of ϕ in the flatland pipe problem.

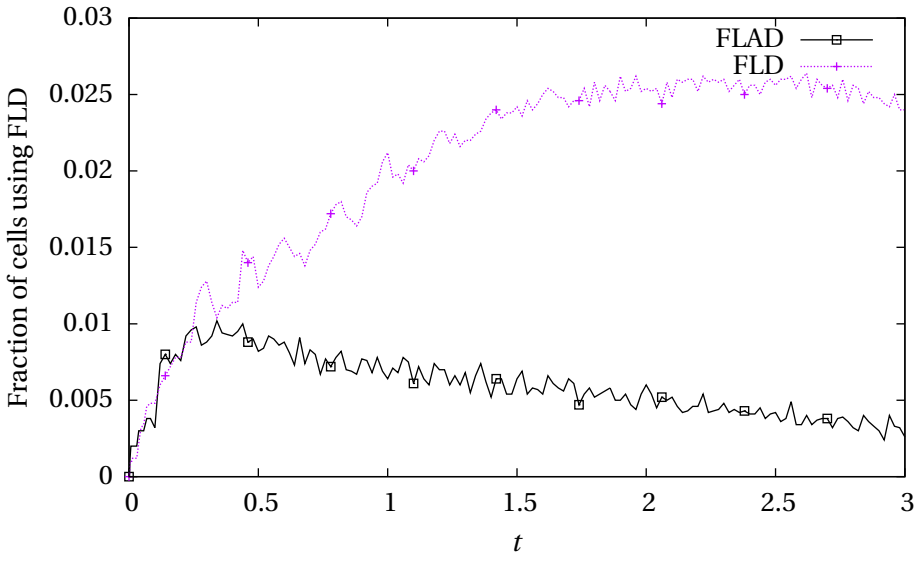

Figure 8.8: Application of flux limiters for anisotropic and standard diffusion in the flatland pipe problem.

a coarse grid, as discussed in §7.1.4. Even though the wall time for the calculation was significantly decreased, errors on the order of 10% or more were introduced in the solution. In the steady-state calculation of AD coefficients, material boundaries are well-defined, so a coarse grid may be easily chosen that shares those boundaries. With nonlinear opacities, the boundary between high- and low-opacity materials changes at every time step, preventing the naïve imposition of a coarse grid.

This test problem has demonstrated the feasibility of the anisotropic diffusion approximations to outperform conventional methods in multi-dimensional TRT problems. The strongly anisotropic diffusion tensor approximates the flow of radiation through the channel more accurately than the conventional isotropic diffusion coefficient.

8.3 Crooked pipe

To add additional complexity, we modified the flatland pipe problem by adding two bends in it and adjusting the physical coefficients to more closely resemble the "crooked pipe" problem from Ref. [75].

8.3.1 Problem description

This "crooked pipe" or "dogleg" problem (Fig. 8.9) uses flatland geometry rather than the r-z geometry typically seen in pipe/obstacle problems. It also uses the model system

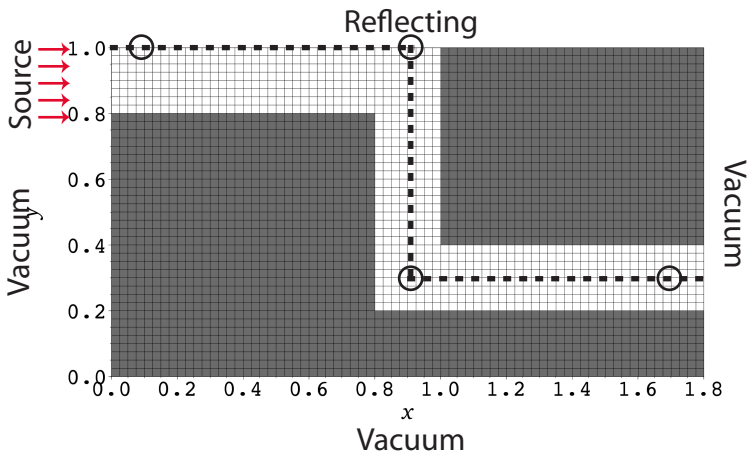

Figure 8.9: The crooked pipe problem configuration. The streaming region is white, and the diffusive region is gray. The arrows indicate an isotropic incident radiation boundary. The centerlines of the three legs are shown with a dotted line; the four fiducial points are circled.

$a = c = 1$ rather than physical coefficients. The problem consists of an optically thin streaming region embedded in an optically thick diffusive region. The thin "pipe" has a very small heat capacity and opacity: $c_v = 0.01$ and $\sigma = 0.25T^{-3}$. The diffusive region has $c_v = 5$ and $\sigma = 200T^{-3}$. The pipe has a width of 0.2 (although, because of the reflecting boundary at the top of the problem, it represents a channel with width 0.4 at that point); the legs are 1.0, 0.8, and 1.0 units long.

As with the previous scaled problem, the material and radiation temperatures have a uniform initial condition of $\phi = T^4 = 0.001$, and $a = c = 1$. The problem is driven by an isotropic boundary source on the left edge of the pipe with an incident radiation temperature $T_{\text{rad}} = 5^{1/4}$. (This gives an incident radiation flux of $5/\pi$; see Eq. (6.8).) The top boundary is reflecting, and all other boundaries are vacuum.

The problem runs until $t = 10$, with varying time steps (Fig. 8.10) that range from $\Delta_t = 0.00125$ to $\Delta_t = 0.1$ to account for the stronger temporal gradients at the beginning of the problem. (Small time steps are needed to prevent IMC, and other methods to a lesser extent, from violating the maximum principle.[2]) The chosen grid width is $\Delta_x = 0.025$ for IMC and $\Delta_x = 0.0125$ for the deterministic methods. (In this problem, the spatial discretization error for the diffusion methods was higher than the other problems we ran because of the very optically thick region, so we refined the mesh for those methods.)

The analysis will primarily consider segments along the centerline of the legs (dashed lines in Fig. 8.9) and certain fiducial points in the channel that are representative of the radiation behavior over time. These points, circled in Fig. 8.9, have the following (x, y)

[2]See Ref. [26] for a discussion of the maximum principle.

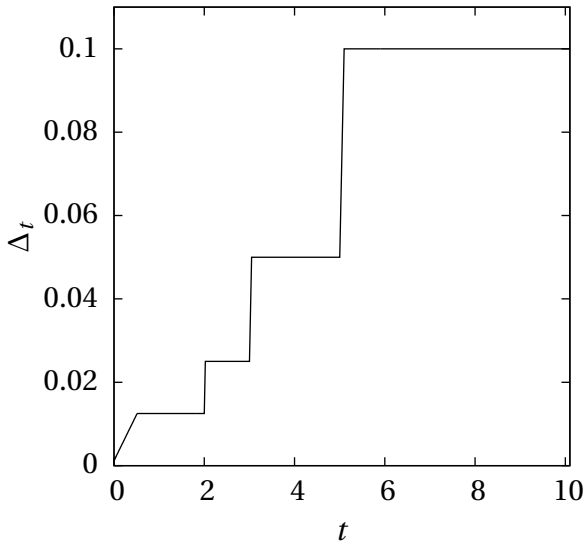

Figure 8.10: Time steps used in the crooked pipe problem.

coordinates: (0.1, 1.0), (0.9, 1.0), (0.9, 0.3), and (1.7, 0.3).

8.3.2 Results and discussion

With the semi-implicit linearization, the problem is highly scattering and thus expensive for MC solvers. In fact, our particular choice of $\sigma \propto T^{-3}$ and $c_v \propto 1$ means that the material-related component of the Fleck factor, $\beta\sigma$ [see Eq. (2.9)], is temperature-independent inside each material, and we can calculate *a priori* the effective scattering ratio $\sigma_{\text{es}}/\sigma$:

$$\begin{aligned}
\text{effective scattering} = 1 - f &= 1 - \left[1 + \beta c \Delta_t \sigma\right]^{-1} \\
&= 1 - \left[1 + \left(\frac{4aT^3}{c_v}\right) c\Delta_t(\alpha T^{-3})\right]^{-1} \\
&= 1 - \left[1 + 4\Delta_t \frac{\alpha}{c_v}\right]^{-1},
\end{aligned}$$

where $\frac{\alpha}{c_v} = 25$ in the channel and $\frac{\alpha}{c_v} = 40$ in the medium. In the final time step with $\Delta_t = 0.1$, the Fleck factor is about 0.09 in the channel and 0.06 in in the diffusive medium: the effective scattering ratio is above 0.9 throughout the problem.

Figure 8.11 plots the radiation temperature at the final state $t = 10$ for the reference solution (IMC), the flux-limited anisotropic solution (FLAD), and the flux-limited diffusion solution (FLD). Clearly, the complicated features in this problem lead to very different approximate answers, unlike the self-similar results seen in in the simple 1-D case of §8.1.

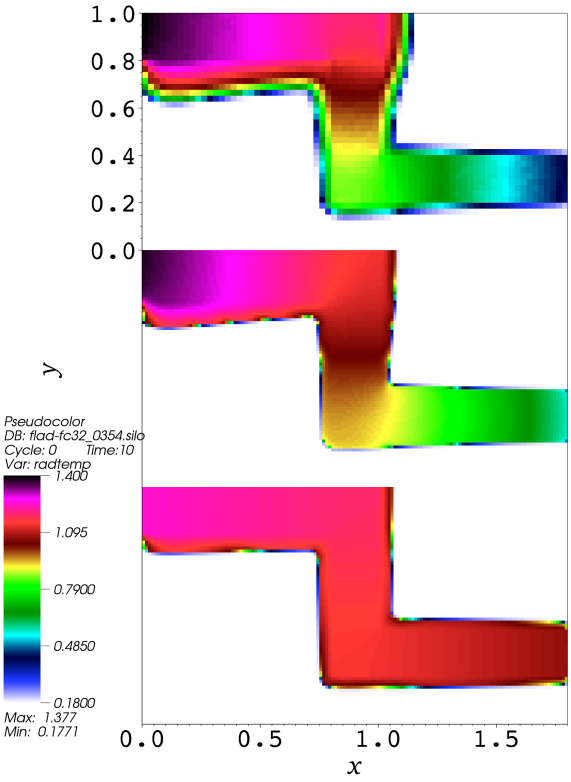

Figure 8.11: Radiation temperature at $t = 10$ in the crooked pipe problem. From top to bottom, the methods compared are IMC, FLAD, and FLD.

This problem has the same qualitative behavior as the previous flatland pipe problem: radiation streams through the optically thin pipe, heating it and the surrounding diffusive material. One notable difference is that the smaller heat capacity more tightly couples the radiation and material temperatures: the incident radiation heats the material in the channel more quickly.

The choice of a boundary source rather than an interior source further differentiates the anisotropic diffusion methods from the conventional diffusion methods (see Fig. 8.12). Because the conventional and anisotropic diffusion methods yield such different diffusion coefficients (Fig. 8.13), the slope of the radiation temperature at the boundary is very different. The flatter slope of the standard diffusion methods (due to the very large D) strongly affects the rate at which radiation penetrates the problem: even with a flux limiter, diffusion overestimates the amount of radiation that moves through the channel.

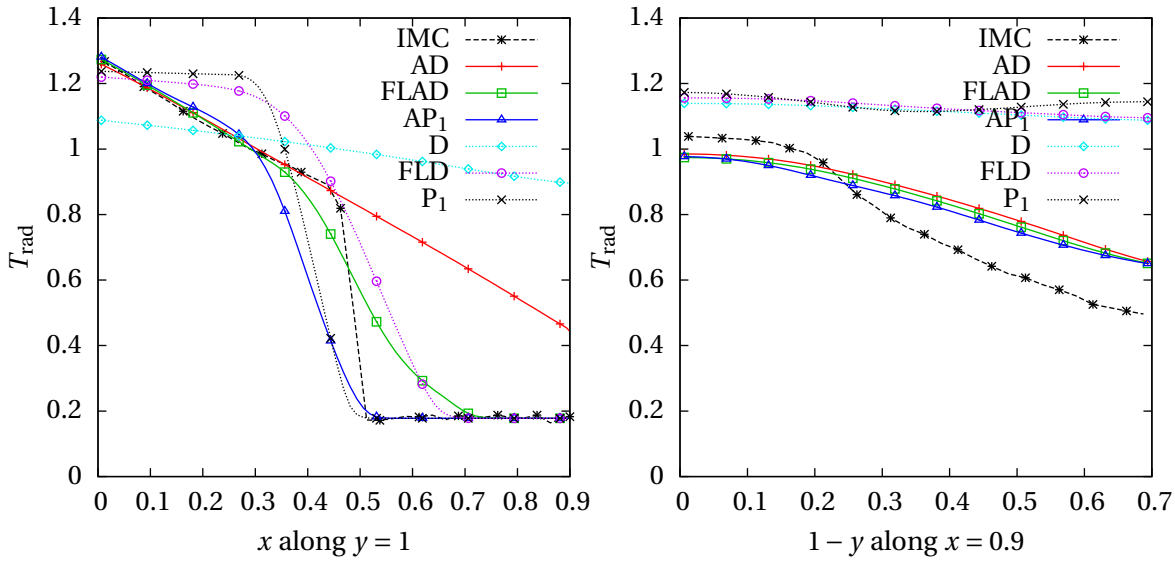

(a) Leg 1 at $t = 0.5$

(b) Leg 2 at $t = 3.0$

Figure 8.12: Representative plots of the radiation temperature in the crooked pipe problem.

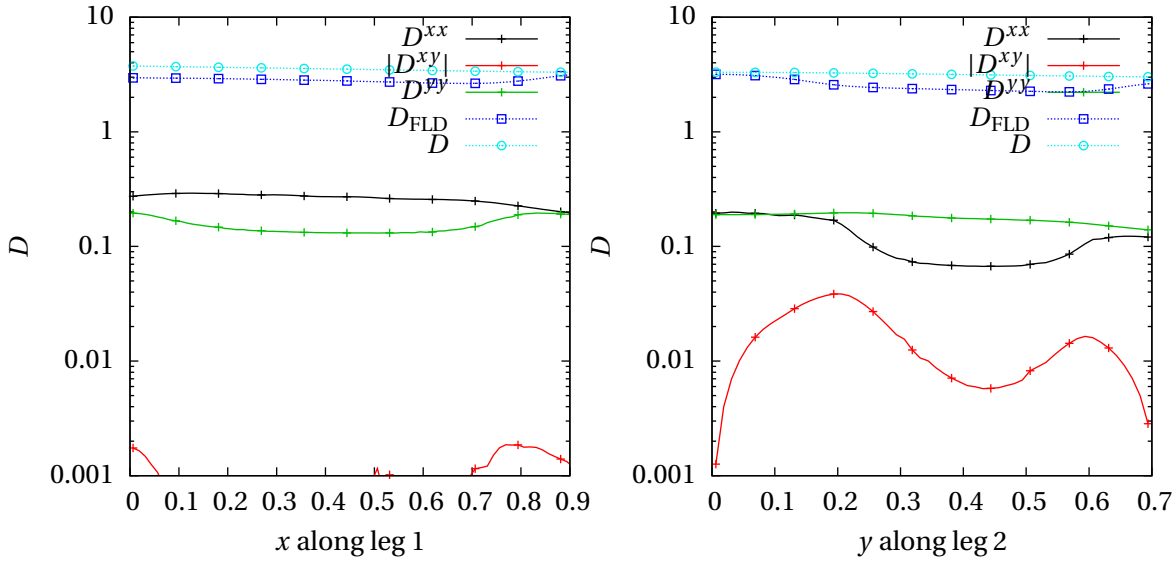

(a) Leg 1

(b) Leg 2

Figure 8.13: Diffusion coefficients at $t = 10$ in the crooked pipe problem. The three components of the FLAD tensor are plotted as solid lines; the flux-limited diffusion and standard diffusion coefficients are plotted for comparison.

An additional complication is the strongly multi-dimensional layout of this problem. The true transport solution (IMC) shows highly collimated radiation streaming through the channel, impacting the obstacle at $x = 1$, and heating it so that it re-emits isotropically. The limited approximations of standard diffusion do not take this into account at all: radiation flows isotropically through the bends with nary a care for the obstacle. Flux-limited anisotropic diffusion captures some of the strong anisotropy of the intensity, thereby driving energy into the obstacle and heating it up. We have plotted the flux-limited anisotropic diffusion tensors (as well as the opacity, which determines those coefficients) at the final state in Fig. 8.14. The smaller magnitude of the AD coefficients in

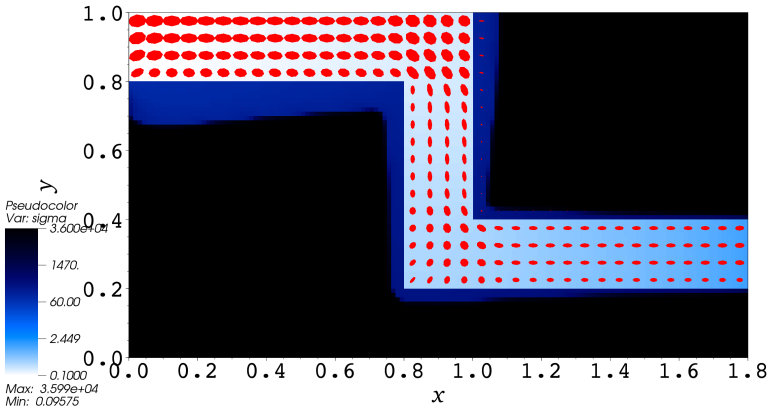

Figure 8.14: Opacity and flux-limited anisotropic diffusion tensors at $t = 10$ in the crooked pipe problem. The opacity is shown (scaled logarithmically) in white, blue, and black, and a subset of the anisotropic diffusion tensors are shown in red. The size of each ellipse is proportional to the magnitude of the AD tensor at that point, the eccentricity is proportional to the anisotropy, and the principal direction indicates the strongest action of the tensor.

the channel, compared to standard diffusion and FLD, allow the surrounding diffusive regions to absorb more energy than the conventional diffusion methods.

Yet only the transport method (IMC) is able to capture the full multi-dimensional aspects of the solution. In Fig. 8.12b, for example, there is a sudden drop-off in the IMC solution at $y = 0.8$ along the centerline of leg 2: this is at the bottom edge of the first leg, where the relatively opaque diffusive region obstructs radiation emitted by the boundary source. Only transport can accurately model that the primary source of particles into the second leg is by radiative emission from the heated wall. (The channel has a very small σ, implying that its emission term σacT^4 is also small.) Diffusion and anisotropic diffusion only approximate this effect by allowing particles to diffuse around corners.

To better compare the time-dependent behavior of the methods, we turn to the radiation temperature as a function of time at the first and second fiducial points (Fig. 8.15). As

we have already discussed, the diffusion and AD solutions allow radiation to exceed the speed of light in the channel. (The result is that the radiation temperature for these methods rises *sooner* than the other methods.) However, the *rate* of the temperature rise is different between the conventional and the anisotropic methods. Diffusion, flux-limited diffusion, and P_1 all allow too much energy into the channel, heating it to an unphysically high temperature. The anisotropic methods show a more gradual rise in the radiation, closer to the reference solution.

In Fig. 8.16 we have overlaid the reference solution (IMC), flux-limited diffusion, and flux-limited anisotropic diffusion at all four representative points. The leading tail in FLD and FLAD is an artifact of the temporal discretization error. The IMC and FLAD show good agreement at the first two points for nearly all times, but after the first bend in the problem, the accuracy of FLAD suffers. The FLD approximation allows energy to travel through the problem too rapidly: its calculated solution in the pipe is nearly constant by $t = 2$, whereas the transport solution does not show radiation heating the final point until $t = 5$.

In Table 8.1 we compare the amount of computer time taken for each of the problems. The one transport sweep per time step needed to calculate **D** accounts for about half of the run time for the anisotropic methods, but the total wall time for each AD method is approximately equal to that of the conventional diffusion methods. Our explanation is

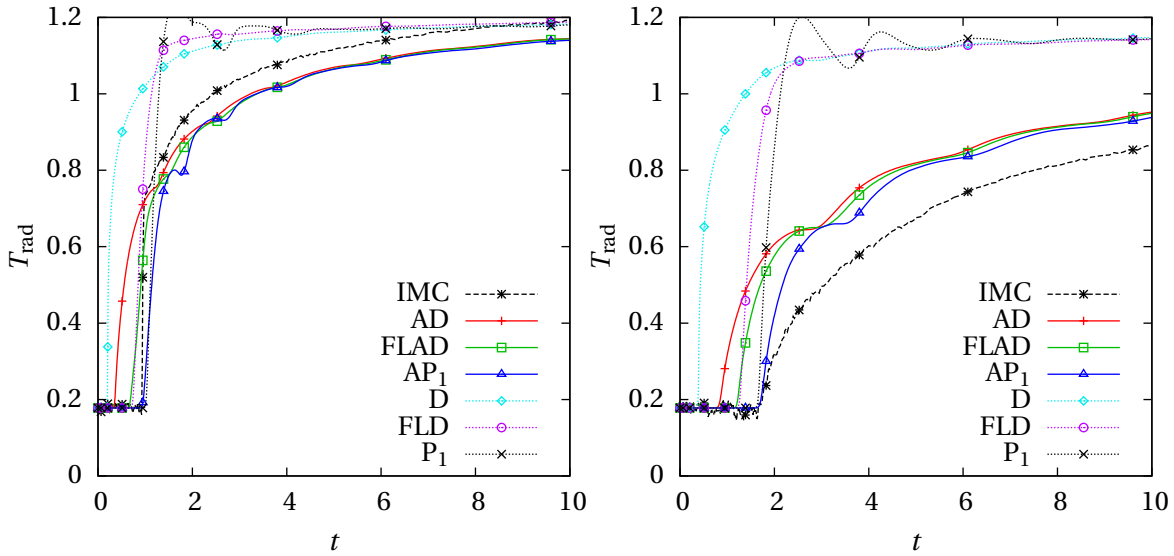

(a) $x = 0.9$, $y = 1.0$ **(b)** $x = 0.9$, $y = 0.3$

Figure 8.15: Fiducial points at the end of the first (a) and second (b) legs. These plots show the time-dependent behavior of all the methods tested.

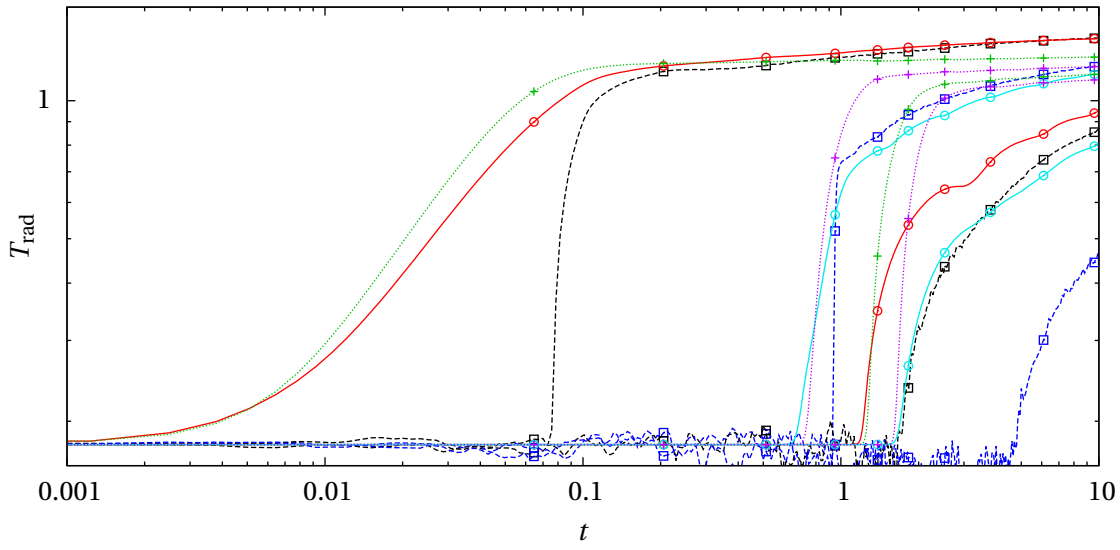

Figure 8.16: Plot of the radiation temperature at the four fiducial points. IMC (blue and black dashed lines), FLD (green and magenta dotted lines), and FLAD (red and cyan solid lines) are compared. The y scale ranges from 0.16 to 1.6.

	Wall time (s)
IMC	54300
AP_1	94
FLAD	48
AD	44
P_1	73
FLD	43
Diffusion	44

Table 8.1: Timing comparison for the crooked pipe problem.

that the magnitude of the diffusion coefficients affects the conditioning of the diffusion matrix, which in turn affects the convergence rate of the iterative matrix solvers. The anisotropic diffusion coefficients are a factor of ten smaller than those of flux-limited diffusion (see Fig. 8.13). By explicitly saving the sparse diffusion matrices to files and importing them into MATLAB, we determined that the approximate 1-norm condition numbers for the FLD and FLAD matrices (at the final state $t = 10$) are 1.6×10^4 and 1.2×10^3, respectively. The CG solver converges more quickly for better-conditioned matrices [56], so the low-order AD solution is faster than the FLD solution. The additional expense of the calculation of the anisotropic diffusion coefficients by chance brings the wall time of the AD methods to parity with the conventional diffusion methods. (We suspect that a

well-chosen preconditioner for each method will equalize the computational effort spent in the diffusion solve, so the AD methods will require slightly more time overall.)

In this test problem, the anisotropic diffusion methods consistently produce more accurate solutions than the standard diffusion methods without an increase in computing time. The flux limiter (FLAD) further improves the result by reducing the speed of the initial radiation wave. As seen in the previous flatland pipe problem, the AP_1 approximation yields solutions similar to those of FLAD. None of the approximate methods can exactly reproduce the transport solution, but by all metrics the new anisotropic diffusion methods approximate the transport solution much better than conventional diffusion methods.

8.4 2-D "easy" obstacle problem

One might argue that the previous flatland problems are particularly suited to the anisotropic approximations because of the clear-cut "voided channel" configuration. How then do the methods perform on problems *without* simple, optically thin channels in a thicker medium? To answer this question, we have tested the methods against existing multi-D test problems in the literature.

8.4.1 Problem description

The "easy" obstacle problem (Fig. 8.17), described in Ref. [11] (and also used in Ref. [76]),

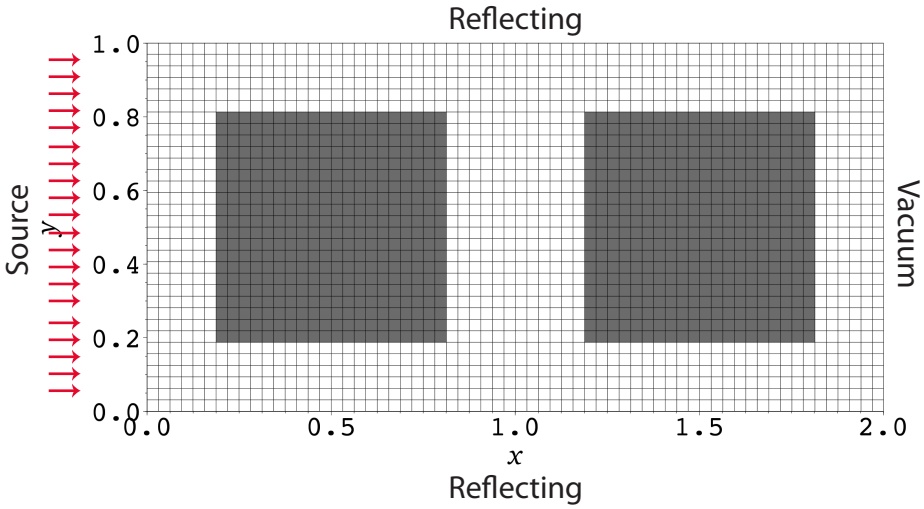

Figure 8.17: Problem layout for the "easy" obstacle problem. The gray blocks are 50% more opaque than the white region at the same temperature.

is a simple radiation transport designed to have relatively weak gradients and constant dynamic timescales.

The problem contains two square obstacles that impede a front of radiation emitted by a boundary source. It is a two-dimensional problem on the domain $0 \le x \le 2$, $0 \le y \le 1$ with $\Delta_x = \Delta_y = 1/32$. The problem has a uniform heat capacity $c_v = 1$, and the opacity is $\sigma = T^{-3}$ everywhere except inside two obstacles, where $\sigma = 1.5T^{-3}$. These obstacles are squares of width 5/8, with lower-left corners at (3/16, 3/16) and (19/16, 3/16). It uses the model unit system $c = a = 1$.

The top and bottom boundaries are reflecting; the left of the problem has an incident black body radiation source with $T_{\text{rad}} = 5^{1/4}$, and the right side of the problem has a vacuum boundary. (The black body boundary condition has an incident radiation flux of 5/4; see Eq. (6.7).) The initial condition is $\phi = T^4 = 0.001$.

In Ref. [11], the problem halts at $t = 3$; for the sake of completeness we compare the convergence of the solutions until $t = 8$ in Fig. 8.20. We use a uniform time step $\Delta_t = 0.01$. The original problem also contains a material energy conduction term[3] which we omit.

We use a "level-symmetric" Chebyshev–Legendre S_{16} quadrature set for calculating the AD coefficients. (This quadrature set uses a Gauss–Legendre quadrature to obtain polar angles, and Chebyshev–Gauss quadratures for the azimuthal directions, with fewer azimuthal ordinates with increasing polar level.)

8.4.2 Results and discussion

This problem is a slight variation on a one-dimensional Marshak wave problem. The presence of the moderately optically thick obstacles introduces some mild non-uniformity into the solution along the y axis.

Qualitatively, flux-limited diffusion and flux-limited anisotropic diffusion perform equally well (Fig. 8.18). Whereas FLD contains spatial gradients that are slightly too steep, FLAD is unnaturally smooth due to its smoother anisotropic diffusion coefficients.

A more detailed comparison of the methods at the intermediate time $t = 3$ (Fig. 8.19) shows that the IMC reference solution agrees with the conventional FLD more closely inside the obstacle, but FLAD gives a better result in the channel.

[3] To incorporate conduction in the material, a diffusion term $-\nabla D_m \nabla T$ must be added to Eq. (2.1b).

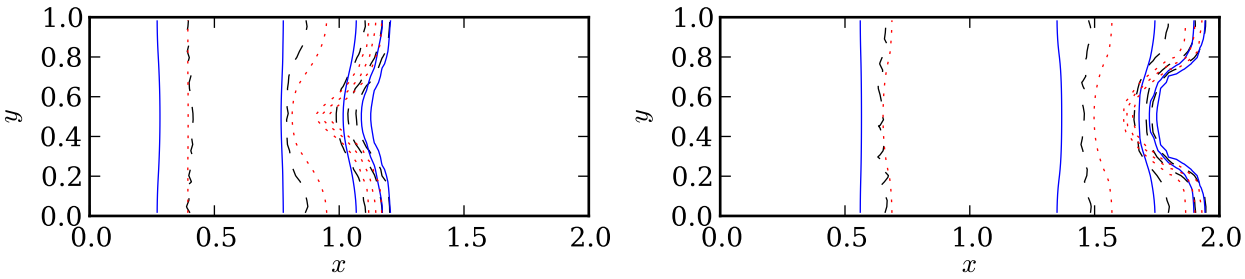

(a) Radiation temperature at $t = 3$

(b) Radiation temperature at $t = 6$

Figure 8.18: Contour plot of the solution at $t = 3$ and $t = 6$ in the easy obstacle problem. The black dashed line is the IMC solution, the blue solid line is the FLAD solution, and the red dotted line is the FLD solution. Contours are at $0.25, 0.5, \ldots, 1.25$.

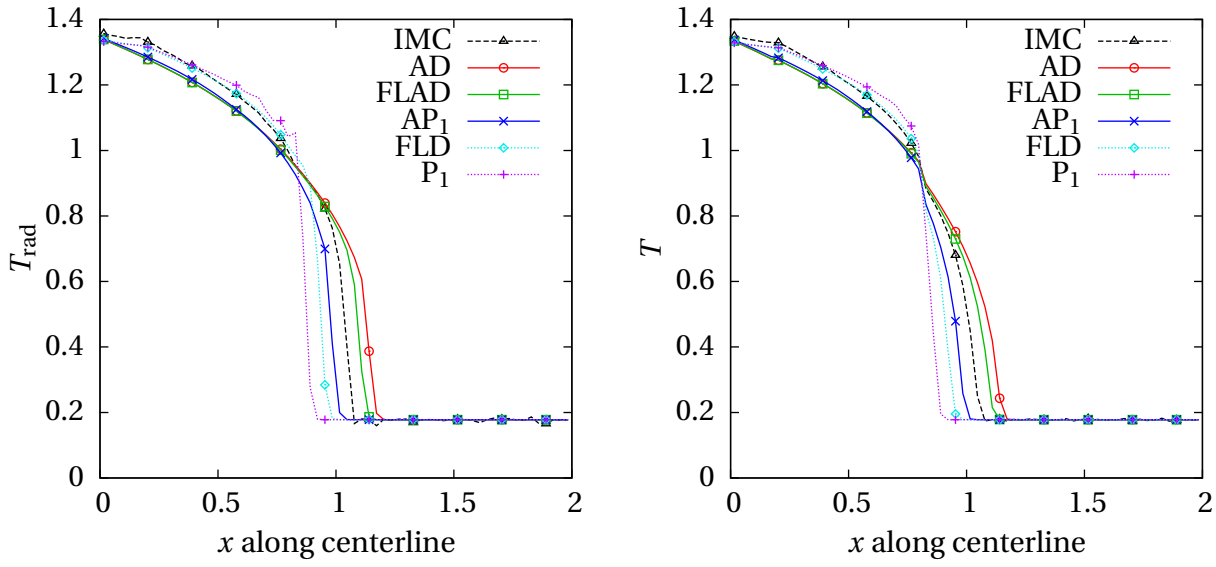

(a) Radiation temperature

(b) Material temperature

Figure 8.19: Solution along the centerline at $t = 3$ in the easy obstacle problem.

To provide a quantitative comparison of the methods, we have compared the difference in the temperature (volume-weighted relative 2-norm) between each method and the reference solution as a function of time (Fig. 8.20). This metric,

$$\text{reported difference} = \left[\sum_{i \in \text{cells}} \left(\frac{T_i}{T_{i,\text{reference}}} - 1 \right)^2 (V_i)^2 \right]^{1/2},$$

is similar to Eq. (7.2) used in the previous chapter.

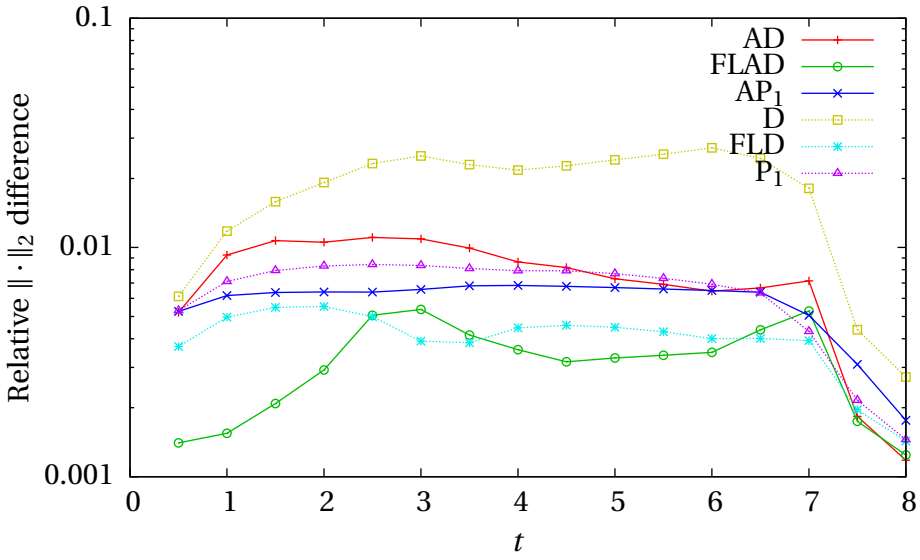

Figure 8.20: Relative difference of the material temperature in the easy obstacle problem, compared against IMC.

From the plotted relative differences, it appears that the most accurate method overall is flux-limited anisotropic diffusion. Diffusion is the least accurate, and the AP_1 and P_1 methods perform similarly.

In this problem, our new anisotropic methods do not notably outperform the conventional diffusion-based methods, just as it was not advantageous in the earlier 1-D numerical test. Anisotropic diffusion can be an improvement over standard diffusion in some but not all problems.

8.5 2-D "hard" obstacle problem

A second problem from Ref. [11] has steeper spatial gradients and large voided regions: it should therefore lie outside the comfort zone of both conventional and anisotropic diffusion methods.

8.5.1 Problem description

The "hard" obstacle problem has the 2-D domain $0 \le x, y \le 1$ and uses a cell width $\Delta_x = \Delta_y = 1/64$. The heat capacity is uniform, $c_v = 1$, and the opacity is $\sigma = T^{-3}$ outside of two square obstacles, which have $\sigma = 10T^{-3}$. The square obstacles, each of which has a width of $1/4$, are stationed with lower-left corners at $(3/16, 9/16)$ and $(9/16, 3/16)$. As with the previous problem, we omit material conduction.

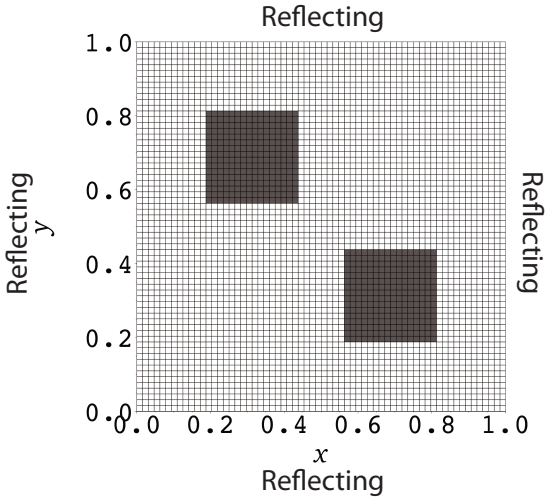

Figure 8.21: Problem layout for the "hard" obstacle problem. The gray blocks are ten times as opaque than the white region at the same temperature.

All energy in the problem comes from the Gaussian initial condition peaked near $x = y = 0$:

$$\phi(x, y, 0) = [acT(x, y, 0)]^4 = 0.001 + 100\,\mathrm{e}^{-100(x^2+y^2)}.$$

In the model's unit system, $a = c = 1$.

The problem is run until $t = 3$. The time step increases linearly from $\Delta_t = 0.0001$ at $t = 0$ to $\Delta_t = 0.01$ at $t = 1$ and is constant thereafter. To calculate the anisotropic diffusion coefficients, we use the same Chebyshev–Legendre level symmetric quadrature set as in the "easy" obstacle problem.

8.5.2 Results and discussion

The large optically thick region and the sharp discontinuity in temperature at the obstacles pose a challenge to all of the approximate methods. As we saw in the linear test problem of §7.5, only a transport method is able to accurately capture the hyperbolic behavior of the transport equation. In Fig. 8.22 we have plotted the radiation field at a

time in the problem where the transport effects are particularly visible. The optically thick obstacles have impeded the flow of radiation, heating up slowly at their exterior, re-radiating from their outer boundary into the medium, but preventing radiation from passing through. The radiation streams through the gap in the middle, at first almost as a mono-directional beam. As it heats up the upper right section of the problem, isotropic black-body emission warms the reverse sides of the blocks.

The diffusion methods cannot reproduce the hyperbolic behavior of radiation streaming through a void. In the conventional diffusion methods, radiation diffuses isotropically through the problem: it flows unnaturally around the obstacles. In Fig. 8.22, this is seen in the FLD solution (lower left): the more homogeneous radiation field has fully surrounded the obstacle.

Fig. 8.23 gives a more detailed look at the final state. With the exception of P_1, the approximate methods qualitatively capture the behavior of the radiation and material temperatures along the diagonal of the problem. The initial gradient proved too strong for P_1, which showed unphysical wavelike behavior throughout the problem. The smoother coefficients in the AP_1 equation moderate the wavelike behavior, allowing it to represent

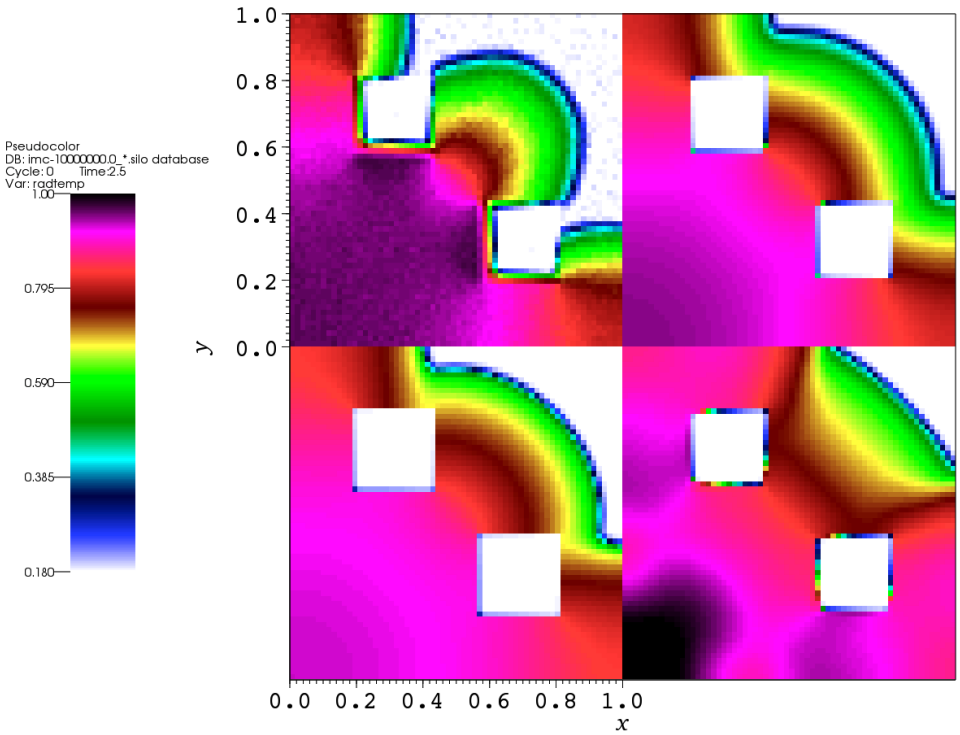

Figure 8.22: Pseudocolor plots of the radiation temperature at $t = 2.5$. The methods compared are: IMC (upper left), FLAD (upper right), FLD (lower left), AP1 (lower right). The temperature scale is linear and ranges from 0.18 (white) to 1 (black).

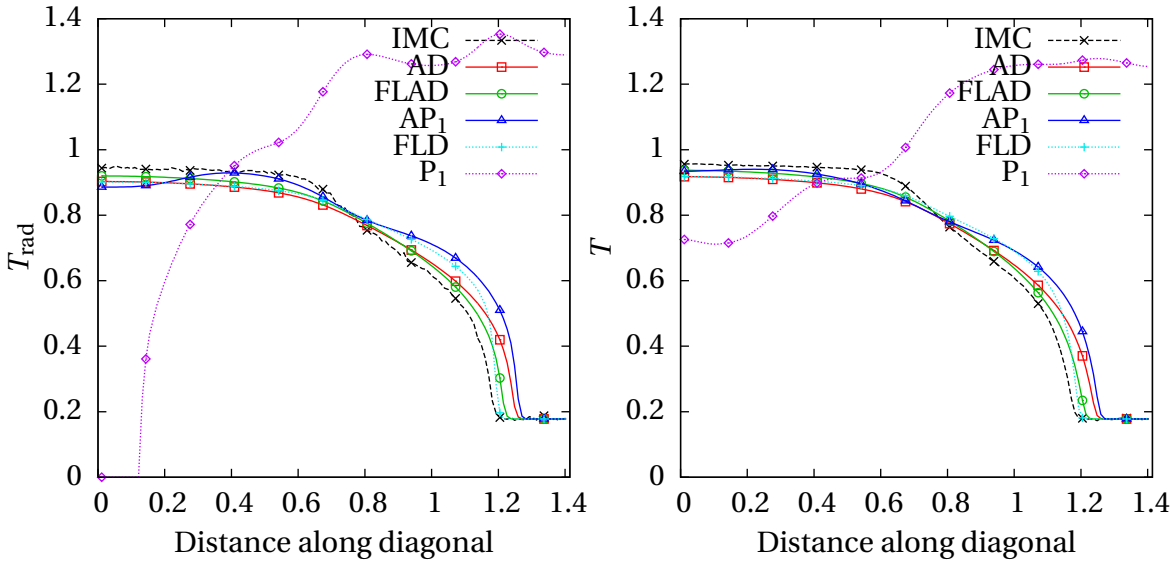

(a) Radiation temperature

(b) Material temperature

Figure 8.23: Solution along the diagonal at $t = 3$ in the hard obstacle problem.

the behavior of the radiation more accurately.

Because the primary symmetry in this problem is along the diagonal (as opposed to the x or y axis), the D^{xy} component of the diffusion coefficients are larger than in any of the other problems we tested. The discretizations we use (from Chapter 5) are not designed for strong off-diagonal anisotropy, so the negative result for anisotropic diffusion in this problem is somewhat clouded.

This problem demonstrates again that anisotropic diffusion is not a "silver bullet." It cannot model the hyperbolic behavior of the transport equation, but at the same time it performs no less poorly than conventional flux-limited diffusion.

8.6 Conclusions

The wide variety of problems we chose to test in this section give a full picture of the behavior of the anisotropic diffusion methods in TRT problems. Although the new approximations do not perform much better than conventional diffusion approximations in 1-D geometry or problems with large voids, FLAD and AP_1 provide qualitatively good answers for problems where radiation travels through small voided regions.

In small regions of optically thin materials, the AD method calculates strongly anisotropic coefficients in those regions, providing better answers than conventional diffusion.

Using a flux limiter with the AD approximation (FLAD) fixes the unphysical violation of the speed of light seen in early time steps.

We conclude that in many realistic, multi-dimension problems of interest, flux-limited anisotropic diffusion is a more accurate solution method than conventional flux-limited diffusion. The small amount of computational effort needed to calculate the AD coefficients is repaid by superior results.

Chapter 9
Conclusions

In this thesis, we have developed and numerically tested three anisotropic diffusion approximations to time-dependent radiation transport and nonlinear radiative transfer. Ancillary to the numerical testing, we investigated flatland geometry and new discretization schemes suitable for the anisotropic diffusion methods. We conclude by reviewing the new developments and results, then discussing future refinements and improvements to the methods.

9.1 Anisotropic diffusion

The anisotropic diffusion (AD) approximation, initially formulated in prior work, has been extended to finite and time-dependent problems (Chapter 3). Using an asymptotic derivation that appeals to the physical scaling of the problem, we obtained a new, arbitrarily anisotropic (as opposed to linearly anisotropic in the case of standard diffusion) approximation to the angular intensity. Boundary and initial layer analyses gave transport-matched boundary and initial conditions for the new method.

We then discussed properties of the new AD approximation solely on the basis of the underlying equations. We postulated that the method should be only slightly more expensive than diffusion: in an infinite-medium problem with time-independent opacities, only one transport sweep is needed to calculate the anisotropic diffusion coefficients for all time steps. (In finite medium problems, an additional few sweeps may be needed to converge the opposing reflecting/white boundary conditions.) Furthermore, unlike time-dependent transport methods, the time-dependent AD methods do not require the storage of the full angle-dependent intensity. Anisotropic diffusion is faster and less memory-intensive than transport methods.

One complication present in the anisotropic diffusion methods is that, in most problems, the diffusion tensor has nonzero off-diagonal terms. These terms cause a gradient in one direction to induce particle flow in a perpendicular direction. To account for this

"transverse" leakage, we generalized an existing cell-centered difference scheme (Chapter 5). It reduces to a conventional 5-point finite difference method when the diffusion tensors are isotropic, and it does not increase the number of unknowns compared to cell-centered finite difference diffusion. With the penalty of a slightly less sparse matrix structure, these new difference schemes account for the transverse leakage in anisotropic diffusion.

Our numerical results (Chapter 7) began by testing the fidelity of S_N-calculated AD coefficients. We obtained accurate answers with a coarse quadrature set (16 ordinates per quadrant), few transport sweeps (about two), and a coarse grid (so long as material boundaries were preserved).

Comparing plots of the intensity as a function of angle, we confirmed the hypothesis that the arbitrary anisotropy inherent to the AD approximation allows it to better represent the shape of the true intensity. We found the linear-in-angle representation of conventional diffusion to be inadequate in problems with strong anisotropy in the solution.

We also tested the newly derived boundary conditions. In most cases, they accurately preserved the transport solution away from the boundaries, even in the presence of voids. The exceptions that performed poorly were in cases of strongly anisotropic specified boundaries incident on a void. (Because the AD boundary conditions reduce to the diffusion boundary conditions in a homogeneous medium, these same boundary conditions perform well in problems without voids.)

In time-dependent problems, the anisotropic diffusion approximation produced more accurate answers than standard diffusion, but in voids, it allowed energy to travel too quickly. The same behavior was seen in thermal radiative transfer problems but was less pronounced: even the streaming areas are relatively opaque at their initial cold temperatures.

The anisotropic diffusion method shows great promise in steady-state problems. Yet because the anisotropic diffusion equations are parabolic, they have the shortcoming that in time-dependent problems, radiation may travel faster than c, the speed of light. We addressed this issue by proposing a modification to the AD approximation (flux limiting) and by developing a second "anisotropic" approximation (anisotropic P_1).

9.2 Flux-limited anisotropic diffusion

Adding a flux limiter to the anisotropic diffusion approximation (§3.3) artificially reduced the diffusion tensor's magnitude in the presence of strong gradients, inhibiting the spread of energy at a wavefront to restore the qualitative feature of transport that transfer is limited to the speed of light. Flux-limited anisotropic diffusion (FLAD) yields results similar to AD in problems with weak time derivatives and large opacities, but our results show that it improves the accuracy of the solution during the initial transients of a Marshak wave. Testing showed the "max" limiter with AD is used less frequently than with standard diffusion: as expected, the *ad hoc* fix-up is less necessary for the anisotropic diffusion approximation.

We found that FLAD produced very accurate solutions in a wide variety of problems with voided channel-like regions. The anisotropic diffusion approximation, when modified by the flux limiter, was especially efficacious in pipe-like problems with strong multi-dimensional behavior, which conventional flux-limited diffusion could not approximate well.

9.3 Anisotropic P_1

In the derivation of the anisotropic diffusion approximation, we assumed a very slowly changing solution. Revisiting that assumption and allowing a stronger $O(\epsilon)$ time derivative, we derived a set of P_1-like equations that contained the anisotropic diffusion tensor $\mathbf{D}$ (Chapter 4).

These equations had a shortcoming which was corrected by the *ad hoc* replacement of the opacity σ with a nonlocal ς that could be calculated in the same transport sweep as $\mathbf{D}$. The resulting Anisotropic P_1 (AP_1) approximation behaves well in voids, reduces to the AD approximation at steady state, and becomes the standard P_1 approximation in a homogeneous medium. Using a boundary layer analysis, we also obtained boundary conditions for this new method.

The low-order unknowns for AP_1 comprise both ϕ and $\boldsymbol{F}$, compared to just ϕ needed with the AD method. As a result, a different spatial discretization is also needed. We formulated a staggered-mesh scheme for AP_1 based on an extant P_1 discretization.

We found that AP_1-calculated solutions behaved like standard P_1 in some problems (with large voided regions) and like anisotropic diffusion in others (with smaller voided regions). In the case of large voids, AP_1 showed less unphysically oscillatory behavior than P_1.

In none of our test problems was AP_1 superior to FLAD, despite that the equations

of AP_1 are more complex than those of FLAD. (They are not self-adjoint, and they have a larger unknown space and therefore require more computer memory.) We therefore cannot recommend the new anisotropic P_1 approximation over flux-limited anisotropic diffusion.

9.4 Flatland geometry

Many of our test problems used the "flatland" geometry (Chapter 6), which has a smaller angular phase space than 2-D geometry and qualitatively simulates channels more realistically. (In 2-D geometry, what appears as a channel is a slice through two infinite walls.) Flatland geometry is not as straightforward as it seemed at first glance, however. The diffusion coefficients, Marshak boundary conditions, transport-matched boundary conditions, and black-body radiation boundary conditions all are different from their standard 2-D formulations.

In addition to prescribing sampling routines for flatland Monte Carlo calculations and presenting S_N quadrature sets that preserve the flatland angular moments (the equivalent of spherical harmonic functions), we more thoroughly investigated the diffusion approximation in flatland. We derived flatland Marshak boundary conditions and variational boundary conditions for diffusion, and generalized them so that they could apply to AD and AP_1 as well. We verified these boundary conditions numerically in Chapter 7.

9.5 Future work

The anisotropic diffusion approximations are still in their infancy. Their accuracy may be improved in a number of ways, which we here discuss.

9.5.1 Improved discontinuity treatment

In the derivation of the anisotropic diffusion method, we discarded terms of $O(\epsilon^2)$ using a particular asymptotic scaling. Retaining more terms—making fewer approximations—should result in a more accurate approximation to the radiative intensity.

By keeping the $\frac{1}{4\pi}\boldsymbol{\nabla}\cdot\boldsymbol{F}$ term in Eq. (3.7), we can derive at a new approximation that takes the place of Fick's law:

$$\boldsymbol{F} = -\mathbf{D}\cdot\boldsymbol{\nabla}\phi + \boldsymbol{E}(\boldsymbol{\nabla}\cdot\boldsymbol{F}),$$

where

$$\boldsymbol{E} = \int_{4\pi} \boldsymbol{\Omega} f \, \mathrm{d}\Omega .$$

Away from material discontinuities, $\boldsymbol{E}$ is exponentially small; but near a discontinuity, $\boldsymbol{E}$ is non-negligible. This additional advection term may improve the accuracy of the anisotropic diffusion approximation in an asymptotic order-of-accuracy sense, and it will reintroduce a qualitative property that our anisotropic diffusion approximation lacks: a "kink" in the solution ϕ. (Because $\boldsymbol{E}$ is discontinuous at a material boundary, it will induce a discontinuity in $\boldsymbol{\nabla}\phi$.) This new method will then have at a material interface both a boundary layer (which transport and AD have but standard diffusion does not) and a discontinuous first derivative (which transport and standard diffusion have but AD does not).

The difficulty with this extra term is that advection-diffusion equations require troublesome discretization schemes. Also, advection-diffusion is not self-adjoint, so the fast and simple conjugate gradient (CG) method could no longer be used to solve the resulting matrix: more costly methods (such as GMRES) would be required.

9.5.2 Alternative flux limiters

In §3.3, we proposed a flux-limited modification to anisotropic diffusion theory. For ease of understanding and implementation, we chose a "max" limiter that multiplies the tensor by a scalar that preserves the physical property $\boldsymbol{F} \leq \phi$. However, other flux limiting methods—some of which may be more well behaved numerically—are possible. These flux limiters would be more complicated than the standard scalar diffusion coefficients: the extra degrees of freedom in being anisotropic *tensors* rather than isotropic *scalars* would allow more options in formulating the tensor. They may also be more computationally expensive. For a "square root"-type limiter, as an example, a "matrix square root" would have to be calculated in each cell at each time step.

9.5.3 Multigroup

Flux-limited diffusion is often used with multiple energy groups (frequency groups) to improve the simulation's fidelity. Because of the strong variation of opacity with frequency, parts of the problem that are optically thick in one group may be optically thin in another. The AD approximation will likely provide a better treatment of the thin groups than standard FLD. However, a disadvantage of multigroup solutions is that each group will require its own transport-calculated $\mathbf{D}$. This might be too costly a requirement for it to remain competitive against IMC and other transport methods.

9.5.4 Three-dimensional problems

Time-dependent anisotropic diffusion has been formulated for general 3-D geometry (see Chapter 3), but it has not been implemented or tested in 3-D. The major differences between our work and 3-D are that the diffusion tensor is a 3×3 matrix, the diffusion matrix is more complex, and the cost of the transport sweep increases.

9.5.5 Discretization schemes

The cell-centered discretization schemes of Chapter 5 are only a first attempt at developing an accurate, cheap discretization for anisotropic diffusion. The Support Operators Method [58, 59], even though it uses more unknowns than cell-centered diffusion, may compensate for this added expense by being more accurate. Finite element methods might also be applied effectively to the anisotropic diffusion methods. Because the cell-centered scheme we derived is only applicable to "brick" geometry (regular Cartesian mesh), other discretization schemes will undoubtedly be needed (and equally undoubtedly already exist in other fields) for more complex geometries.

9.5.6 Preconditioners

As with standard diffusion methods, the performance of the anisotropic diffusion method could be improved by using Krylov solvers with well-chosen preconditioners. Multigrid preconditioning has already been applied to nonlinear diffusion [77, 11]; the extension to anisotropic diffusion should be straightforward.

9.6 Final remarks

The anisotropic diffusion methods that we derived and tested incorporate an arbitrary amount of anisotropy into their approximation of the angular intensity, producing results superior to diffusion in a number of problems. Of these new methods, flux-limited anisotropic diffusion is the most accurate. Even though the calculation of the anisotropic diffusion tensor requires the moderate cost of a transport sweep, the FLAD solution in many problems is commensurately more accurate compared to conventional FLD. Our goal of developing a newer method more accurate than FLD yet less expensive than transport has been attained. Based on our numerical testing, we believe FLAD to be a strong contender for accurate, inexpensive multi-dimensional simulations for time-dependent transport and thermal radiative transfer.

Bibliography

[1] J. LEWIS, *Rub-a Dub-Dub Science in the Tub*, Meadowbrook Press (1989).

[2] E. W. LARSEN and T. J. TRAHAN, "2-D Anisotropic Diffusion in Optically Thin Channels," *Trans. Am. Nucl. Soc.*, **101**, 387–389 (2009).

[3] T. J. TRAHAN and E. W. LARSEN, "3-D Anisotropic Neutron Difffusion in Optically Thick Media with Optically Thin Channels," *Proc. Intl. Conf. on Math. and Comput. Methods Applied to Nucl. Sci. Eng. (M&C 2011), Rio de Janeiro, Brazil, May 8–12* (2011), [CD-ROM].

[4] J. E. MOREL, "A Non-Local Tensor Diffusion Theory," Tech. Rep. LA-UR-07-5257, Los Alamos National Laboratory (2007).

[5] E. A. ABBOTT, *Flatland: A Romance of Many Dimensions*, Seely & Co (1884).

[6] M. ASADZADEH and E. W. LARSEN, "Linear transport equations in flatland with small angular diffusion and their finite element approximations," *Math. Comput. Modell.*, **47**, 495–514 (2008).

[7] S. R. JOHNSON and E. W. LARSEN, "Diffusion Boundary Conditions in Flatland Geometry," *Trans. Am. Nucl. Soc.*, **105**, 446–448 (2011).

[8] R. M. RAUENZAHN, V. A. MOUSSEAU, and D. A. KNOLL, "Temporal accuracy of the nonequilibrium radiation diffusion equations employing a Saha ionization model," *Comput. Phys. Commun.*, **172**, 2, 109–118 (2005).

[9] S. R. JOHNSON and E. W. LARSEN, "An Anisotropic Diffusion Approximation to Thermal Radiative Transfer," *Proc. Intl. Conf. on Math. and Comput. Methods Applied to Nucl. Sci. Eng. (M&C 2011), Rio de Janeiro, Brazil, May 8–12* (2011), [CD-ROM].

[10] R. P. DRAKE, M. L. ADAMS, K. G. POWELL, and Q. F. STOUT, "Center for Radiative Shock Hydrodynamics Project Year 2 Report," `http://aoss-research.engin.umich.edu/crash/` (2010).

[11] V. A. MOUSSEAU and D. A. KNOLL, "Temporal Accuracy of the Nonequilibrium Radiation Diffusion Equations Applied to Two-Dimensional Multimaterial Simulations," *Nucl. Sci. Eng.*, **154**, 174–189 (2006).

[12] G. C. POMRANING, *The Equations of Radiation Hydrodynamics*, Dover Publications, Inc., Mineola, New York (1973).

[13] D. MIHALAS and B. W. MIHALAS, *Foundations of Radiation Hydrodynamics*, New York, Oxford University Press (1984).

[14] J. J. DUDERSTADT and L. J. HAMILTON, *Nuclear Reactor Analysis*, Wiley, New York (1976).

[15] R. E. MARSHAK, "Effect of Radiation on Shock Wave Behavior," *Physics of Fluids*, **1**, 1, 24–29 (1958).

[16] P. M. CAMPBELL and R. G. NELSON, "Methods for Nonlinear Radiation Transport," Tech. Rep. UCRL-7838, Lawrence Radiation Laboratory (1964).

[17] P. M. CAMPBELL, "A Numerical Method for Discrete Ordinate and Moment Equations in Radiative Transfer," *Int. J. Heat Mass Transfer*, **12**, 4, 497–507 (1969).

[18] G. L. OLSON, L. H. AUER, and M. L. HALL, "Diffusion, P_1, and other approximate forms of radiation transport," *J. Quant. Spectrosc. Radiat. Transfer*, **64**, 619–634 (2000).

[19] T. A. BRUNNER, "Forms of Approximate Radiation Transport," Tech. Rep. SAND2002-1778, Sandia National Laboratories (2002).

[20] J. I. CASTOR, *Radiation Hydrodynamics*, Cambridge University Press (2004).

[21] A. B. WOLLABER, *Advanced Monte Carlo Methods for Thermal Radiation Transport*, Ph.D. thesis, University of Michigan (2008).

[22] F. B. BROWN, "Fundamentals of Monte Carlo particle transport," Tech. Rep. LA-UR-04-8817, Los Alamos National Laboratory (2004).

[23] J. A. FLECK, JR. and J. D. CUMMINGS, "An Implicit Monte Carlo Scheme for Calculating Time and Frequency Dependent Nonlinear Radiation Transport," *J. Comput. Phys.*, **8**, 3, 313–342 (1971).

[24] T. J. URBATSCH and T. M. EVANS, *Milagro Version 2—An Implicit Monte Carlo Code for TRT: Capabilities, Development, and Usage*, Los Alamos National Laboratory (February 2006).

[25] R. G. MCCLARREN, *Spherical Harmonics Methods for Thermal Radiation Transport*, Ph.D. thesis, University of Michigan (2007).

[26] E. W. LARSEN and B. MERCIER, "Analysis of a Monte Carlo method for nonlinear radiative transfer," *J. Comput. Phys.*, **71**, 1, 50–64 (1987).

[27] E. D. BROOKS, III, "Symbolic Implicit Monte Carlo," *J. Comput. Phys.*, **83**, 433–446 (1989).

[28] T. N'KAOUA, "Solution of the Nonlinear Radiative Transfer Equations by a Fully Implicit Matrix Monte Carlo Method Coupled with the Rosseland Diffusion Equation via Domain Decomposition," *SIAM Journal on Scientific and Statistical Computing*, **12**, 3, 505–520 (1991).

[29] B. CHANG, "The incorporation of the semi-implicit linear equations into Newton's method to solve radiation transfer equations," *J. Comput. Phys.*, **226**, 1, 852–878 (2007).

[30] J. D. DENSMORE and E. W. LARSEN, "Asymptotic equilibrium diffusion analysis of time-dependent Monte Carlo methods for grey radiative transfer," *J. Comput. Phys.*, **199**, 175–204 (2004).

[31] E. W. LARSEN and J. E. MOREL, "Advances in Discrete-Ordinates Methodology," in Y. AZMY and E. SARTORI, editors, "Nuclear Computational Science: A Century in Review," Springer Netherlands, chap. 1, pp. 1–84 (2010).

[32] E. W. LARSEN and J. B. KELLER, "Asymptotic solution of neutron transport problems for small mean free paths," *J. Math. Phys.*, **15**, 1, 75–81 (1974).

[33] E. W. LARSEN, G. C. POMRANING, and V. C. BADHAM, "Asymptotic Analysis of Radiative Transfer Problems," *J. Quant. Spectrosc. Radiat. Transfer*, **29**, 4, 285–310 (1983).

[34] E. W. LARSEN, "Advanced Nuclear Reactor Theory," (2007), class notes for NERS 543 at the University of Michigan.

[35] A. K. PRINJA and E. W. LARSEN, *Handbook of Nuclear Engineering: General Principles of Neutron Transport*, Springer (2010).

[36] M. L. ADAMS, "Transport Physics and UQ," (October 2010), CRASH Annual Review.

[37] D. A. KNOLL, L. CHACON, L. G. MARGOLIN, and V. A. MOUSSEAU, "On balanced approximations for time integration of multiple time scale systems," *J. Comput. Phys.*, **185**, 2, 583–611 (2003).

[38] J. D. DENSMORE, T. J. URBATSCH, T. M. EVANS, and M. W. BUKSAS, "A hybrid transport-diffusion method for Monte Carlo radiative-transfer simulations," *J. Comput. Phys.*, **222**, 485–503 (2007).

[39] D. A. KNOLL, W. J. RIDER, and G. L. OLSON, "An efficient nonlinear solution method for non-equilibrium radiation diffusion," *J. Quant. Spectrosc. Radiat. Transfer*, **63**, 15–29 (1999).

[40] D. A. KNOLL, W. J. RIDER, and G. L. OLSON, "Nonlinear convergence, accuracy, and time step control in nonequilibrium radiation diffusion," *J. Quant. Spectrosc. Radiat. Transfer*, **70**, 1, 25–36 (2001).

[41] R. B. LOWRIE, "A comparison of implicit time integration methods for nonlinear relaxation and diffusion," *J. Comput. Phys.*, **196**, 566–590 (2004).

[42] M. L. ADAMS and P. F. NOWAK, "Asymptotic Analysis of a Computational Method for Time- and Frequency-Dependent Radiative Transfer," *J. Comput. Phys.*, **146**, 1, 366–403 (1998).

[43] J. E. MOREL, "Diffusion-limit asymptotics of the transport equation, the $P_{1/3}$ equations, and two flux-limited diffusion theories," *J. Quant. Spectrosc. Radiat. Transfer*, **65**, 5, 769–778 (2000).

[44] R. J. LEVEQUE, *Finite Difference Methods for Ordinary and Partial Differential Equations*, SIAM (2007).

[45] J. S. WARSA, T. A. WAREING, and J. E. MOREL, "Krylov Iterative Methods and the Degraded Effectiveness of Diffusion Synthetic Acceleration for Multidimensional S_N Calculations in Problems with Material Discontinuities," *Nucl. Sci. Eng.*, **147**, 218–248 (2004).

[46] E. E. LEWIS and W. F. MILLER, *Computational Methods of Neutron Transport*, John Wiley and Sons, Inc., New York, NY (1984).

[47] M. L. ADAMS, "Discontinuous Finite Element Transport Solutions in Thick Diffusive Problems," *Nucl. Sci. Eng.*, **137**, 298–333 (2001).

[48] R. G. MCCLARREN, J. P. HOLLOWAY, and T. A. BRUNNER, "On solutions to the P_n equations for thermal radiative transfer," *J. Comput. Phys.*, **227**, 5, 2864–2885 (2008).

[49] J. S. WARSA, T. A. WAREING, and J. E. MOREL, "Fully Consistent Diffusion Synthetic Acceleration of Linear Discontinuous S_N Transport Discretizations on Unstructured Tetrahedral Meshes," *Nucl. Sci. Eng.*, **141**, 236–251 (2002).

[50] G. C. POMRANING, "Flux limiters and Eddington factors," *J. Quant. Spectrosc. Radiat. Transfer*, **27**, 5, 517–530 (1982).

[51] C. D. LEVERMORE, "Relating Eddington factors to flux limiters," *J. Quant. Spectrosc. Radiat. Transfer*, **31**, 2, 149–160 (1984).

[52] G. L. OLSON, "Efficient solution of multi-dimensional flux-limited nonequilibrium radiation diffusion coupled to material conduction with second-order time discretization," *J. Comput. Phys.*, **226**, 1, 1181–1195 (2007).

[53] F. MALVAGI and G. C. POMRANING, "Initial and Boundary Conditions for Diffusive Linear Transport Problems," *J. Math. Phys.*, **32**, 3, 805–820 (1991).

[54] E. W. LARSEN, "Asymptotic Theory of the Linear Transport Equation for Small Mean Free Paths. II," *SIAM J. Appl. Math.*, **33**, 3, 427–445 (1977).

[55] S. CHANDRASEKHAR, *Radiative transfer*, Dover Publications, New York (1960).

[56] L. N. TREFETHEN and D. BAU, *Numerical Linear Algebra*, SIAM (1997).

[57] J. S. WARSA, T. A. WAREING, and J. E. MOREL, "Solution of the Discontinuous P_1 Equations in Two-Dimensional Cartesian Geometry with Two-Level Preconditioning," *SIAM Journal on Scientific Computing*, **24**, 6, 2093–2124 (2003).

[58] J. E. MOREL, R. M. ROBERTS, and M. J. SHASHKOV, "A Local Support-Operators Diffusion Discretization Scheme for Quadrilateral r-z Meshes," *J. Comput. Phys.*, **144**, 1, 17–51 (1998).

[59] S. RUNNELS, K. LIPNIKOV, and M. SHASHKOV, "Mathematic and Algorithmic Details for Applying the Local Support Operator Method on Polyhedral Grids," Tech. Rep. LA-UR 10-07498, Los Alamos National Laboratory (2006).

[60] I. V. FRYAZINOV, "Difference Schemes for Two-Dimensional Elliptic and Parabolic Equations with Mixed Derivatives in Polar, Cylindrical, and Spherical Coordinates," *IPM Akad. Nauk SSSR* (1976).

[61] N. N. AKSENOV and V. YA. GOL'DIN, "Computation of the two-dimensional stationary equation of neutron transfer by the quasi-diffusion method," *USSR J. Comp. Math and Math. Phys.*, **19**, 5, 263–266 (1979).

[62] N. D. VALETTE, *Discretization and Solution of Quasi-diffusion Equations*, Master's thesis, Texas A&M University (August 2002).

[63] W. A. WIESELQUIST, *The Quasidiffusion Method for Transport Problems on Unstructured Meshes*, Ph.D. thesis, North Carolina State University (2009).

[64] C. BÖRGERS and S. MACLACHLAN, "An angular multigrid method for computing mono-energetic particle beams in Flatland," *J. Comp. Phys.*, **229**, 8, 2914–2931 (2010).

[65] J. GREENWOOD, "The correct and incorrect generation of a cosine distribution of scattered particles for Monte-Carlo modelling of vacuum systems," *Vacuum*, **67**, 2, 217–222 (2002).

[66] M. R. ZIKA, *Iterative Acceleration for Two-Dimensional Long-Characteristic Transport Problems*, Ph.D. thesis, Texas A&M University (1997).

[67] C. RABITI, E. R. WOLTERS, M. A. SMITH, and G. PALMOTTI, "Spherical Quadratures for the Discrete Ordinates Method," *Trans. Am. Nucl. Soc.*, **96**, 475–476 (2007).

[68] A. H. STROUD and D. SECREST, *Gaussian Quadrature Formulas*, Prentice-Hall (1966).

[69] R. E. MARSHAK, "Theory of the Slowing Down of Neutrons by Elastic Collision with Atomic Nuclei," *Rev. Mod. Phys.*, **19**, 185–238 (1947).

[70] K. M. CASE, F. DE HOFFMANN, and G. PLACZEK, "Introduction to the Theory of Neutron Diffusion," Tech. rep., Los Alamos Scientific Laboratory (1953).

[71] S. R. JOHNSON, "PyTRT: an Open Source Radiation Transport Research Code," (2011), `http://pytrt.org/`.

[72] M. HEROUX, R. BARTLETT, V. H. R. HOEKSTRA, J. HU, T. KOLDA, R. LEHOUCQ, K. LONG, R. PAWLOWSKI, E. PHIPPS, A. SALINGER, H. THORNQUIST, R. TUMINARO, J. WILLENBRING, and A. WILLIAMS, "An Overview of Trilinos," Tech. Rep. SAND2003-2927, Sandia National Laboratories (2003).

[73] G. G. DAVIDSON, J. D. DENSMORE, A. K. PRINJA, and J. E. MOREL, "Asymptotically Correct Angular Distributions for Monte Carlo–Diffusion Interfaces," *Trans. Am. Nucl. Soc.*, **94**, 517–520 (June 2006).

[74] M. D. MCKAY, R. J. BECKMAN, and W. J. CONOVER, "A Comparison of Three Methods for Selecting Values of Input Variables in the Analysis of Output from a Computer Code," *Technometrics*, **21**, 2, 239–245 (1979).

[75] N. A. GENTILE, "Implicit Monte Carlo Diffusion—An Acceleration Method for Monte Carlo Time-Dependent Radiative Transfer Simulations," *J. Comput. Phys.*, **172**, 543–571 (2001).

[76] D. A. KNOLL, R. B. LOWRIE, and J. E. MOREL, "Numerical analysis of time integration errors for nonequilibrium radiation diffusion," *J. Comput. Phys.*, **226**, 2, 1332–1347 (2007).

[77] W. J. RIDER, D. A. KNOLL, and G. L. OLSON, "A Multigrid Newton–Krylov Method for Multimaterial Equilibrium Radiation Diffusion," *J. Comput. Phys.*, **152**, 164–191 (1999).